The Ocean-Continent Transition Along The Northeast Brazilian Rifted Margin

THESIS SUBMITTED IN ACCORDANCE WITH THE REQUIREMENTS OF THE UNIVERSITY OF LIVERPOOL FOR THE DEGREE OF DOCTOR IN PHILOSOPHY

BY GILVAN PIO HAMSI JUNIOR

OCTOBER 2010

To Vânia, Isadora and Beatriz.

Acknowledgements

This training opportunity was provided and sponsored for me as an employee of Petrobras through the decisive support from the E&P Director, Dr. Guilherme de Oliveira Estrella, and from the exploration executive managers: Dr. Mario Carminatti, Dr. Paulo de Tarso Guimarães and Paulo Manuel Mendonça.

Prof. Nick Kusznir provided me a high level scientific orientation, based on stimulating discussions, which kept me always in high spirits. I am grateful for the use in my research the software *FlexDecomp*, the program for the Gravity Inversion and the sub-routine to calculate flexural isostatic compensations.

I dedicate special thanks to the exploration manager at PETROBRAS/UN-SEAL in Aracaju, Brazil, Dr. Sergio Luciano Moura Freire, who encouraged me to seek an international PhD degree.

I would like to extend thanks for all at the University of Liverpool who provided me all the needed support, in particular to the staff at the Earth and Ocean Sciences Department: Ian Bamber, Jeanette Brown, Alan McCormack, Maureen Dodd, Moira Ginelly, Paula Houghton, Chris Hunt and Helen Kokelaar.

The two missions for seismic interpretation in Brazil could be accomplished by the support from Petrobras exploration managers: Dr. Sylvia Maria Couto do Anjos, Dr. José Antonio Cupertino, Dr. Almério Barros França and Dr. Luiz Antonio Trindade in Rio de Janeiro, and Braulio Oliveira Silva, James Vitor Ferreira and Aluísio Santos Junior in Aracaju.

I was benefited from valuable technical discussions with explorationists Manoel Nabuco and Fernando Barros in Aracaju, among others. The exploration technician Weliton Athaide of Petrobras, Aracaju, was always available to help me with the seismic data management. I am very grateful to the exploratory team of East Brazilian Coast in Rio who provided me the interpretations and depth conversion of the Jacuipe and Almada cross-sections: Claudir Francisco, Fabrizio Dias Lima, Talles Souza Ferreira and Mirnis Araujo Nóbrega.

I wish to dedicate especially warm gratitude to the geophysicist Geraldino Queiroz Setúbal from Petrobras, Aracaju, who generously helped me with the depth conversion of the seismic sections from Sergipe, Alagoas and Pernambuco Margins. The geophysicist Celso Moura Jardim from Petrobras, Rio, was also more than a colleague, a friend, always available to help me with the seismic interpretation and data management. I am grateful to my friends geologists Marcos Domingues and Dario Chiossi for the valuable discussions about the subject..

My expatriated life was made easy by the competent support of the human resources team of Petrobras exploration headed by Ms. Lucila Reis. I could also account to the kind assistance of the secretaries Mrs. Enilde in Aracaju, Ms. Aparecida Flor and Ms. Carmen Oliveira in Rio.

I could enjoy a nice academic companionship among the Earth Structure and Geodynamics Group. I am especially grateful to Erica Greenhalgh, Ricardo Angelo Santos Silva and Roseanna Fletcher for their patience.

My colleagues at Petrobras and friends Jorge Picanço de Figueiredo and Carlos Mauricio Monnerat de Oliveira and their families, who preceded me at the Department, made my adaptation in Liverpool easier, presenting the “keys” to Liverpool.

ABSTRACT

The aim of this thesis was (i) to develop analytical methodologies and a workflow to identify the ocean-continent transition (OCT) and to locate the continent-ocean crustal and lithosphere boundaries (COCB and COLB) at continental rifted margins and (ii) to apply these methodologies and workflow to six cross-sections of the Northeast Brazilian rifted margin. The six cross-sections were taken from the margin segments Almada-Jequitinhonha, Jacuípe, Sergipe, Alagoas and Pernambuco and were constructed using seismic reflection sections from the borders of sedimentary basins to the oceanic crust. The OCT of the Northeast Brazilian rifted margin is complex due to variable extrusive and intrusive magmatism and antithetic tectonics. COCB locations interpreted on seismic reflection data have been tested with those determined using the analytical methodologies and workflow developed in this study.

The workflow comprises: 1) the determination of sediment-corrected basement depth profiles, 2) the analysis of the residual depth anomalies of the oceanic crust and its extrapolation into the rifted margin, 3) the gravity inversion of the Moho with crustal thinning determination and 4) the inversion of lithosphere thinning using subsidence analysis. The calibration of the gravity inversion through the fit of the residual depth anomaly in unequivocal oceanic crust is a new approach to determine the reference Moho depth in areas without seismic refraction data.

The Almada-Jequitinhonha OCT corresponds to a region of antithetic faulting and low free-air gravity anomaly. The Jacuípe OCT corresponds to a region of development of normal magmatic addition, expressed in the seismic sections as seaward-dipping reflectors, and has a relatively high free-air gravity anomaly. Although the Jacuípe margin represents a narrow rift, this margin seems to be wider and offshore syn-rift sediments are either not imaged or have been eroded. The Sergipe margin is interpreted as being magma-poor during rifting and evolved to slightly magma rich in the early post-rift. The OCT corresponds to a region of continental crust thinner than the adjacent oceanic crust, with antithetic faulting and a stable free-air gravity anomaly. The Alagoas margin is interpreted as being magma-poor during rifting and evolved to normal magmatic addition in the early post-rift, while the Pernambuco margin is interpreted as being slightly magma-rich. The OCT of both margins corresponds to a region of synthetic and antithetic faulting with a low free-air gravity anomaly.

The predicted COCB and COLB locations for each cross-section tend to be similar to each other. Only minor differences between the crustal and lithosphere thinning profiles have been observed. The rifted margin width, measured along the cross-sections, does not vary significantly in the South between Almada-Jequitinhonha and Sergipe North, ranging from 110 to 130 km. While, in the North between Alagoas and Pernambuco it is wider, around 170 km. The Northeastern Brazil margin varies from magma-poor in the Almada-Jequitinhonha region to slightly magma-rich in Sergipe and Pernambuco, both probably affected by the Santa Helena Hot Spot. The workflow developed here can be considered successful in locating the COCB and COLB positions and in identifying the OCT in the cross-sections across the Northeast Brazil margin and can be applied to other rifted margins without seismic refraction data.

CONTENTS

FIGURES

TABLES

CHAPTER 1

1. INTRODUCTION

1.1 AIM

A continental rifted margin comprises the gradual transition from a thick and less dense continental lithosphere to a thinner and denser oceanic lithosphere. The ocean-continent transition (OCT) is assumed as the region where the continental lithosphere is intensely thinned and where complex tectonics, variable magmatism and possible mantle exhumation make the identification of the continent-ocean boundary (COB) difficult. Moreover, the distal limit of the continental crust may not coincide with the distal limit of the continental lithosphere mantle (Roberts et al., 1998; Whitmarsh et al., 2001), in which case the continent-ocean crustal boundary (COCB) is distinct from the continent-ocean lithosphere boundary (COLB).

Continental rifted margins are important frontiers for petroleum exploration at the present. Although reservoir rocks occur all through the sedimentary pile, petroleum systems are constrained by the presence of source rocks, mostly confined to the syn-rift sedimentary succession. Syn-rift sediments are deposited over continental crust; therefore the COCB is an important distal constraint for the petroleum systems developed in continental rifted margins. Additionally, continental rifted margins are also a scientific frontier. The nature of the OCT and the COCB and COLB locations are generally unclear due to: a) scarcity of well data, b) poor quality of the available seismic data, c) tectono-sedimentary complexity and d) only recently identified geological analogues.

This research has two aims:

1. The development of a workflow to identify the OCT and to locate the COCB and COLB in continental rifted margins transversal cross-sections, through a sequential application of a set of analytical techniques to geological cross-sections and gravity data.
2. The application of the workflow for the OCT identification and location of the COCB and COLB in six geological cross-sections of the Northeast Brazilian rifted margin.

1.2 THE SCIENTIFIC PROBLEM

Continental rifted margins formation can be considered as the result of a chain of changes in the mass distribution in the lithosphere and their resulting isostatic compensation, which leads to either subsidence or uplift (Chang et al., 1991). Continental rifted margins develop as a consequence of the extensional forces that split continents apart during the rift phase and through the dissipation of the lithosphere and asthenosphere thermal anomaly in the post-rift. Crustal and continental lithosphere thinning determine the fundamental isostatic loads created during the syn-rift phase. Sedimentation occupies space created by the isostatic response to the syn-rift crustal and lithosphere loads and generates additional isostatic load and subsidence. Continental lithosphere thinning leads to additional load from magmatic addition by decompression melting, which counteracts the crustal thinning load. During post-rift times, lithosphere cooling loads promote additional subsidence, which allows additional sedimentary loading.

Figure 1.1a shows a schematic lithosphere-scale cross-section of a typical continental rifted margin, modified from. The distinction between the syn and post-rift packages and the boundary between old continental and new oceanic lithospheric

mantle have been added to the original figure. The model shows that a continental rifted margin comprises a fault controlled continental basement, covered by a syn-rift sedimentary package that pinches out towards the oceanic crust. The syn-rift blocks and the oceanic crust are both overlain by a less deformed post-rift sedimentary package, deposited after continental break-up. A typical ocean-continent transition would be related to an average 7.1 km-thick adjacent oceanic crust (White et al., 1992).

In this classical model, it is generally assumed that the position where the continental lithosphere mantle pinches to zero thickness corresponds to the contact between the continental and oceanic crusts (figure 1.1a). However, the simplicity of such sharp and vertical COB hides a much more complex situation. The continental rifted margins have as end-members, magma-poor and magma-rich margins, which are shown in figures 1.1b and c, respectively.

Recent investigation of the magma-poor West Iberia margin (Roberts et al., 1998; Whitmarsh et al., 2001) have shown that the distal limit of the continental crust can be separated from the oceanic crust by an up to 200 km-wide zone of exhumed continental mantle (figure 1.1b). In this case, the COCB and the COLB are distinct. Magma-rich margins (figure 1.1c) are characterized by a wide zone occupied by sub-aerial extrusive igneous rocks as seaward-dipping reflectors (SDR) and crust thickened by a high velocity layer (figure 1.1c), interpreted as underplated or intruded mafic-ultramafic rocks (Gladczenko et al., 1997; Hinz, 1981; Skogseid, 2001; White and McKenzie, 1989; White et al., 2008). The seaward-dipping reflectors spread across the OCT, from the oceanic to the continental crust (White et al., 1987). The increasing presence oceanward of intrusive and extrusive magmatic

bodies is observed in magma-rich as well as in normal margins. Therefore, the COB can also be difficult to locate in normal and magma-rich margins.

Additionally, complex extensional tectonics with fault system exhumation and re-rifting are generally observed in magma-poor OCT (Reston, 2009). However, in many magma-poor and magma-rich margins where thinning can be measured for different levels of the continental lithosphere, stretching of the brittle upper crust is generally less than thinning of the whole lithosphere and of the whole crust implied by a depth-uniform stretching and thinning model (Davis and Kusznir, 2004; Karner and Driscoll, 1999; Karner et al., 2003). Hence, some continental rifted margins appear to have been formed by depth-dependent lithosphere thinning and stretching (Menezes and Milhomem, 2008).

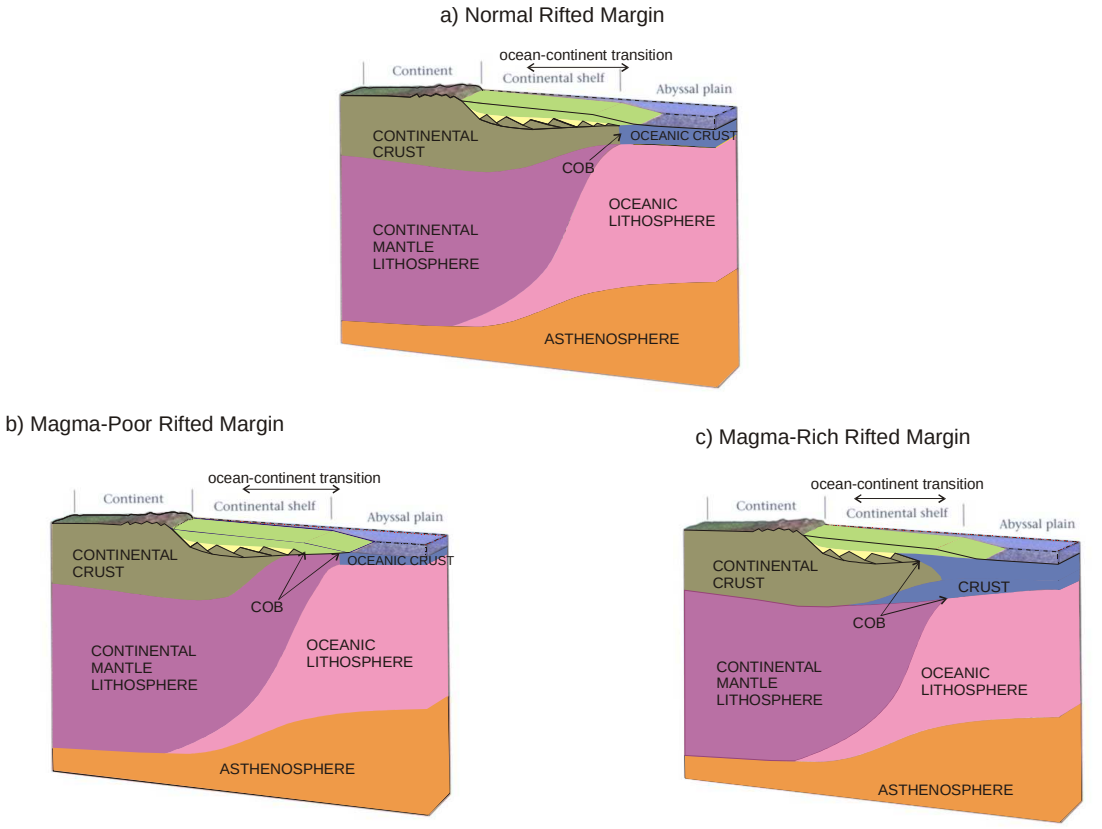

Figure 1.1: Schematic models of continental rifted margins based on (Marshak, 2008). The limits between continental mantle and oceanic lithosphere were added, as the division between syn and post-rift sedimentary packages. The simple COB is idealized for a) normal rifted margins, but it can be difficult to identify in b) magma-poor and c) magma-rich margins

Thick piles of evaporite salt rocks can be formed in continental rifted margins during the transition between the syn-rift and post-rift phases. While evaporitic layers constitute an important element of the petroleum systems as an effective seal for petroleum migration, these layers are a challenge for reflection seismic surveys by absorbing energy that should sample the syn-rift and basement. The structural complexity of rifted margins OCTs, allied to increasing volcanism and the possible presence of salt layers contribute to the poor quality of the available seismic reflection data, which are also biased towards economic targets. Besides the complex setting and poor sampling, studies of ocean-continent transition analogues are only recently available, especially from magma-poor settings. These analogue studies confirm the structural complexity and mantle exhumation zones, initially observed at the Iberia-Newfoundland continental rifted margins by seismic and well data, in a Tethys margin preserved in the Swiss Alps (Kusznir and Karner, 2007; Manatschal, 2004).

1.3 Workflow to Identify the OCT and to Locate the COCB and COLB

Numerical analysis and modelling of geological and geophysical data can be used to determine the architecture of the ocean-continent transition and to place the locations of the continent-ocean crustal and lithosphere boundaries. The numerical techniques applied in this research are based on the identification of mass distribution heterogeneities in the lithosphere in order to determine the crustal and lithosphere thinning. Crustal and lithosphere thinning are the fundamental loads created in the syn-rift phase, which also control the thermal maturation of petroleum source rocks.

The workflow comprises the application of four interconnected numerical techniques (figure 1.2): 1) removal of the sedimentary loads of the geological cross-sections through flexural backstripping, 2) analysis of the oceanic crust residual depth anomalies (RDA), 3) gravity inversion of the Moho and 4) subsidence analysis for the numerical inversion of the lithospheric thinning. Gravity anomalies are the main data for the gravity inversion, while geological cross-sections are the main data for the flexural backstripping, RDA analysis and for the numerical inversion of the lithospheric thinning, as like as auxiliary data for the gravity inversion. The sequential workflow starts with the subsidence analysis through flexural backstripping of the cross-sections resulting in sediment-corrected basement depth profiles, step 1 in figure 1.2. Then, the workflow follows with the application of the three main numerical techniques:

1. Determination of the residual depth anomalies (RDA) in the OCT and in the unequivocal oceanic crust segments of the sediment-corrected basement profiles, constraining the oceanic igneous crust thickness, steps 2 and 3 in figure 1.2.

2. Gravity inversion of the Moho in the 3D spectral domain with iterative correction of the lithosphere thermal gravity anomaly, steps 4 and 5 in figure 1.2. From the Moho determination, crustal thickness and crustal thinning are also calculated. The gravity inversion is calibrated with the RDA obtained previously in the true oceanic crust segments and constrains the initial crustal thickness.

3. Lithosphere thinning profiles are inverted from the sediment-corrected basement profiles with a new numerical method, using the magmatic addition

constrained by the RDA analysis and the crustal thickness determined in the gravity inversion, step 6 in figure 1.2.

1.4 THE STUDIED AREA

The numerical techniques workflow to identify the OCT and to locate the COCB and the COLB was applied to six cross-sections of the Northeast Brazilian margin, situated between parallels 15^{o}S and 8^{o}S and meridians 32^{o}W and 39^{o}W (figure 1.3). The Northeast Brazilian rifted margin was formed during the second phase of rupture of the Gondwana Supercontinent, with lithosphere stretching and thinning from 144 to 112 Ma (Chang et al., 1992) and break-up eventually reaching the region around Late Aptian to Early Albian (115 to 110 Ma) (Nürnberg and Müller, 1991; Storey, 1995).

Important variations in the sedimentary infill along the segments of this margin reflect differences in the subsidence patterns, controlled by lithosphere thinning. Lack of seismic refraction data and continental break-up during the Early Cretaceous quiet magnetic zone anomaly make the study of this margin particularly challenging. Schematic lithosphere stretching models of simple shear lithosphere stretching (Wernicke, 1985), based on gravity data and on geological observations (Castro, 1987; Karner et al., 1992; Ussami et al., 1986), have been proposed to explain the relationship between the Jacuípe, Sergipe and Gabon rifted margins with the aborted Reconcavo-Tucano-Jatobá rift. However, no study has tried to measure crustal and lithosphere thinning in regional cross-sections.

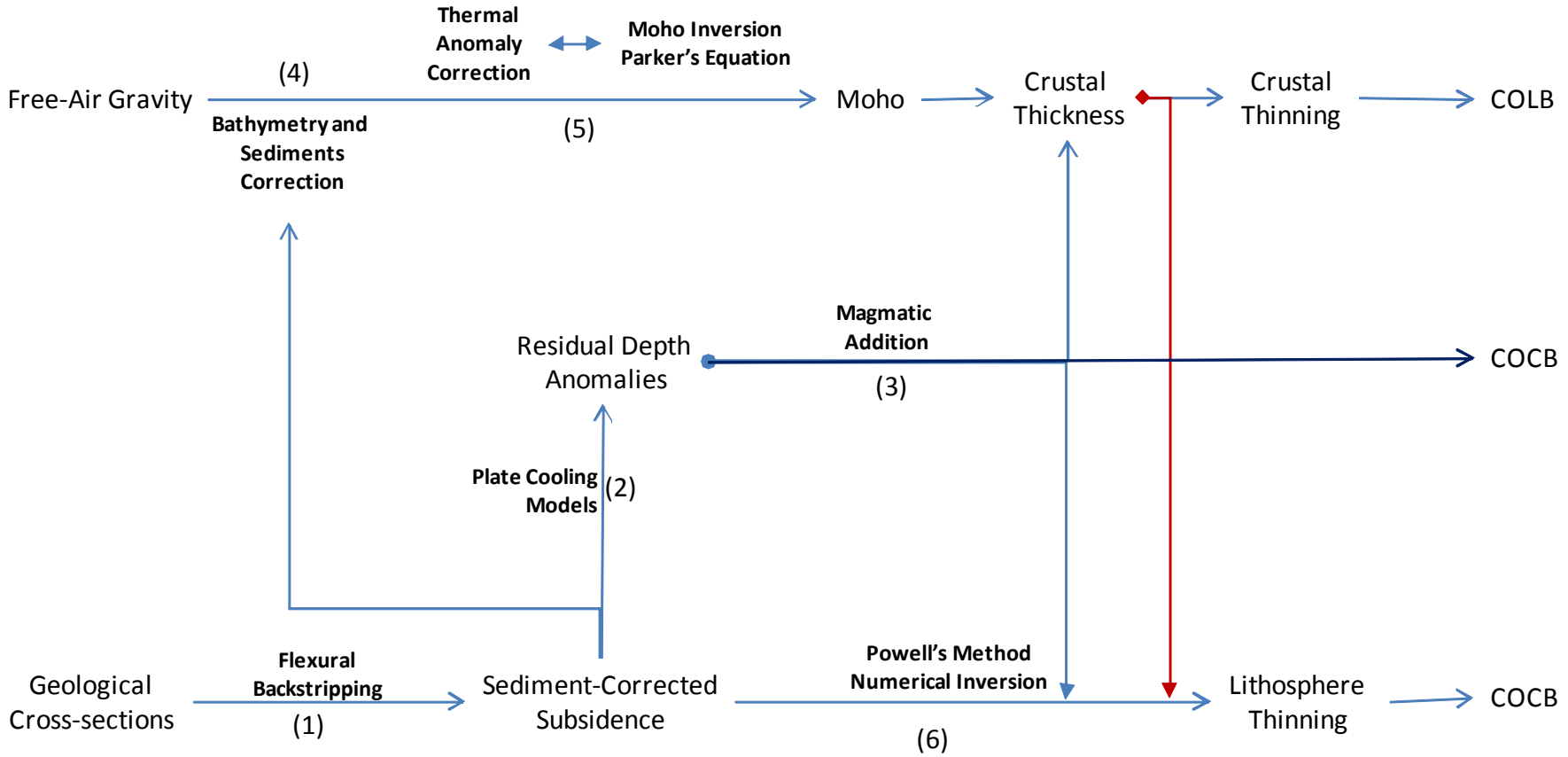

Figure 1.2: Workflow for identification of the ocean-continent transition and location of the continent-ocean crust and lithosphere boundaries.

Data is unevenly distributed in the area, concentrated in the Sergipe-Alagoas margin. The cross-sections have been constructed by integration of reflection seismic sections from the sedimentary basins borders to the oceanic crust, constrained wherever possible, by well data. The continent-ocean crustal boundary locations have been initially interpreted in the reflection seismic sections, but are generally uncertain.

1.5 THESIS STRUCTURE

- Review of the geodynamic processes involved in the formation of continental rifted margins with emphasis on the contribution and limitations of the depth-uniform lithosphere stretching model is presented in Chapter 2.
- The geodynamic setting of Northeast Brazilian rifted margin is presented in Chapter 3.
- Chapter 4 presents description of the six cross-sections, identifying the OCT and the COCB from the reflection seismic interpretation.
- Chapter 5 presents the sediment-load correction of the six geological cross-sections studied in this thesis through the flexural backstripping technique, which results in sediment-corrected basement depth profiles from the margin borders to the oceanic crust.
- Chapter 6 presents the residual depth anomaly analysis for the OCT and unequivocal oceanic crust segments of the cross-sections, with emphasis on the relationship between the RDA and igneous oceanic crust thickness. Inflections in the RDA profile suggest the COCB in some cross-sections, which are compared to the seismic interpretations.

- Chapter 7 presents the gravity inversion of the Moho with the lithosphere thermal gravity anomaly correction. Crustal thinning profiles are the main results of the gravity inversion and indicate the COCB locations, which are compared to the seismic interpretations and to the RDA estimates.
- Chapter 8 presents the development of a new forward numerical calculation of total subsidence according to lithosphere thinning, based on the dissipation of the continental lithosphere thermal anomaly in the post-rift. The numerical model incorporates magmatic addition, depth-dependent thinning, radiogenic heat contribution from the crust and flexural isostatic response.
- Chapter 9 presents the modifications in the total subsidence model developed in chapter 8 in order to incorporate the effects of continental shields lithosphere: a) the correction of subsidence calculation for initial elevation, according to the continental lithosphere thickness, and b) the variable lower boundary depth condition for the dissipation of the thermal anomaly from a steady state continental lithosphere at the margin border to an old oceanic lithosphere at the COLB.
- Chapter 10 presents the mathematical formulation developed to invert lithosphere thinning from the total subsidence model developed in chapters 8 and 9.
- Chapter 11 presents the lithosphere thinning inversion results of the studied Northeast Brazilian rifted margin cross-sections.
- The results of the three analytical techniques applied are compared and discussed in Chapter 12, and Chapter 13 summarizes the methodology and results.

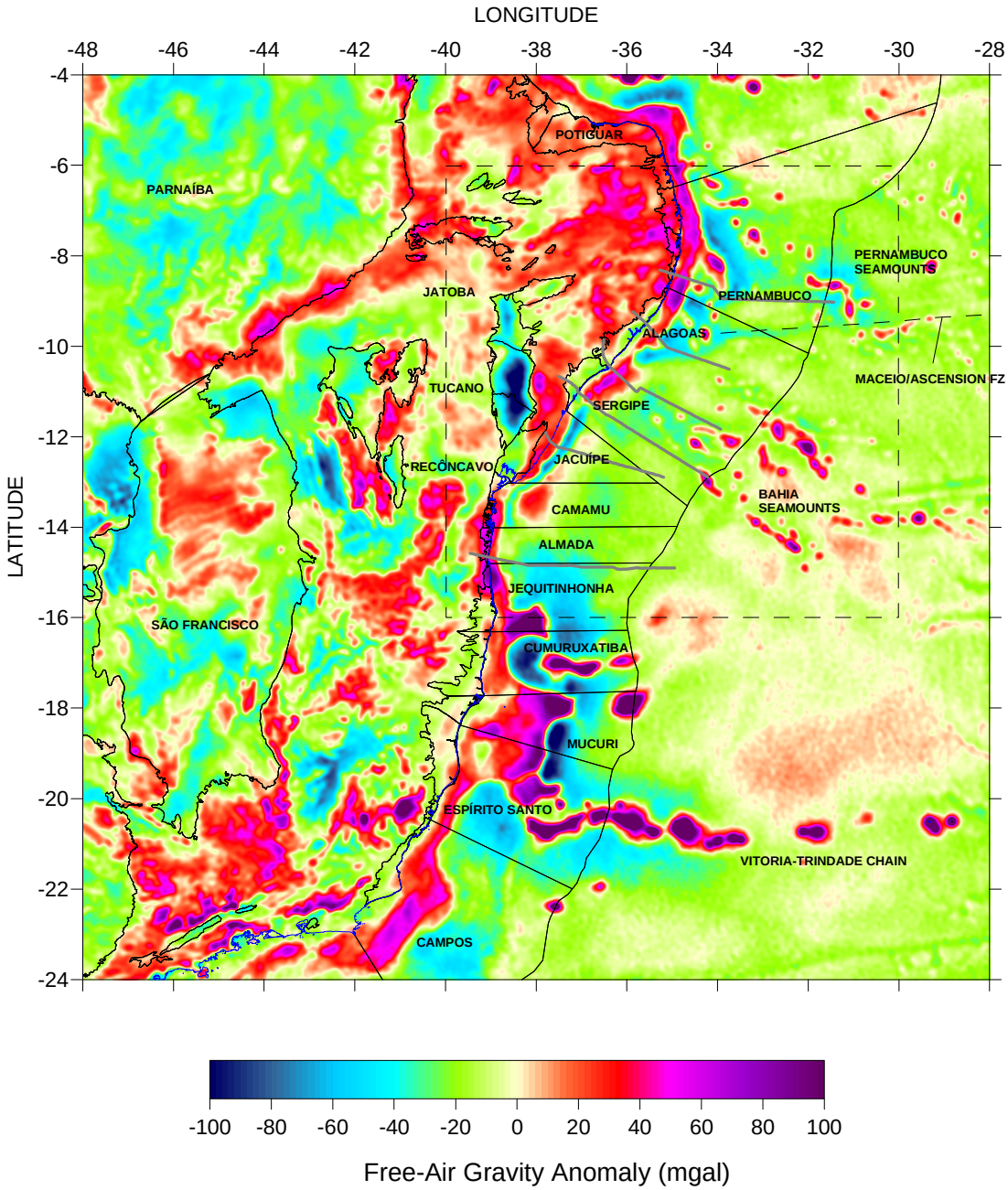

Figure 1.3: Free-air gravity anomaly map of East Brazilian margin, extracted from recent satellite and onshore compilation (Sandwell and Smith, 2009). The studied area comprises the hatched square. Sedimentary basins limits are shown in thin black line and geological cross-sections in thick grey lines.

CHAPTER 2

2. GEODYNAMIC PROCESSES INVOLVED IN THE FORMATION OF CONTINENTAL RIFTED MARGINS

2.1 INTRODUCTION

The aim of this chapter is to review the concepts behind the numerical methods used in this research. Initially, a review about the physical characteristics of the lithosphere is introduced. The crustal and lithosphere thinning loads developed in the rift phase are the fundamental loads that define the continent-ocean crust boundary and the continent-ocean lithosphere boundary, respectively, and result in syn-rift subsidence. Crustal and lithosphere thinning loads are presented according to the depth-uniform stretching model . The increasing load due to the post-rift lithosphere cooling generates thermal subsidence, which is presented as a comparison between the predictions of the depth-uniform lithosphere stretching model (McKenzie, 1978) and the lithosphere plate cooling model(Parsons and Sclater, 1977). Magmatic addition by decompression melt must be taken into account for the determination of the crustal and lithosphere thinning. Magmatic addition is a consequence of lithosphere thinning and can be evaluated from the residual depth anomaly analysis of oceanic bathymetry. The sediments mass must be corrected for the gravity inversion of the Moho and the sedimentary loads, controlled by compaction, are corrected from the geological cross-sections by flexural backstripping. Finally, the limitations of the depth-uniform lithosphere stretching model are discussed as a basis to the improvements proposed in the forward subsidence model developed in this research.

2.2 CONTINENTAL AND OCEANIC LITHOSPHERE

The isostatic response to load variations in the lithosphere depends on its initial thickness and composition. Continental shields and oceanic lithosphere are two end members (figure 2.1). The continental lithosphere of shields was formed prior to the Paleoproterozoic and can reach a thickness greater than 250 km (Jaupart and Mareschal, 1999). The composition and thickness of continental lithosphere change across rifted margins towards those presented by oceanic lithosphere. Continental lithosphere stabilized after the Paleoproterozoic are thinner than 250 km but thicker than the 100 km predicted thickness for oceanic lithosphere older than 80 My (Crosby et al., 2006) (figure 2.1). Heat flow at the base of lithosphere varies from 13-18 mW m^{-2} in shields (Jaupart and Mareschal, 1999) to around 30 mW m^{-2} in old oceans (Parsons and Sclater, 1977), suggesting variation in the convective heat flow in the asthenosphere under the different lithosphere types.

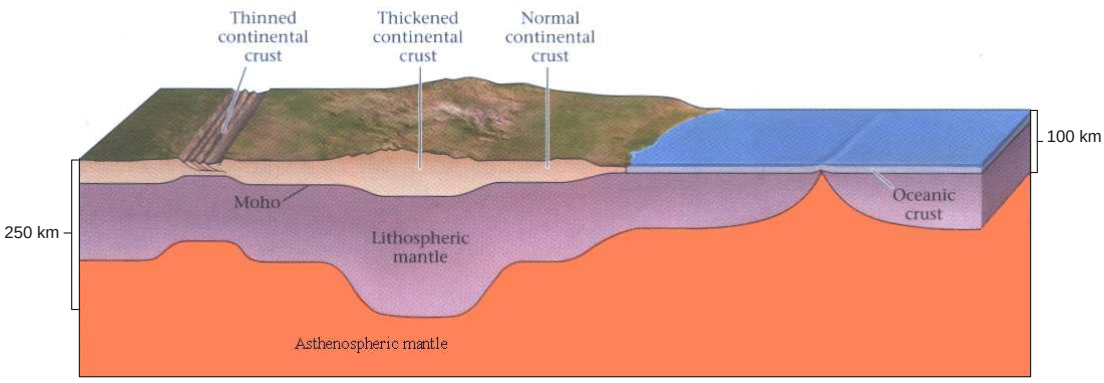

Figure 2.1: Schematic cross-section of the lithosphere from continental interiors to oceanic region, modified from (Marshak, 2008).

Composition is a major control on the density of a lithosphere column. The shallower crust presents an average 41 km thickness in the continents (Christensen and Mooney, 1995) and around 7 km in the oceans (White et al., 1992), while the thickness of lithospheric mantle ranges from 100 to 200 km (figure 2.1). The continental crust density varies from around 2700 kg m^{-3} at the surface to more than

2900 kg m^{-3} at the base, and the global average density ρ_{cc}^{a}, according to seismic velocity data, is 2830 km m^{-3}(Christensen and Mooney, 1995). The average oceanic crust density is slightly higher, ρ_{oc}^{a}=2860 km m^{-3} (Carlson and Herrick, 1990). Mantle rocks are much denser than the crust, ρ_{m}^{0}=3300 km m^{-3}.

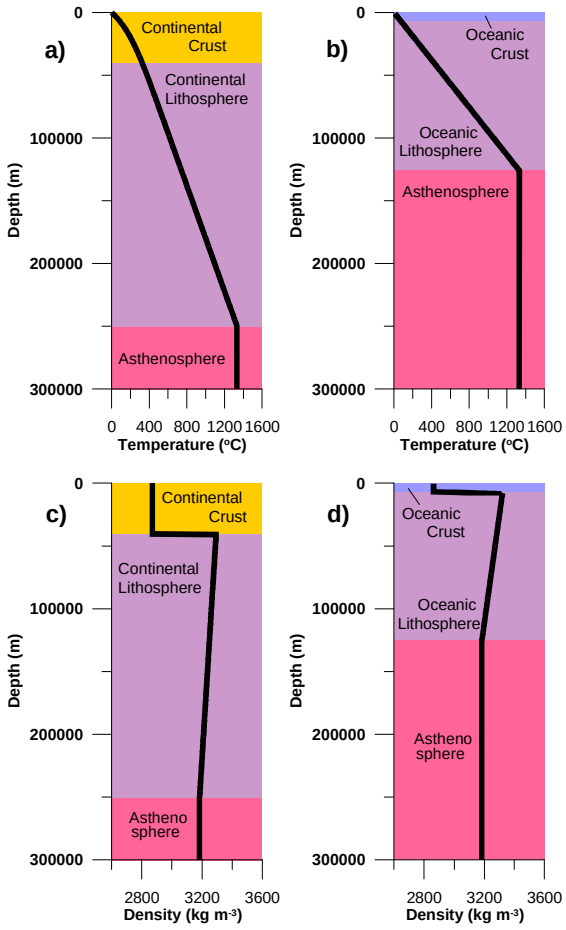

Figure 2.2: Temperature and density variation through lithosphere columns in thermal equilibrium: a) and b) temperature profiles of continental and old oceanic lithospheres, respectively; c and d: density profiles of continental old oceanic lithosphere, respectively.

Like composition, temperature has a strong effect on lithosphere density, which decreases in depth until asthenosphere temperature is reached (figure 2.2.a and b). Heat flows through the lithosphere mainly by conduction from the hot lower boundary to the surface (Turcotte and Schubert, 2002). Enrichment in radioactive elements in the continental crust adds more heat to the flow that comes up from the thermal boundary at the base of lithosphere. Therefore, the geotherm in thermal

equilibrium of a continental lithosphere is curved (figure 2.2.a), while the geotherm of an old oceanic lithosphere is linear from the surface to the base of lithosphere (figure 2.2.b).

2.3 The Depth-Uniform Lithosphere Stretching Model (McKenzie, 1978)

The depth-uniform lithosphere stretching model (McKenzie, 1978) (DULSM) laid the basis to understanding the consequences of continental lithosphere extension by homogeneous pure shear (figure 2.3). This simple model explains the consequences of the crustal and lithosphere thinning isostatic loads in extensional settings. Crust and lithospheric mantle are assumed to deform equally.

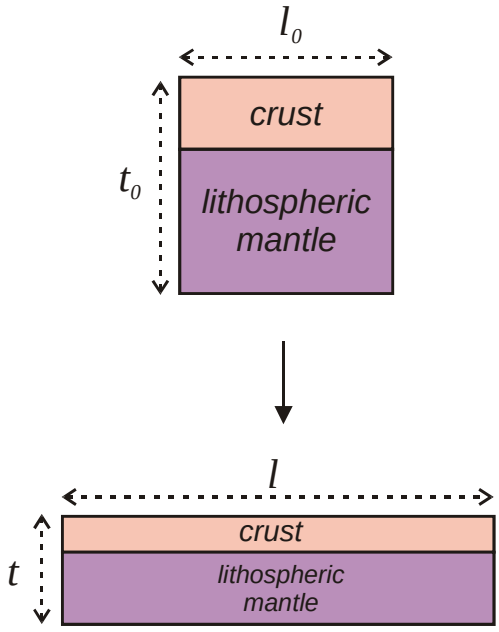

Figure 2.3: Schematic representation of the depth-uniform lithosphere stretching and thinning model by pure shear, modified from (McKenzie, 1978).

The stretching factor, β, is the ratio between final and initial lithosphere lengths, l and l_0 , respectively (McKenzie, 1978). Homogeneous pure shear implies that the stretching factor β also corresponds to the ratio between initial, t_0, and final lithosphere thickness, t:

$$\beta = \frac{l}{l_0} = \frac{t_0}{t}. \qquad (2.1)$$

The required data to determine stretching in a continental margin or in a sedimentary basin are cross-sections that cut across whole margins, but they are not commonly available. So, stretching factor β has been frequently determined from 1D thinning measurements, assuming depth-uniform lithosphere thinning. The transformation of the stretching factor to a thinning factor γ (Hellinger and Sclater, 1983) can be useful:

$$\gamma = 1 - \frac{1}{\beta}. \qquad (2.2)$$

While the stretching factor β varies from 1 to infinitum, the thinning factor γ varies from 0 to 1. In this research, the deformation of the lithosphere is referred to the thinning that can be treated according to the loads profiles developed during the evolution of continental rifted margins and their flexural isostatic compensations. In the depth-uniform stretching model, instantaneous and local isostatic compensation is assumed for the two distinct loads created by lithosphere thinning (McKenzie, 1978): a) crustal thinning load and b) lithosphere thinning thermal load.

CRUSTAL THINNING LOAD

Thinning of the crust results in a positive load at the lithosphere (L_{ct}) due to the substitution of crustal rocks by denser mantle rocks (figure 2.4), expressed by:

$$L_{ct} = \Delta t_c \left(\rho_m^a - \rho_c^a\right) g, \text{ or} \qquad (2.3.a)$$

$$L_{ct} = \left(t_c - \frac{t_c}{\beta}\right)\left(\rho_m^a - \rho_c^a\right) g, \text{ or} \qquad (2.3.b)$$

$$L_{ct} = t_c \cdot \gamma \cdot \Delta\rho \cdot g, \qquad (2.3.c)$$

where t_c is initial crustal thickness, Δt_c is the change in crustal thickness, ρ_c^a is average crustal density, ρ_m^a is average mantle density and g is the acceleration of gravity, approximately 9.78 m s^{-1}. The positive crustal load contributes with subsidence to the isostatic compensation of lithosphere thinning (figures 2.4.c and 2.6.a). Crustal thinning is a permanent feature in the margin that can be determined from gravity anomalies, Chapter 7.

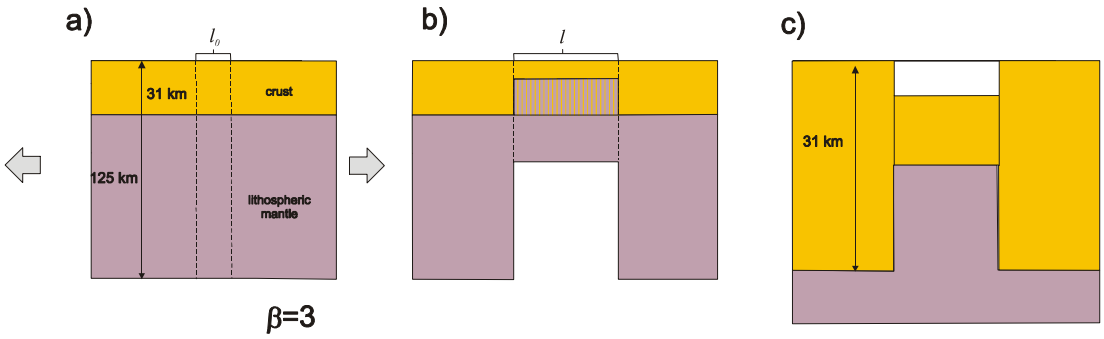

Figure 2.4: Schematic representation of the crustal thinning load according to the DULSM for β=3. a) Initial situation. b) Thinning and stretching of the central region (l_0). Crustal load corresponds to the hatched area. c) Subsidence as result of the local isostatic compensation.

LITHOSPHERE THINNING THERMAL LOAD

The depth-uniform lithosphere stretching model (McKenzie, 1978) assumes that density decreases linearly with temperature along a reference continental lithosphere rock column, similarly to an old ocean lithosphere (figure 2.2.b), ignoring the contribution of heat produced in the crust. Therefore, lithosphere thinning generates a thermal load due to the increase in the geothermal gradient (figure 2.5.a-b):

$$L_{th} = \int_0^\infty \Delta T \alpha \rho_m^0 g dz = \alpha \rho_m^0 g \int_0^\infty \Delta T dz \,, \qquad (2.4)$$

where α is the thermal expansion coefficient (table 2-1), $\rho_m^{\,0}$ is the density of mantle rocks at surface and ΔT is the temperature difference between the thermally perturbed and the original geotherm. The negative syn-rift thermal load contributes

with uplift to the isostatic compensation of lithosphere thinning (figures 2.5c and 2.6.b).

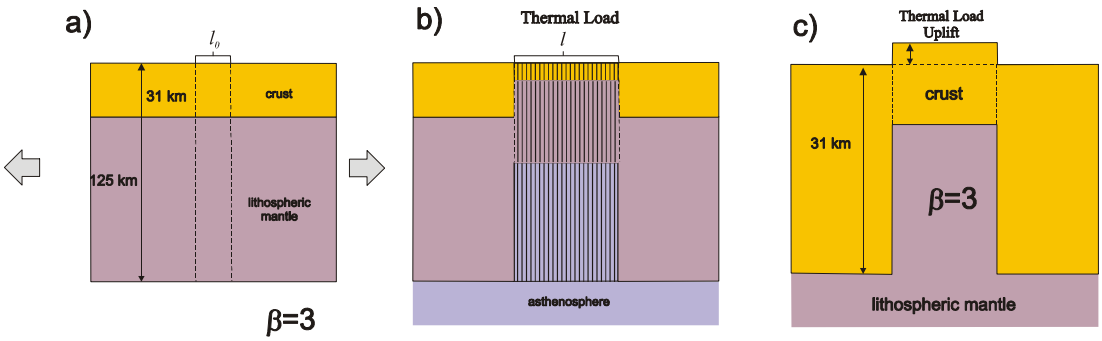

Figure 2.5: Schematic representation of the thermal load according to the DULSM for β=3. a) Initial situation. b) Thinning and stretching of the central region (l_0). Thermal load corresponds to the hatched area. c) Uplift as result of the isostatic compensation.

INITIAL SUBSIDENCE

The combined effects of the crustal and thermal loads in the syn-rift are expressed through the analytical solution of the initial subsidence (McKenzie, 1978):

$$S_i = \frac{a\left[\left(\rho_m{}^0 - \rho_c{}^a\right)\frac{t_c}{a}\left(1-\alpha T_1\frac{t_c}{2a}\right)-\frac{\alpha T_1 \rho_m{}^0}{2}\right]\left(1-\frac{1}{\beta}\right)}{\rho_m{}^0\left(1-\alpha T_1\right)-\rho_w}, \qquad (2.5)$$

where a is the initial lithosphere thickness, T_1 is the temperature at the base of lithosphere and ρ_w is water density.

The subsidence contribution from the crustal load to the isostatic compensation is greater than the uplift contribution from the thermal load for initial crustal thickness larger than 18 km and an average crustal density of 2800 kg m^{-3} (McKenzie, 1978) (figure 2.6.c).

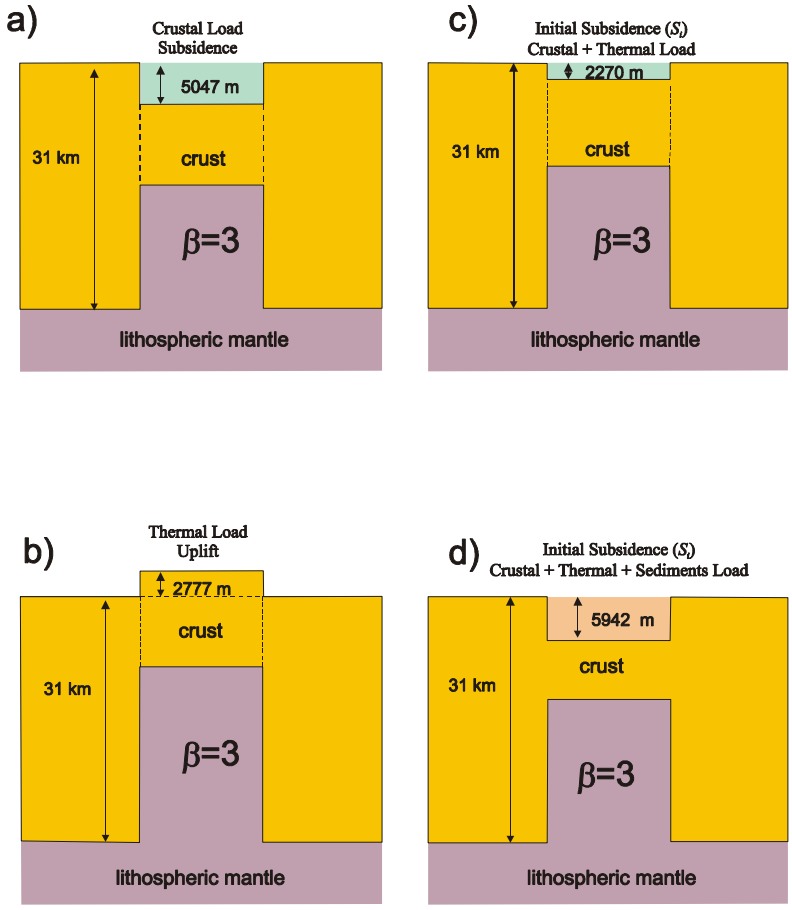

Figure 2.6: Schematic representation of the isostatic compensations due to lithosphere thinning of β=3, according to the DULSM. a) Crustal load. b) Thermal load. c) Crustal plus Thermal loads. d) Crustal plus Thermal plus Sediments loads.

2.4 POST-RIFT THERMAL SUBSIDENCE

Dissipation of the thermal anomaly by cooling changes asthenosphere into lithosphere and increases the lithosphere density and thickness with time (McKenzie, 1978). The increased weight of the rock column thus generates a positive load, which causes post-rift subsidence. Sedimentary load can further amplify the thermal subsidence. Post-rift subsidence is the only information available to determine the thermal load.

The lithosphere plate cooling model was developed to explain the evolution of an oceanic plate (Parsons and Sclater, 1977). The depth-uniform lithosphere stretching model is an extrapolation of the plate cooling model for a general case

where thinning of the continental lithosphere is controlled by the stretching factor β (McKenzie, 1978). A discussion of the lithosphere plate cooling model with its implications for the depth-uniform lithosphere stretching model is presented below as it lays the basis of the lithosphere cooling loads. The lithosphere plate cooling model is also relevant for the determination of the residual depth anomaly of oceanic bathymetry in Chapter 6.

2.4.1 THE LITHOSPHERE PLATE COOLING MODEL

Sediment-corrected sea-floor depths from the Pacific and North Atlantic oceans, averaged at magnetic anomalies ages (figure 2.7), were shown to increase with time from the depth presented at the mid-ocean ridges, around 2500 m, to around 6200 m at old ocean crusts (Parsons and Sclater, 1977). These oceanic regions present the oldest oceanic crusts preserved, around 150 and 160 Ma respectively, which permit the construction of the most complete datasets.

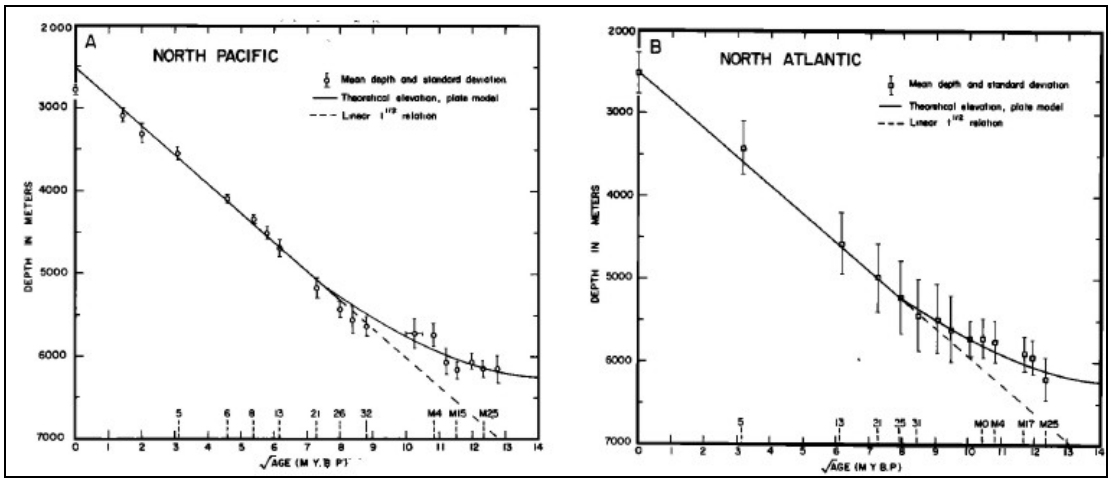

Figure 2.7: Sediment-corrected oceanic bathymetry evolution plotted against squared age from (Parsons and Sclater, 1977): A) North Pacific data, B) North Atlantic data. Dashed line corresponds to the square root relationships, while continuous line corresponds to exponential decay fits.

The data show that the oceanic crust bathymetry decay from the mid-ocean ridge is fast in the initial 60 Myr according to a square root relationship with time

(figure 2.7a-b). However, sediment-corrected oceanic bathymetry increases slower after around 60 Myr according to an exponential relationship, reaching a constant value for large cooling times (Parsons and Sclater, 1977). Although more scattered, heat flow measurements at the surface also decrease quickly away from the mid-ocean ridge, from more than 100 mW m^{-2} until they stabilize around 33 mW m^{-2} in old oceanic crust (Parsons and Sclater, 1977; Sclater et al., 1981).

The lithosphere plate cooling model (figure 2.8a) explains the evolution of bathymetry and surface heat flow of an oceanic plate as consequence of the isostatic equilibrium of an increasing lithosphere plate thickness, limited by a constant upward heat flow from the asthenosphere (Parsons and Sclater, 1977; Turcotte and Schubert, 2002). The thermal anomaly is caused by a column of asthenosphere that reaches the surface, being later dissipated by conductive cooling as it moves away the mid-ocean ridge by sea-floor spreading.

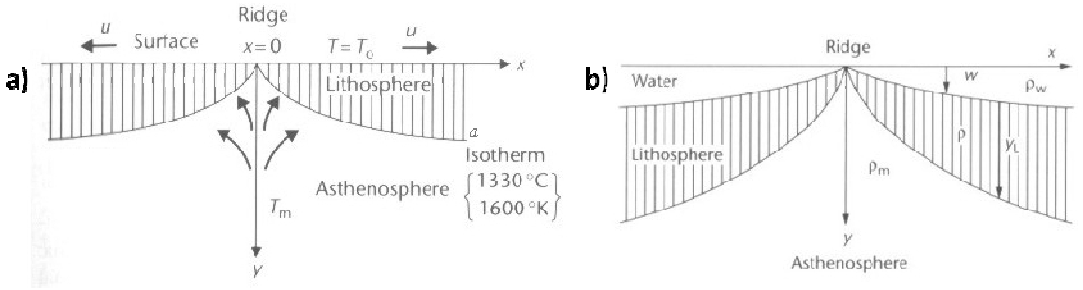

Figure 2.8: Lithosphere plate cooling model modified from (Allen and Allen, 2005) after (Turcotte and Schubert, 2002). a) Increasingly thick oceanic plate away the mid-oceanic ridge. b) Increasing bathymetry is the isostatic response for lithosphere plate cooling load.

An arbitrary column of oceanic lithosphere is assumed in isostatic equilibrium with an asthenosphere column in the mid-ocean ridge (figure 2.8b). Change in bathymetry is a consequence of isostatic compensation for the change in thermal load. For long wavelength loads, the density contrast $\Delta\rho$ along the lithosphere depth z must be 0:

$$\int_0^a \Delta\rho(z)dz = \int_0^a (\rho - \rho_a)dz + w(\rho_w - \rho) = 0, \qquad (2.11)$$

where ρ is oceanic lithosphere density and w is bathymetry.

Solving equation 2.11 for bathymetry w with time (McKenzie, 1978; Parsons and Sclater, 1977):

$$w(t) = \frac{a\rho_0\alpha T_1}{(\rho_0 - \rho_w)}\left\{\frac{4}{\pi^2}\sum_{m=0}^{\infty}\frac{1}{(2m+1)^2}\cdot c_n \cdot \exp\left(-(2m+1)^2\frac{t\pi^2\kappa}{a^2}\right)\right\}, \qquad (2.12)$$

where t is time, κ is the thermal diffusivity and c_n = 1 for oceanic lithosphere while for continental rifted margins c_n depends on β:

$$c_n = \left[\frac{\beta}{n\pi}\sin\frac{n\pi}{\beta}\right]. \qquad (2.13)$$

For a continental rifted margin, equation 2.12 corresponds to the analytical expression of the post-rift thermal subsidence (McKenzie, 1978).

LITHOSPHERE PARAMETERS

The dissipation of the thermal anomaly is described by the heat conservation equation, Appendix I:

$$\frac{\partial T}{\partial t} = \kappa\frac{\partial^2 T}{\partial z^2} = \frac{K}{\rho_0 C_p}\frac{\partial^2 T}{\partial z^2}, \qquad (A.6)$$

where T is temperature, t is time, z is depth, K is the thermal conductivity, ρ_0 is the mantle density at surface, Cp is the specific heat and κ is the thermal diffusivity. Equation A.6 was solved for temperature and heat flow permitting the determination of the heat flow and temperature at the base of lithosphere.

Bathymetry data from the North Atlantic and North Pacific regions (figure 2.7) as well as heat flow data were fitted with equations of the Parsons-Sclater plate model (PSM). Considering the basal heat flow interpreted for large ages, and assuming typical values of mantle rock density at surface ρ_0, heat capacity *Cp* and mantle heat conductivity *K*, as well as water density ρ_w, the lithosphere thickness *a*, the basal temperature T_1 and the thermal expansion coefficient of lithosphere α were determined (table 2-1). The parameters adjusted for the North Pacific in the PSM plate model have been assumed for the reference continental lithosphere in the depth-uniform lithosphere stretching model (McKenzie, 1978) and in many academic and industrial basin modelling applications (McKenzie, 1978; Press et al., 2004; Watts, 2001).

Table 2-1: Lithosphere parameters assumed (in beige) and obtained (in purple) by the plate cooling models: PSM (Parsons and Sclater, 1977), GDH1 (Stein and Stein, 1992), CM (Crosby and McKenzie, 2009). In the CM model K and C_p were calculated as functions of temperature.

Parameters	*PSM*		*GDH1*	*CM*
	N. Pacific	*N. Atlantic*	*N.P. + N.A.*	*Global*
ρ_0 (kg m^{-3})	3330	3330	3330	
ρ_w (kg m^{-3})	1000	1000	1000	
Cp (J kg^{-1} C^{-1})	1171.52	1171.52	1171.52	
K (W m^{-1} K^{-1})	3.1380	3.1380	3.1380	f(T)
HF_b(W m^{-2})	33.46	33.46	48	
a (km)	125	128	95	90
Tm (^oC)	1333	1365	1425	
α ($^oC^{-1}$)	3.28E-05	3.10E-05	3.10E-05	f(T)

EMPIRICAL OCEANIC BATHYMETRY EVOLUTION

Empirical equations were proposed by Parsons & Sclater (1977) for the relationships between bathymetry and heat flow with time. A square root relationship was proposed for ocean floor bathymetry younger than 70 Ma, while an exponential asymptote was proposed for ocean bathymetry older than 20 Ma (table 2-2). The PSM plate cooling model has been reviewed with updated datasets of sediment-

corrected oceanic bathymetry and heat flow, filtered of anomalous regions, which have resulted in different lithosphere parameters (table 2-1).

Initially, oceanic bathymetry and heat flow data from the North Pacific and the Northwest Atlantic, selected from a larger and revised global dataset, were fit with smaller lithosphere thickness, larger basal temperature and smaller coefficient of thermal expansion in the GDH1 plate model, global depth and heat flow (Stein and Stein, 1992). The GDH1 model also implied in reviewed empirical bathymetry (figure 2.9) and heat flow relationships with time (table 2-2). Whilst the PSM model predicts deeper oceanic bathymetry for old ages, as it is based on data that included anomalous deep ocean floor, the GDH1 model predicts shallower oceanic bathymetry for old ages because data from anomalous shallow ocean floor were not removed (Crosby et al., 2006).

Table 2-2: Empirical relationships for the evolution of (sediment-corrected) oceanic bathymetry with time. PSM, GDH1 and CM as in table 2-1. The exponential and square root functions of the PSM model superimpose between 20 and 70 Ma.

Model	Age (Ma)	Bathymetry (m)	Age (Ma)	Heat Flow (mW m^{-2})
PSM	$0 < t < 70$	$w(t) = 2500 + 350(t)^{1/2}$	$0 < t < 120$	$q(t) = 472.8t^{-1/2}$
	$t > 20$	$w(t) = 6400–3200 \exp(-t/62.8)$		
GDH1	$0 < t < 20$	$w(t) = 2600 + 365(t)^{1/2}$	$t \leq 55$	$q(t) = 11.3t^{-1/2}$
	$t > 20$	$w(t) = 5651– 2473 \exp(-0.0278t)$	$t > 55$	$q(t) = 48+96\exp(-0.0278t)$
CM	$0 < t < 80$	$w(t) = 2652 + 324(t)^{1/2}$		

Global grids of bathymetry from satellite altimetry (Sandwell and Smith, 1997), ocean age isochrons (Müller et al., 2008) and sediment thickness (Divins, 2004) were used to re-evaluate the bathymetry evolution of all oceans (Crosby and McKenzie, 2009; Crosby et al., 2006). Anomalous negative and positive oceanic bathymetry areas were removed from the grids by visual inspection. Deviations from the expected exponential decay for shallower bathymetry between 81 and 140 Ma

were observed for all oceans and were attributed to small-scale mantle convection (Crosby et al., 2006). The global average plot shows smooth deviation from the exponential decay, while strong deviations can be observed for specific oceans (figure 2.9).

The data from the West and Northwest Atlantic (Crosby and McKenzie, 2009), which comprises the study area, fluctuates between the PSM and GDH1 models predictions for ages greater than 64 Ma (figure 2.9). A lithosphere of 90 km could be fitted to the global data in a plate model, based on thermal conductivity and heat capacity of mantle rocks variable with temperature (Crosby and McKenzie, 2009; McKenzie et al., 2005) (table 2-1).

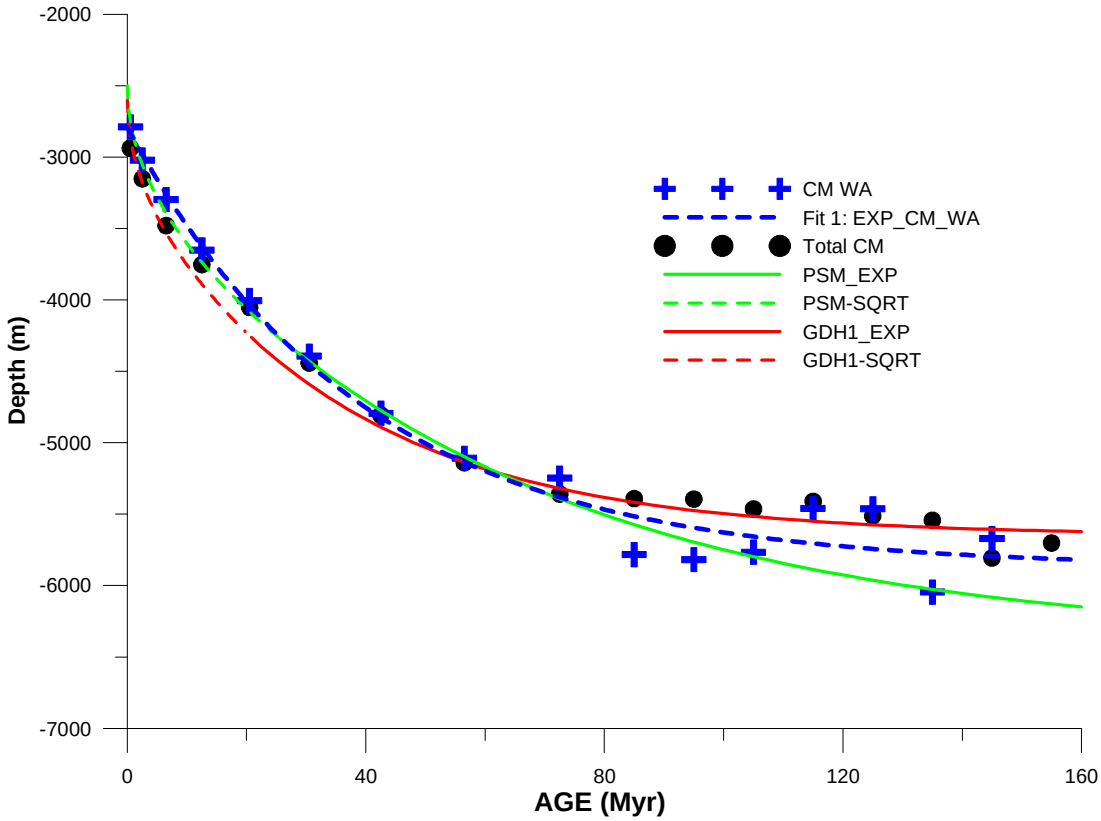

Figure 2.9: Empirical relationships of sediment-corrected oceanic bathymetry with age. Continuous green and dashed green corresponds to exponential and squared root fits of the PSM model, respectively. Continuous red and dashed red corresponds to exponential and squared root fits of the GDH1 model, respectively. Black dots are global average from CM, while blue crosses are average for the West Atlantic. Dashed blue corresponds to exponential fit to West Atlantic data of CM.

2.5 MAGMATIC ADDITION BY DECOMPRESSION MELTING

Thinning of the lithosphere raises its isothermal lower limit (1333 ^{o}C), promoting decompression melting of mantle rocks (McKenzie and Bickle, 1988). Magmatic rocks with crustal density and basaltic composition are added to the thinned continental crust by extrusion, intrusion or underplating (White and McKenzie, 1989). Hence, magmatic addition is a consequence of the thermal anomaly. The melt thickness is proportional to lithosphere thinning and leads ultimately to the formation of igneous oceanic crust (White and McKenzie, 1989). Magmatic load controls oceanic crust thickness and bathymetry (White et al., 1992).

Addition of magmatic rocks with crustal density to a thinned margin, t_{ma}, counteracts the isostatic effect of crustal thinning β (White and McKenzie, 1989). Therefore, the crustal thinning measured in a continental rifted margin by gravity may correspond to an apparent value β_{app}, lesser than the true crustal thinning β_c:

$$\beta_{app} = \frac{t_c}{\left(t_{ma} + t_c / \beta_c \right)}. \qquad (2.14)$$

Magmatic addition depends on the lithosphere thickness and on the asthenosphere potential temperature T_p (McKenzie and Bickle, 1988; White and McKenzie, 1989). Figure 2.10 plots the results of melt thickness against $\gamma = 1 - 1/\beta$ (McKenzie and Bickle, 1988). Magmatic addition starts when a certain threshold of lithosphere thinning is reached and maximum magmatic addition results from extreme thinning, $\gamma = 1$. For a normal rifted margin, with lithosphere thickness of 125 km and potential temperature of 1280 ^{o}C, the expected maximum melt thickness corresponds to around 7 km, the average thickness of a normal oceanic crust (White et al., 1992). Extensional settings affected by mantle plumes present larger potential temperature, consequently magmatic addition starts with low lithosphere thinning and can reach more than 10 km in the rifted margin and in the adjacent oceanic crust (White et al., 1992). The extreme situation shown in figure 2.10 corresponds to a plume located exactly under a spreading centre. Conversely, magmatic addition is suppressed at magma-poor margins due to low potential temperature or very slow spreading (figure 2.10). Magmatic addition needs to be taken into account in the determination of crustal thinning from the gravity data and in the inversion of the lithosphere thinning from subsidence profiles.

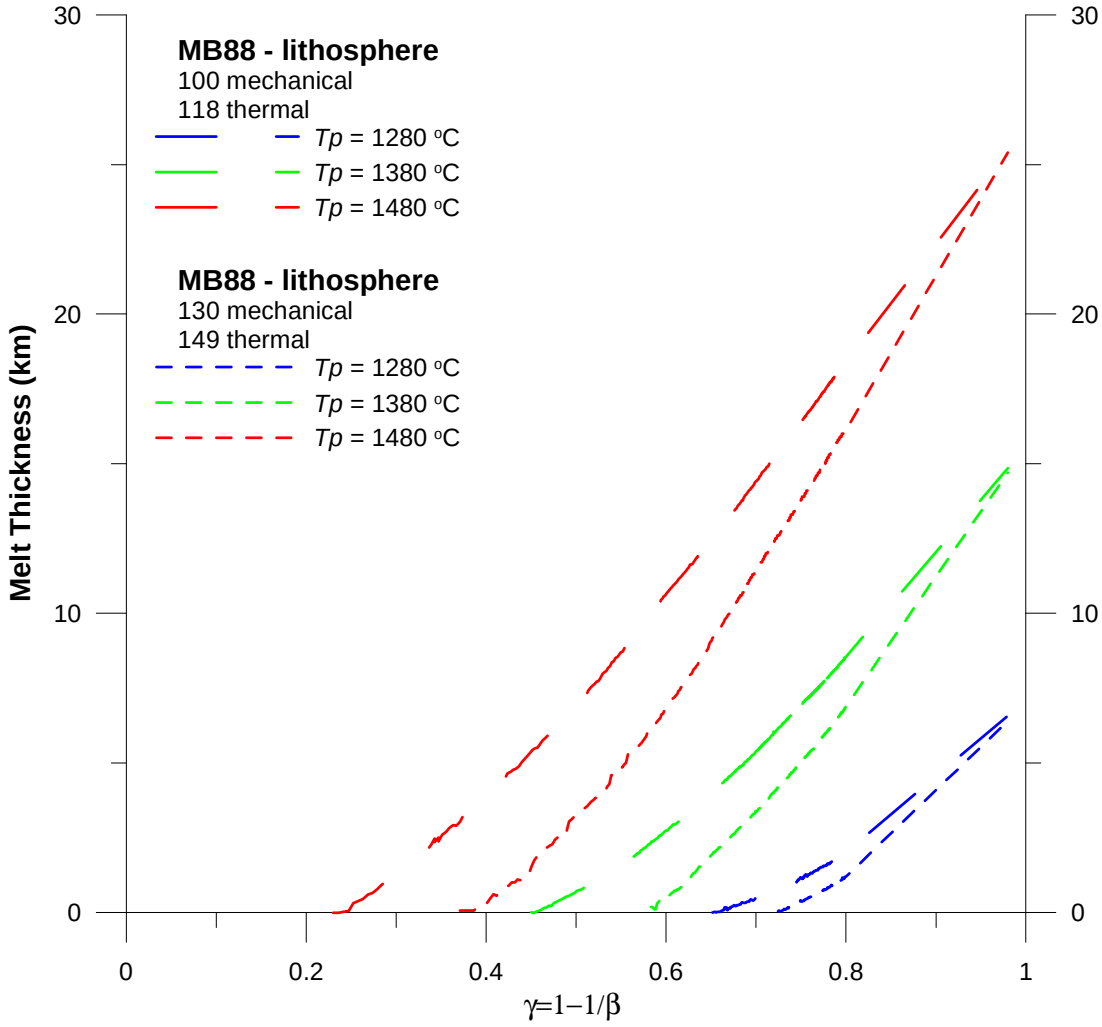

Figure 2.10: Relationships between melt thickness and the lithosphere thinning factor γ=1−1/β, for thermal lithosphere thickness of 118 and 149 km from (McKenzie and Bickle, 1988). Melt thickness is assumed as magmatic addition.

2.6 The Sedimentary Load

Initial subsidence in the syn-rift and thermal subsidence in the post-rift phases are both amplified by the load of sediments. Removal of the effect of sediments from gravity data and removal of the sedimentary load from geological cross-sections are necessary in order to determine crustal and lithosphere thinning.

The sedimentary load is incremental through the deposition of parasequences and controlled by compaction from the burial surface down to the basement. For the determination of the sedimentary load in a cross-section or in a grid, it is necessary to

calculate the load of each sedimentary column and then integrate this load along the profile or grid, as exemplified for the Sergipe-South cross-section in figures 2.11 and 2.12. The load of a column of sediments, L_s, corresponds to the integral of the product of density by gravity acceleration along depth, as illustrated in figure 2.12 for a sedimentary column of a hypothetical well located at 80 km in the Sergipe-South cross-section:

$$L_s = \int_0^{basement} \rho g dz \,. \qquad (2.15)$$

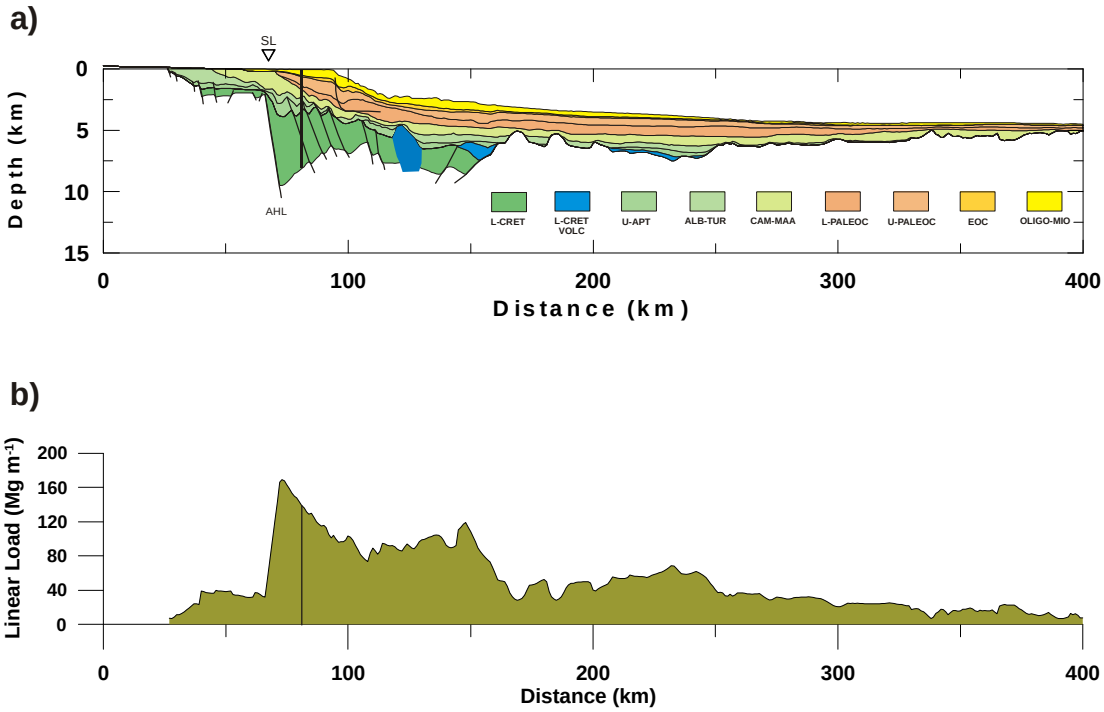

Figure 2.11: a) Sergipe South cross-section. b) Linear sediments load of Sergipe-South cross-section calculated from the variation of density with burial. Vertical line at 80 km corresponds to the sedimentary column of a hypothetical well shown in figure 2.12.

Density ρ varies with porosity ϕ according to the equation:

$$\rho = \phi\rho_w + (1-\phi)\rho_b, \qquad (2.16)$$

where ρ_w is the water density and ρ_b is the sediments matrix density. Sediments compact according to an exponential relationship between porosity ϕ and burial depth *s* (Athy, 1930):

$$\phi = \phi_0 \cdot e^{-c \cdot s}, \qquad (2.17)$$

where ϕ_0, the porosity at burial surface, and *c*, the exponential decay, are specific for each lithofacies. For basin modelling purposes, the lithofacies are grouped in the main rock assemblages of each basin: “Shale” for pelitic rocks, “Sand” for sandstone and conglomerate and “Carbonates”. Figure 2.12 shows the variation of porosity along depth of a column of sediments of a hypothetical well located at 80 km of distance in the Sergipe South cross-section and the corresponding density variation. Porosity along the sedimentary column is calculated using the exponential decay equation 2.17 with the parameters obtained from well data of Sergipe margin for the post-rift sedimentary sequences and with the parameters obtained from well data of Alagoas margin for the syn-rift sedimentary sequences.

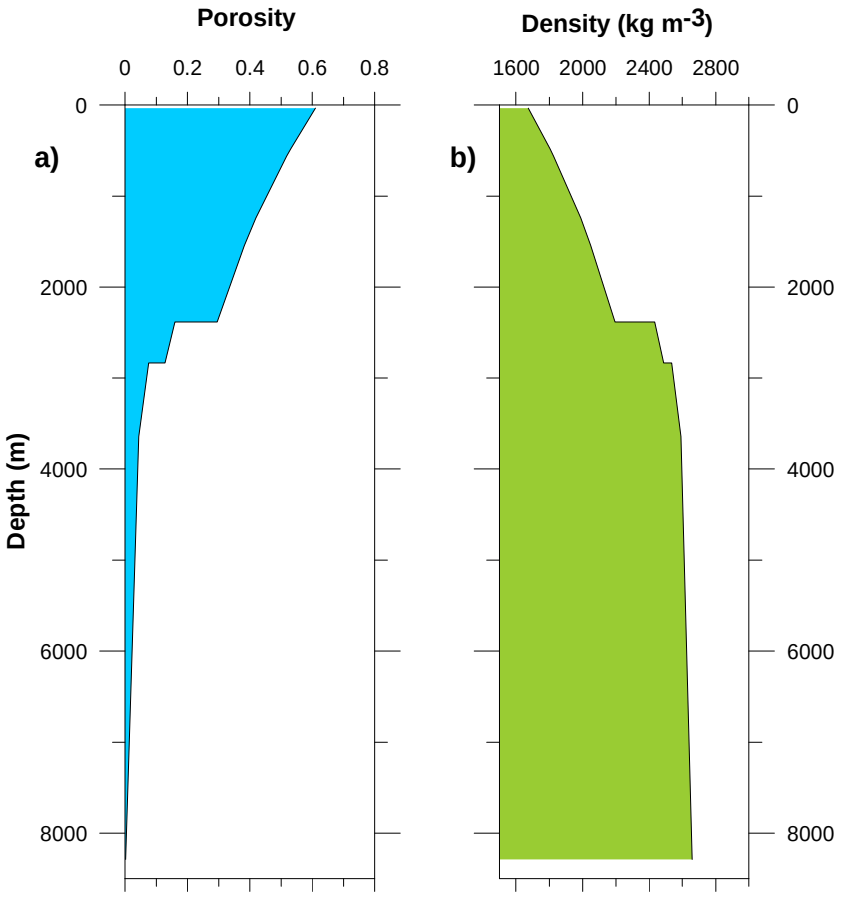

Figure 2.12: a) Porosity variation with depth at a distance 80 km along Sergipe South cross-section (figure 2.11), calculated using exponential decay parameters fit with porosity data of Sergipe and Alagoas margin. b) Corresponding density variation

In Chapter 5, the isostatic response of the sedimentary load is calculated for the studied cross-sections using flexural isostasy (Kusznir et al., 1995). For the gravity inversion, Chapter 7, the effect of sediments is removed by substitution of sediment density columns by basement density columns.

2.7 Limitations of the Depth-Uniform Lithosphere Stretching Model

The depth-uniform lithosphere stretching model (McKenzie, 1978) has been largely applied for 1D data, stratigraphic column of exploratory wells, the most accessible data for quantitative basin analysis (Sclater and Christie, 1980). Because of its simplicity, this model has been successful in explaining the basic relationship

between subsidence and the loads created during lithosphere thinning in many extensional settings. However, with the increasing availability of reflection seismic sections in rift basins and rifted margins, lithosphere stretching and thinning models have evolved to take into account observations and processes not considered by the depth-uniform stretching model. The main assumptions of the depth-uniform stretching model that have been reviewed in the literature are: 1) instantaneous rifting, 2) uniform stretching, 3) local isostasy and 4) reference continental geotherm without radiogenic heat contribution.

2.7.1 Instantaneous Rifting Assumption

The depth-uniform lithosphere stretching model has been successfully applied in some extensional settings, like the Bay of Biscay (Le Pichon and Sibuet, 1981), where overall pure shear results from strain variation in the hinge lines (figure 2.13a). However, large differences between syn and post-rift sedimentary packages have been recognized in rifted margins as a consequence of either finite rifting (Jarvis and McKenzie, 1980), magmatic addition (White and McKenzie, 1989) or depth-dependent stretching (Royden and Keen, 1980). In the first case, larger syn-rift sedimentation can result from a prolonged extensional phase in response to a finite thinning rate, instead of the infinite rate implied by the instantaneous thinning assumption of the DULSM. Thus, part of the thermal anomaly could be dissipated during the syn-rift, adding thermal subsidence to the initial subsidence and decreasing the thermally-driven post-rift subsidence. This effect is especially significant where the rift phase lasts more than 20 Myr (Jarvis and McKenzie, 1980). However, due to the poor seismic-stratigraphic control offshore in the studied cross-sections this research considers the total lithosphere thinning from total subsidence, initial plus thermal subsidence, instead of dealing with both separately.

2.7.2 Depth-Uniform Lithosphere Stretching And Thinning Assumption

Depth-dependent lithosphere stretching implies heterogeneous strain, instead of the homogeneous strain assumed by the depth-uniform lithosphere stretching model. Consequently, thinning can vary along the lithosphere layers, according to differences in their rheological properties. Initially, applications for 1D data considered that whole crustal thinning could be different from lithospheric mantle thinning (Royden and Keen, 1980). In the simple shear model (Wernicke, 1985), the resultant syn and post-rift sedimentation can be completely displaced by a shear zone that crosses the whole lithosphere (figure 2.13b). However, lithosphere scale faults have not been corroborated by seismological evidence from extensional regions (Kusznir et al., 1991). Instead, deformation of lower crust and lithospheric mantle is believed to occur by distributed ductile deformation (Kusznir et al., 1991).

Complex geometries observed in extensional settings and variations between syn and post-rift sedimentation can be explained by the hybrid simple shear-pure shear models (figure 2.13c). Fault controlled brittle deformation of the upper crust can be displaced from ductile pure shear of the lower crust and lithospheric mantle. The brittle and ductile regions are separated by a detachment zone at the base of the upper crust (Kusznir et al., 1991; Weissel and Karner, 1989).

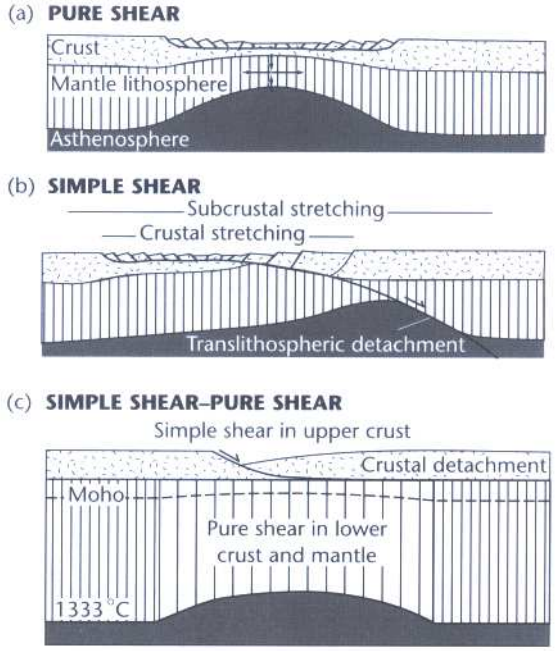

Figure 2.13: 2D lithospheric stretching models (Allen and Allen, 2005). a) Pure shear (McKenzie, 1978). b) Simple shear (Wernicke, 1985). c) Hybrid simple shear in the upper crust, pure shear in lower crust and mantle (Kusznir et al., 1991).

Depth-dependent lithosphere stretching and thinning has been tested by thinning measurements along lithosphere layers in transects that sample rifted margins from their borders to the oceanic crust. Upper crustal stretching can be measured from fault heaves of syn-rift faults. In the context of depth-uniform pure shear assumption, the amount of upper crustal stretching is assumed to be the same as of upper crustal thinning. Whole crust thinning can be measured in cross sections that present the crust-mantle boundary constrained by seismic refraction or gravity inversion. Whole lithosphere thinning can be inverted from post-breakup thermal subsidence, evaluated from post-rifted packages (Davis and Kusznir, 2004).

Wherever different thinning measurements could be performed in rifted margins that evolved to continental break-up, upper crust thinning is less than whole crust and whole lithosphere thinning (Davis and Kusznir, 2004; Kusznir and Karner, 2007). Moreover, observed brittle deformation of the upper crust in many settings

seems to be incompatible with the observed syn-rift accommodation space (Karner et al., 1997). These discrepancies have not been seen in intra-continental settings (Kusznir and Karner, 2007; Le Pichon and Sibuet, 1981). Therefore, depth-dependent lithosphere thinning and stretching seems to be a characteristic of extensional settings that evolve towards continental break-up (Kusznir and Karner, 2007).

Although small upper crust stretching measurements have been contested for the Iberia margin (Reston, 2009), the highly complex tectonic style of that margin seems to be uncommon in other rifted margins, like West Africa and Eastern Brazil. Increasing thinning with depth in continental lithospheric plate must be normally expected towards the continent-ocean boundary. Exhumed continental lithosphere, observed in the Iberia-Newfoundland conjugate magma-poor margins, implies reversal of depth-dependent thinning close to the COB (Davis and Kusznir, 2004). The mechanism responsible for sea-floor spreading, upward and divergent asthenosphere flow, can interfere with continental extension during break-up time (Kusznir and Karner, 2007). The problem of volume conservation of the increasing thinning and stretching with depth still needs to be further addressed (Reston, 2009).

2.7.3 Loads Compensation Through Local Isostasy

The depth-uniform lithosphere stretching model assumes local isostatic compensation for the crustal and thermal loads, which implies a lithosphere without flexural rigidity. Local isostasy is an idealized situation, unlikely to occur in nature. The hybrid simple shear-pure shear models incorporate regional isostatic compensation of the crustal and thermal loads, through flexural isostatic response. Flexural response is compatible with rift flank uplift observed in extensional settings.

2.7.4 CONTINENTAL LITHOSPHERE WITH RADIOGENIC HEAT PRODUCTION

The analytical solution of the initial subsidence S_i from the DULSM (McKenzie, 1978) assumes isostatic equilibrium between a thermally stable continental lithosphere and a thinned continental lithosphere with increased geothermal gradient, ignoring radiogenic heat contribution from the crust. Any modification in the initially assumed simplified steady-state continental geotherm has an impact on the determination of the thermal anomaly, and therefore also in the syn and post-rift subsidence.

The steady state continental lithosphere has to be also in isostatic equilibrium with the oceanic crust. Applications of the DULSM in basin analysis generally assume that the initial continental elevation is at sea-level at the rift onset. The crustal thickness that corresponds to rift onset elevation at sea-level is generally assumed. For example, a 125 km-thick lithosphere with continental crust with the commonly adopted average density of 2800 kg m^{-3} , in isostatic equilibrium with an average 2500 m-deep mid-ocean ridge, implies an initial continental crust thickness of 31.2 km-thick (Allen and Allen, 2005; McKenzie, 1978). The DULSM assumption that the steady-state continental lithosphere has the same thickness and geotherm as an old oceanic plate (McKenzie, 1978) may be invalid, especially in margins that resulted from rifting of continental shields. Some apparent plausible combinations of lithosphere and crustal thickness may result in unrealistic initial elevations, as presented in Chapter 9.

2.8 SUMMARY

The crustal thinning is a permanent feature in continental margins that can be inverted from gravity anomalies. Removal of the effects of sediments from gravity

data is necessary in order to determine crustal thinning. The effect of the sedimentary load in the cross-sections can be removed through flexural backstripping, Chapter 6. The empirical relationships of oceanic bathymetry with time have been used to determine the residual depth anomalies, which are related to the magmatic addition by decompression melting. A method to calculate magmatic addition as a function of lithosphere thinning is proposed in Chapter 7 to correct crustal and lithosphere thinning.

In Chapter 8, a 2D continental lithosphere thinning model is developed to determine subsidence from crustal and lithospheric thinning incorporating magmatic addition, depth-dependent thinning, radiogenic heat production and flexural isostasy. Post-rift thermal subsidence is the only information required to invert the thermal load. Due to the poor seismo-stratigraphic control of the syn-rift sequences offshore in the studied cross-sections this research considers the total lithosphere thinning from total subsidence, initial plus thermal subsidence, instead of dealing with both separately. Sediment-corrected basement profiles calculated from flexural backstripping are assumed as total subsidence profiles. This subsidence forward model produces the function to be minimized with the new method for inversion of the lithosphere thinning from total subsidence profiles, developed in Chapter 9.

CHAPTER 3

3. GEODYNAMIC SETTING OF THE NORTHEAST BRAZILIAN CONTINENTAL RIFTED MARGIN

3.1 INTRODUCTION

The Northeast Brazilian continental rifted margin comprises the region where the Brazilian coast bends from a north trending to a northeast trending direction around Salvador city, parallel 13 ^{o}S (figure 3.1), and then bends again towards north around parallel 8 ^{o}S. Between parallels 13.5 ^{o}S and 9.5 ^{o}S the continental shelf is around 20-km wide (figure 3.1), then through a eastward deflexion it becomes 40-km wide northwards in the Alagoas and Pernambuco margins (Asmus and Carvalho, 1978). The continental slope is populated by seamounts in the region of the Ascension-Maceió Fracture Zone and in the Pernambuco Plateau. The particularly narrow continental shelf and slope of the Northeast Brazilian margin suggests modest sediment influx in the post-rift (Palma, 1984). Important variations in the sedimentary infill along the segments of this margin reflect differences in the subsidence pattern, which must be a consequence of distinct lithosphere thinning distribution. The purpose of this chapter is to review the evolution of this segment of the East Brazilian continental rifted margin.

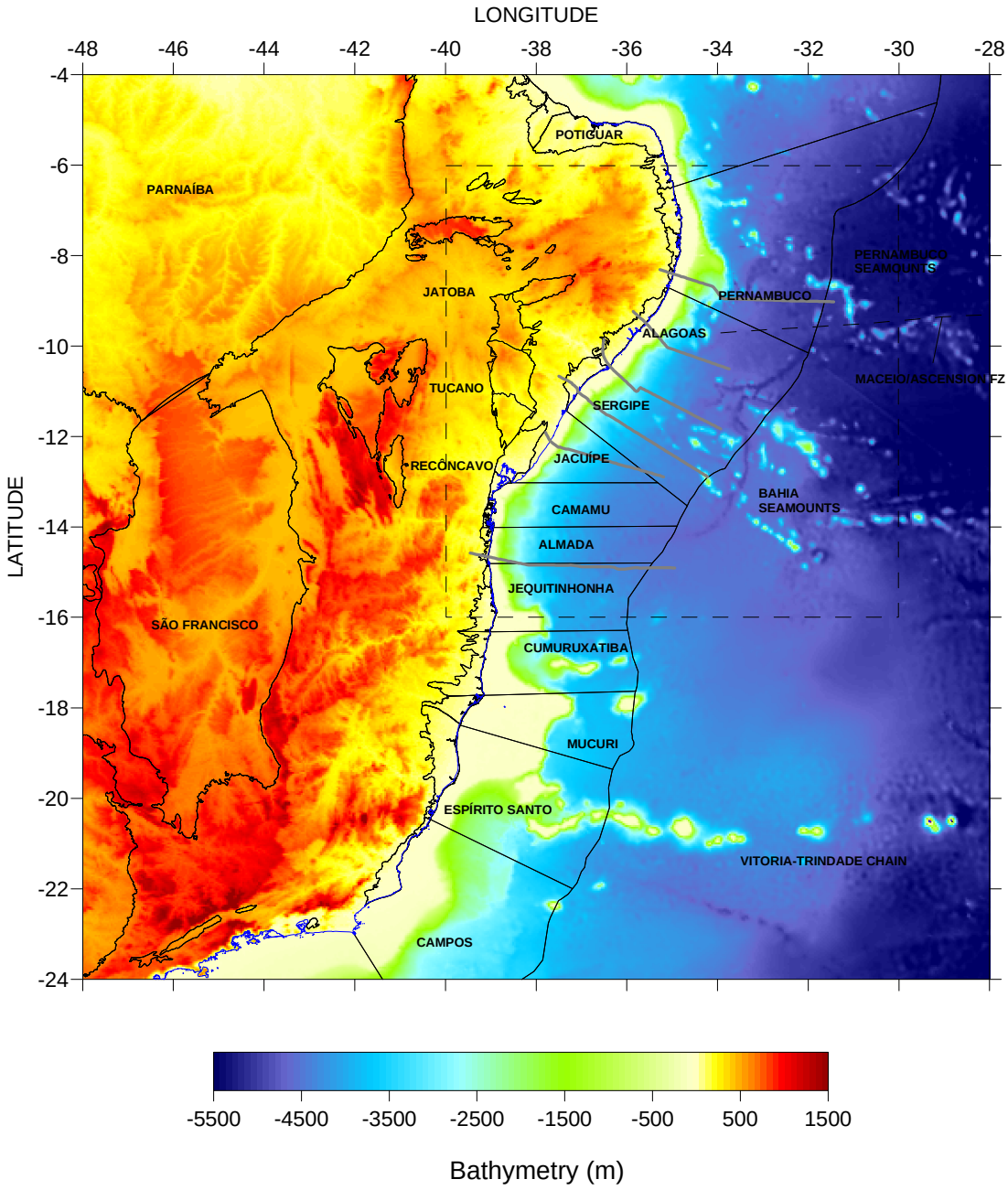

Figure 3.1. Eastern Brazil topography and adjacent South Atlantic Ocean bathymetry. Data from (Sandwell and Smith, 2009).

3.2 South Atlantic Ocean Opening

The East Brazil rifted margin and its West Africa counterpart evolved from an Early Cretaceous rift system since the end of the Pangaea Supercontinent cycle, around the Late Triassic (210 Ma), the last time when all the continental masses were joined together. Continental lithosphere stretching and thinning along rift systems pre-dated continental break-up and splitting of conjugate margins. The South

Atlantic opened during the Early Cretaceous (144 to 110 Ma), in the second phase of lithosphere break-up of the Gondwana (Storey, 1995), the southern hemisphere supercontinent that resulted from the initial Pangaea split. The West Gondwana continental lithosphere break-up propagated in two steps throughout a branch of the East Brazil rift system (Chang et al., 1992). In the first step, the South American margin between Argentina and Southern Brazil (figure 3.2) was split from South Africa and Namibia margins between around 135 and 125 Ma (Moulin et al., 2010; Nürnberg and Müller, 1991). During the second step of West Gondwana continental lithosphere break-up, from 125 to 110 Ma, the Brazilian margin between Santos and Pernambuco Plateau was split from the West Africa margin between Angola and Nigeria.

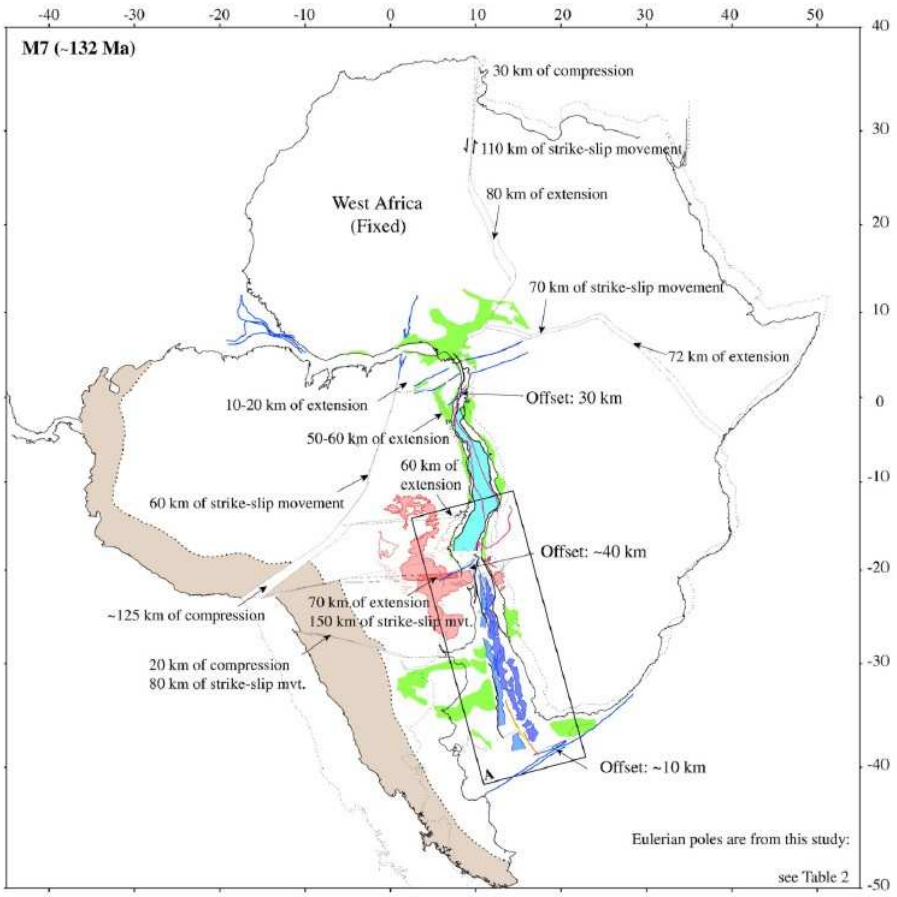

Figure 3.2: Brazil-Africa reconstruction at 132 Ma (Moulin et al., 2010). The region in dark blue was initially split between 137 and 125 Ma, while the region in light blue was split from 125 to 110 Ma.

While continental lithosphere break-up and sea-floor spreading were developing during the first step of the West Gondwana break-up, lithosphere extension focused in the East Brazil Rift System, EBRIS (Chang et al., 1992) to the north, along the Neoproterozoic fold belts of Ribeira, Araçuaí, Kaoko and West Congo (Bueno, 2004; Cordani et al., 1984; de Wit et al., 2008; Moulin et al., 2010) (figure 3.3). This rift system evolved during Early Cretaceous with fluvio-lacustrine sedimentation, increasing salinity and marine influence towards the Aptian. The southern segment of the rift system comprises Santos, Campos, Espírito Santo, Cumuruxatiba, Jequitinhonha and Almada basins in the Brazilian margin. The rift system was split into two branches across the São Francisco Craton, following the bifurcation of the Atlantic Granulitic belt to the south of Salvador city (figure 3.4). The western branch followed the north trending fabric and corresponds to the aborted Reconcavo-Tucano-Jatobá rift system, while the eastern branch followed the north-northeast trending fabric and comprises the Northeast Brazilian rifted margin and its African conjugate (figure 3.4), Gabon and Rio Muni.

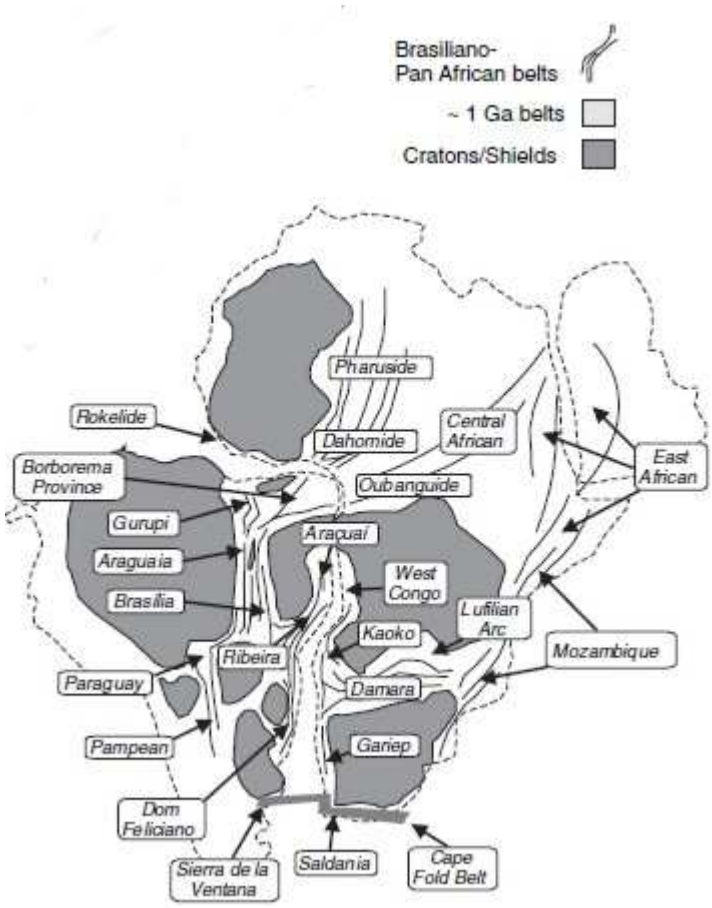

Figure 3.3: Brazil-Africa reconstruction showing the distribution of Neoproterozoic fold belts and craton/shields, by (de Wit et al., 2008).

During the second step of the West Gondwana continental lithosphere break-up, from 125 to 110 Ma, lithosphere rupture was probably attracted by the Saint Helena Hot-Spot, located around Sergipe and Pernambuco margins at that time (O'Connor and Le Roex, 1992; Storey, 1995; Wilson, 1992), which left the Bahia and Pernambuco seamounts as hot spots vestiges (figure 3.1). However, the age of the continental break-up northward of the Florianopolis fracture zone cannot be accurately determined because the signature of the sea floor magnetization corresponds to the Cretaceous Normal Superchron, a period without magnetic anomalies in the oceanic crust. Break-up age can be constrained by the development of marine conditions in the proto-Atlantic basin. The age of the transitional

megasequence constrains the opening of the central segment of South Atlantic between Late Aptian and Early Albian (around 115 to 110 Ma).

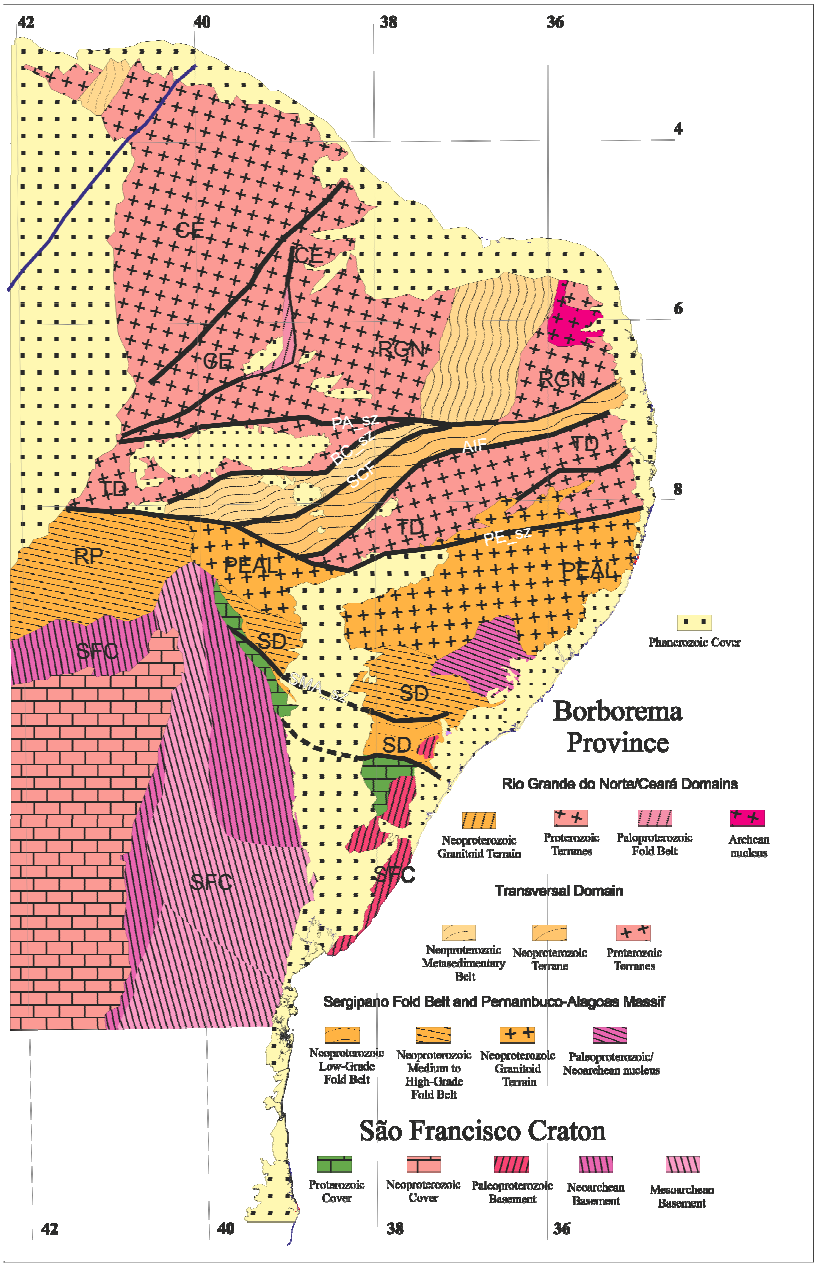

Figure 3.4: Major domains and terrains of the Borborema province and north of São Francisco craton (van Schmus et al., 2008). SD, Sergipano fold belt; SFC, São Francisco craton; PEAL, Pernambuco-Alagoas massif; TD, Transverse domain; CE, Ceara domain; RGN, Rio Grande do Norte domain; PA_sz, Patos shear zone; BC_sz, Boqueirão dos Conchos shear zone; Afogados de Ingazeira fault, SCF, Serra dos Caboclos fault; PEsz, Pernambuco shear zone, and SMAsz, São Miguel do Aleixo shear zone. The Jequié Block and the Itabuna-Salvador-Curaçá belt make part of the Atlantic Granulitic belt.

3.2.1 BRAZIL-AFRICA RECONSTRUCTIONS

The resemblance of Brazil and Africa shorelines is one of the most intriguing geodynamics features of the continents and one of the earliest arguments in support of continental drift (Kearey and Vine, 1996). The continuity between the Ascension-Maceió oceanic fracture zone with the Siriri-Penedo transfer zone onshore Sergipe-Alagoas, and also with the Fang transfer zone between Rio Muni and Gabon margins is an important key for the fit of the studied region (Hamsi, 2006). The preferred reconstruction focusing on the studied area (Matos, 1999) is based on the accurate fit of geological features in both continents and shows the best correlations between the segments of the equatorial and eastern branches of the Brazilian margin with the conjugate West African margins (figure 3.5) (Hamsi, 2006). A better adjustment between the Siriri-Penedo transfer zone and the Maceió-Ascension fracture zone could be achieved by Matos (1999) model by bringing the Brazilian margin a little further to the south (figure 3.5). The Matos (1999) reconstruction is an improvement in relation to others much used reconstructions that fit the physiographic features of the *Todos os Santos* Bay in Brazil with the Port Gentil peninsula in Gabon (Castro, 1987; Rosendahl et al., 2005). Therefore, according to the reconstruction proposed by Matos (1999) the conjugate margins in the studied area are (figure 3.5): 1) the segment between Jequitinhonha and Camamu in Brazil with north Angola in Africa; 2) Jacuípe with South Gabon, 3) Sergipe with North Gabon, 4) Alagoas with Rio Muni, and 5) Pernambuco with Douala.

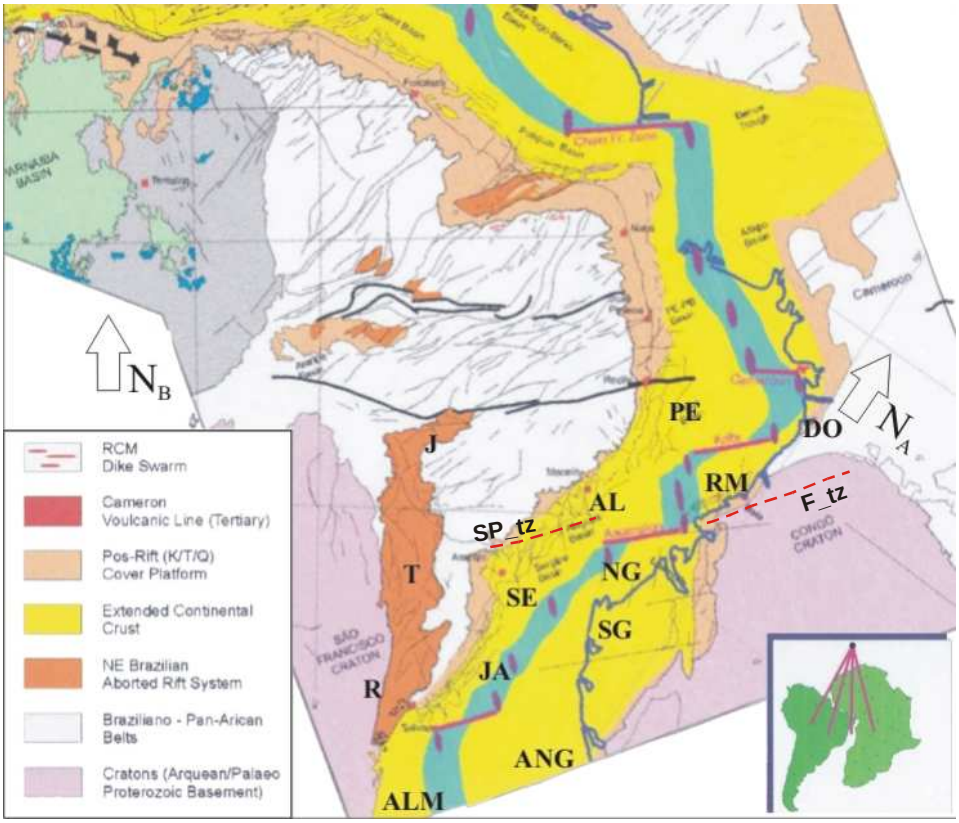

Figure 3.5: Northeast Brazil-West Africa fit at 110 Ma (Matos, 1999). J, Jatobá basin; T, Tucano basin; R, Recôncavo basin; ALM, Almada; ANG, Angola; JA, Jacuípe, SE, Sergipe; SG, South Gabon; NG, North Gabon; AL, Alagoas; RM, Rio Muni; PE, Pernambuco, and DO, Douala. SP_tz, Siriri-Penedo transfer zone and F_tz, Fang transfer zone.

3.3 TECTONIC-STRATIGRAPHIC EVOLUTION OF THE NORTHEAST BRAZILIAN RIFTED MARGIN

The tectonic-sedimentary evolution of the East Brazilian margin comprises four main stages (Chang et al., 1992): 1) pre-rift, 2) early rift, 3) transitional and 4) post-rift (figure 3.6). The Sergipe-Alagoas basin is the best exposed of the East Brazil rift system, probably because its location was subject to uplift phases along the evolution. Its sedimentary pile is typical of the East Brazil rifted margin infill, and much of the comprehension about the tectonic-sedimentary evolution of the margin came from observations of its exposures and well data (Chang et al., 1992).

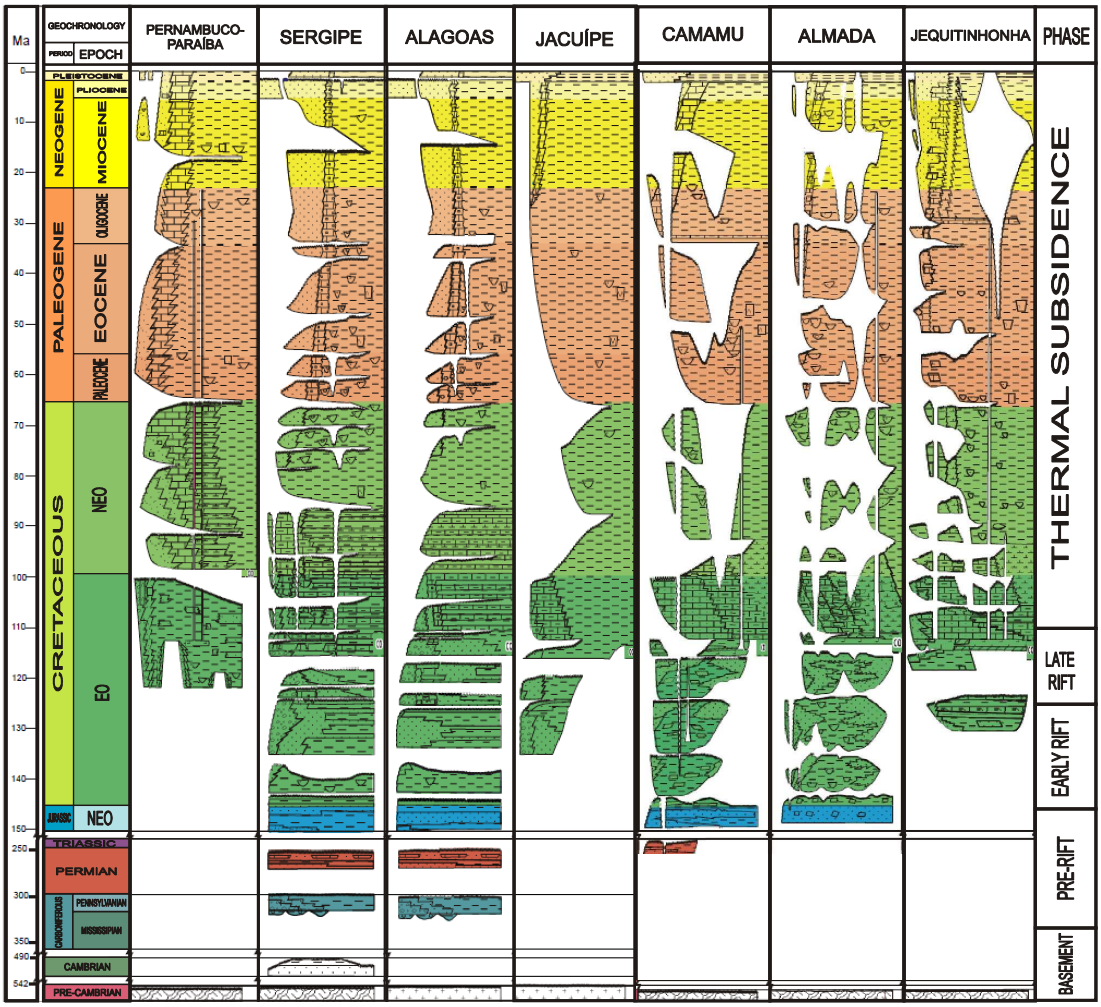

Figure 3.6: Simplified stratigraphic charts of the sedimentary basins developed in the study region, modified from (Milani et al., 2007).

3.3.1 PRE-RIFT - LATE PALAEOZOIC AND JURASSIC

In Sergipe-Alagoas, as in the Tucano rift, permo-carboniferous intracratonic strata are preserved as remains of a major intra-cratonic basin (figure 3.6). The Palaeozoic pile can reach locally up to 400 m (Campos Neto et al., 2007). This succession is followed by the Upper Jurassic red-beds deposited in the Afro-Brazilian Depression (Estrella, 1972; Garcia, 1991), a large, shallow water intra-continental basin that comprised the regions of Almada, Camamu, Recôncavo, Tucano, Jatobá, Jacuípe, Sergipe, Alagoas and Gabon basins. The Upper Jurassic megasequence can reach a maximum thickness of 300 m (Campos Neto et al., 2007).

3.3.2 Rift Tectonics from Berriasian to Early Albian

Basement Control

The two branches of the East Brazil rift system that followed the bifurcation of the Atlantic Granulitic belt (figure 3.4) developed across the São Francisco Craton and the southern part of the Neoproterozoic Borborema Province (900-540 Ma). The boundary between these two provinces is defined by the Vaza Barris arch (figure 3.7), which can be recognized in the new free-air gravity data (Sandwell and Smith, 2009). In the rigid cratonic region, rifting followed Paleoproterozoic anisotropies, semi-parallel to the extension direction. The western Reconcavo-Tucano-Jatobá rift system follows the north trending fabric, while the eastern branch follows the north-northeast trending fabric and comprises the Camamu, Jacuípe, Sergipe, Alagoas and Cabo rifted margins in the Brazilian side and the conjugate rifted margins in the African side (figure 3.5).

The northern segments of the two rift branches developed in the Borborema Province that presents east to east-southeast trending fabric, sub-parallel to the extensional forces, and almost perpendicular to the north to north-northeast trending São Francisco Craton fabric to the south (figure 3.4). Therefore, many Precambrian faults were reactivated as transfer faults and transfer zones in the rift phase (Milani and Davison, 1988). The western branch of the rift system is limited at the northern edge of the pull-apart Jatobá basin, while the eastern branch is limited at the onshore Cabo basin and at the Pernambuco Plateau. Both rift branches are interrupted by the Pernambuco shear zone, one of the prominent east-west trending strike-slip faults in the Borborema Province (figures 3.4 and 3.7).

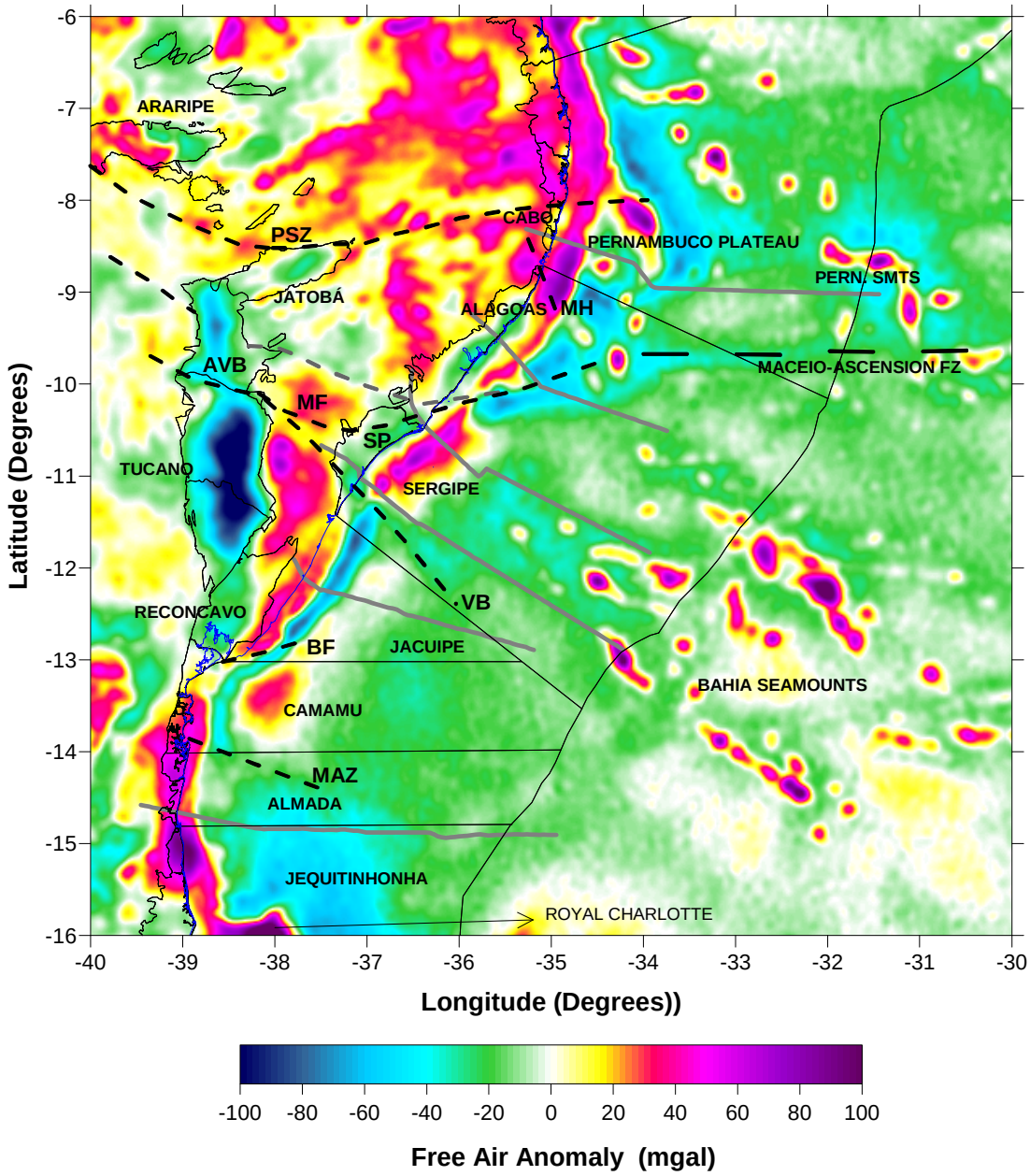

Figure 3.7: Free-air gravity anomaly map of the studied region, constructed with data from (Sandwell and Smith, 2009). MAZ, Mutá Accommodation Zone; BF, Barra fault; AVB, Vaza Barris arch; VB, Vaza Barris fault system; MF, Mocambo fault; SP, Siriri-Penedo transfer zone; MH, Maragogipe High; PSZ, Pernambuco shear zone.

The Vaza Barris fault system separates Jacuípe and Sergipe margins (figure 3.7), as also the central and north segments of Tucano basin, which have tectonic polarity reverted (Magnavita et al., 1994). The Siriri-Penedo transfer zone separates Sergipe and Alagoas margins, linking an NNE trending fault system in Sergipe, with *en echelon* pattern, which suggests a transtensional character (Hamsi, 2006). This

transfer zone seems to be related to the Mocambo fault at the adjacent basement, which corresponds to the suture between the São Francisco craton and the Pernambuco-Alagoas massif (D'el-Rey Silva, 1995), developed under the metasediments of the Sergipano fold belt. This suture zone seems to also converge towards the Vaza-Barris arch that separates the central and north segments of Tucano basin. The Siriri-Penedo transfer zone (figure 3.7) terminates offshore in the Ascension-Maceio fracture zone (Castro, 1988), which suggests that adjacent segments of continental lithosphere with different thinning are in contact with oceanic crust segments with different rates of sea-floor spreading.

OBLIQUE RIFTING OF THE NORTHEAST BRAZILIAN MARGIN

Along the two northern branches of the East Brazil rift system, the dominant direction of the extensional faults are north to north-northeast (Hamsi, 1998; Lana, 1991; Milani and Davison, 1988), implying an approximate east-west opening (figure 3.5). Faults with orientation from NW-SE to ENE-WSW correspond to oblique reactivations of faults of the Borborema province. The obliquity of the margin segment between Jacuípe and Alagoas with the overall direction of the East Brazil margin to the south is a suggestion of oblique rifting. The average fault direction in Sergipe-Alagoas, N30E (Hamsi, 1998; Lana, 1985), combined with basement anisotropies oriented N60E direction, like the Siriri-Penedo transfer zone, are compatible with an opening direction around WNW-ESE, not too far from the direction of the oceanic fracture zones adjacent to the margin. An alternative interpretation of the geodynamic setting proposes that the Sergipe-Alagoas margin developed as a pure transform margin in the early rifting (Rosendahl et al., 2005). The Siriri-Penedo transfer zone must have been active during late extension, as pre-Aptian sequences thickness seem to present continuity across the regions separated

by this transfer zone (Campos Neto et al., 2007). Oblique rifting has also been characterized for the Rio Muni margin (Turner et al., 2003), conjugate of Alagoas. The implication of the E-W or NE-SW oblique rifting is that the available NW-SE geological cross-sections are not parallel to the direction of tectonic transport, therefore inadequate to measure upper crust stretching.

THE APTIAN HINGE LINE

Most of the faults in Sergipe-Alagoas cut across pre-Aptian sequences and control the deposition of Late Aptian to Early Albian sedimentary sequences. The Aptian hinge line in shallow waters exerted a strong control on sedimentation, but it is not clear whether this hinge line also controlled thickening of pre-Aptian sequences. This hinge line corresponds to a set of E-W and NNE-SSW faults offshore Sergipe that enters onshore Alagoas, where it merges with the border fault. The Aptian hinge line also seems to control sedimentation between the Jequitinhonha and Camamu margins (Menezes and Milhomem, 2008). The Aptian hinge line is followed offshore by domino style, synthetic rotated blocks, which seem to be eroded by variable amounts. A distal hinge line limits a zone where tectonic polarity is reversed (Hamsi et al., 2006). Antithetic listric faults apparently control wedges of seaward-dipping reflectors, best developed offshore Jacuípe. The segment between where antithetic faults are observed and the unequivocal oceanic crust is considered as the ocean-continent transition (OCT). In this zone crustal and lithosphere thinning are large and magmatic addition causes difficulty in the location of the COCB.

3.3.3 EARLY SYN-RIFT: LOWER CRETACEOUS SUCCESSION

The rift onset was characterized by deepening of the depositional surface in the Neocomian, controlled by the fault network, which allowed sedimentation of lacustrine shale, conformably above the Late Jurassic fluvial-eolian sandstones

(figure 3.6). Three rift pulses developed from the Neocomian to the Early Aptian. The third rift pulse occurred during the Aptian onset, at the end of the Jiquiá local stage and was the rifting peak in Sergipe and Alagoas. The corresponding sedimentary sequence have been sampled onshore Alagoas with thickness around 3000 meters (Campos Neto et al., 2007), deposited in less than 1 Myr, between 124 and 123 Ma. However, the rift peak occurred earlier in the Reconcavo-Tucano-Jatobá system (Magnavita et al., 1994). In the remaining basins well sampling is not complete enough to permit a conclusion about the rift peak. Typical asymmetrical wedges with huge conglomerate piles, controlled by continuous border faults, are characteristic of the Recôncavo-Tucano-Jatobá system (Magnavita and da Silva, 1995), but they are not a clear feature of Sergipe-Alagoas basin. Border faults are neither continuous nor seem to control most of the syn-rift infill, as sediment thickening is not easily characterized (Hamsi and Karner, 2006).

3.3.4 Late Syn-Rift – Transitional Phase: Aptian To Lower Albian

The Transitional Megasequence is characterized by the presence of the northwardly thinning evaporite layer in the East Brazil margin between Santos and Pernambuco (Cainelli and Mohriak, 1999). While the Lower Aptian sequence was deposited in the southern and eastern blocks of the Aptian hinge line in Sergipe-Alagoas, the Aptian unconformity developed in the footwall blocks. Onshore and in shallow water regions of the Sergipe margin, the Aptian unconformity rests above early syn-rift, pre-rift strata and low-grade metamorphic rocks of the basement. The Upper Aptian succession, or transitional sequence (Chang et al., 1992), is characterized as retrogradational in Sergipe onshore and covers the Aptian unconformity. This succession starts with a coarse siliciclastic, continental sedimentation, changing to tidal controlled shallow marine sandstones, carbonates,

evaporites and shale (Campos Neto et al., 2007). The Upper Aptian succession has been informally assigned as a "*sag*" as it is not clearly controlled by faults (Milani et al., 2007), although thickening has been identified in the hinge line (Cruz, 2008) and this succession was clearly affected by faults that reached the basement in Early Albian.

The Aptian unconformity, the most remarkable of the East Brazil rift system, is correlated along the length of the South Atlantic margin and has been related to the break-up unconformity (Cainelli and Mohriak, 1999; Milani et al., 2007). The break-up unconformity was proposed as a separation of syn-rift and post-rift successions, as a consequence of uplift promoted during the continental lithosphere break-up (Falvey, 1974). However, upper crustal stretching through brittle deformation still persisted until Early Albian, at least between the Sergipe and Pernambuco regions. Alternatively, the Aptian unconformity could be interpreted either as resulting from the main episode of rift flank uplift at the end of the rift phase, or to stress changes caused by intrusion of magmatic rocks, not necessarily coincident with the continental break-up. The Aptian unconformity can still be recognized up to north Alagoas. Onshore Alagoas, Lower Aptian and pre-Aptian sequences are overlain by less than 200 m cover of continental Tertiary sediments. This suggests that the Alagoas margin was subject to major uplift and erosive events from Late Aptian to Miocene (Cainelli and Mohriak, 1999; Milani et al., 2007).

3.3.5 Late Rift Offshore Volcanism: Late Aptian To Early Albian

While an Early Albian volcanic suite can be recognized in the Cabo basin, onshore Pernambuco (Almeida et al., 2005; Long et al., 1986; Nascimento and Souza, 2005), the onshore and shallow water segment between Almada and Alagoas margins is practically devoid of igneous rocks. Nevertheless, the acquisition of

seismic and potential methods data in the deep waters region has revealed complex interactions involving seamounts, volcanoes and extrusive igneous rocks. The association of seaward-dipping reflectors, identified offshore, with positive magnetic anomalies suggests they correspond to basaltic rocks, and so they have been interpreted as early oceanic crust (Mohriak et al., 1998).

Buried seamounts and volcanoes have been initially identified in seismic reflection sections offshore Sergipe (Pontes et al., 1991). Although originally assigned a Coniacian age, these volcanic bodies may be as old as Late Aptian. These volcanic mounds are probably the first expressions of the Bahia seamounts, considered as tracks of the Saint Helena hot spot (O'Connor and Le Roex, 1992). Similarly, the alkaline volcanic suite of the Ipojuca Formation of Cabo basin and the volcanic bodies identified in the Pernambuco Plateau by geophysical data can be associated to the Pernambuco seamounts, also considered as a track of the Saint Helena plume. Along with the seaward-dipping reflectors, these igneous rocks are a strong suggestion of the activity of the Santa Helena hot spot at the late rift phase or early post-rift of the margin.

3.3.6 POST-RIFT PHASE

Following break-up, the margin underwent significant post-rift subsidence allowing the deposition of the following megasequences (figure 3.6): 1) Shallow Carbonate Platform, from Albian to Coniacian, 2) Open Marine Transgressive, from Santonian to Paleocene, and 3) Open Marine Regressive, from Eocene to the present (Cainelli and Mohriak, 1999; Chang et al., 1991). These megasequences are separated by very remarkable unconformities, created in events that promoted widespread erosion of previous strata: 1) the Santonian Event, 2) the Cretaceous-Tertiary Event (top-Cretaceous unconformity), 3) the Middle Eocene Event, not

identified in all margins, and also 4) a remarkable event in the Lower Miocene. Fourth and fifth order limits of sequence subdivide even more the post-rift succession and are responsible for deposition of siliciclastic reservoirs.

3.4 SUMMARY AND CONCLUSIONS

The Northeast Brazilian continental rifted margin evolved from the northern segment of the Early Cretaceous East Brazil rifted system. The East Brazil rift system splits in two branches around Salvador city. This research focuses in the segment southward of the splitting region and in the eastern rift system branch that was successful in evolving into a rifted margin. The eastern branch of the East Brazil rift system followed the north-northeast trending Precambrian fabric. Precambrian structures reactivated as transfer zones in the rift phase compartmentalized the different segments of the margin. Most of the brittle deformation responsible for the upper crustal stretching seems to have occurred from Late Aptian to Early Albian between the Sergipe and Pernambuco margins. The rift tectonics in the Sergipe-Alagoas margin developed through oblique rifting controlled by ENE-trending Precambrian faults. Oblique rifting of this margin implies that the cross-sections directions are not adequate to measure upper crustal stretching. Although the rift phase lasted from Neocomian to Early Albian, 144 to 112 Ma, the rift peak was around 124 Ma at the Aptian onset in Sergipe and Alagoas. The rift peak was earlier in the Recôncavo-Tucano-Jatobá system, around 130 Ma. Following continental lithosphere stretching and thinning, continental lithosphere break-up propagated into the Northeast Brazilian rifted margin from 125 to 110 Ma. Thermal subsidence overlapped fault-controlled subsidence during the transitional phase, from 115 to 112 Ma. Marine conditions have prevailed since the Aptian.

CHAPTER 4

4. THE SELECTED TRANSECTS OF THE NORTHEAST BRAZILIAN CONTINENTAL RIFTED MARGIN

4.1 INTRODUCTION

The purpose of this chapter is to present the studied cross-sections as examples of the different segments of the rifted margin, with emphasis on the characterization of their OCT and on the position of the unequivocal oceanic crust. The term unequivocal oceanic crust is used here to denote the distal segments of the cross-sections with typical seismic signature of oceanic crust: strong basement reflector with hummocky type pattern. This contrasts with extrusive and intrusive magmatic bodies that can be interpreted either as being placed in stretched continental lithosphere or at the continent-ocean crust boundary (COCB).

The Northeast Brazilian continental rifted margin is both a frontier for petroleum exploration as for scientific investigation. Although igneous bodies have been recognized in the ocean-continent transition (OCT) and clear segments of oceanic crust can be identified offshore, the continent-ocean crustal boundary (COCB) is not clearly identified. The quality of seismic sampling is variable along the ocean-continent transition (OCT). Lack of refraction seismic data and a quiet magnetic zone during break-up time contribute to the poor understanding of this margin.

Six cross-sections were constructed along the Northeast Brazilian rifted margin based on conventional and special seismic reflection surveys, from the sedimentary basin borders onshore to the oceanic crust offshore. The different

segments of the margin represent distinct patterns of combined syn-rift and post-rift subsidence that must reflect different lithosphere thinning patterns. From south to north, the cross-sections that have been analysed sample the following segments of the margin (figure 3.7): 1) Almada-Jequitinhonha, 2) Jacuípe, 3) Sergipe South, 4) Sergipe North, 5) Alagoas and 6) Pernambuco. This study didn't include the Camamu margin. The Almada-Jequitinhonha and Jacuípe cross-sections were interpreted and depth-converted by the *PETROBRAS* interpretation team of the East Brazil margin, in Rio de Janeiro. The cross-sections from Sergipe, Alagoas and Pernambuco margins were reinterpreted by the author based on previous interpretations by the *PETROBRAS* exploration team of the Aracaju exploration office. The seismic sections were depth converted in the Aracaju office with velocity fields evaluated from velocity analysis acquired along the seismic sections, optimized with well data.

The cross-sections from Sergipe and Alagoas margins start with onshore seismic sections, while the others start with shallow water seismic sections. All of them were selected to link with *LEPLAC* project *(Brazilian Continental Shelf Survey Plan*) seismic sections, which extend beyond the ocean-continent transition (Gomes et al., 2000). Some offshore seismic sections were shot with conventional acquisition parameters and the syn-rift blocks and basement could not be well imaged. Deep seismic reflection sections from offshore Sergipe and Alagoas were used with improved imaging of the basement and deep reflectors but even so the interpretation in the ocean-continent transition (OCT) is not straightforward. The *LEPLAC* seismic sections were shot to image the OCT and the oceanic crust basement, but the definition of continental rift blocks and basement is poor.

The continental basement generally is identified in onshore and shallow water seismic sections by a trail of reflectors, which corresponds to the pre-rift succession. Syn-rift sequence limits can also be recognized in onshore and shallow water seismic sections, but it is generally difficult to track them into deep waters. Hence, the following low order sequences were interpreted in the seismic sections: 1) Lower Cretaceous, early syn-rift; 2) Aptian, late syn-rift; 3) Albian-Turonian carbonatic; 4) Campanian-Maastrichtian; 5) Lower Palaeocene; 6) Upper Palaeocene; 7) Eocene, and 8) Oligocene-Miocene. The position where the typical seismic pattern of oceanic crust could be identified in each line was identified in the cross-sections as OC. The COCB location interpretations are the proximal limit of the true oceanic crust and will be tested in next chapters through residual depth analysis and gravity inversion of the Moho.

4.2 PREVIOUS OCT IDENTIFICATIONS IN THE NORTHEASTER BRAZIL RIFTED MARGIN

The ocean-continent transition (OCT) of the region between Jacuípe and Pernambuco has been discussed in previous works based on seismic reflection data. The seismic sections of a deep reflection project and the seismic sections of the *LEPLAC* project, *Brazilian Continental Shelf Survey*, are contiguous with limited superposition, approximately close to the COCB. The deep seismic survey does not extend into the oceanic crust region; while the *LEPLAC* survey does not sample much into the OCT. Seaward-dipping reflectors (SDR) have been recognized in deep seismic reflection sections of the Sergipe and Jacuípe margins (figure 4.1) and interpreted as oceanic crust (Mohriak et al., 1998; Mohriak et al., 1995). These seaward-dipping reflectors were interpreted in seismic reflection sections of the

Sergipe and Alagoas margins from the *LEPLAC* (figure 4.2) with narrow distribution and as extruded over continental crust (Gomes et al., 2000). The interpretation of the SDR as extruded over continental crust is assumed in this thesis because the Northeast Brazilian rifted margin lacks other evidences that related it to a large igneous province or to a volcanic margin, where typical seaward-dipping reflectors have been recognized (Gladczenko et al., 1997; Hinz, 1981).

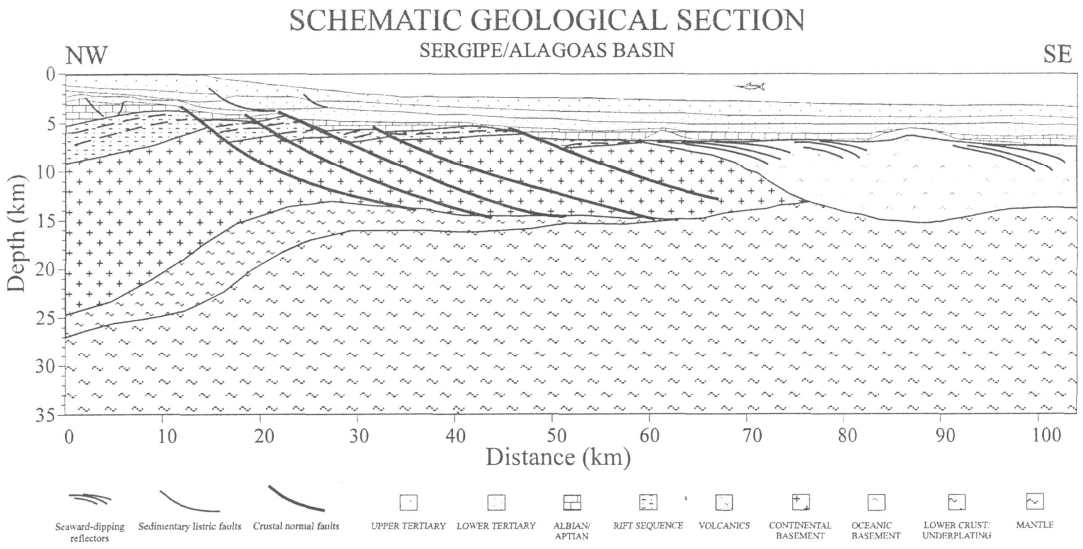

Figure 4.1: Interpretation of the deep seismic reflection section 239-RL-343, part of the Sergipe South cross-section, by (Mohriak et al., 1998).

4.3 ALMADA-JEQUITINHONHA CROSS-SECTION

The southernmost cross-section starts in the Almada basin, close to Ilhéus city, and crosses the boundary with the Jequitinhonha margin (figure 3.7). The important characteristics of this margin segment are the thick syn and post-rift sedimentary piles and the presence of the thick evaporite salt layer, which thins northwardly. The Almada-Jequitinhonha rifted margin evolved from the northern segment of the East Brazil rift system to the south of the position where the rift system split in two branches. Its basement corresponds to the Atlantic Eoproterozoic belt of the São Francisco craton.

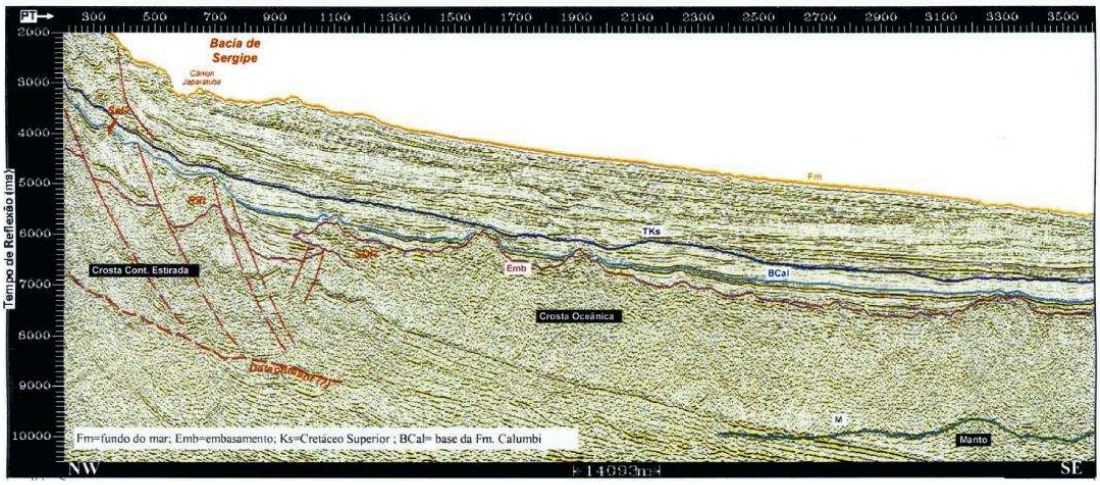

Figure 4.2: Interpretation of *LEPLAC* seismic section, part of the Sergipe South cross-section, by (Gomes, 2005).

The Jequitinhonha margin is separated from the Mucuri margin to the south by the Royal Charlotte High (figure 3.7). The Jequitinhonha and Almada margins are separated by the Olivença High (Rangel et al., 2007). The geological limit between Almada and Camamu is very subtle and could be assigned approximately to the Mutá accommodation zone (Menezes and Milhomem, 2008). The Aptian hinge line runs slightly transversely to the coastline, getting closer to the Almada border in relation to the Camamu border (D. Chiossi personal comm.). This tectonic hinge corresponds to large-displacement normal faults with planar geometry in Almada (Aritagua Fault) and with more listric geometry in Camamu. The hanging walls in Almada and Camamu are characterized by thick packages of medium to coarse grained sandstones and conglomerates (D. Chiossi personal comm.).

The Jequitinhonha-Almada transect is imaged by an arbitrary 3D seismic section in shallow water, linked to a *LEPLAC* cross-section in the distal region (figure 4.3a). This cross-section presents the thickest sedimentary pile and the widest OCT among the selected ones (figure 4.3b). The Aptian sequence includes a continuous salt layer with a piercing structure around 100 km. The hinge line can be

identified around 50 km close to the shoreline and coincides with a gravimetric high, suggesting the initiation of the continental crust thinning (figure 4.3b).

The thick post-rift sedimentary pile seems to flex the basement in the region of the COCB. The initial seismic interpretation suggests the location of the COCB around 360 km of distance, where the pre-neo-Aptian sediments pinch out (figure 4.3b). However, the interpretation of the top and base of salt beyond 245 km seems to be mistaken. An interpretation of the COCB location at 245 km of distance is preferred. The OCT is assumed as the region where antithetic faulting starts, at 100 km of distance, and the COCB location at 245 km of distance. The gravity anomaly edge effect is sharp in the shelf break, and follows with a decreasing gradient in the OCT until around 200 km of distance (figure 4.3a). From this point, free-air gravity increases slowly towards the oceanic crust value.

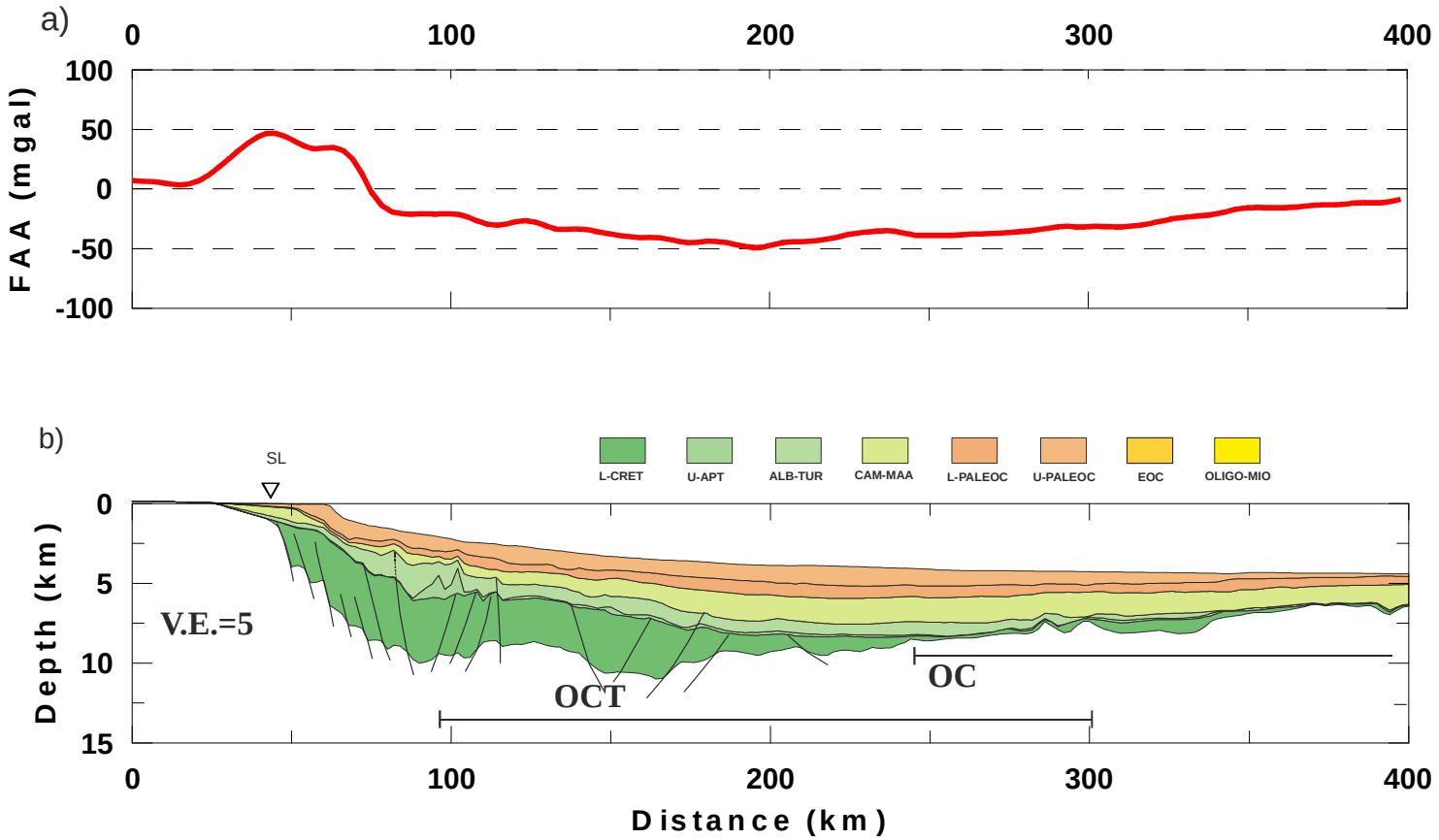

Figure 4.3: Almada-Jequitinhonha transect: a) free air gravity profile, b) geological cross-section. SL, shoreline; OCT, ocean-continent transition, and OC, oceanic crust. The COCB, continent-ocean crust boundary, location is the proximal limit of the oceanic crust, OC.

4.4 JACUÍPE CROSS-SECTION

The Jacuípe margin is located to the north of the rift bifurcation (figures 3.4 and 3.7). This segment is developed over the Paleoproterozoic Atlantic Belt of the São Francisco craton. The Barra fault system (figure 3.7) separates Jacuípe margin from Camamu to the south (Caixeta et al., 2007). The northwest trending Vaza Barris fault system limits Jacuípe margin from Sergipe to the north (figure 3.7).

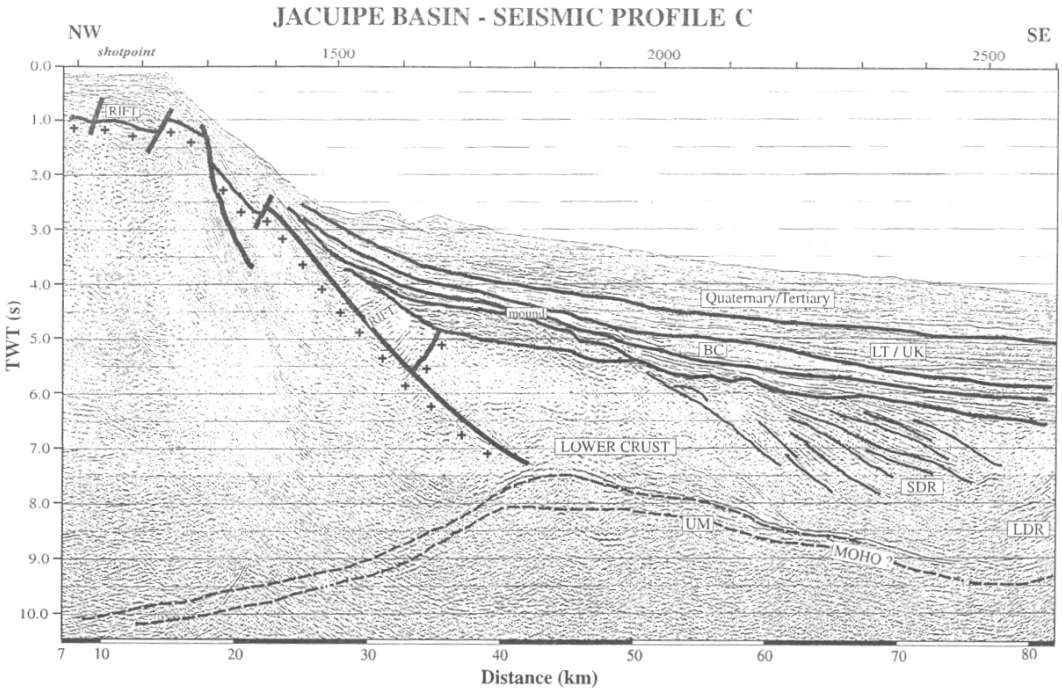

Figure 4.4: Seismic section from Jacuípe margin with interpretation of a strongly rotated rift block, SDR, seaward-dipping reflectors, and deep reflector interpreted as the Moho (Mohriak et al., 1998). UM, Upper Mantle; LDR, landward-dipping reflectors; Calumbi Base unconformity (Campanian); LT/UK, Lower Tertiary/Upper Cretaceous unconformity.

The main characteristic of this margin in cross-sections is a strongly rotated and eroded rift block, without any clear salt structure (figure 4.4). Interpretation of the deep seismic reflection section to the north shows that the rift block is onlapped in the distal part by high amplitude reflectors (figure 4.4), interpreted as early post-rift carbonates or extrusive igneous rocks, in the ocean-continent transition (OCT) (Mohriak et al., 1998). The high amplitude reflectors are then connected to the large

wedge of seaward-dipping reflectors (SDR), interpreted as the initial expression of the oceanic crust (Jackson et al., 2000; Mohriak et al., 1998). Additionally, the SDR downlap a continuous deep reflector, interpreted as the oceanic Moho.

The Jacuípe cross-section has an approximately east-southeast trend and involves the composition of a shallow waters commercial seismic section with a *LEPLAC* seismic section (figure 3.7). It was not possible to merge the *LEPLAC* seismic section with a deep seismic reflection section, located to the north. The COCB location is suggested where syn-rift sediments pinch out at 120 km and unequivocal oceanic crust is identified (figure 4.5b). The OCT is interpreted as the region between 80 and 140 km of distance where Early Cretaceous packages probably correspond to seaward-dipping reflectors. The selected cross-section shows a narrow rift system composed by low angle faults (figure 4.5b), around 40^{o} The gravity anomaly edge effect is characterized by a positive peak, that correlates with the bathymetry shelf break, and by a strong negative anomaly of around -65 *mgal* close to the rift depocentre (figure 4.5a). Then, the free air gravity anomaly recovers to almost 0 *mgal* in the OCT region and stabilizes to the oceanic crust background, between -10 and -20 *mgal*.

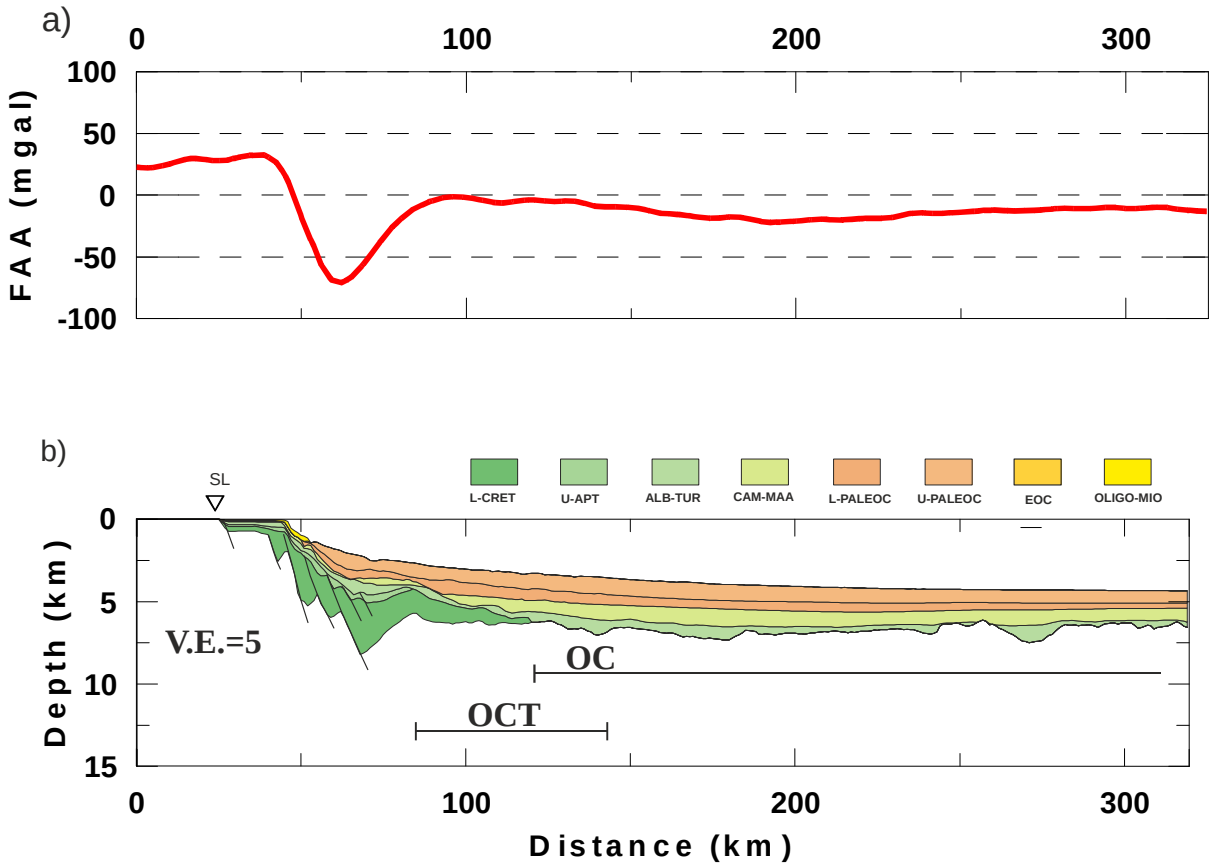

Figure 4.5: Jacuípe transect: a) free air gravity profile, b) geological cross-section. OCT, ocean-continent transition. OC, oceanic crust. The COCB, continent-ocean crust boundary, location is the proximal limit of the oceanic crust, OC..

4.5 SERGIPE SOUTH CROSS-SECTION

The Sergipe margin is developed over metasediments of the Neoproterozoic Sergipano fold belt (figure 3.4). The Sergipe South cross-section comprises the integration of onshore and shallow water conventional seismic sections with an offshore deep seismic section and a *LEPLAC* seismic section (figure 4.6b). The deep seismic section and the *LEPLAC* seismic section have been previously published (figures 4.1 and 4.2) (Gomes et al., 2000; Mohriak et al., 2000; Mohriak et al., 1998). While large salt domes are still present in Jequitinhonha and Almada, small and localized pillows are observed in Sergipe margin, as in the shallow water segment of the Sergipe South cross-section (figure 4.6b). The hinge line crossed by this transect corresponds to an E-W segment, the Atalaia fault, with probable left-slip transtensional movement. The strike-slip component of this important fault is a challenge for structural restoration.

The Aptian hinge line separates an onshore platform with shallow basement from deep basement rift blocks offshore. The ascendant part of the gravity edge effect is attenuated by the presence of sediments onshore (figure 4.6a and b). The positive gravity peak of 50 *mgal* coincides with the shelf break. The OCT starts at around 110 km, where fault polarity is switched. Antithetic rift blocks are characterized by syn-depositional faults dipping to the continent and strata dipping to the sea (figures 4.1, 4.2 and 4.6). These seaward-dipping strata are interpreted in this thesis as syn-rift sedimentary or volcano-sedimentary strata deposited over stretched continental crust (Gomes et al., 2000; Hamsi et al., 2006) due to the paucity of magmatism along the Northeastern Brazilian rifted margin, but they have been alternatively interpreted as oceanic crust (Mohriak et al., 1998).

The external structural high at around 125 km is an extension of the Vaza Barris High, a probable buried, old component of the Bahia seamounts. Unequivocal oceanic crust is identified eastward of 250 km. The segment between 160 and 250 km is probably oceanic crust; however, it is disturbed by igneous mounds and does not present the same clear signature as observed immediately offshore. The sharp descendent part of the free-air gravity anomaly edge effect corresponds to the beginning of the OCT, where it stabilizes around 0 mgal. Then the gravity anomaly slowly decreases until stabilizes around -20 *mgal* (figure 4.6a).

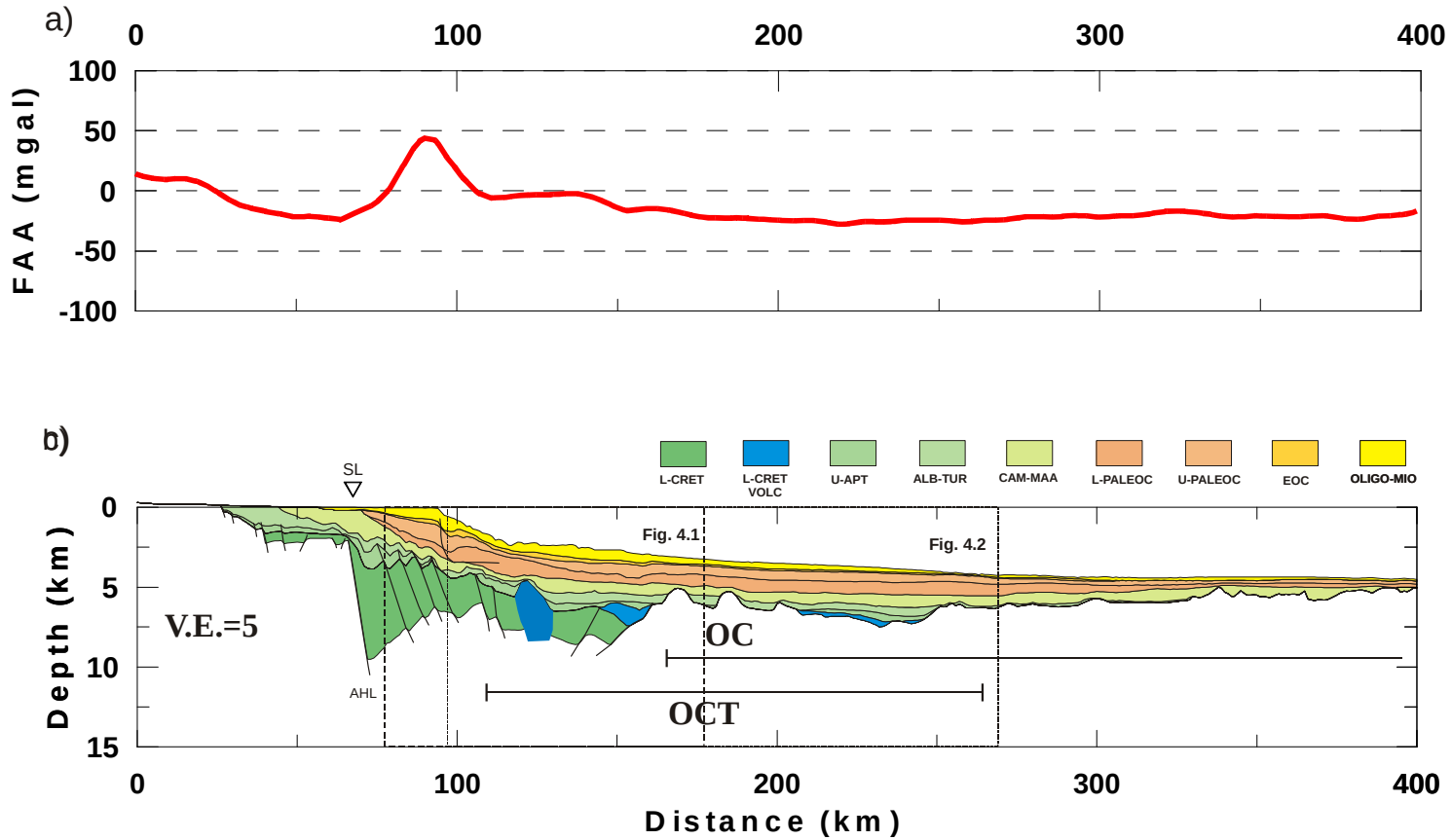

Figure 4.6: Sergipe South transect: a) free air gravity profile, b) geological cross-section. AHL Aptian hinge line; SL, shoreline; OCT, ocean-continent transition, and OC, oceanic crust. The COCB, continent-ocean crust boundary, location is the proximal limit of the oceanic crust, OC..

4.6 SERGIPE NORTH CROSS-SECTION

The Sergipe North cross-section also comprises the integration of onshore and shallow water, conventional seismic sections with offshore deep seismic sections, complemented with a *LEPLAC* seismic section (figure 4.8b). This cross-section is also developed over the Neoproterozoic Sergipano fold belt. The basin border is an erosive limit in this section. The Penedo fault is the major onshore hinge, controlling thickening of pre-Aptian sequences. The Penedo fault is considered as a component of a transfer zone that reaches the Maceió-Ascension fracture zone offshore (figure 3.7). The Sergipe North cross-section presents thicker syn and post-rift successions than Sergipe South, suggesting that it samples a region subjected to larger lithosphere thinning.

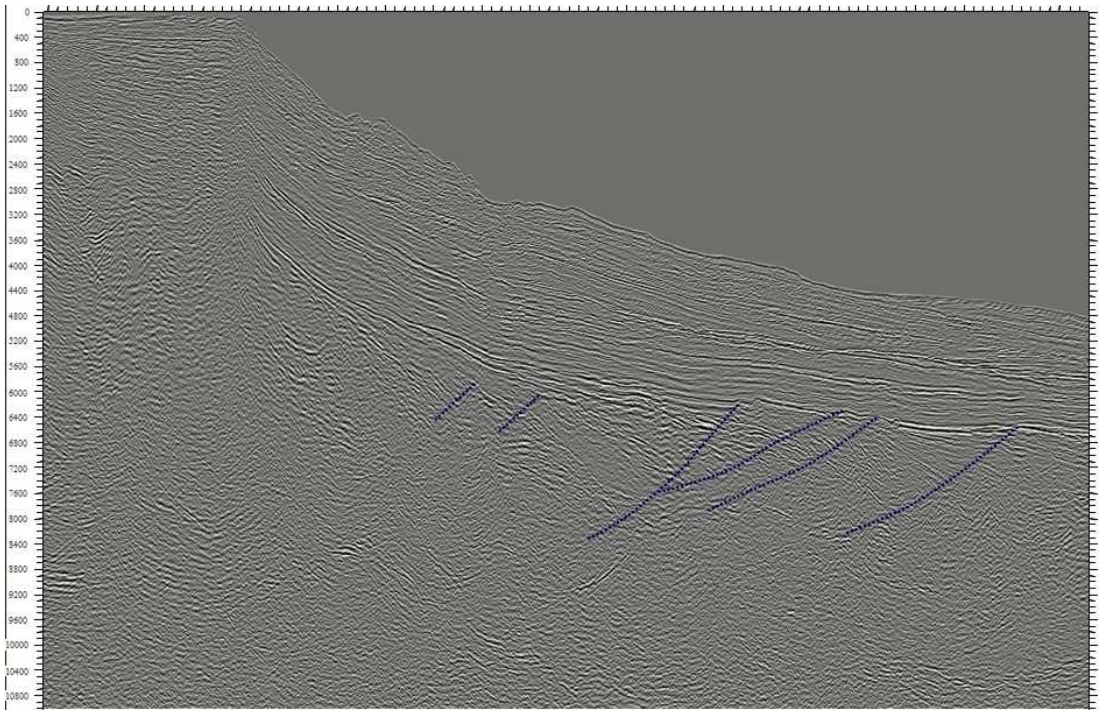

Figure 4.7: Detail of the antithetic faulting developed offshore in the Sergipe North cross-section, alternatively interpreted as oceanic crust-related seaward-dipping reflectors (Mohriak et al., 1995).

The Aptian hinge line occurs in the shallow water region, and the fault polarity is switched beyond an external high under the shelf break (figure 4.7), where

the ocean-continent-transition (OCT) starts, similarly to the previous cross-section. The positive peak of the free-air gravity anomaly edge effect coincides with the shelf break and with the external high (figure 4.8a). The OCT in this cross-section comprises the region where antithetic blocks offshore are well developed, bounded by growth faults and filled with seaward-dipping reflectors (figure 4.7). If these seaward-dipping reflectors correspond to oceanic crust, the continent-ocean crust boundary should be placed closer to the shelf break. The limit of the unequivocal oceanic crust is an external high eastward 175 km that corresponds either to an oceanic crust rift flank or to a buried seamount (figure 4.8b). The descendent part of the gravity anomaly edge effect comprises the OCT. The gravity anomaly stabilizes close to the limit of the unequivocal oceanic crust around -20 mgal (figure 4.8a).

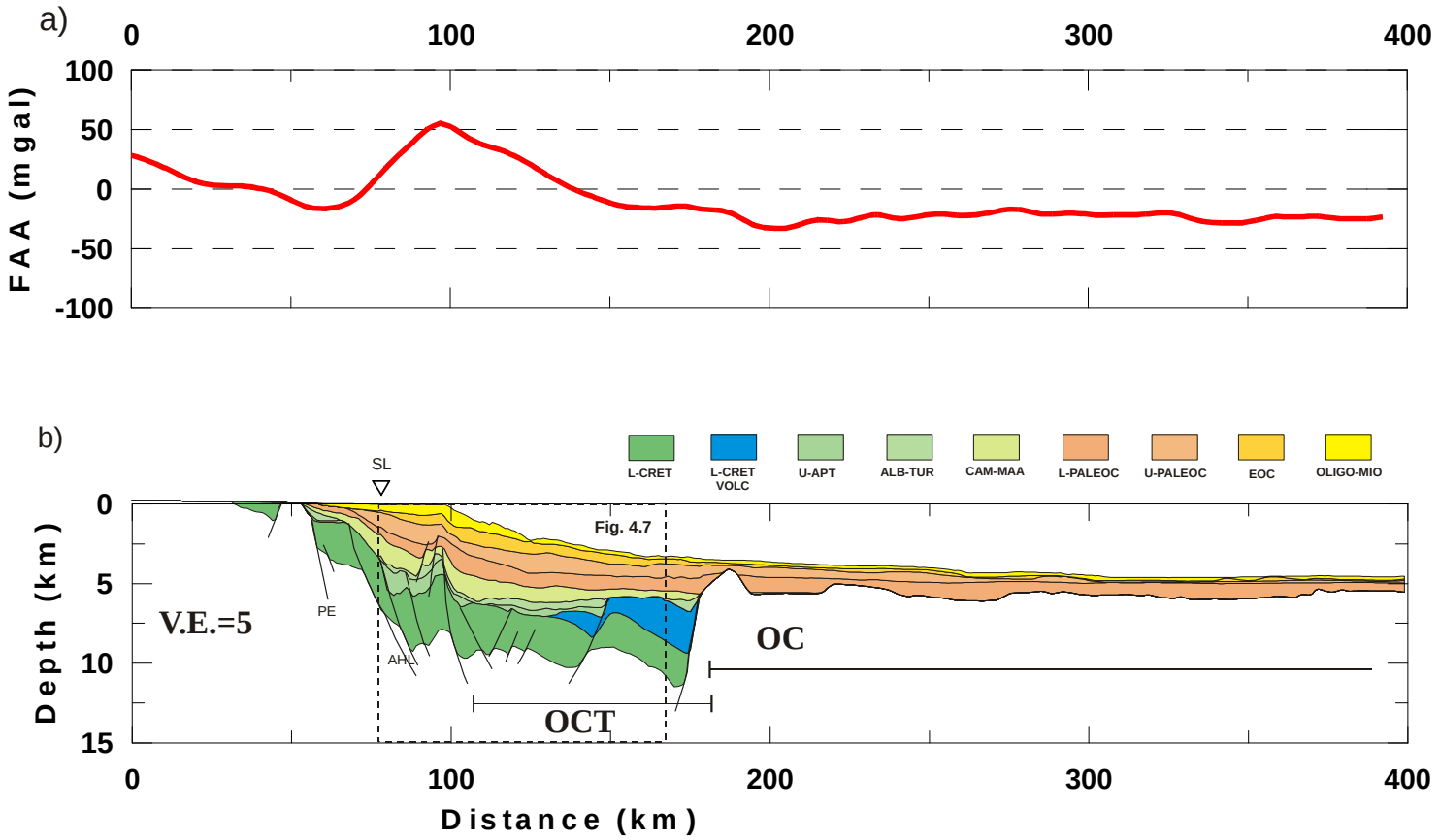

Figure 4.8: Sergipe North transect: a) free air gravity profile, b) geological cross-section with position of detail in figure 4.7. PE, Penedo Fault; AH Aptian hinge line; SL, shoreline; OCT, ocean-continent transition, and OC, oceanic crust. The COCB, continent-ocean crust boundary, location is the proximal limit of the oceanic crust, OC..

4.7 ALAGOAS CROSS-SECTION

The proximal segment of the Alagoas cross-section is placed over the granitic terrain of the Neoproterozoic Pernambuco-Alagoas Massif. The limit between Alagoas and Cabo basins is considered as the Maragogipe basement high (Pontes et al., 1991) (figure 3.7), active during syn-rift (Campos Neto et al., 2007). However, this structural high is clearly also a late to post-rift inversion feature, as shallow water seismic sections, parallel to the coast, show syn-rift layers truncated at an erosive unconformity. Transpressional zones are observed in shallow water seismic sections, parallel to the shoreline, and seem to enhance uplift locally.

The Alagoas cross-section comprises the integration of an onshore seismic section with deep and conventional seismic sections offshore, complemented by a *LEPLAC* seismic section (figure 4.9b). It was not possible to construct a cross-section that sampled only the Alagoas margin context and avoiding the Maceió lineament (figure 3.7). The selected cross-section exemplifies the main characteristic of this margin segment, the lack of post-rift sequences onshore and in the continental shelf. Data from onshore and shallow waters wells show denudation in the order of 2000 m. However, it is not clear whether the post-rift succession was deposited and eroded or never deposited onshore.

The hinge line corresponds to the onshore border fault. The positive peak of the free-air gravity anomaly edge effect coincides with the shelf break (figure 4.9a) and the descendent portion of the gravity edge effect is sharp, marking the beginning of the OCT. The prominent Maceió high, interpreted as a volcano (Pontes et al., 1991), is located in the prolongation of the Maceió-Ascension fracture zone, between 105 and 120 km of distance (figure 4.9b). A fault system was interpreted in the OCT

between 120 and 200 km of distance, limited offshore by a small wedge of seaward-dipping reflectors. The small wedge of SDR is bounded by a structural high that constrains the unequivocal oceanic crust around 200 km (Gomes et al., 2000) (figure 4.9b). The Maceió high corresponds to a small positive peak in the free-air gravity anomaly, which then ascends towards the oceanic crust background, around -20 *mgal*, in the interpreted COCB (figure 4.9a and b).

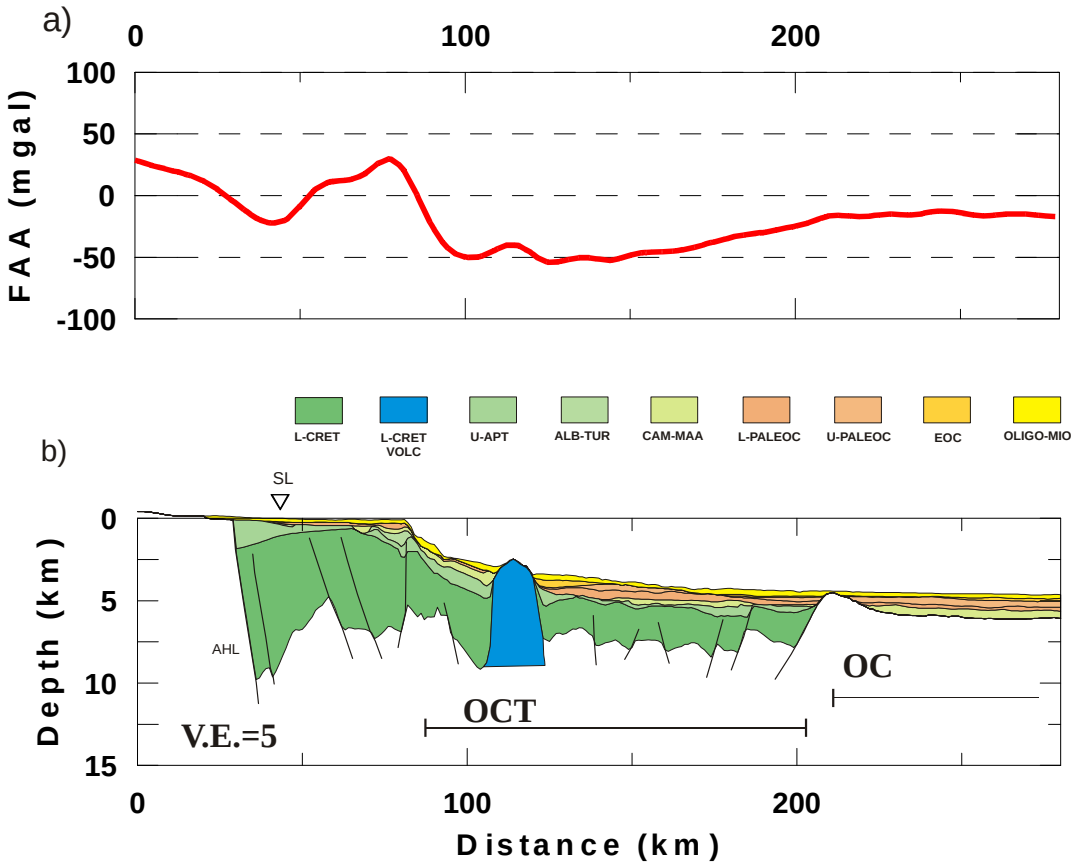

Figure 4.9: Alagoas transect: a) free air gravity profile, b) geological cross-section. AHL Aptian hinge line; SL, shoreline; OCT, ocean-continent transition, and OC, oceanic crust. The COCB, continent-ocean crust boundary, location is the proximal limit of the oceanic crust, OC.

.

4.8 PERNAMBUCO

The poorly understood Pernambuco Plateau is an anomaly in the continental slope, which is expanded and less inclined. The Pernambuco Plateau was formed either by continental stretching or magmatic addition, or most probably by combination of both. The Pernambuco Plateau also developed in the region of the Pernambuco-Alagoas Massif. The northern limit is defined by the Pernambuco lineament (figures 3.4, 3.5 and 3.7). Some continuity of rift depocentre is observed between offshore Alagoas and the Pernambuco Plateau (M. Nabuco pers. comm.). Syn-rift depocentres are separated by structural highs and must present infill similar to the onshore Cabo basin (Almeida et al., 2005). At least some of the structural highs are igneous bodies according to aeromagnetic and gravity data (F. Barros pers. comm.). Like the Alagoas margin, the Pernambuco Plateau margin is clearly sediment starved in the post-rift and a very thin sedimentary cover is preserved (figure 4.10b). Thus, the combination of rift tectonics, magmatic addition and peculiar bathymetry makes the Plateau an interesting target for the study of the relationship between lithosphere thinning and total subsidence.

The Pernambuco cross-section comprises the composition of two conventional seismic sections in the region of the Pernambuco Plateau, complemented with a *LEPLAC* seismic section (figure 4.10b). The Cabo basin is the onshore *graben*, where the only deep well has been drilled in the area, around 3000 m-deep. The Aptian hinge line corresponds to the border fault of the Cabo basin, interpreted from gravity data. Another hinge line is defined just beyond the shelf-break, around 75 km, where the gravity anomaly edge effect develops (figure 4.10a).

Rift tectonics have been previously interpreted offshore up to a marginal escarpment that corresponds to the COCB (Gomes et al., 2000). Due to the presence of volcanic bodies and due to the presence of antithetic faults, the whole Pernambuco Plateau can be considered as an ocean-continent transition (OCT). As the COCB is clearly identified in seismic reflection section this margin is suitable to test the analytical methodology developed in this thesis. Two structural highs in the plateau correspond to a volcanic mound and to a horst (Alves and Costa, 1986; Pontes et al., 1991). An escarpment around 160 km in the cross-section seems to be related to a syn-rift fault that was not covered by post-rift sediments. The free-air gravity anomaly is low between the edge effect and the COCB, being interrupted by the volcanic mound around 110 km and by the horst at 160 km (figure 4.10a).

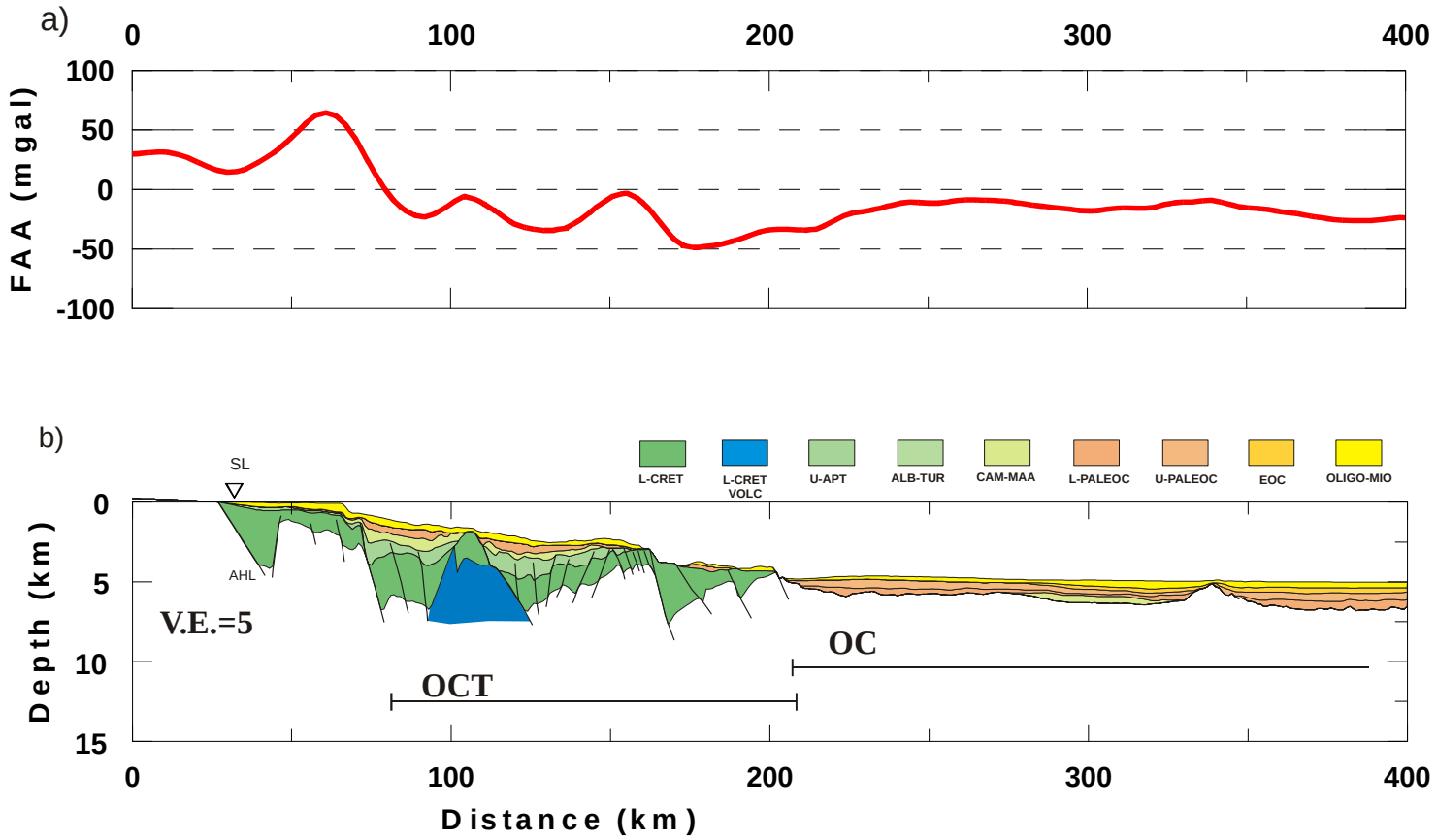

Figure 4.10: Pernambuco transect: a) free air gravity profile, b) geological cross-section. AHL Aptian hinge line; SL, shoreline; OCT, ocean-continent transition, and OC, oceanic crust. The COCB, continent-ocean crust boundary, location is the proximal limit of the oceanic crust, OC..

CHAPTER 5

5. SEDIMENT LOAD CORRECTION THROUGH FLEXURAL BACKSTRIPPING

5.1 INTRODUCTION

Total subsidence caused by lithosphere thinning in the syn-rift and by dissipation of the thermal anomaly during the post-rift is amplified by sedimentary loading. The purpose of this chapter is to present the methodology to correct for the sedimentary loading and to produce sediment-corrected basement depth profiles. Flexural backstripping corrects the effect of sedimentary loads on basement depth through the successive removal of each sedimentary layer, from top to bottom and considering flexural isostatic response (figure 5.1). Sediment-corrected basement depth profiles are used for the determination of the residual depth anomalies (RDA) in the adjacent oceanic crust and for the inversion of whole lithosphere thinning.

Flexural backstripping of the sedimentary load involves the following steps (Kusznir et al., 1995; Nadin and Kusznir, 1995; Roberts et al., 1998):

1) Removal of the free water load.
2) Determination of the load of the topmost sedimentary layer.
3) Removal of the topmost layer.
4) Decompaction of the underlying layers.
5) Calculation of the flexural isostatic response of the removed layer.
6) Calculation of the isostatic response of the water added to the decompacted underlying layers.

7) Reapplication of the free water load.

8) Steps 1 to 7 are repeated until the removal of the oldest sedimentary layer, deposited at the beginning of the rift phase.

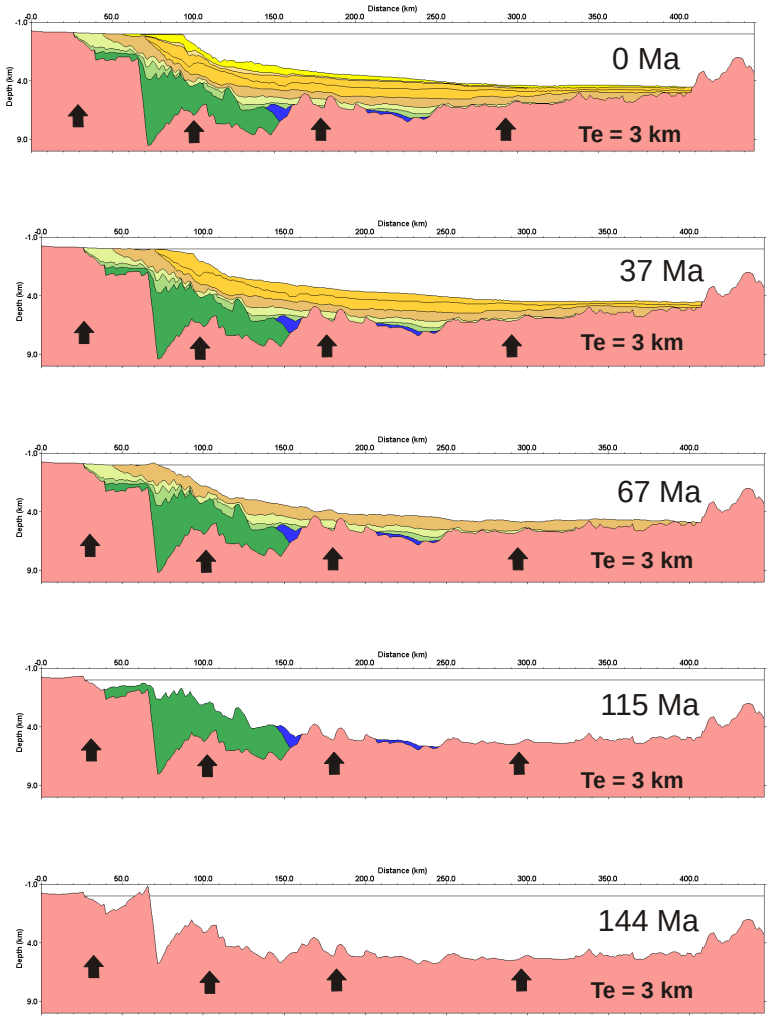

Figure 5.1: Stages of the Sergipe-South cross-section flexural backstripping with effective elastic thickness *Te*=3 km. Sediment-corrected basement depth profile is obtained after the removal of the oldest sedimentary sequence at 144 Ma.

5.2 SEDIMENTS COMPACTION

Sediments compact with depth from the burial surface according to an exponential porosity decay (Athy, 1930):

$$\phi = \phi_0 \cdot e^{-c \cdot s}, \qquad (2.16)$$

The decay parameters ϕ_0 and c are specific for each main rock assemblage of each basin (Sclater and Christie, 1980). Porosity decay parameters for shale, mixed shale-sandstone and mixed shale-carbonate from the Sergipe and Alagoas basins were applied for the determination of the load of the sedimentary sequences of the studied cross-sections (table 5.1). The Sergipe and Alagoas sedimentary basins are intensely sampled by petroleum exploratory wells, while the neighbour margins are still poorly drilled. Post-rift shale sonic velocity log data of 7 wells located offshore Sergipe suggest lower porosity decay than the data obtained by Sclater & Christie (1980) from North Sea shale (figure 5.2). Mixed shale-sandstone sonic velocity log data of 9 exploratory wells located onshore and offshore Alagoas suggest faster porosity decay than the data from Sclater & Christie (1980) (figure 5.2).

It is not expected that the post-rift sedimentary succession compaction, mostly controlled by shale, vary so much along the margin. The compaction of the syn-rift sedimentary succession, predominantly intercalation of shale and sandstone beds, can vary along the margin due to uplift and erosion, among other controls, like lithology and diagenesis. However, the errors in compaction are not expected to be large enough to affect the results of the flexural backstripping.

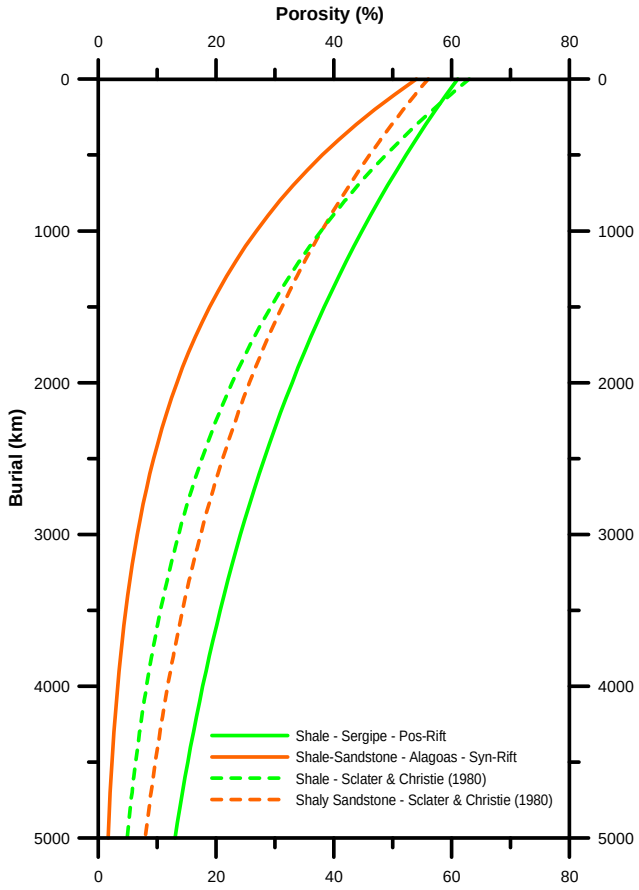

Figure 5.2: Porosity decay curves of Shale and Mixed Shale-Sandstone obtained with data from Sergipe and Alagoas, compared to the corresponding curves from Sclater & Christie (1980).

5.3 FLEXURAL ISOSTATIC RESPONSE

The flexural isostatic compensation of a laterally varying load *l* applied to the lithosphere results in deflection of its surface by flexure *w*:

$$D\frac{\partial^4 w}{\partial x^4} + P\frac{\partial^2 w}{\partial x^2} + (\rho_{fluid} - \rho_{infill})g \cdot w(x) = (\rho_{load} - \rho_{displaced})g \cdot l(x), \quad (5.1)$$

where D is the lithosphere flexural rigidity. For sedimentary loading at rifted margins, the in-plane horizontal forces P can be ignored. This equation is solved in the wave-number domain, through the application of the Fourier Transform and its inverse (Turcotte and Schubert, 2002):

$$w(k) = \frac{(\rho_{sed} - \rho_{water}) \cdot g \cdot l(k)}{(\rho_{ast} - \rho_{water}) \cdot g + Dk^4}, \quad (5.2)$$

where k is the wave number, ρ_{sed} is the average sediments density, ρ_{ast} is the asthenosphere density, (ρ_{sed}-ρ_{water}) is the density contrast caused by the load and (ρ_{ast}-ρ_{water}) is the density contrast caused by the deflection. The lithosphere flexural rigidity D is given by (Turcotte and Schubert, 2002):

$$D = \frac{ETe^3}{12(1-\upsilon^2)}, \qquad (5.3)$$

where Te is the effective elastic thickness, E is the Young's modulus and ν is the Poisson's ratio, rheological parameters of the lithosphere.

Local isostatic compensation generally assumed in the depth-uniform lithosphere stretching model (McKenzie, 1978) and in the sediment correction for evaluation of oceanic bathymetry (Crosby et al., 2006; Parsons and Sclater, 1977; Stein and Stein, 1992) corresponds to zero effective elastic thickness and zero flexural rigidity. The deflection w then becomes directly proportional to the load in equation 5.2. This situation is unlikely in nature but can be a reasonable approximation for the isostatic response of large wavelength loads.

Effective elastic thicknesses between 1.5 and 5 km have been determined for extensional settings (Roberts et al., 1998). These values are much lower than the thickness of the cool brittle upper crust, between 10 and 15 km (Kusznir et al., 1991). The effective elastic thickness depends on: the bending stresses applied to the plate, the rate of stress application, the lithosphere composition and geothermal gradient (Kusznir and Karner, 1985; Kusznir et al., 1991; Kuznir and Park, 1987). Low effective elastic thickness in extensional basins probably results from brittle failure of the upper crust during continental extension (Kusznir et al., 1991).

Table 5-1: Compaction parameters of equation 2.16, ϕ_0 and c, and matrix densities, ρ_b, obtained from well log data of Sergipe basin for Albo-Turonian to Upper Miocene sequences and from well log data of Alagoas basin for Neocomian to Upper Aptian sequences.

Layer	Lithology	Age Base (Ma)	ρ_b	ϕ_0	c
Upper Miocene	Shale	16	2680	0.61	0.31
Oligo-Miocene	Shale	37	2680	0.61	0.31
U. Paleoc-Eocene	Shale	57	2680	0.61	0.31
Lower Paleocene	Shale	65	2680	0.61	0.31
Upper Cretaceous	Shale	89	2680	0.61	0.31
Albo-Turonian	Mixed Shale-Carbonate	112	2700	0.50	0.48
Upper Aptian	Mixed Shale-Sandstone	115	2660	0.54	0.70
Meso Aptian	Basalt	118	2850	0.10	0.90
Neocomian	Mixed Shale-Sandstone	144	2660	0.54	0.70

5.4 FLEXURAL BACKSTRIPPING OF THE SIX STUDIED CROSS-SECTIONS

The sensitivity to the effective elastic thickness is shown for the Sergipe North cross-section in figure 5.3. Sediment-corrected basement depth profiles were calculated with *Te* of 0.01, 0.1, 0.5, 1.0, 3.0, 5.0 and 10 km. Sediment-corrected basement depth in the oceanic crust is insensitive to *Te*. Sediment-corrected basement depth profiles determined with elastic thickness of 3 km are preferred (figure 5.1) because they result in less distorted syn-rift basement in the shallow region, close to the margin border (figures 5.3 and 5.4).

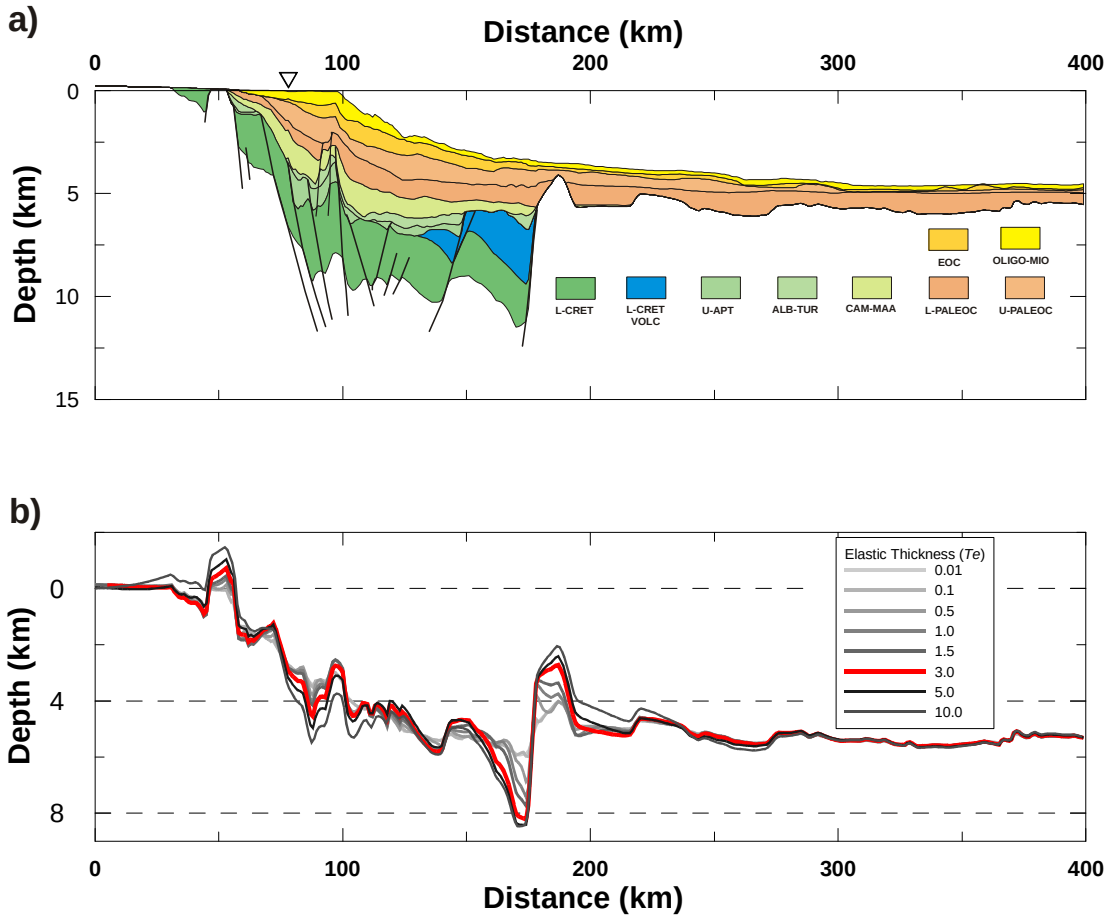

Figure 5.3: Sensitivity of flexural backstripping of the Sergipe-North cross-section to effective elastic thickness, *Te*.

The sediment-corrected basement depth profiles can be described as asymptotes curves that start with approximately zero depth in the margin border and increase to a constant value at the oceanic region. These asymptotes curves are disturbed across the rifted margin by faults and igneous bodies (figure 5.3 and 5.4), while the segments in the oceanic crust are fairly smooth. The Alagoas and Sergipe North profiles show sharp discontinuities in the continent-ocean crustal boundary (COCB) interpreted in seismic sections, around 200 and 180 km respectively (figure 5.4.b and c). However, correlating sharp discontinuities to the COCB location in other profiles can be misleading. As an example, a similar sharp discontinuity appears around 160 km in the Pernambuco profile, although the COCB is clearly identified in reflection seismic section around 225 km (figures 4.10b and 5.4a).

The sediment-corrected basement depth profiles are compared in next chapter with the oceanic bathymetry predicted by plate cooling models for the age of the margin (Crosby and McKenzie, 2009; Parsons and Sclater, 1977; Stein and Stein, 1992). In chapter 11, the sediment-corrected basement depth is assumed as total subsidence and used to invert whole lithosphere thinning. Initial bathymetry is assumed at sea-level.

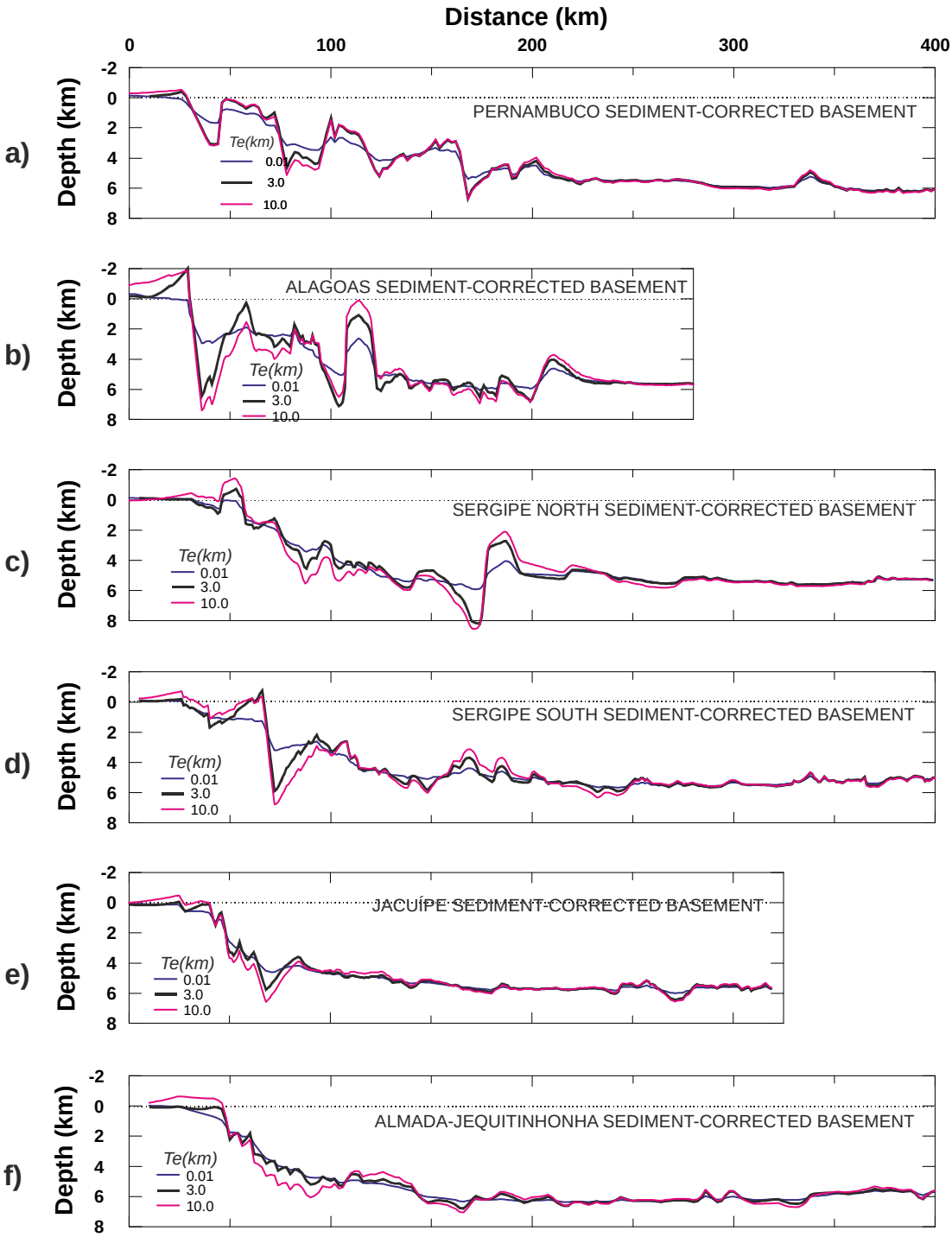

Figure 5.4: Sediment-corrected basement depth profiles of the six studied cross-sections, calculated by flexural backstripping.

CHAPTER 6

6. RESIDUAL DEPTH ANOMALY ANALYSIS OF THE OCT AND THE ADJACENT OCEANIC CRUST SEGMENTS OF THE NORTHEAST BRAZILIAN RIFTED MARGIN

6.1 INTRODUCTION

In order to locate the continent-ocean crustal boundary (COCB) and the ocean-continent transition (OCT) it is necessary to compare the oceanic crust sediment-corrected basement depth and thickness with those of the thinned continental lithosphere. The residual depth anomaly, RDA, is the difference between the basement depth predicted for an oceanic region by empirical relationships with age, derived from plate cooling models (Crosby and McKenzie, 2009; Parsons and Sclater, 1977; Stein and Stein, 1992), and the basement depth measured in this region, both corrected for sediment loading (White et al., 1992). Oceanic crustal thickness measurements by refraction seismic are not available in the area. However, oceanic crustal thickness can be indirectly estimated by RDA. The objectives of this chapter are:

1) Determine the RDA for the six selected cross-sections.

2) Interpret the COCB wherever possible from the RDA results.

3) Estimate the oceanic crustal thickness from the RDA.

6.2 RESIDUAL DEPTH ANOMALIES DETERMINATION

Residual depth anomalies (RDA) generally arise from thickness variations of the oceanic crust or from dynamic topography (White et al., 1992). Negative RDA

come from subduction zones, flexural moats around seamounts and fracture zones, whereas positive RDA corresponds to seamounts, hot spot tracks and areas with active volcanism (Crosby and McKenzie, 2009; White et al., 1992). Assuming an approximately constant crustal density, it is expected that the RDA extrapolated to the OCT be larger than in the oceanic crust, because the stretched continental crust must be thicker than the oceanic crust. Thus, a change from large positive RDA in the OCT towards the oceanic background can be used for identification of the COCB.

An average oceanic crustal thickness of 7080 m was obtained from seismic refraction data for regions with RDA between – 0.5 and 0.5 km, calculated in relation to the PSM model (White et al., 1992). The RDA determinations obtained by those authors are plotted against oceanic crustal thickness measurements in figure 6.1, according to the oceanic crust types. The cross-plot shows a linear relationship except for some anomalous values from fracture zones. The RDA data from the areas affected by the Icelandic Plume and generated directly above plumes plot above the linear relationship; probably due to dynamic topography (figure 6.1). A simple local isostatic compensation calculation, relating RDA to oceanic crustal thickness t_c, fits most of the data below 10 km:

$$RDA = (t_c - 7.08) \cdot \frac{(\rho_c - \rho_m)}{(\rho_w - \rho_m)}, \qquad (6.1)$$

where ρ_c, ρ_m and ρ_w are densities of crust, mantle and water respectively.

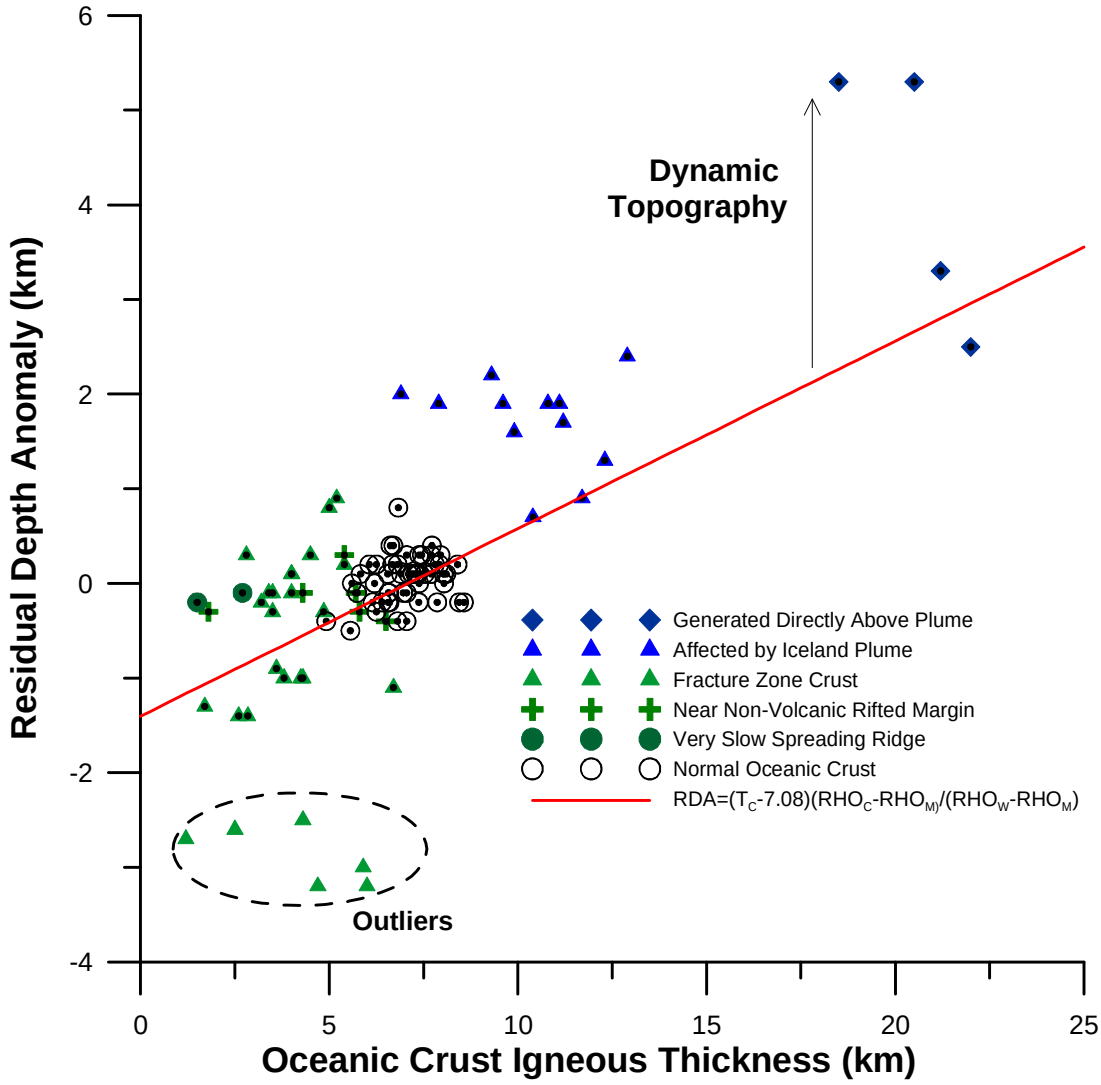

Figure 6.1: Residual depth anomaly plotted against oceanic crust igneous thickness. Data from (White et al., 1992). Red line corresponds to RDA predicted by a simple local isostatic compensation equation. Some data from fracture zones are outliers with RDA smaller than expected for the crustal thickness.

The normal trend of sediment-corrected oceanic bathymetry with age, derived from the plate cooling model (Parsons and Sclater, 1977), corresponds to oceanic crust whose thickness is expected to be very close to the average. Consequently observed oceanic bathymetry, deeper than predicted, results in negative RDA and can be associated with oceanic crust thinner than the average, except in regions of dynamic topography. Thin oceanic crust results from suppression of magmatic addition by slow decompression rate (Fletcher et al., 2009). In contrast, oceanic

bathymetry shallower than predicted results in positive RDA associated with oceanic crust thickened by magmatic addition. Therefore, magma-rich margins are related to positive RDA, while magma-poor margins are related to negative RDA (White et al., 1992). Shallower oceanic bathymetries suggested by the GDH1 and CM models imply that the average oceanic crustal thickness according to the PSM model ((White et al., 1992) could be underestimated. Residual depth anomalies has also been denominated as residual topography (Crosby and McKenzie, 2009) and residual bathymetry (Korenaga and Korenaga, 2008).

6.3 Residual Depth Anomaly Profiles of The Northeast Brazilian Rifted Margin

The determination of the residual depth anomalies for the six studied cross-sections of the Northeast Brazilian rifted margin involved the subtraction of the sediment-corrected basement depth profiles bat_{obs} from those predicted by the PSM, GDH1 and CM models, $bat(t)_{pred}$:

$$RDA = bat(t)_{pred} - bat_{obs} . \quad (6.2)$$

The predicted oceanic basement depth profiles were calculated through the equations of PSM, GDH1 and CM models (table2-2) using the ocean age isochrons from (Müller et al., 2008) (figure 6.2). The ages trends were extrapolated into the ocean-continent transition (OCT) of each profile (figures 6.3-9c). In general, the RDA value extrapolated to the continental region decreases to the RDA of the adjacent oceanic crust asymptotically. However, this decrease is usually irregular in the OCT due to the presence of faults and igneous bodies. The COCB can be considered as the most proximal position where the RDA profile achieves the background value of the adjacent oceanic crust . The calculated RDA profiles are presented in figures 6.3 to

6.9 and discussed in next sections. Free-air gravity anomaly, geological cross-section and sediment-corrected basement depth profile are also shown for comparison.

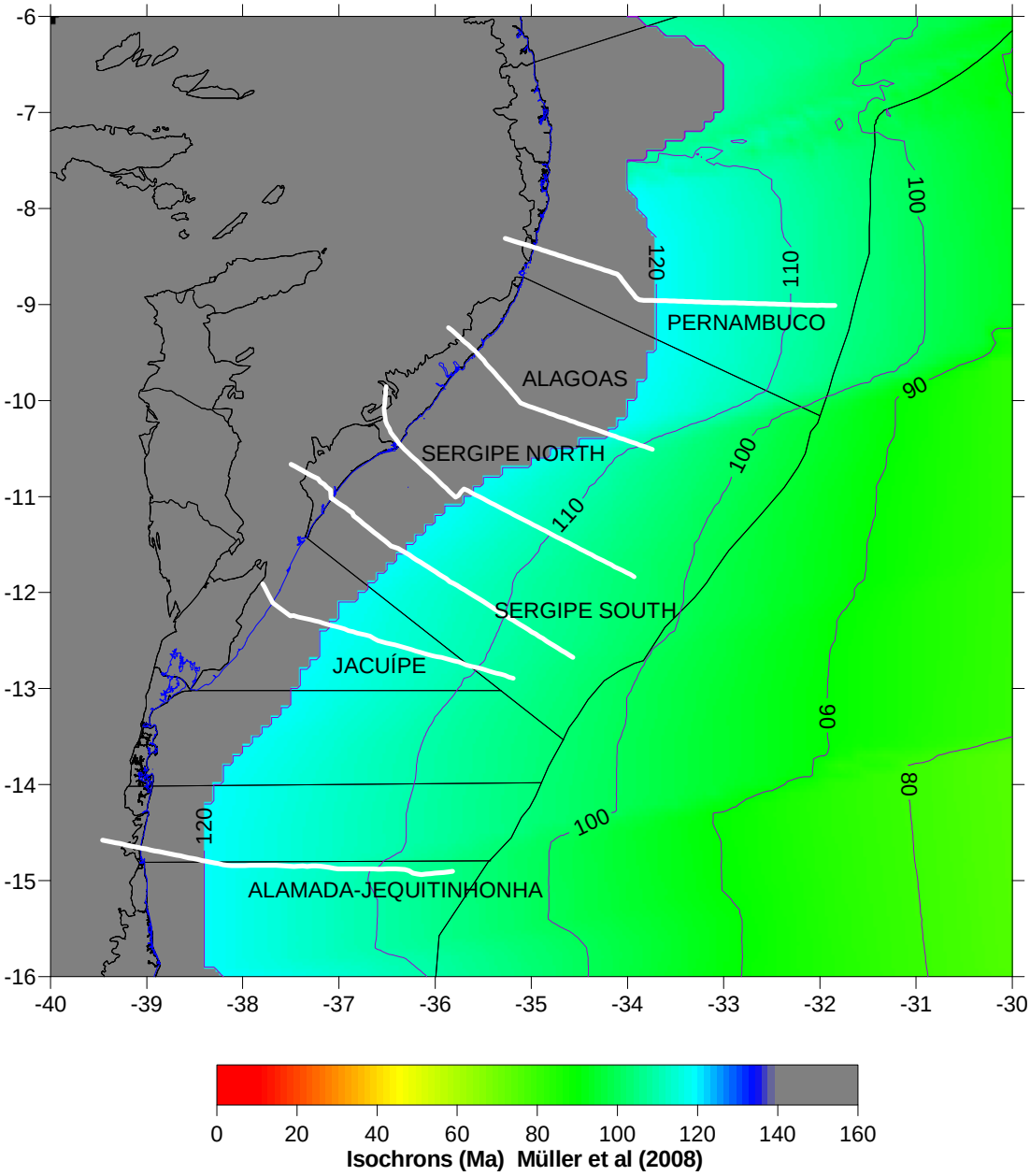

Figure 6.2: Oceanic crust age map of the Northeastern Brazilian rifted margin. Data from (Müller et al., 2008).

The ocean age isochrones are not accurate in this margin due to lack of magnetic anomalies. For the age range expected for the continental lithosphere break-up time, between 100 and 120 Ma, the predicted bathymetry curves as a function of age are practically stable (figure 2.9). The largest ocean age error

expected for this margin would occur by wrongly mistaking isochrons 120 and 100 Ma. According to the PSM model (Parsons and Sclater, 1977), this ocean age error implies a maximum predicted bathymetry error of 178 m. Therefore, small errors in ocean ages must imply very small error in predicted bathymetry that will not considerably affect the residual depth anomaly profiles.

At the age range of Northeast Brazilian margin (100 to 120 Ma), the predicted oceanic basement depth varies between 5500 and 6000 m, according to the range of the plate cooling model considered (figure 2.9). The PSM model predicts the greatest oceanic depths, while the GDH1 model predicts the smallest. Sediment-corrected oceanic basement data from the West and Northwest Atlantic, CM_NA (Crosby and McKenzie, 2009), were fit with an exponential function intermediary between PSM and GDH1 functions (table 2-2 and figure 2.9).

6.3.1 ALMADA-JEQUITINHONHA RDA PROFILE

The Almada-Jequitinhonha profile shows RDA of -500 m between 160 and 340 km in unequivocal oceanic crust (figure 6.3f). This region has a free-air gravity anomaly around -40 *mgal* (figure 6.3a). RDA then jumps to around 0 km in the distal region, where free-air gravity anomaly is around -15 mgal. According to equation 6.1, RDA of -500 m in the proximal oceanic crust (figure 6.3f) corresponds to a crustal thickness of 4.6 km. Therefore, the Almada-Jequitinhonha margin can be considered as magma-poor. However, the distal segment of the profile seems to be related to a normal oceanic crust with thickness around 7.1 km (figure 6.1 and table 6-1).

The RDA profile reaches the oceanic crust background of – 250 m at 140 km of distance from the continent (figure 6.3e and f). As this RDA value can be reached

due to faulting, the position at 140 km can be considered as a proximal limit of the COCB.

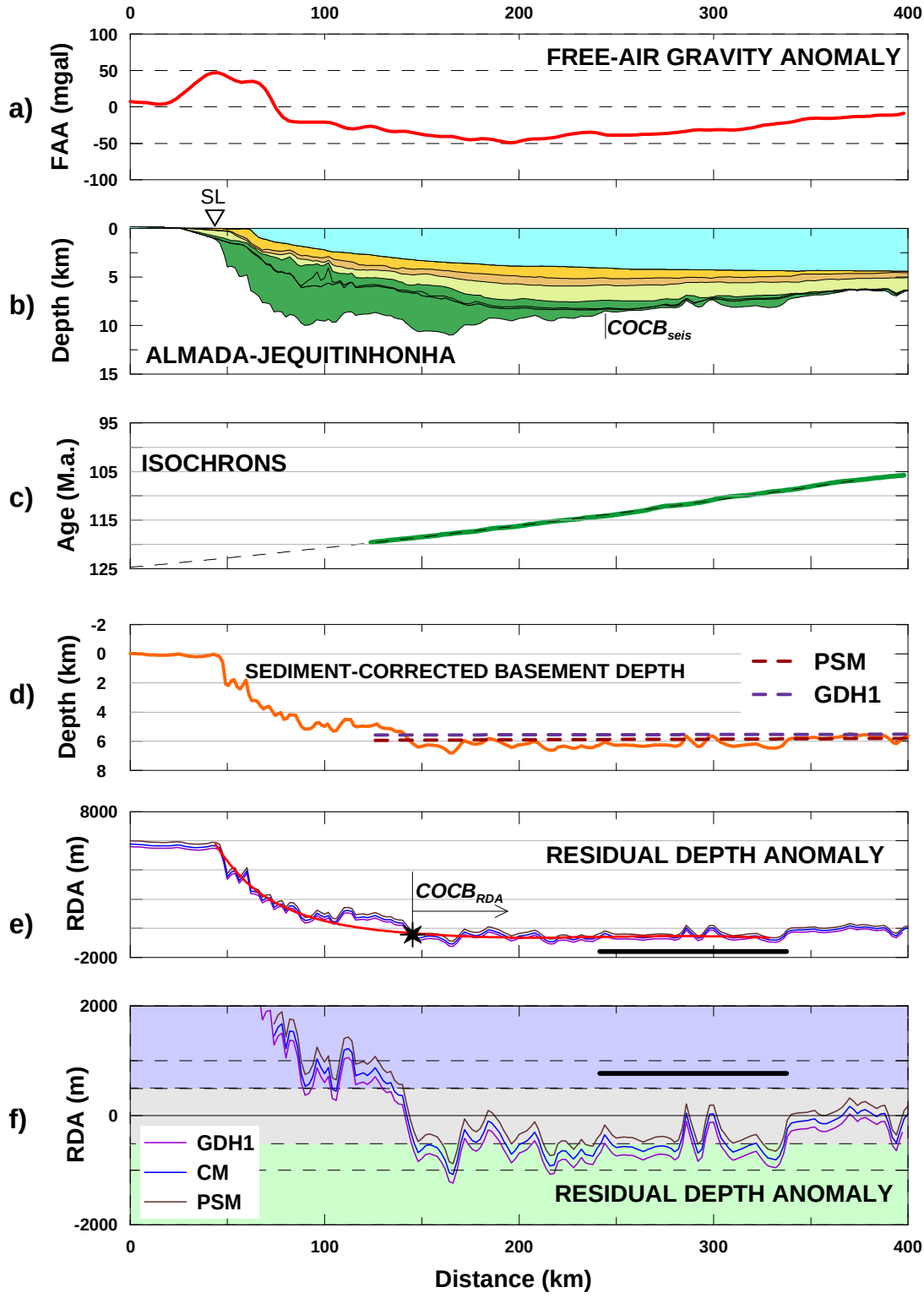

Figure 6.3: Almada Jequitinhonha results. a) free-air gravity anomaly; b) geological cross-section; c) ocean isochrons from (Müller et al., 2008); d) sediment-corrected basement depth profile and e) residual depth anomaly profiles calculated with the PSM, GDH1 and CM-NWA models; in red, the smoothed RDA profile; in bracket the most proximal unequivocal oceanic crust. In f) same RDA as in e), plotted from -2000 to 2000 m: in powder blue, magma-rich crust; in gray, normal crust; in ghost green, magma-poor crust.

6.3.2 JACUÍPE RDA PROFILE

The Jacuípe RDA profile decreases from 2000 to 0 m between the distances of 65 and 130 km, in the OCT affected by seaward dipping reflectors (figure 6.4e). The RDA becomes flat at around 0 m in unequivocal oceanic crust, beyond 180 km of distance. This region is related to free-air gravity anomaly that varies from -25 to -10 *mgal* (figure 6.4a). The relationship between RDA and oceanic crustal thickness (equation 6.1) suggests that RDA around 0 m close to the margin corresponds to normal oceanic crustal thickness, around 7.1 km. The RDA jumps to 250 m beyond 240 km of distance in the distal segment, which indicates oceanic crustal thickness around 8.3 km (figure 6.4f and table 6-1).

The closest position to the continent where the RDA profile reaches the oceanic crust background of 0 m is at 140 km of distance (figure 6.4e), a little further than the COCB indicated by seismic interpretation at 130 km.

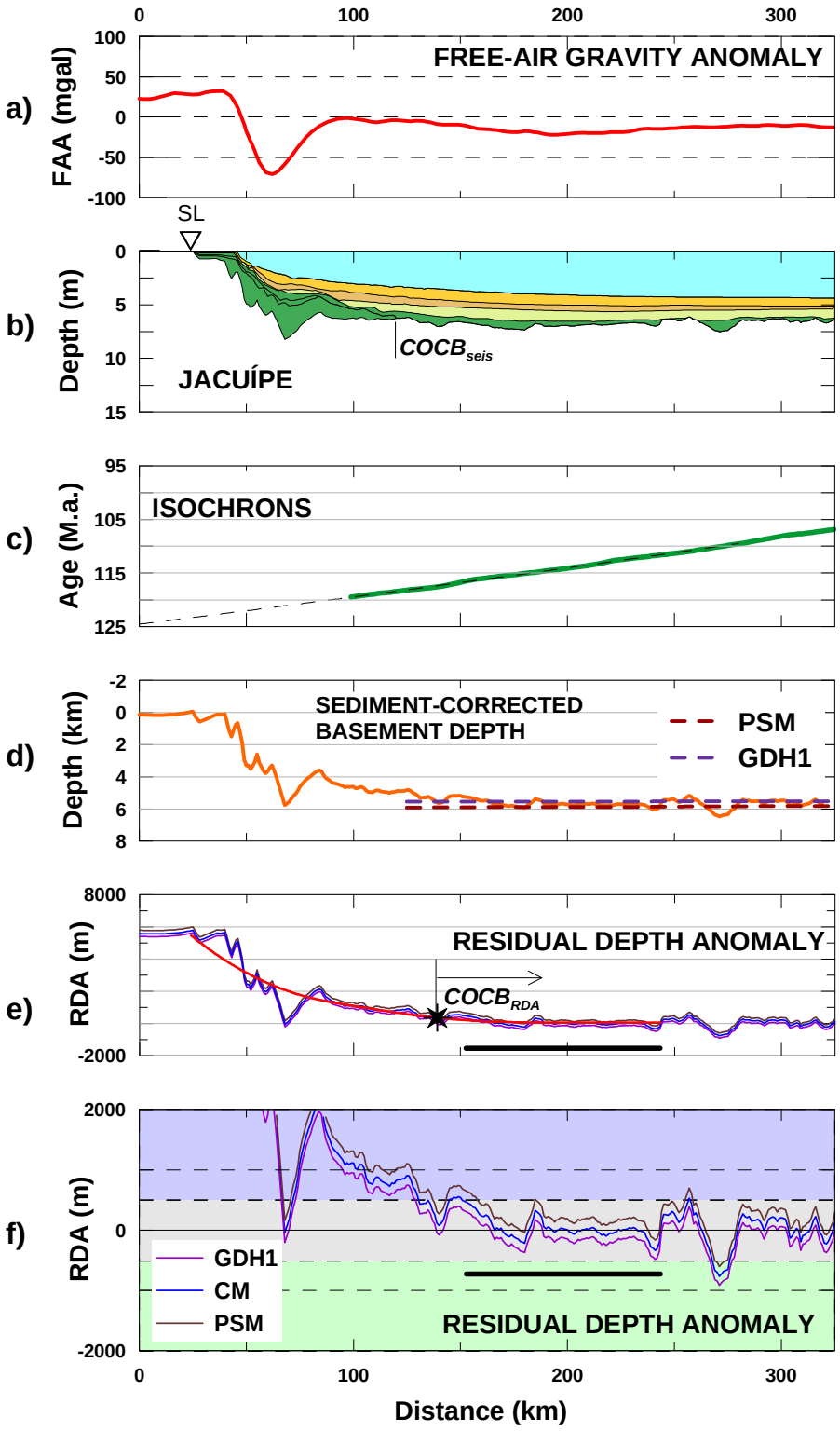

Figure 6.4: Jacuípe results. a) free-air gravity anomaly, b) geological cross-section, c) ocean isochrons from (Müller et al., 2008), d) sediment-corrected basement depth profile, e) residual depth anomaly profiles calculated with the PSM, GDH1 and CM-NWA models; in red, the smoothed RDA profile; in bracket the most proximal unequivocal oceanic crust. In f) same RDA as in e), plotted from -2000 to 2000 m: in powder blue, magma-rich crust; in gray, normal crust; in ghost green, magma-poor crust.

6.3.3 SERGIPE SOUTH RDA PROFILE

The Sergipe South RDA profile stabilizes at around 250 m between 250 and 330 km of distance in unequivocal oceanic crust (figure 6.5f). This region has free-air gravity anomaly of around -20 mgal (figure 6.5.a). Beyond 330 km, the RDA increases to around 600 m, next to the Bahia Seamounts (figure 3.7). The relationship between RDA and oceanic crustal thickness (equation 6.1) suggests that RDA of 250 m in unequivocal oceanic crust close to the margin corresponds to an oceanic crustal thickness of 8.3 km (figure 6.1 and table 6-1). Hence, Sergipe South margin can be considered as slightly magma rich (figure 6.5f). The region between 150 and 250 km is anomalous. Although this region looks more like oceanic crust in the seismic sections, the RDA is very positive and distinct from the adjacent oceanic crust, initially arising up to 2000 m and then decreasing irregularly to 0 m. This region probably corresponds to a buried seamount well imaged in a parallel seismic section to the north.

The position closest to the continent where the RDA profile reaches the oceanic crust background of 250 m is at 140 km of distance, close to the location of the COCB from seismic interpretation (figure 6.5.e).

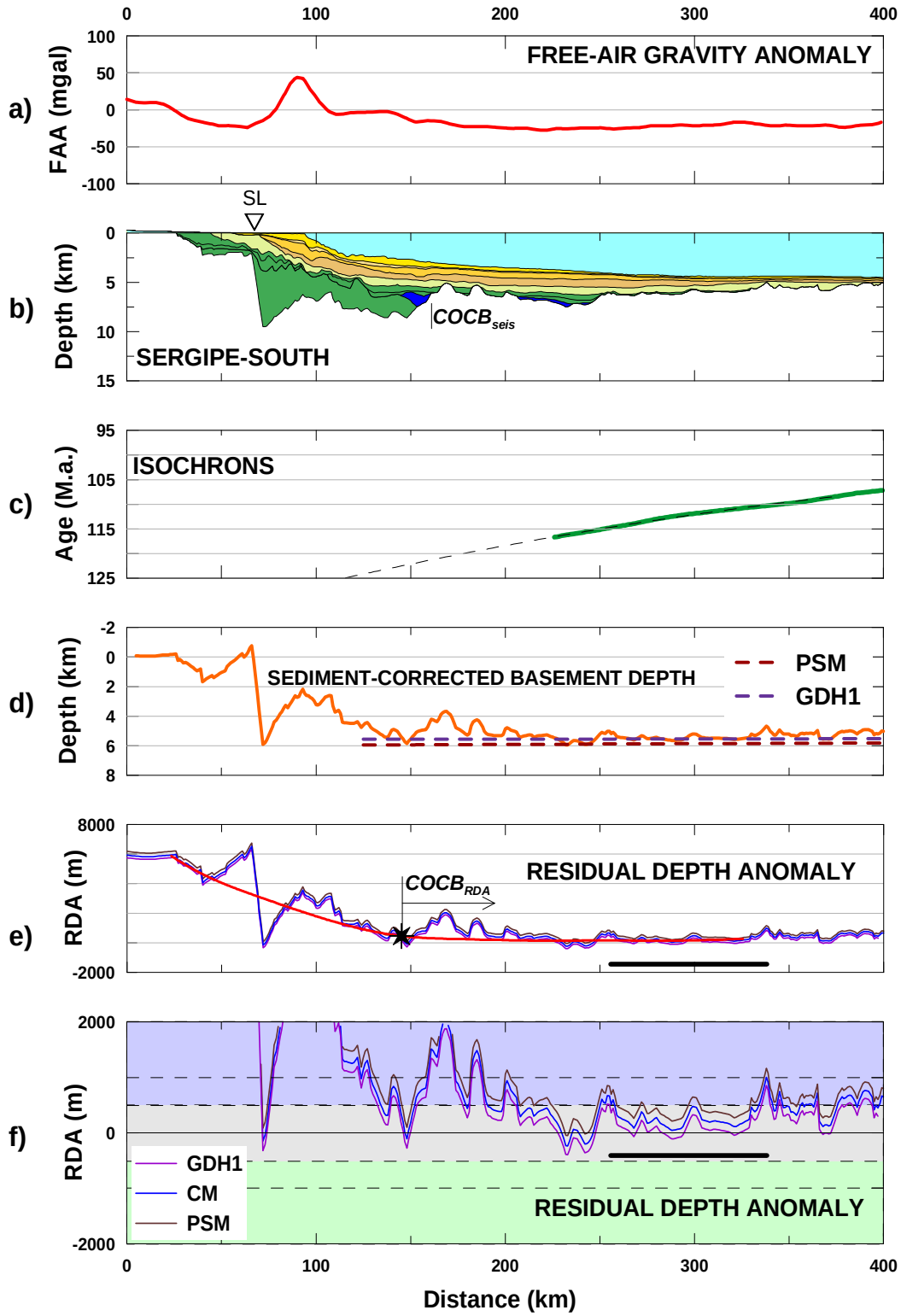

Figure 6.5: Sergipe South results. a) free-air gravity anomaly, b) geological cross-section, c) ocean isochrons from (Müller et al., 2008), d) sediment-corrected basement depth profile, e) residual depth anomaly profiles calculated with the PSM, GDH1 and CM-NWA models; in red, the smoothed RDA profile; in bracket the most proximal unequivocal oceanic crust. In f) same RDA as in e), plotted from -2000 to 2000 m: in powder blue, magma-rich crust; in gray, normal crust; in ghost green, magma-poor crust.

6.3.4 SERGIPE NORTH RDA PROFILE

The Sergipe North RDA profile flattens between 0 and 250 m from 250 to 370 km of distance in unequivocal oceanic crust (figure 6.6e-f). This segment is related to free-air gravity anomaly of around -20 mgal (figure 6.6a). Beyond 360 km, the RDA increases to around 400 m, next to the Bahia Seamounts (figure 3.7). Similar to Sergipe South, the relationship between RDA and oceanic crustal thickness suggests that RDA of 250 m in unequivocal oceanic crust close to the margin indicates an oceanic crustal thickness of 8.3 km (figure 6.1 and table 6-1). Therefore, Sergipe North margin can be also considered as being slightly magma-rich (figure 6.6f).

The position closest to the continent where the RDA profile reaches the oceanic crust background of 250 m is at 125 km of distance (figure 6.6e). This position is near the sharp discontinuity observed in the sediment-corrected basement depth profile between 150 and 200 km (figure 6.6d) that corresponds to the COCB interpreted in seismic section.

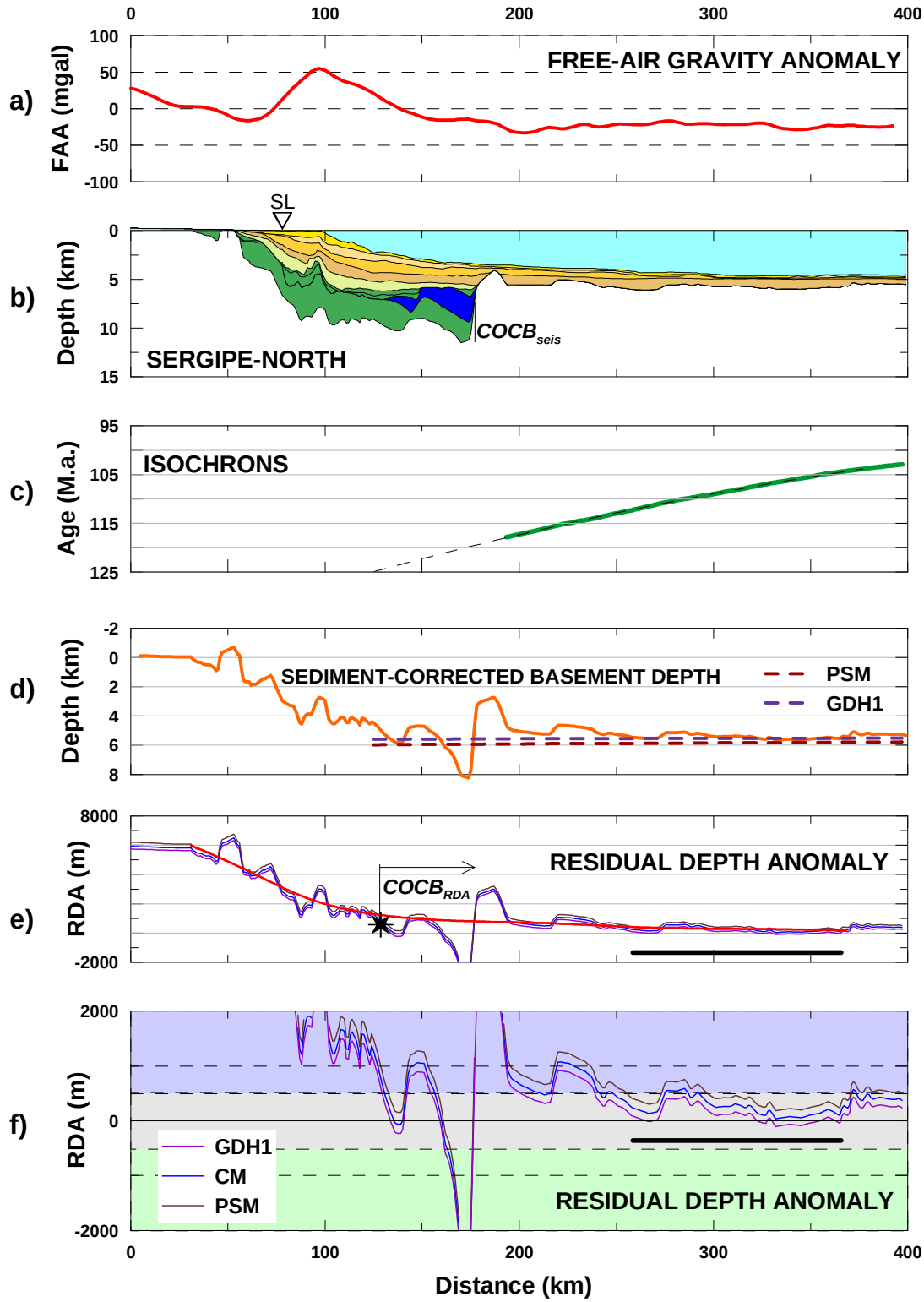

Figure 6.6: Sergipe North results. a) free-air gravity anomaly, b) geological cross-section, c) ocean isochrons from (Müller et al., 2008), d) sediment-corrected basement depth profile, e) residual depth anomaly profiles calculated with the PSM, GDH1 and CM-NWA models; in red, the smoothed RDA profile; in bracket the most proximal unequivocal oceanic crust. In f) same RDA as in e), plotted from -2000 to 2000 m: in powder blue, magma-rich crust; in gray, normal crust; in ghost green, magma-poor crust.

6.3.5 ALAGOAS RDA PROFILE

The Alagoas cross-section samples only a small oceanic region (figures 4.9 and 6.7b). The RDA profile decreases sharply from 2000 to 0 m between 210 and 225 km in unequivocal oceanic crust (figure 6.7.e-f). Beyond 210 km of distance, the RDA profile flattens to 0 m, related to a free-air gravity anomaly of -20 *mgal* (figure 6.7.a). RDA around 0 m in unequivocal oceanic crust close to the margin corresponds to a normal oceanic crustal thickness of 7.1 km (figure 6.1 and table 6-1).

The position closest to the continent where the RDA profile reaches the oceanic crust background of 0 m is at 125 km of distance (figure 6.7e), at the offshore border of the volcanic body of the Maceió High. This location is onshore in relation to the sharp discontinuity observed in the sediment-corrected basement depth profile, between 190 and 225 km that corresponds to the COCB interpreted in seismic section (figure 6.7d).

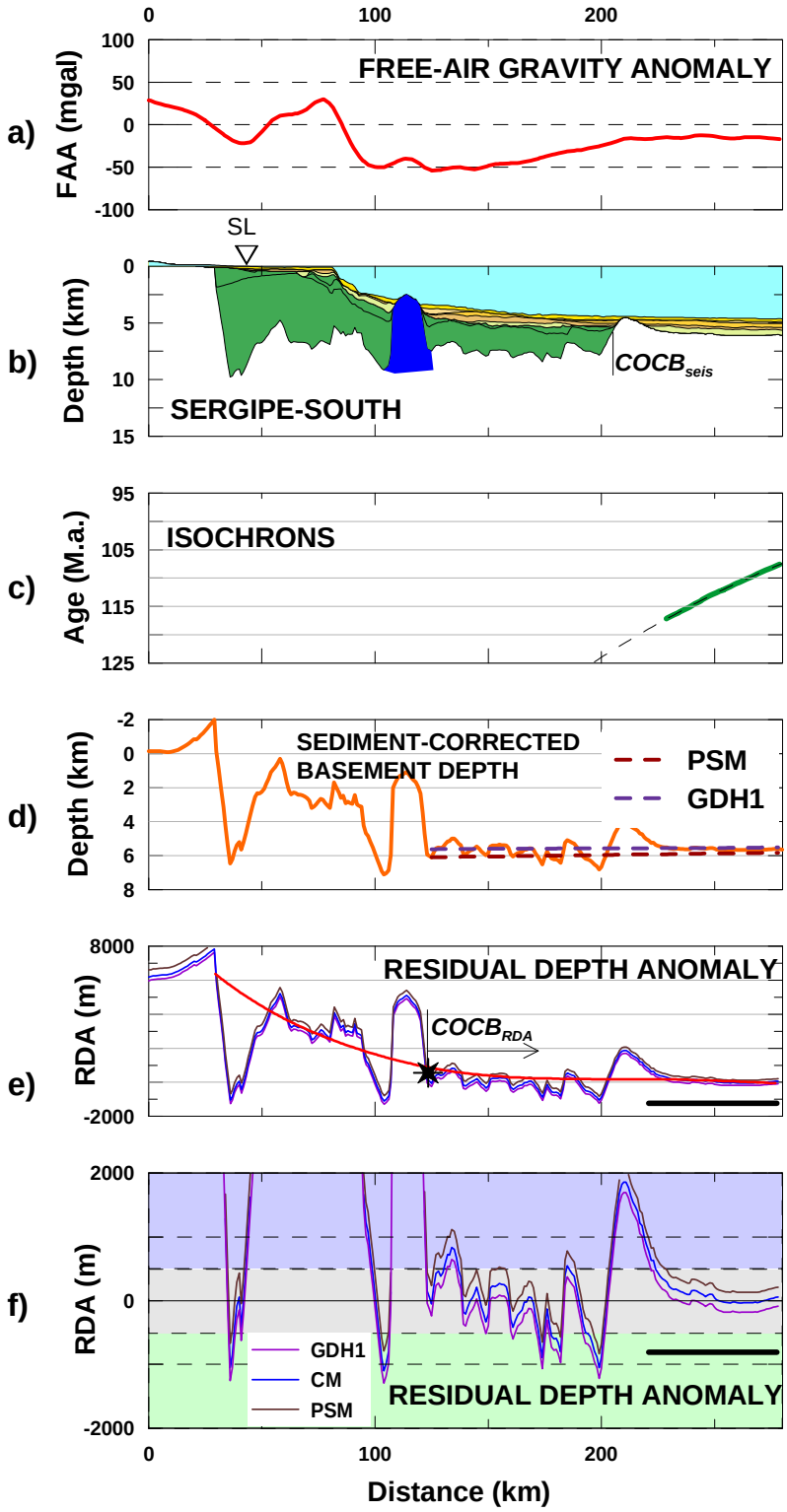

Figure 6.7: Alagoas results. a) free-air gravity anomaly, b) geological cross-section, c) ocean isochrons from (Müller et al., 2008), d) sediment-corrected basement depth profile, e) residual depth anomaly profiles calculated with the PSM, GDH1 and CM-NWA models; in red, the smoothed RDA profile; in bracket the most proximal unequivocal oceanic crust. In f) same RDA as in e), plotted from -2000 to 2000 m: in powder blue, magma-rich crust; in gray, normal crust; in ghost green, magma-poor crust.

6.3.6 PERNAMBUCO RDA PROFILE

The Pernambuco RDA profile flattens to 250 m between 240 and 280 km in unequivocal oceanic crust. This region is related to a free-air gravity anomaly of around -10 *mgal* (figure 6.8.a). Beyond 280 km, the RDA profile decreases to between - 250 and - 500 m, corresponding also to a decreasing free-air gravity anomaly around -10 to -25 mgal. This distal region with negative RDA seems to correspond to flexural moats of the Pernambuco Seamounts, shown in free-air gravity anomaly map (figure 3.7), and is interrupted by a high in the basement where RDA rises to 300 m. The COCB can be clearly identified in the inflection of RDA from positive values towards the oceanic crust background at around 210 km (figure 6.8e) and corresponds to the COCB identified by seismic interpretation. The other sharp inflection around 165 km of distance corresponds to a fault escarpment related to a syn-rift block.

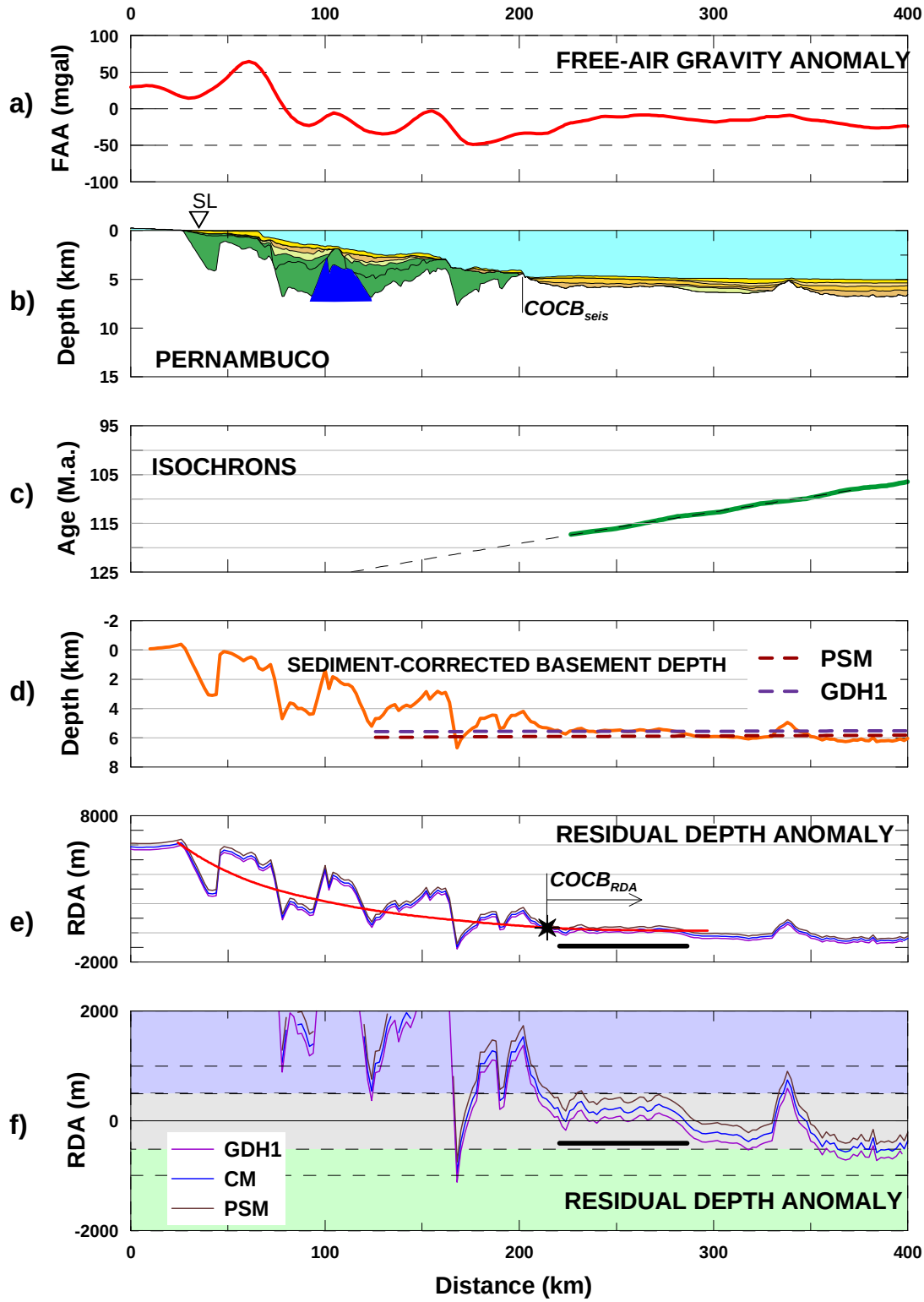

Figure 6.8: Pernambuco results. a) free-air gravity anomaly, b) geological cross-section, c) ocean isochrons from (Müller et al., 2008), d) sediment-corrected basement depth profile, e) residual depth anomaly profiles calculated with the PSM, GDH1 and CM-NWA models; in red, the smoothed RDA profile; in bracket the most proximal unequivocal oceanic crust. In f) same RDA as in e), plotted from -2000 to 2000 m: in powder blue, magma-rich crust; in gray, normal crust; in ghost green, magma-poor crust.

6.4 DISCUSSION AND CONCLUSIONS

The residual depth anomalies (RDA) profiles of the selected cross-sections were calculated from the differences between age-predicted and measured sediment-corrected top basement depth. RDA profiles were calculated with age-predicted oceanic basement depth according to exponential equations of three plate cooling models: PSM (Parsons and Sclater, 1977), GDH1 (Stein and Stein, 1992) and CM-NWA (Crosby and McKenzie, 2009). Crosby & McKenzie (2009) data corrects the sampling bias of the previous models and includes data from the West Atlantic.

The RDA profiles show a range between – 500 m and + 500 m for unequivocal oceanic crust, corresponding to the range of normal oceanic crust (White et al., 1992). Nevertheless, a subtle increase trend of RDA can be interpreted from south to north, as the Almada-Jequitinhonha cross-section presents the smallest RDA, around – 500 m, while Sergipe South, Sergipe North and Pernambuco transects present RDA larger than 250 m.

The RDA profile decreases asymptotically from the values extrapolated to the continental region to the background of the adjacent oceanic crust. This decrease is irregular in the OCT due to the presence of faults and igneous bodies. The position where the smoothed RDA profile achieves the background value of the adjacent oceanic crust is considered as a proximal limit for the COCB. COCB determinations offshore this position are considered as possible, while interpretations onshore this position are considered invalid. The COCB locations interpreted in seismic sections correspond to strong sharp discontinuities in the RDA profiles of Sergipe North and Alagoas. Those sharp discontinuities are related either to extrusive volcanic rocks or to structural highs.

The RDA measured in proximal segments of unequivocal oceanic crust constrains the oceanic crustal thickness in the cross-sections. The Almada-Jequitinhonha margin seems to be magma poor with oceanic crust around 4.6 km-thick, while Jacuípe and Alagoas margins seem to be normal, with oceanic crust around 7.1 km-thick. The Sergipe and Pernambuco margins seem to be slightly magma-rich with oceanic crustal thickness around 8.3 km (table 6-1). The RDA profiles are used in next chapter to calibrate the gravity inversion of the Moho depth.

Table 6-1: Residual depth anomalies interpreted in unequivocal oceanic crust and corresponding oceanic crustal thickness. The preferred values are of the proximal unequivocal oceanic crust highlighted.

Cross-Section	Proximal Oceanic Crust		Distal Oceanic Crust	
	RDA_{min} (m)	tc_{min} (km)	RDA_{max}(m)	tc_{max} (km)
Almada-Jequitinhonha	-500	4.6	0	7.1
Jacuípe	0	7.1	250	8.3
Sergipe South	250	8.3		
Sergipe North	250	8.3		
Alagoas	0	7.1		
Pernambuco	250	8.3	-500	4.6

CHAPTER 7

7. MOHO DEPTH AND CONTINENTAL CRUSTAL THINNING FROM GRAVITY INVERSION

7.1 INTRODUCTION

The purpose of this chapter is to present the gravity inversion of the crust-mantle interface, the Moho discontinuity. Crustal thickness is calculated as the difference between the Moho interface and the observed basement depth. Crustal thinning profiles of the studied cross-sections are then calculated assuming a reference crustal thickness.

Geodynamic studies of the Northeast Brazilian margin are particularly challenging due to lack of measurements of crustal thickness by refraction seismic surveys, both in the continental and in the oceanic areas. Deep seismic reflection sections available offshore show deep reflectors that have been interpreted as the Moho (Mohriak et al., 1995). However, the absence of reliable seismic velocities from refraction seismology leads to inaccuracy of the depth conversions of such deep reflectors. Furthermore, lack of reliable crustal thickness determinations onshore inhibits crustal thinning calculations along the margin.

The Moho gravity inversion methodology applied in this research uses the free-air gravity anomaly grid, corrected for the gravity anomaly contributions of water, sediments and lithosphere thermal anomaly (Chappell and Kusznir, 2008; Greenhalgh and Kusznir, 2007). Moho depth is numerically inverted using a Fourier transform equation that assumes a density contrast for the crust-mantle interface and a reference Moho depth. The reference Moho depth is calibrated in the oceanic crust

region with results from the RDA analysis. A relationship between magmatic addition and lithosphere thinning is used to determine the crustal thickness that corresponds to oceanic crust.

7.2 Sources Of Gravity Anomalies at Rifted Continental Margins

The free-air gravity anomaly Δg_{faa} is the superposition of several gravity anomalies components, caused by variations in interface topographies with specific density contrasts at different depths. The shallower the interface and the larger its density contrast, the stronger will be its local contribution to the free-air gravity anomaly. Consequently, most of the contributions to the free-air gravity anomaly come from density contrasts in the lithosphere. In this thesis it is assumed that the free-air gravity anomaly Δg_{faa} is composed of the following components (Chappell and Kusznir, 2008):

$$\Delta g_{faa} = \Delta g_e + \Delta g_s + \Delta g_t + \Delta g_{mra}, \qquad (7.1)$$

where:

i) Δg_e is the contribution of elevation, topography and bathymetry, controlled by the air-crust and water-crust density contrasts, respectively.

ii) Δg_s is the contribution of the sediments, controlled by the density contrast between sediments and crust.

iii) Δg_t is the contribution of the lithosphere thermal gravity anomaly, where the density contrast is defined by the increase in geothermal gradient.

iv) Δg_{mra} is the contribution of the Moho relief, which involves density contrast between mantle and crust.

In order to invert for the Moho topography from gravity anomaly data, it is necessary to obtain the mantle residual anomaly (Δg_{mra}) by correcting the free-air gravity anomaly Δg_{faa} for the other gravity anomaly contributions (Chappell and Kusznir, 2008; Greenhalgh and Kusznir, 2007):

$$\Delta g_{mra} = \Delta g_{faa} - \Delta g_e - \Delta g_s - \Delta g_t , \qquad (7.2)$$

7.3 Gravity Inversion to Determine the Moho Depth with Lithosphere Thermal Gravity Anomaly Correction

The gravity anomaly inversion for the Moho depth was performed on a squared area grid that contains the selected cross-sections and is bounded by latitudes 6^o S and 16^o S and longitudes 40^o W and 30^o W (figures 1.2 and 3.7). The gravity inversion used free-air gravity anomaly measured with satellite altimetry for the oceanic area (Sandwell and Smith, 2009), merged with improved continental gravity anomaly data (Oliveira et al., 2006). Sediments thickness, elevation (Sandwell and Smith, 2009) and ocean isochrons (Müller et al., 2008) (figure 6.2) completed the dataset. The gravity inversion was computed in the 3-dimensional spectral domain, but the Moho depth results were extracted only for the cross-sections, where the sediment thickness data are reliable. For the gravity inversion, the geographic coordinates were transformed into UTM grids with nodal spacing of 2.96 km. The method to invert Moho from gravity data comprises the following steps (figure 7.1):

1. Removal of elevation and sediment gravity anomaly components from the free air anomaly obtaining a first estimate of the mantle residual anomaly Δg_{mra}.
2. Inversion of Moho depth from the mantle residual anomaly Δg_{mra} using a 3D spectral domain technique (Parker, 1973).

3. Determination of crustal thickness by subtracting the depth to basement from the Moho depth.

4. Calculation of crustal thinning, assuming an initial crustal thickness.

5. Location of continent-ocean crust boundary (COCB) through a relationship between magmatic addition and crustal thinning.

6. Correction of the lithosphere thermal anomaly, assuming the age of initiation of thermal subsidence.

7. Update the mantle residual anomaly Δg_{mra}.

8. Repeat steps 2 to 7 until thermal gravity anomaly Δg_t converges.

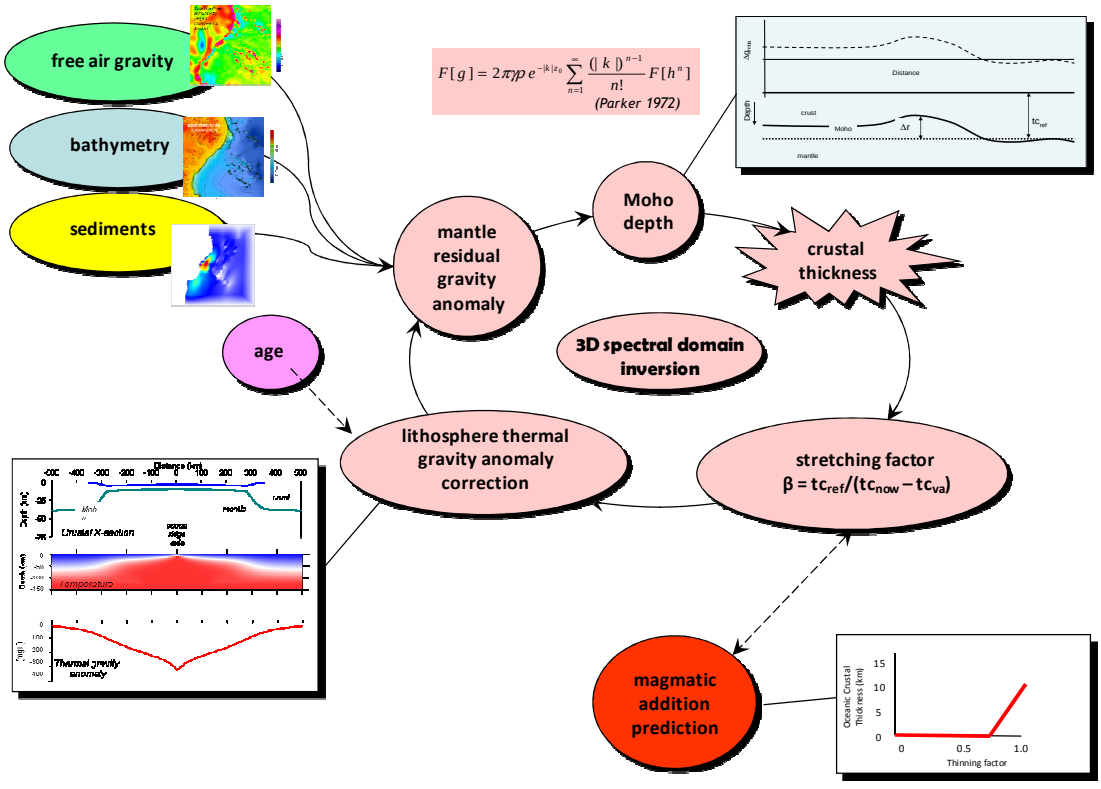

Figure 7.1: Workflow of the gravity inversion of the Moho with thermal anomaly correction (Chappell and Kusznir, 2008; Greenhalgh and Kusznir, 2007).

7.3.1 Corrections Of Elevation And Sediments Gravity Anomaly Components

The corrections of the gravity effect of elevation Δg_e and sediments Δg_s (figure 7.2) were performed using the Bouguer slab formula:

$$\Delta g_e = 2\pi G \Delta \rho_e h_e \text{ and} \qquad (7.3)$$

$$\Delta g_s = 2\pi G \Delta \rho_s h_s . \qquad (7.4)$$

where G is the gravitational constant (6.6726×10^{-11} N m^2 kg^{-2}), h_e is the elevation from sea-level, h_s is the sedimentary pile thickness, both positive below sea level. For bathymetry, $\Delta\rho_e = (\rho_w - \rho_c)$ is the density contrast between water and crust, while for topography, $\Delta\rho_e = (\rho_c - \rho_a)$ is the density contrast between air and crust.

The assumed densities are presented in table 7-1. Post-rift and syn-rift average sediments matrix densities were evaluated from bulk density and travel time sonic logs of Sergipe and Alagoas basins, respectively. The post-rift sediments matrix density is typical of shale matrix densities, while the syn-rift sediments matrix density is an average between shale and sandstone densities. While many important works in geodynamics assume crustal density of 2800 kg m^{-3} (Le Pichon and Sibuet, 1981; McKenzie, 1978), global average surveys of oceanic and continental crust densities point to higher values, close to 2850 kg m^{-3} (Carlson and Herrick, 1990; Christensen and Mooney, 1995). A constant crustal density of 2850 kg m^{-3} is an approximation of the global averages of continental crust, 2830 kg m^{-3} (Christensen and Mooney, 1995), and of oceanic crust, 2860 kg m^{-3} (Carlson and Herrick, 1990). In both cases the density evolves from less than 2700 kg m^{-3} at the surface to around 3000 kg m^{-3} at the base of the crust.

Table 7-1: Densities used in the gravity inversion, discussed in the text.

Layer	Density (kg m^{-3})
Air	0
Water	1030
Post-rift Sediments Matrix	2680
Syn-rift Sediments Matrix	2660
Crust	2850
Mantle	3300

The density contrast between crust and sediments $\Delta\rho_s = (\rho_s - \rho_c)$ varies along the grid with thickness, due to compaction, and with the lithological composition of the sedimentary layers. The average density of a sedimentary column ρ^a corresponds to the integral of the density along depth *dz*, divided by the thickness of the sedimentary column *h*:

$$\rho^a = \frac{\int_0^{basement} \rho g dz}{h}. \qquad (7.5)$$

Sediments density ρ_{sed} is calculated as a function of porosity ϕ:

$$\rho_{sed} = \phi\rho_w + (1-\phi)\rho_b, \qquad (2.16)$$

where ϕ_0, the porosity at burial surface, and *c*, the exponential decay, are parameters of the porosity decay function (Athy, 1930), equation 2.17, and ρ_b is the density of the sediments matrix (table 7-1).

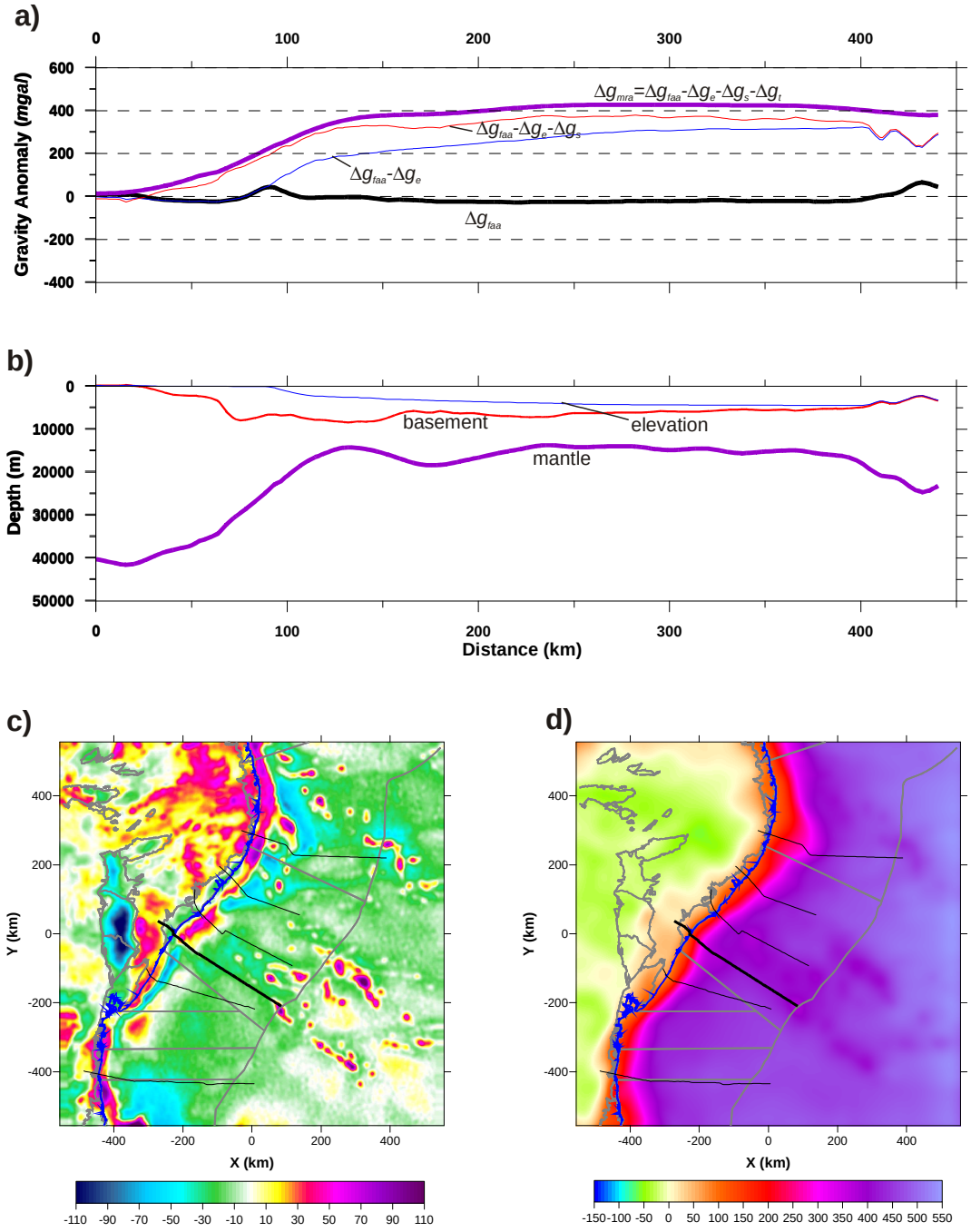

Figure 7.2. a) Effects of gravity corrections in the free-air gravity anomaly profile of Sergipe South cross-section. b) In purple, the Moho inverted from the mantle residual anomaly. c) Free-air gravity anomaly map. d) Mantle residual anomaly map.

The sediments thickness grid was computed with data from the six cross-sections, complemented offshore with data from the *LEPLAC* survey (Gomes, 2005) (figure 7.3a). The average density grid was then computed from the sediments thickness profiles (figure 7.3b).

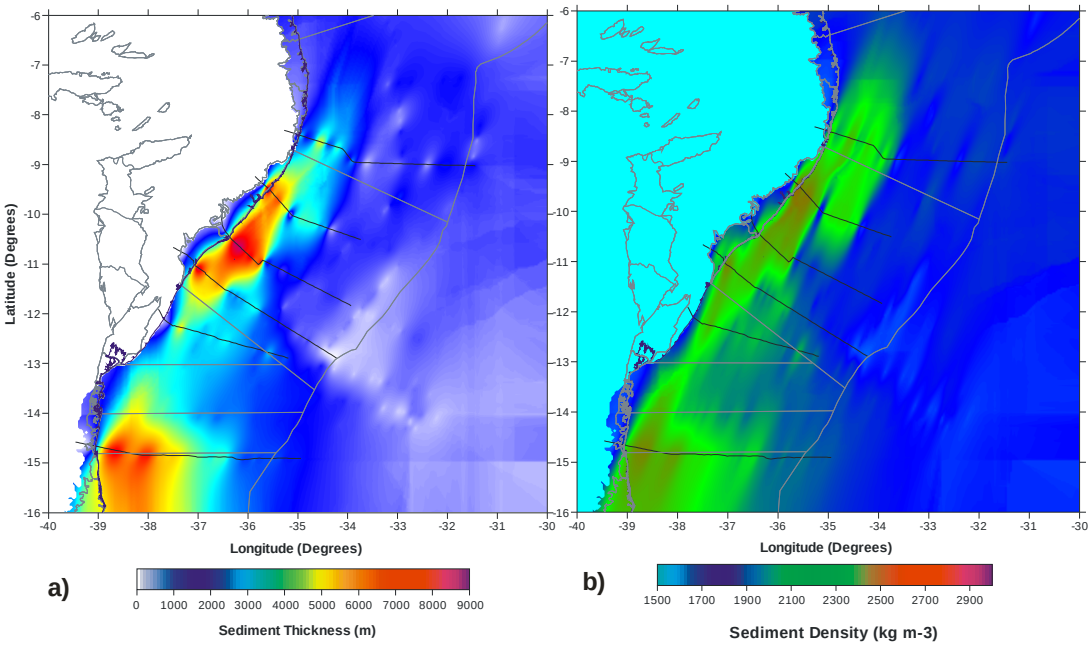

Figure 7.3. a) Sediments thickness and b) sediments average density maps used in the correction of the gravimetric effect of sediments.

7.3.2 MOHO DEPTH INVERSION USING THE PARKER EQUATION

Moho depth is calculated in the 3D spectral domain as the solution of a Fourier transform of the mantle residual anomaly $F(\Delta g_{mra})$ (Parker, 1973):

$$F(\Delta g_{mra}) = 2\pi G \Delta\rho e^{-|k|z_0} \sum_{n=1}^{\infty} \frac{(|k|)^{n-1}}{n!} F[\Delta r^n], \qquad (7.6)$$

where k is the wave number, $\Delta\rho$ is the mantle-crust density contrast (table 7-1), Δr is the Moho relief measured from reference Moho Depth z_0 (figure 7.4). The Moho relief Δr is determined iteratively until the calculated mantle residual gravity anomaly converges to the observed, Δg_{mra}, using the Method of (Bott, 1960). The Moho depth inversion is applied to the mantle residual anomaly, Δg_{mra}, previously filtered from the effects of bathymetry, sediments and thermal gravity anomaly. The main variables are the crust and mantle densities and the reference Moho depth z_0, assumed as the unthinned crust during the pre-rift and in the adjacent basement. The reference Moho depth z_0 is adjusted by trial and error through the fit of the sediment-

corrected residual depth anomalies (RDA) at the oceanic crust with the synthetic RDA calculated with results of the gravity inversion.

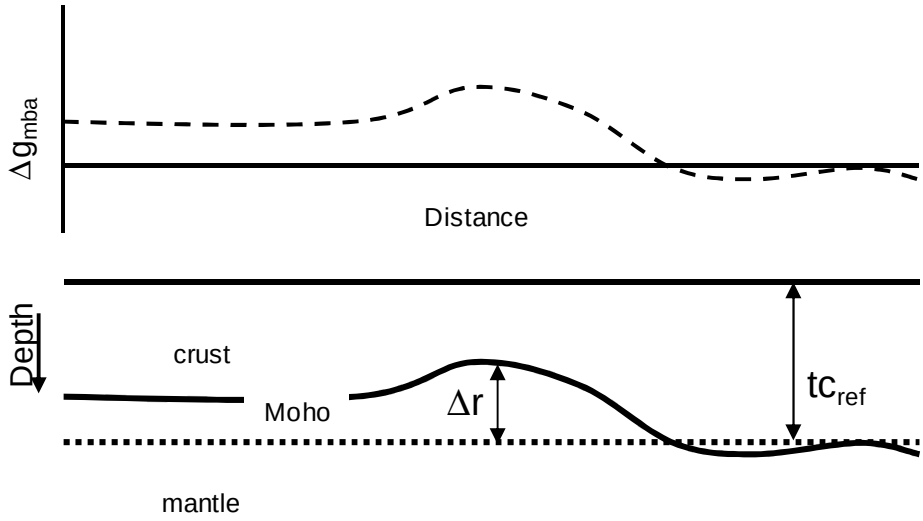

Figure 7.4. Inversion of the Moho depth from a mantle gravity anomaly (Δg_{mba}) using Parker's equation (NJ Kusznir pers. comm.). The Moho topography Δr is determined from a reference depth (tc_{ref}), which corresponds to the reference Moho depth z_0.

Prior to the inversion for Moho depth, a *Butterworth* filter is applied in the Δg_{mra} grids in order to remove high frequency components (Chappell and Kusznir, 2008). The effects of application of different wavelengths to the Δg_{mra} are exemplified for the Sergipe South cross section in figure 7.5. A 50-km cut-off filter allows unrealistic short wavelengths in the Moho topography. The preferred *Butterworth* filter wavelength cut-off for all cross-sections was 150 km, which resulted in smooth solutions.

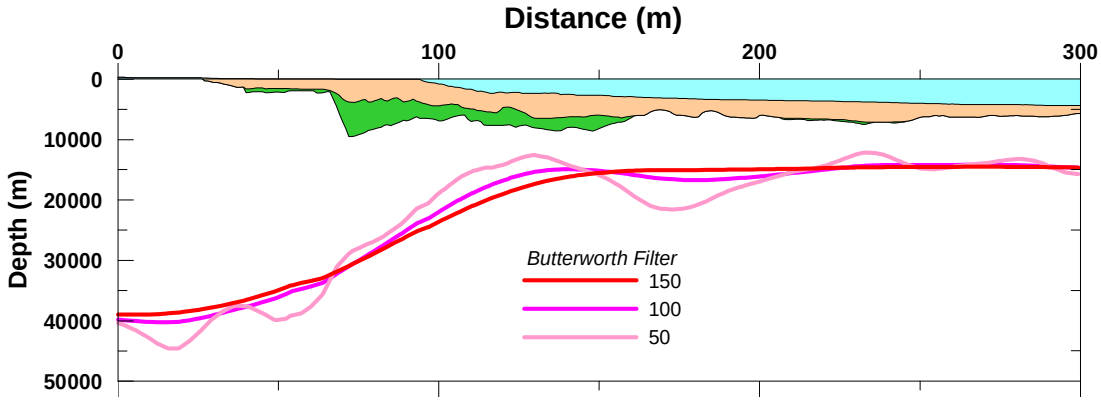

Figure 7.5. Effect of the Butterworth low-pass frequency filter applied in the mantle residual anomaly for Moho depth inversion of Sergipe-South cross-section. The application of a filter of 50 km seems to show unrealistic Moho relief, while a filter of 150 km allows a smooth Moho inversion.

REFERENCE CRUSTAL THICKNESS CALIBRATION TO RESIDUAL DEPTH ANOMALIES (RDA)

An important input of the gravity inversion is the reference Moho Depth z_0. Although the reference Moho Depth z_0 may be slightly different from the initial continental crust thickness $tc_{cc}^{\,0}$ (figure 7.4), in the absence of seismic refraction data it is a good approximation. Synthetic residual depth anomalies *RDAgi* were calculated through local isostatic balance between the gravity inversion crustal thickness tc_{cc} and the average oceanic crustal thickness tc_{oc}:

$$RDA_{gi} = (tc_{cc} - tc_{oc}) \cdot \frac{(\rho_c - \rho_m)}{(\rho_w - \rho_m)}, \qquad (7.7)$$

where the average oceanic crustal thickness tc_{oc} is 7.08 km (White et al., 1992), while ρ_c, ρ_m and ρ_w are crustal, mantle and water densities (table 7-1). Equation 7.7 is equivalent to equation 6.1 that relates RDA measured in oceanic regions to oceanic crustal thickness.

For each cross-section, a range of reference Moho depth z_0 was tested by trial to adjust the synthetic RDA_{gi}, calculated from the gravity inversion, to the sediment-

corrected RDA at adjacent unequivocal oceanic crust segment (figure 7.8). Calibrating the synthetic with the sediment-corrected RDA in a selected oceanic crust segment by varying the reference crustal thickness is the same as calibrating the crustal thickness of this segment with the thickness indicated by the sediment-corrected RDA according to equation 6.1 (figure 6.1).The adjustment of the oceanic RDA is a new approach to calibrate the gravity inversion and to constrain the reference Moho depth (or reference continental crust thickness), therefore permitting the calculation of crustal thinning profiles in areas without seismic refraction data.

7.3.3 LITHOSPHERE THERMAL GRAVITY ANOMALY CORRECTION

Density of mantle rocks varies with temperature after break-up (figure 7.6). The density contrast between a column of mantle rocks with high geothermal gradient and the steady-state lithosphere contributes to the free-air anomaly and will be stronger at young and warm lithosphere, near mid-oceanic ridges or recently broken-up margins. However, even at rifted margins as old as Northeastern Brazil, around 110 Myr, this lithosphere thermal gravity anomaly can reach values of around 50 *mgal*, and needs to be corrected for the gravity inversion (figure 7.2). The calculation of the lithosphere thermal gravity anomaly Δg_t (Greenhalgh and Kusznir, 2007) is based on the thermal structures of the depth-uniform lithosphere stretching model (McKenzie, 1978) and is given by:

$$\Delta g_t = \frac{8G\alpha\rho a T_m}{\pi} \cdot \sum_{n=1}^{\infty} \frac{-(1)^{n+1}}{n} c_n \exp\left(-\frac{\kappa n^2 \pi^2 t}{a^2}\right) \cdot \qquad (7.8),$$

where

$$c_n = \left[\frac{\beta}{n\pi} \sin\frac{n\pi}{\beta}\right]. \qquad (2.13)$$

and κ; a, α, T_m are parameters from the PSM plate model (Parsons and Sclater, 1977), ρ_0 is the mantle density at 0 ^oC (table 2-1), β is the stretching factor and t is the age of the thermal anomaly.

For the oceanic lithosphere, $\beta = \infty$ and $c_n = 1$, therefore the main variable of the thermal gravity anomaly is t, the age of the oceanic crust. Oceanic crust ages from the global grid of oceanic isochrons (Müller et al., 2008) were used for the determination of the oceanic lithosphere cooling time (figure 6.2).

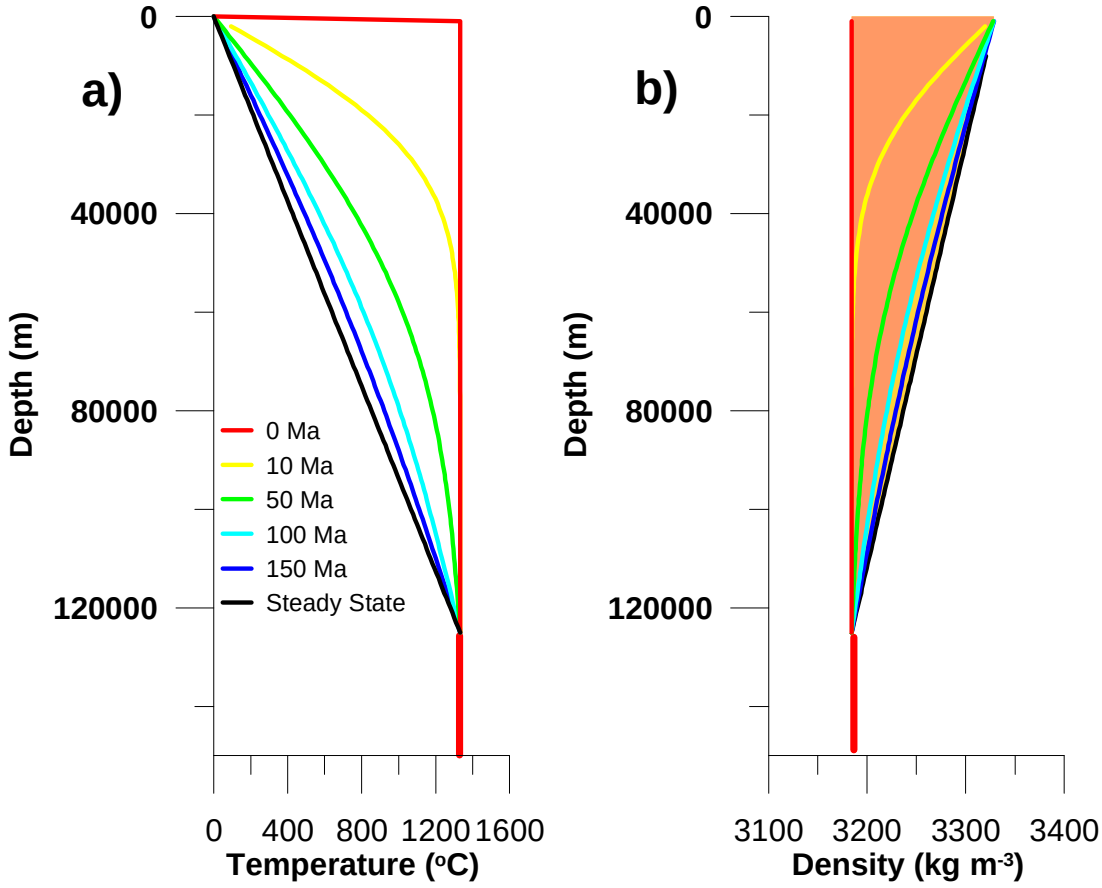

Figure 7.6: a) Temperature variation of mantle rocks at 0, 10, 50, 100 and 150 Myr after the initiation of the thermal anomaly due to the asthenosphere ascension at the surface in a mid-ocean ridge, according to the (Parsons and Sclater, 1977) plate cooling model. b) Corresponding density variation of mantle rocks. The density contrast at each age corresponds to the area between each density profile and the steady state oceanic lithosphere (in black).

The stretching factor β is required for the calculation of the lithosphere thermal gravity anomaly Δg_t, for the stretched and thinned continental lithosphere of

a rifted margin (equation 2.13). In this case, the time *t* corresponds to the break-up age, assumed as 115 Ma for the Northeast Brazilian rifted margin. Although the end of the extensional phase can have occurred later, around 112 Ma at the Aptian-Albian transition, the considered age probably corresponds to the onset of thermal subsidence in Northeast Brazilian rifted margin, after the development of the Aptian unconformity. The initial inversion of the Moho from the residual mantle anomaly (Δg_{mra}) provides an initial determination of β, assuming that crustal and lithosphere thinning are the same (McKenzie, 1978).

A relationship between magmatic addition and lithosphere thinning discriminates the fraction of oceanic crust from the calculated crustal thickness. The residual continental crust provides a corrected continental crustal thinning, which is again assumed as equal to the lithosphere thinning in the thermal gravity (equation 2.13). The thermal gravity anomaly correction updates the mantle residual anomaly and the cycle is repeated until the thermal gravity anomaly Δg_t converges (figure 7.1). The lithosphere thermal anomaly correction is shown with the other corrections in figure 7.2. Even being smaller than the corrections for bathymetry and sediments, the lithosphere thermal anomaly correction has an important impact in the Moho depth gravity inversion.

CRUSTAL THINNING CORRECTION FOR MAGMATIC ADDITION

The gravity inversion by itself cannot discriminate between continental and oceanic crusts. But this separation can be achieved through a relationship between magmatic addition and lithosphere thinning, assuming depth-uniform lithosphere thinning (McKenzie, 1978). Magmatic addition occurs by decompression melting due to lithosphere thinning across a continental rifted margin and depends on the initial lithosphere thickness and on the potential temperature at the asthenosphere T_p

(McKenzie and Bickle, 1988), as discussed in Chapter 2. The relationships between magmatic addition and lithosphere thinning (γ=1-1/β) for different lithosphere thickness and potential temperatures (McKenzie and Bickle, 1988; White and McKenzie, 1989) are shown in figures 2.13 and 7.7. A potential temperature T_p of 1280 ^{o}C corresponds to a normal margin, while higher values correspond to margins affected by mantle plumes.

For each situation, decompression melting starts after a certain amount of lithosphere thinning is reached and then follows a relationship with thinning until the thickness of the oceanic crust is reached. The magmatic addition curves against lithosphere thinning (figure 7.7a) were initially obtained for thermal lithosphere thickness of 118 and 149 km (McKenzie and Bickle, 1988). The parameterization here proposed, similar to the one proposed by (Chappell and Kusznir, 2008), involves initially the interpolation of the curves of a 125 km-thick plate (figure 7.7b). Due to the uncertainties involved in the magmatic addition relationships, the magmatic addition curves for a 125 km-thick plate were transformed into linear functions (figure 7.7c).

In this practical approach, instead of the asthenosphere potential temperature, magmatic addition is parameterized with the oceanic crustal thickness, assumed as the maximum magmatic addition. A function that relates the critical gamma γ_{crit}, from which melt starts, to the maximum magmatic addition, for γ=*1*, was determined for a 125 km-thick lithosphere (figure 7.7.d). Therefore, for a certain igneous oceanic crust predicted by the sediment-corrected RDA, a critical gamma γ_{crit} defines a linear relationship between magmatic addition and lithosphere thinning. For example, to fit a normal oceanic crust, 7.08 km thick (White et al., 1992), a critical gamma factor

γ_{crit} of 0.69 must be applied in the gravity inversion (figure 7.7d). For different lithosphere thickness, the same analysis should be performed.

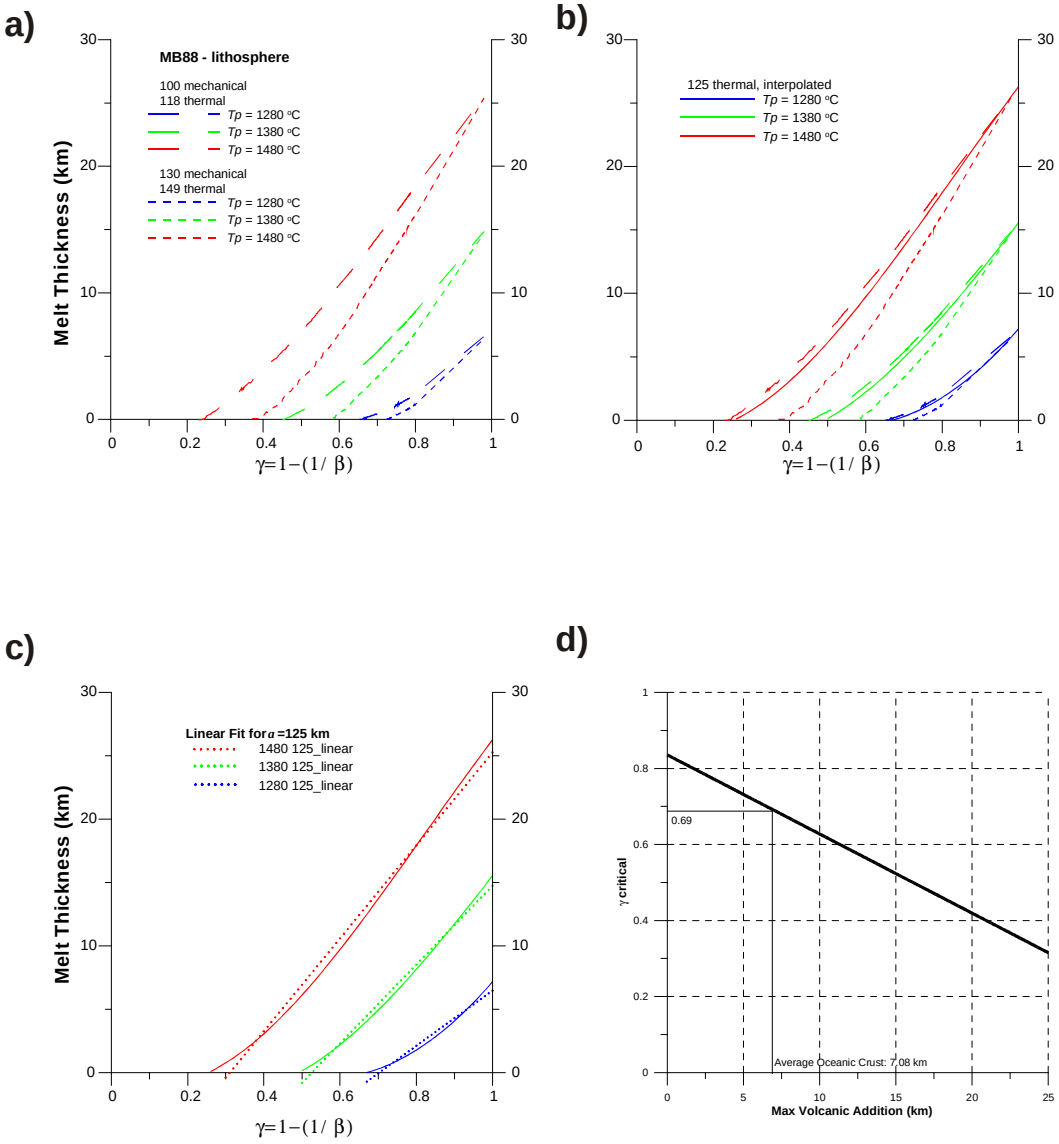

Figure 7.7. a) Original data of melt thickness plotted against thinning factor γ=1-1/β for 118 and 149 km-thick thermal lithosphere from (McKenzie and Bickle, 1988). b) Interpolation of the curves for a 125 km-thick lithosphere. c) Linearization of the curves for 125 km-thick lithosphere. d) Relationship between critical gamma and maximum magmatic addition for a 125 km-thick lithosphere.

The residual continental crustal thickness is obtained from the magmatic addition relationship with lithosphere thinning, which then improve the estimate of the continental crustal thinning. The magmatic addition corrected lithosphere

thinning, expressed as the stretching factor β, is applied in the thermal gravity anomaly calculation in the continental rifted margin:

$$\beta = \frac{t_{cont}^{0}}{t_{cont}^{gi}} \qquad 1 < \beta < \beta_{\text{crit}}, \text{ and} \qquad (7.9)$$

$$\beta = \frac{t_{cont}^{0}}{t_{cont}^{gi} - m_{ad}} \qquad \beta > \beta_{\text{crit;}} \qquad (7.10)$$

where t_{cont}^{0} is the initial continental crustal thickness, assumed as the reference Moho depth, t_{cont}^{gi} is the crustal thickness initially calculated in the gravity inversion and m_{ad} is the magmatic addition by decompression melting.

7.4 Moho Depth and Continental Crustal Thinning Results from Gravity Inversion

The results of the gravity inversion comprise: 1) Moho depth, 2) residual crustal thickness (tc_{gi}), 3) crustal thinning (γ_c) and 4) magmatic addition (m_{ad}). The calibrations of the synthetic RDA from the gravity inversion with the sediment-corrected RDAs in unequivocal oceanic crust are shown in figure 7.8. The synthetic RDA profiles from gravity inversion are smoothed determinations that can be locally smaller or larger than the sediment-corrected RDA profiles in the OCT, which are affected by faults. Maximum magmatic addition was assumed as the oceanic crust thickness that corresponds to the RDA observed in the unequivocal oceanic crust (figure 6.1 and table 6.1). The results of the gravity inversion for each of the cross-sections are presented in figures 7.9 to 7.14. The top of the residual continental crust corresponds to the top basement for the continental crust and to the Moho for the oceanic crust. The decrease of the residual continental crust is controlled by the magmatic addition and indicates the COCB location in the cross-sections. The crustal

thinning factor also indicates the position of continent-ocean crust boundary COCB where γ reaches 1.

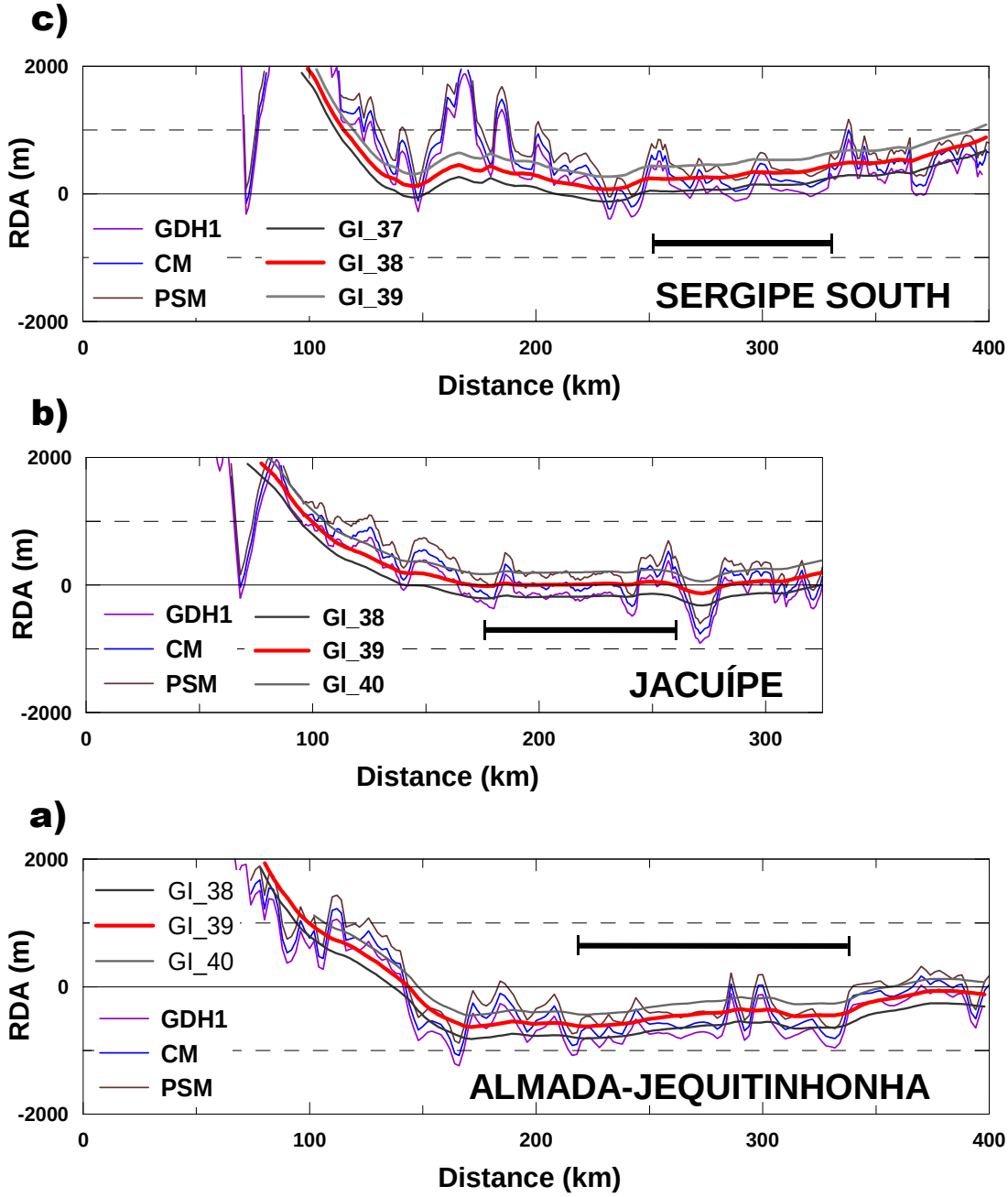

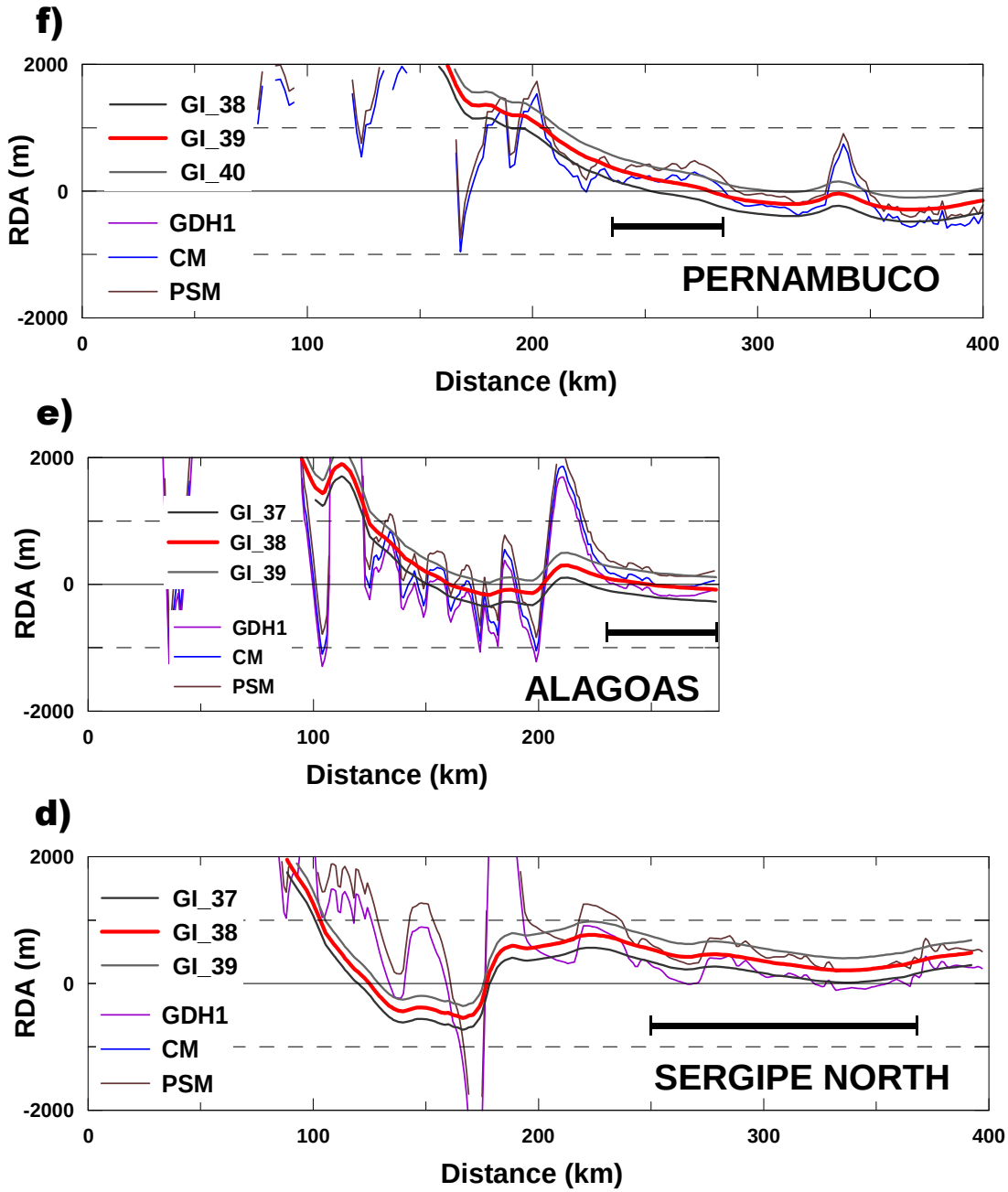

Figure 7.8. Fits of the synthetic RDA profiles from the gravity inversion (in red) to the sediment-corrected RDA profiles, obtained with the CM model in unequivocal oceanic crust segments of the cross-sections: a) Almada Jequitinhonha, b) Jacuípe, c) Sergipe South, d) Sergipe North, e) Alagoas and f) Pernambuco. Also shown in gray, the synthetic RDAs calculated with reference crustal thicknesses 1 km thicker and 1 km less thick than the preferred reference crustal thickness.

7.4.1 ALMADA-JEQUITINHONHA CROSS-SECTION

The synthetic RDA from gravity inversion can fit sediment-corrected RDA in the unequivocal oceanic crust segment using a reference Moho depth of 39 km

(figures 7.8a and 7.9c). The crustal thinning profile increases steadily between 30 and 80 km, and then flattens between 80 and 140 km (figure 7.9b) in the ocean-continent transition (OCT). The continental crustal thinning profile shows COCB location at 160 km (figure 7.9b), a little offshore to the limit of COCB indicated by the RDA analysis (figure 6.3e).

7.4.2 JACUÍPE CROSS-SECTION

The synthetic RDA from gravity inversion can fit sediment-corrected RDA in the unequivocal oceanic crust segment using also a reference Moho depth of 39 km (figures 7.8b and 7.10c). The crustal thinning profile jumps from 0.7 to almost 1.0, between 110 and 170 km of distance in the OCT (figure 7.10b). The COCB location is suggested at 170 km by the crustal thinning profile. This COCB interpretation is further offshore the limit of syn-rift sediments, interpreted in seismic section, around 120 km.

7.4.3 SERGIPE-SOUTH CROSS-SECTION

The synthetic RDA from gravity inversion can fit the sediment-corrected RDA in the unequivocal oceanic crust segment using a reference Moho depth of 38 km (figure 7.8c and 7.11c). Considering RDA in the unequivocal oceanic crust, the maximum magmatic addition expected for this cross-section is around 8.3 km. The residual continental crust suggests COCB location around 135 km (figure 7.11a), more proximal than interpreted in seismic section, around 150 km (figure 6.5b). Consequently, the very thin crust OCT between 100 and 150 km could be interpreted as igneous oceanic crust.

The gravity inversion suggests that the crustal thickness of the segment between 150 and 200 km is thicker than the assumed maximum magmatic addition, and could still be continental (figure 7.11a). This region corresponds to buried

seamounts formed at the beginning of sea-floor spreading, well imaged in a sub-parallel seismic section. Increasing the maximum magmatic addition to fit this segment would bring the COCB location to an even more proximal position. Conversely, the maximum magmatic addition decrease suggests that the COCB would have not been reached in the OCT. Therefore, either the COCB is really proximal or the assumption that the maximum magmatic addition is constant along a cross-section may be not valid.

7.4.4 SERGIPE-NORTH CROSS-SECTION

Similarly to the Sergipe-South cross-section, a reference Moho depth of 38 km could fit the sediment-corrected RDA in unequivocal oceanic crust (figure 7.9d and 7.12c). The RDA in the unequivocal oceanic crust implies in maximum magmatic addition of 8.3 km. The residual continental crust suggests the COCB location at around 115 km (figure 7.12a), close to the shelf break, where the antithetic rift blocks start and much more proximal than the COCB location interpreted in seismic section. Again, the OCT with very thin crust between 115 and 175 km could correspond either to igneous oceanic crust or to thin continental crust developed in a magma-poor setting. The sediment-corrected RDA at the adjacent true oceanic crust is larger than expected for a magma-poor setting.

The gravity inversion suggests that the crustal thickness of the segment between 175 and 250 km is thicker than the assumed maximum magmatic addition, and could still be continental. Increasing the maximum magmatic addition to fit this segment would bring the COCB to an even more proximal position. Conversely, decreasing the maximum magmatic addition suggests that the COCB would haven't been reached in the OCT. Therefore, this observation suggests again either the

COCB location is really proximal or the assumption that the maximum magmatic addition is constant along a cross-section may not be valid.

7.4.5 ALAGOAS CROSS-SECTION

The synthetic RDA from gravity inversion can fit sediment-corrected RDA in the unequivocal oceanic crust segment using a reference Moho Depth of 38 km (figures 7.8e and 7.13c). The crustal thinning profile suggests the COCB location is around 160 km (figure 7.13b), much more proximal than interpreted in seismic section, around 210 km. The segment between 210 and 225 km corresponds to a structural high in the basement, probably already in the oceanic crust and presents a very high RDA, close to 2000 m. This cross-section also suggests that the maximum magmatic addition may vary along the ocean-continent transition and the new oceanic crust.

7.4.6 PERNAMBUCO CROSS-SECTION

The synthetic RDA from gravity inversion can fit sediment-corrected RDA in the unequivocal oceanic crust segment using a reference Moho Depth of 39 km (figures 7.8e and 7.14c). The COCB suggested by the residual continental crust is around 250 km (figure 7.14a and b), not too far from the COCB location interpreted in seismic section and suggested by RDA analysis, around 210 km.

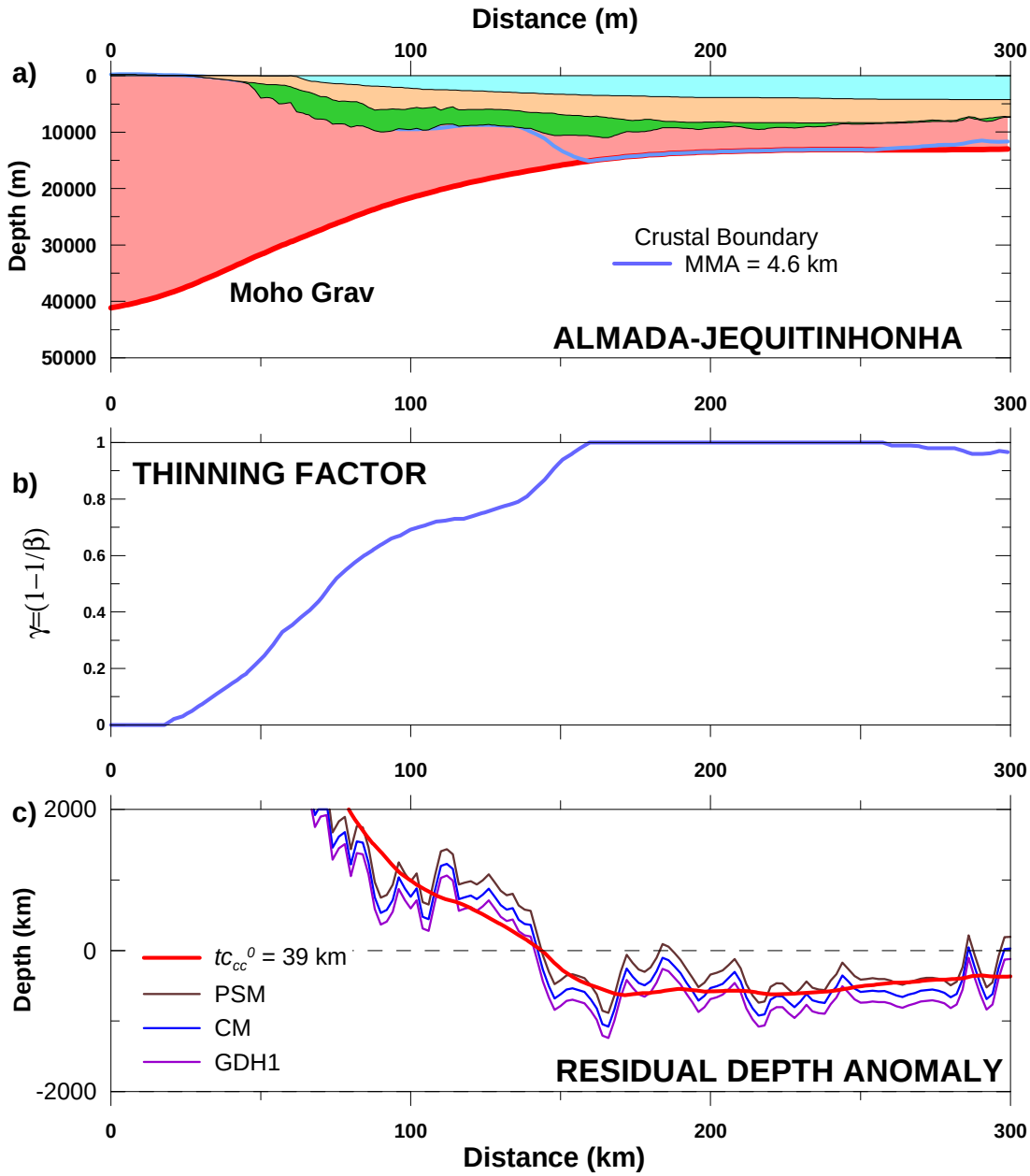

Figure 7.9. Gravity inversion results of Almada-Jequitinhonha. a) geological cross section, post-rift in beige, rift in green, Moho is the thick red line and the continental-ocean crustal boundary is in electric blue line. b) Crustal thinning profile. c) Fit of RDA from gravity inversion (red line) to RDA from flexural backstripping, CM model in blue, in the unequivocal oceanic crust region, between 210 and 290 km, with reference crustal thickness of 39 km.

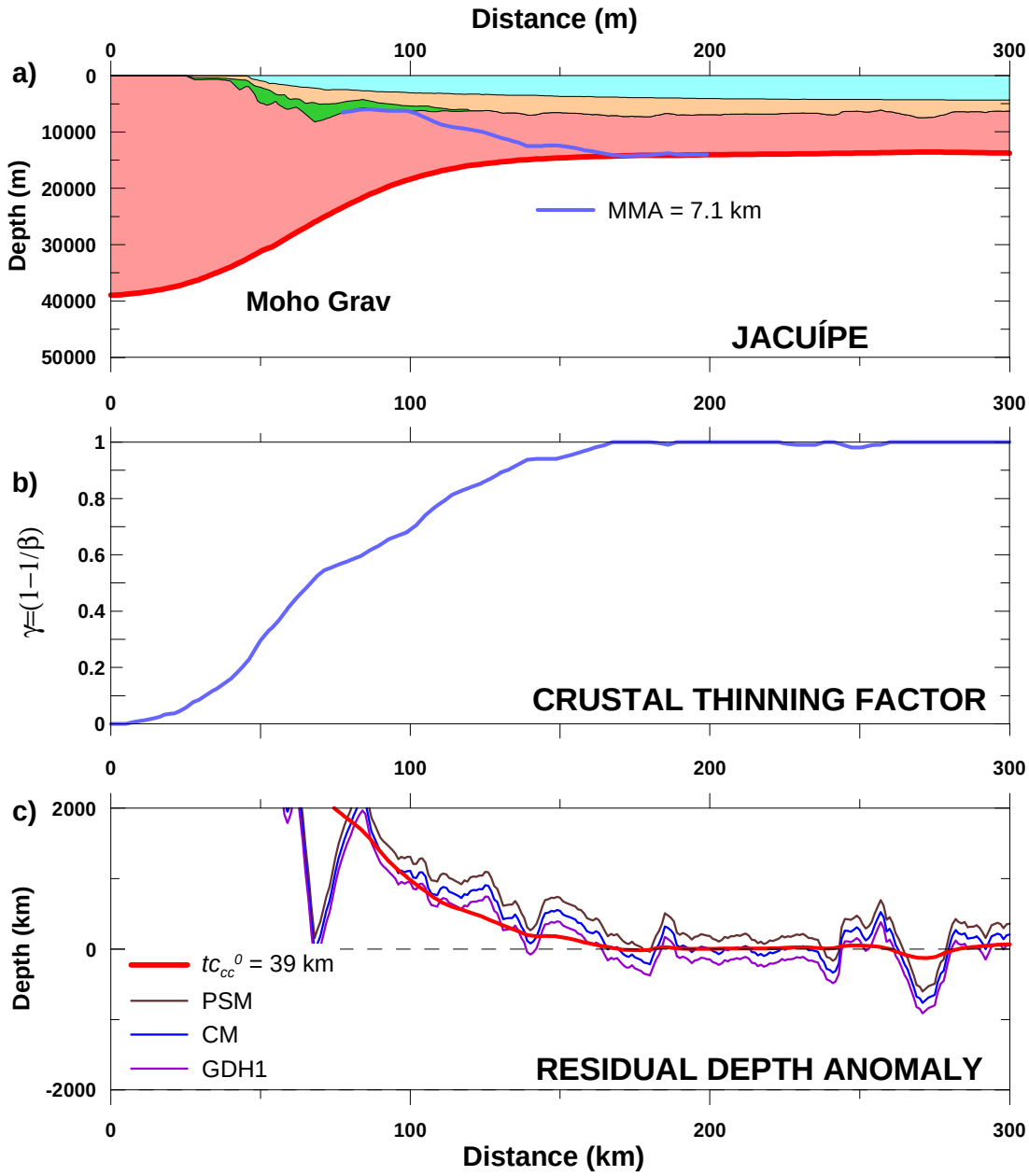

Figure 7.10. Gravity inversion results of Jacuípe. a) Geological cross section, post-rift in beige, rift in green, Moho is the thick red line and the continental-ocean crustal boundary is in electric blue line. b) Crustal thinning profile. c) Fit of RDA from gravity inversion (red line) to RDA from flexural backstripping, CM model in blue, in the unequivocal oceanic crust region, between 180 and 240 km, with reference crustal thickness of 39 km.

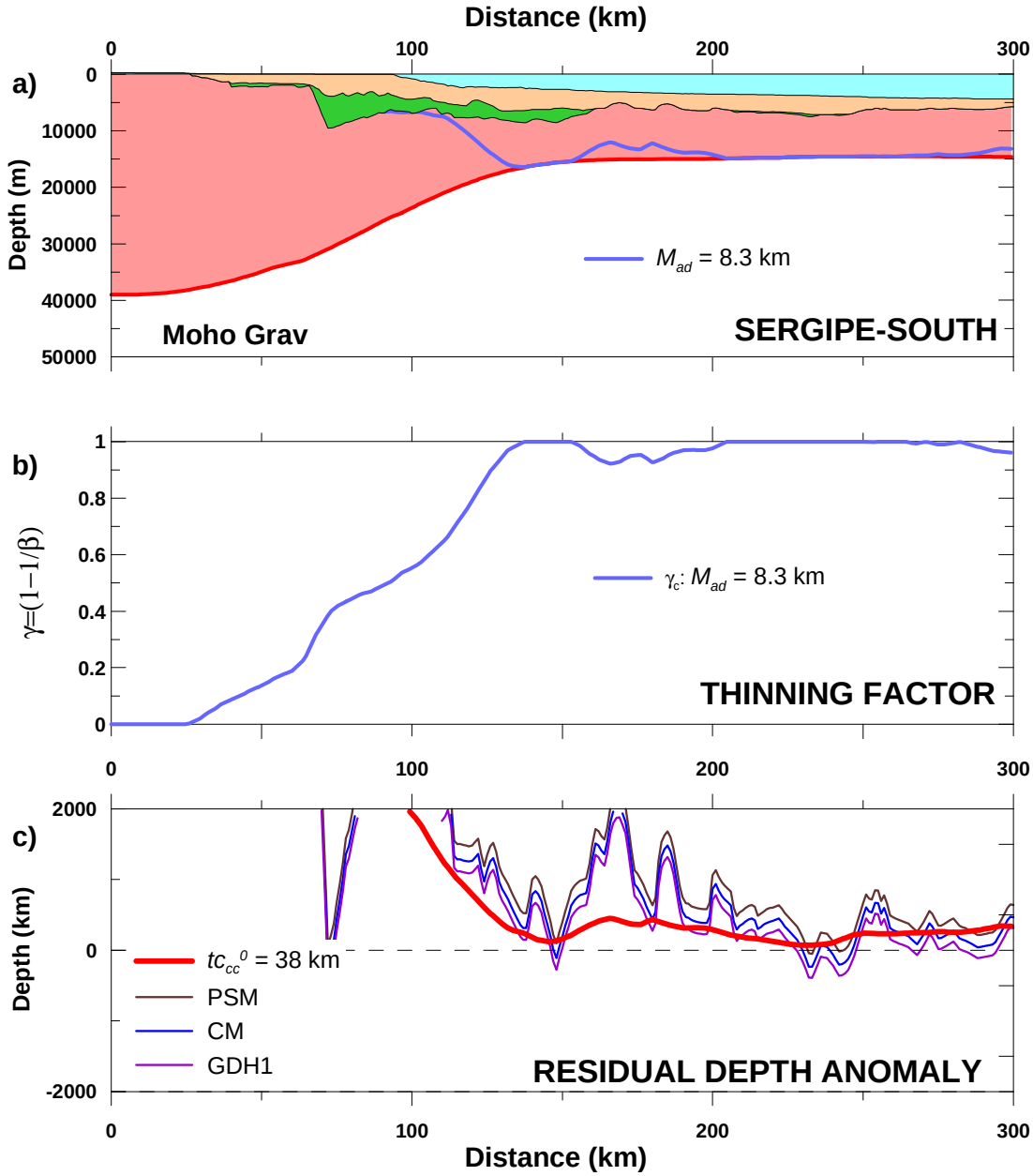

Figure 7.11. Gravity inversion results of Sergipe South. a) Geological cross section, post-rift in beige, rift in green, Moho is the thick red line and the continental-ocean crustal boundary is in electric blue line. b) Crustal thinning profile. c) Fit of RDA from gravity inversion (red line) to RDA from flexural backstripping, CM model in blue, in the unequivocal oceanic crust region, between 180 and 240 km, with reference crustal thickness of 38 km.

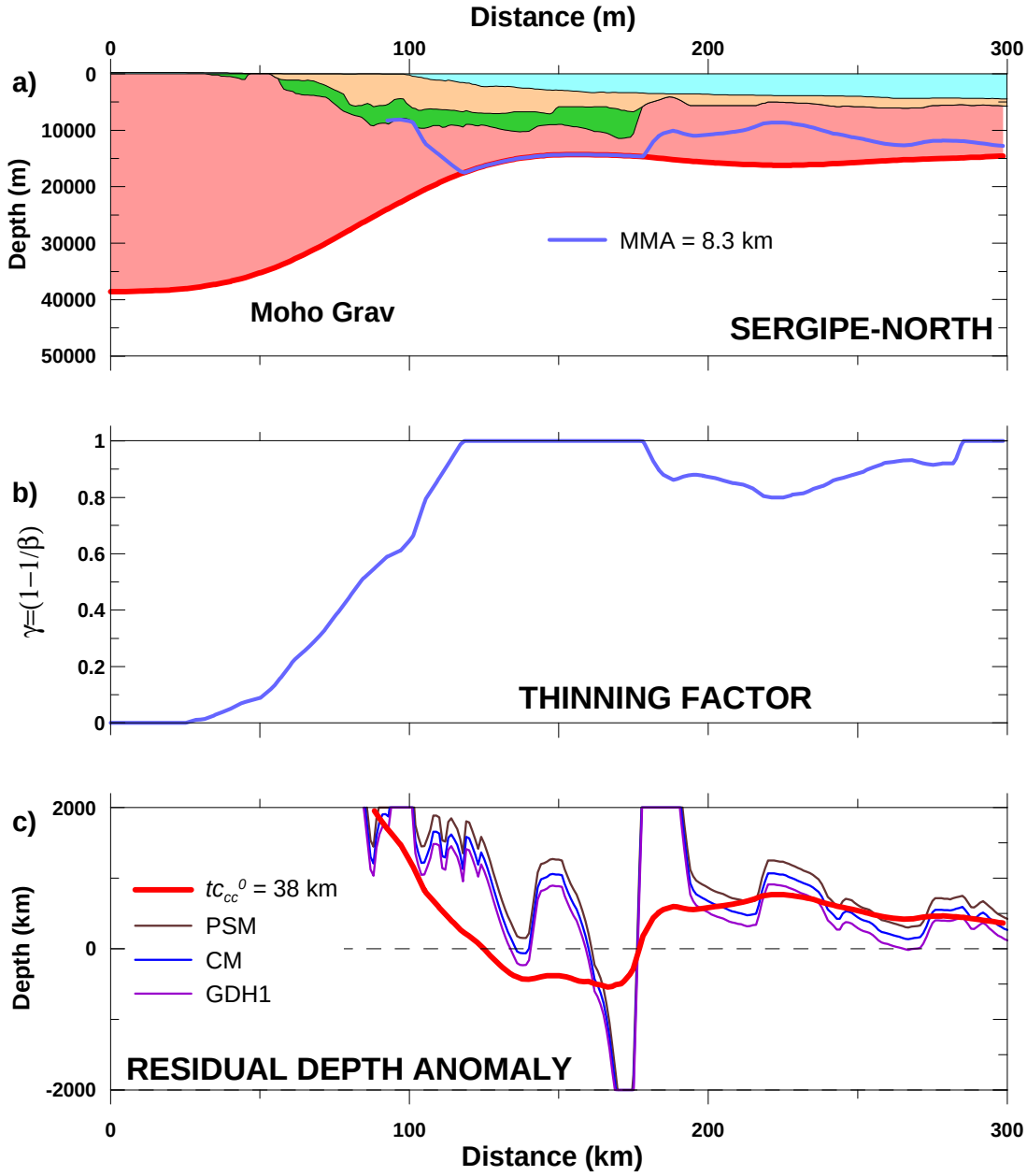

Figure 7.12. Gravity inversion results of Sergipe North. a) Geological cross section, post-rift in beige, rift in green, Moho is the thick red line and the continental-ocean crustal boundary is in electric blue line. b) Crustal thinning profile. c) Fit of RDA from gravity inversion (red line) to RDA from flexural backstripping, CM model in blue, in the unequivocal oceanic crust region, between 250 and 360 km, with reference crustal thickness of 38 km.

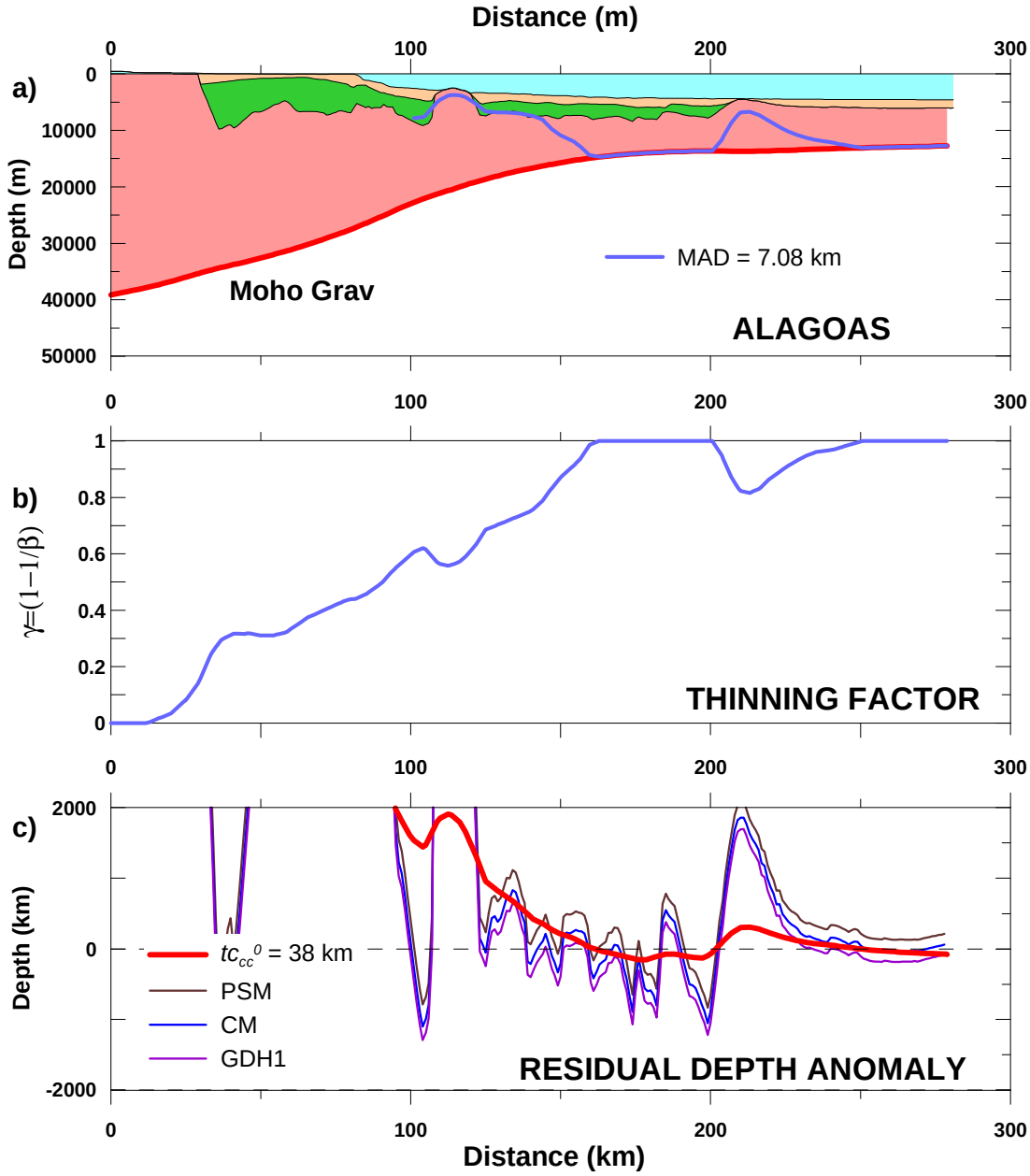

Figure 7.13. Gravity inversion results of Alagoas. a) geological cross section, post-rift in beige, rift in green, Moho is the thick red line and the continental-ocean crustal boundary is in electric blue line. b) Crustal thinning profile. c) Fit of RDA from gravity inversion (red line) to RDA from flexural backstripping, CM model in blue, in the unequivocal oceanic crust region, between 240 and 280 km, with reference crustal thickness of 38 km.

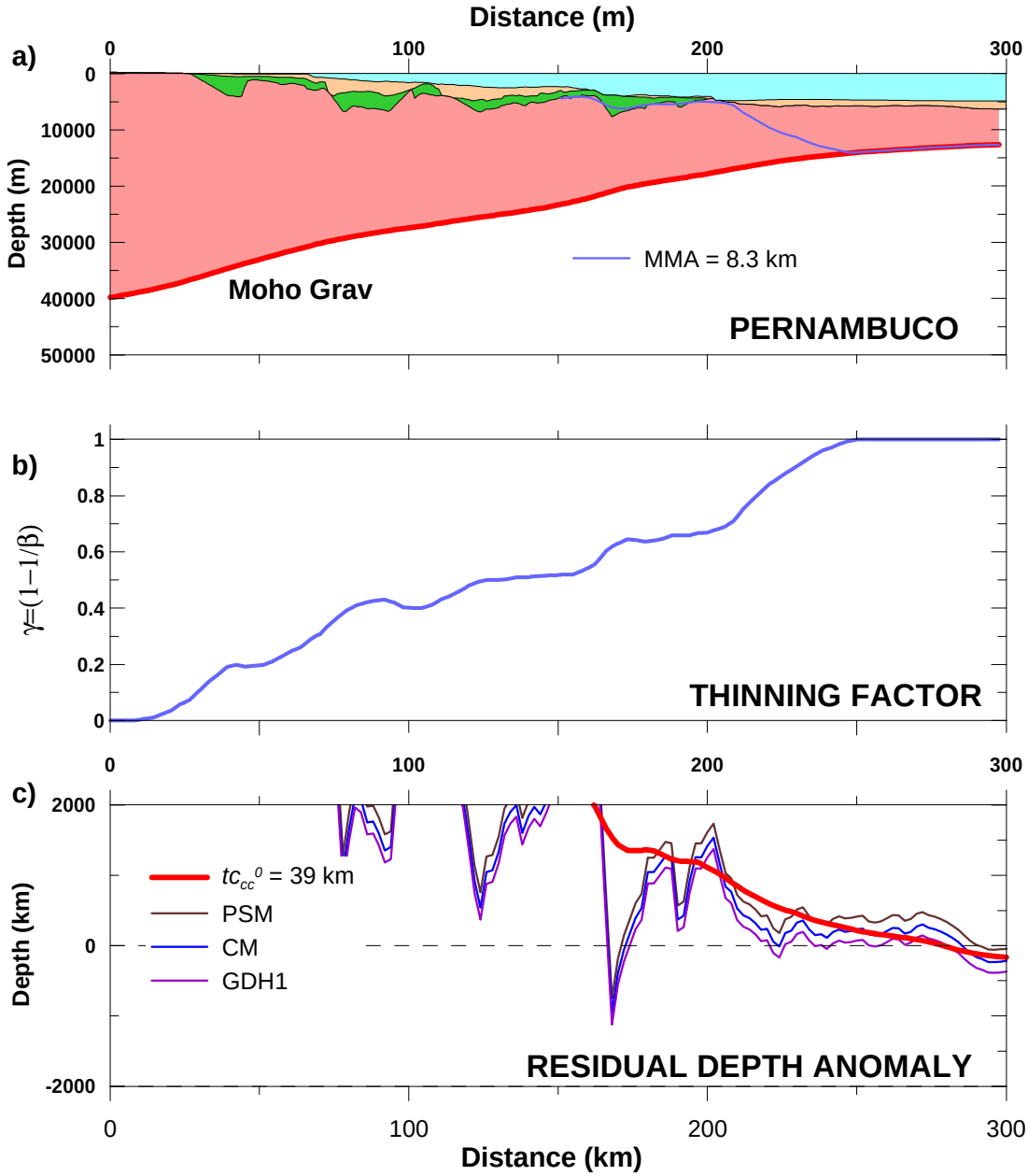

Figure 7.14. Gravity inversion results of Pernambuco. a) geological cross section, post-rift in beige, rift in green, Moho is the thick red line and the continental-ocean crustal boundary is in electric blue line. b) Crustal thinning profile. c) Fit of RDA from gravity inversion (red line) to RDA from flexural backstripping, CM model in blue, in the unequivocal oceanic crust region, between 220 and 280 km, with reference crustal thickness of 39 km.

7.5 Discussion and Conclusions

Moho depth was inverted from the gravity anomaly data in the 3D spectral domain with correction of the lithosphere thermal anomaly. Crustal thickness is calculated from Moho depth and basement interpretation for the continental and

oceanic segments. A relationship between magmatic addition and lithosphere thinning γ was developed to discriminate between continental and oceanic crust, assuming uniform lithosphere thinning. The decrease of the residual continental crust thickness indicates the region affected by the magmatic addition. Maximum magmatic addition is assumed as the oceanic crustal thickness related to the sediment-corrected RDA.

The synthetic RDA from gravity inversion could fit sediment-corrected RDA in the oceanic region of the six cross-sections with a narrow range of reference Moho depth, between 38 and 39 km. The fit of synthetic and sediment-corrected RDA in the oceanic crust is a new approach to calibrate the gravity inversion and to determine the reference Moho depth in areas without refraction data.

The residual continental crust and crustal thinning were determined for the Almada-Jequitinhonha cross-section with a reference Moho depth of 39 km. The preferred fit to a magma-poor margin with 4.6 km-thick oceanic crust corroborates the COCB location suggested as an inflection by the sediment-corrected RDA, around 150 km. Similarly, the COCB location in the Jacuípe cross-section is interpreted at 170 km in the distal limit of seaward dipping reflectors (SDR), assuming a reference Moho depth of 39 km and oceanic crustal thickness of 7.1 km. The clear COCB indicated on the seismic section and in RDA profile was reasonably fit by the crustal thinning from gravity inversion in the Pernambuco cross-section, using a reference Moho depth of 39 km.

The magmatic addition relationship suggests much more proximal COCB locations for cross-sections Sergipe South, Sergipe North and Alagoas than interpreted in seismic reflection. All these cross-sections present an ocean-continent-transition (OCT) with crust thinner than expected for the adjacent unequivocal

oceanic crust. The OCT crust is bounded by oceanic crust segments thicker than the unequivocal oceanic crust. Therefore, the assumption that the maximum magmatic addition is constant along a cross-section may be not valid. The residual continental crust and crustal thinning were determined for these cross-sections with a reference Moho depth of 38 km.

CHAPTER 8

8. DETERMINATION OF SUBSIDENCE FROM LITHOSPHERE THINNING

8.1 INTRODUCTION

The analytical equations of the depth-uniform continental lithosphere stretching model DULSM (McKenzie, 1978) that relate initial and thermal subsidence to lithosphere thinning become more and more complex if depth-dependent stretching and magmatic addition are taken into account (Beaumont et al., 1982; Royden and Keen, 1980). Magmatic addition produced by decompression melting is an important process during the evolution of a continental rifted margin that was not considered in the DULSM equations (McKenzie and Bickle, 1988; White and McKenzie, 1989). In addition, many continental rifted margins show depth-dependent lithosphere thinning (Davis and Kusznir, 2004; Kusznir and Karner, 2007; Royden and Keen, 1980). Moreover, the assumption of a linear continental lithosphere geotherm, as expected for an old oceanic lithosphere (McKenzie, 1978), must be generally invalid for continental lithosphere as the radiogenic heat production from the continental crust modifies the continental geotherm and the thermal loads.

The aim of this chapter is to present a numerical model to calculate the evolution of total subsidence with time in response to lithosphere and crustal thinning. This model incorporates magmatic addition, depth-dependent thinning, radiogenic heat production and flexural isostatic response in order to be used later as a forward model component in a numerical inversion.

8.2 Methodology for Determination of the Isostatic Loads in Response to Lithosphere Thinning

The effects of magmatic addition, depth-dependent thinning and radiogenic heat production were initially implemented in an 1D program that calculates initial and total subsidence through time (figure 8.1). Then, the program was adapted for 2D to incorporate the flexural isostatic response for the crustal and thermal loads. Initial subsidence corresponds to the isostatic response to the crustal and thermal loads in an instantaneous syn-rift, while total subsidence corresponds to the isostatic response to the crustal and thermal loads after a defined time in the post-rift. Crustal load is constant, inherited from the rift phase, while thermal load varies with time due to the dissipation of the syn-rift lithosphere thermal anomaly. Total subsidence corresponds to the sum of initial and thermal subsidence. Depth-dependent thinning and magmatic addition modifies the crustal load, while radiogenic heat production modifies the thermal load. Instantaneous rifting is assumed in this research, allowing the comparisons of the numerically calculated initial and total subsidence with those analytically calculated using McKenzie (1978) model. Although a finite rifting approach should be more appropriate for the East Brazilian rift system, which lasted around 30 Myr, large differences are not expected in total subsidence calculated assuming instantaneous or finite rifting.

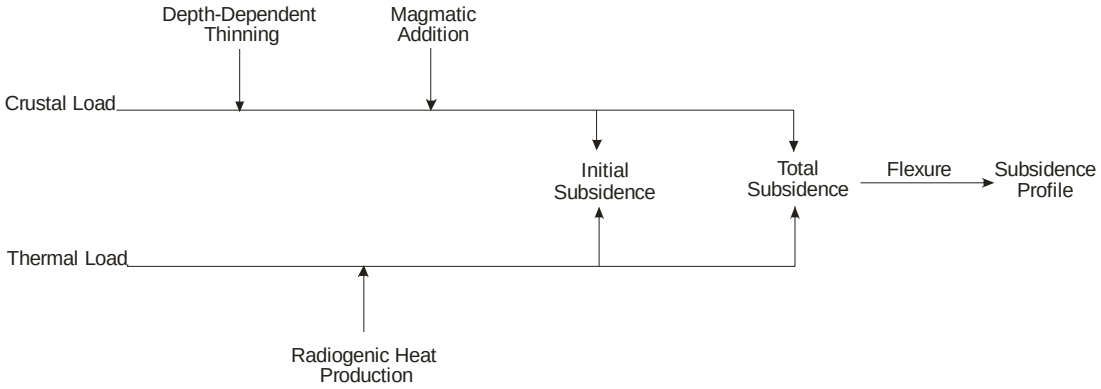

Figure 8.1: Workflow for calculation of subsidence from crustal and thermal loads.

8.2.1 The Crustal Thinning Load And Its Modifications By Depth-Dependent Thinning And Magmatic Addition

As introduced in Chapter 2, the crustal load L_{ct} corresponds to the product of the crustal thickness decrease Δt_c due to crustal thinning $\gamma_c = (1\text{-}1/\beta_c)$ by the density contrast $\Delta\rho_c$ between mantle and crust and by the gravity acceleration g, approximately 9.78 m s^{-1}:

$$L_{ct} = \Delta t_c \left(\rho_m^0 - \rho_c^a\right) g \,, \qquad (2.3.a)$$

where ρ_c^a is the average crustal density and ρ_m^0 is the mantle density at surface. Crustal load L_{ct} is positive for thinning and contributes to subsidence in response to lithosphere thinning.

In the depth-uniform lithosphere stretching model (McKenzie, 1978), crustal and lithospheric mantle thinning are considered equal: $\gamma_c = \gamma_m$. However, situations in which crustal and mantle thinning are different must be taken into account as depth-dependent lithosphere stretching has been identified in many continental rifted margins (Davis and Kusznir, 2004; Kusznir and Karner, 2007). Generally, depth-dependent thinning models assume that the upper crust stretches differently from the lower crust and lithospheric mantle, separated by a detachment surface (Hellinger

and Sclater, 1983). In a more general case, the detachment can be located above or below the crust-mantle interface (Wernicke, 1985) (figure 2.13b).

Depth-dependent lithosphere thinning was incorporated into the model through the redefinition of the crustal thickness variation Δt_c, controlled by a detachment d that separates upper and lower plate thinning (Hellinger and Sclater, 1983):

$$\text{for } d \geq t_c\text{: } \Delta t_c = t_c \cdot \gamma_1 ; \tag{8.1}$$

$$\text{for } d < t_c\text{: } \Delta t_c = d \cdot \gamma_1 + (t_c - d) \cdot \gamma_2 \tag{8.2}$$

where $\gamma_1 = 1 - 1/\beta_1$ is thinning above the detachment and $\gamma_2 = 1 - 1/\beta_2$ is thinning below the detachment (figure 8.2).

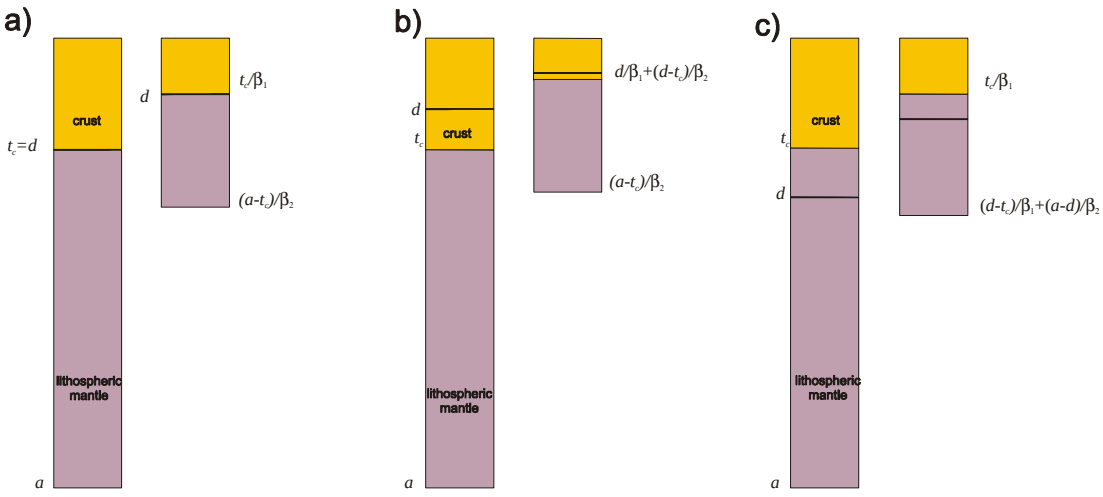

Figure 8.2: Depth-dependent thinning for β_1 = 2 and β_2= 3 with different detachment depths. a) Detachment depth *d* is at the base of the crust. b) Detachment depth *d* is above the base of the crust. c) Detachment depth *d* is below the base of the crust

Magmatic addition is a consequence of decompression melting due to lithosphere thinning, and it adds new crustal material that modifies the crustal thinning load (McKenzie and Bickle, 1988; White and McKenzie, 1989). Thus,

magmatic addition m_{ad} is subtracted from the crustal thickness variation Δt_c (figure 8.3):

$$\Delta t_c^{\,mad} = \left(t_c - \frac{t_c}{\beta} \right) - m_{ad} = t_c \cdot \gamma_c - m_{ad} \,. \tag{8.3}$$

The magmatic addition m_{ad} for specific lithosphere thickness and asthenosphere potential temperature can be calculated through an assumed linear relationship with the lithospheric thinning factor γ, as introduced in Chapter 7 (figure 7.7c):

$$mad(\gamma) = t_{oc} \cdot \frac{(\gamma - \gamma_{crit})}{(1 - \gamma_{crit})} \,. \tag{8.4}$$

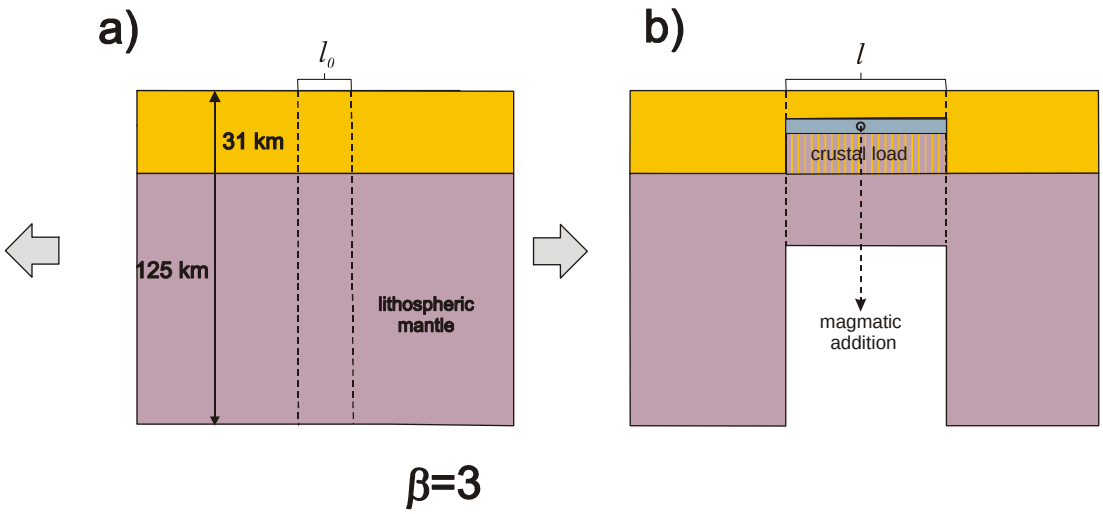

Figure 8.3: Magmatic addition load by decompression melt counteracts the effect of the crustal thinning load.

In this practical approach, instead of the asthenosphere potential temperature, magmatic addition is parameterized with the oceanic crustal thickness, assumed as the maximum magmatic addition. The critical gamma γ_{crit} in equation 8.4 corresponds to the amount of thinning necessary for decompression melting to start, while the expected igneous oceanic crust thickness t_{oc} corresponds to the predicted maximum magmatic addition M_{ad} in a region (White et al., 1992).

The relationship between magmatic addition and thinning factor for a defined continental lithosphere thickness varies with maximum magmatic addition (figure 7.7c). For an assumed lithosphere thickness a, a linear relationship between the critical gamma γ_{crit}, for zero melt thickness, and the maximum magmatic addition M_{ad}, for $\gamma = 1$, may be obtained (figures 7.7d and 8.4). The linear relationship of critical gamma γ_{crit} against maximum magmatic addition M_{ad}, for a standard 125 km-thick lithosphere, is shown in figure 8.4.

The critical gamma γ_{crit} can be determined for the maximum magmatic addition M_{ma}, which is assumed to be equivalent to the igneous oceanic crust thickness t_{oc}, interpreted from RDA data of the area, then:

$$\gamma_{crit} = a_1 * t_{oc} + a_2 , \qquad (8.5)$$

where a_1 = -2.0821^{-02} and a_2 = + 8.3574^{-01} for a 125 km-thick lithosphere. This value of γ_{crit} is applied in equation 8.4 to find magmatic addition as a function of thinning factor. For different lithosphere thickness, the parameters of equation 8.5 must be re-calculated (figure 8.4).

8.2.2 THE LITHOSPHERE THERMAL LOAD

The thermal load L_{th} corresponds to the difference in weight between a mantle rock column whose geothermal gradient has been increased by lithosphere thinning and the reference continental lithosphere, as expressed by equation 2.4 (figure 2.5):

$$L_{th} = \alpha \rho_m^0 g \int_0^{\infty} \Delta T dz . \qquad (2.4)$$

The integral of the temperature contrast with depth in equation 2.4 is calculated using the trapezoid method where α and $\rho_m{}^0$ are previously defined (table 2-1), $\Delta z = a/m$ is

depth sampling distance and *m*+1 are the number of nodes with which the lithosphere *a* is sampled:

Assuming initially that the reference continental lithosphere corresponds to that of an old oceanic basin lithosphere, as given by the PSM plate cooling model (Parsons and Sclater, 1977), the reference load is defined by a linear geotherm (figures 2.2.b-d):

$$T(z) = \frac{Tm \cdot z}{a}. \tag{8.6}$$

where *T(z)* is the variation of temperature with depth *z* and *Tm* is the temperature at the base of the lithosphere *a*.

The geotherm due to the thermal anomaly corresponds to:

$$T(z) = \begin{cases} \frac{T_m \cdot z}{a^{new}}, \text{ for } 0 < z < a^{new}, \text{ and} \end{cases} \tag{8.7}$$

$$T(z) = T_m, \text{ for } z \geq a^{new}. \tag{8.8}$$

For a thinned lithosphere, its new base a^{new} is given by:

$$a^{new} = a - \Delta t_c - \Delta t_{ml} + mad, \tag{8.9}$$

where *a*, Δt_c and *mad* are defined above and Δt_{ml} is the mantle lithospheric thickness variation, also defined according to the detachment depth *d* in depth-dependent thinning (figure 8.2b-c):

$$\Delta t_{ml} = (a - t_c) \cdot \gamma_2, \text{ for } d < t_c, \text{ and} \tag{8.10}$$

$$\Delta t_{ml} = (d - t_c) \cdot \gamma_1 + (a - d) \cdot \gamma_2, \text{ for } d \geq t_c; \tag{8.11}$$

where γ_1 is thinning above the detachment and γ_2 is thinning below the detachment (figure 8.2).

For depth-uniform lithosphere thinning and no magmatic addition, $a^{new}=a/\beta$ (McKenzie, 1978). The density contrast between a column of mantle rock with raised geothermal gradient and a lithosphere in thermal equilibrium is always negative. So, the thermal load L_{th} contributes with uplift to the isostatic compensation of lithosphere thinning.

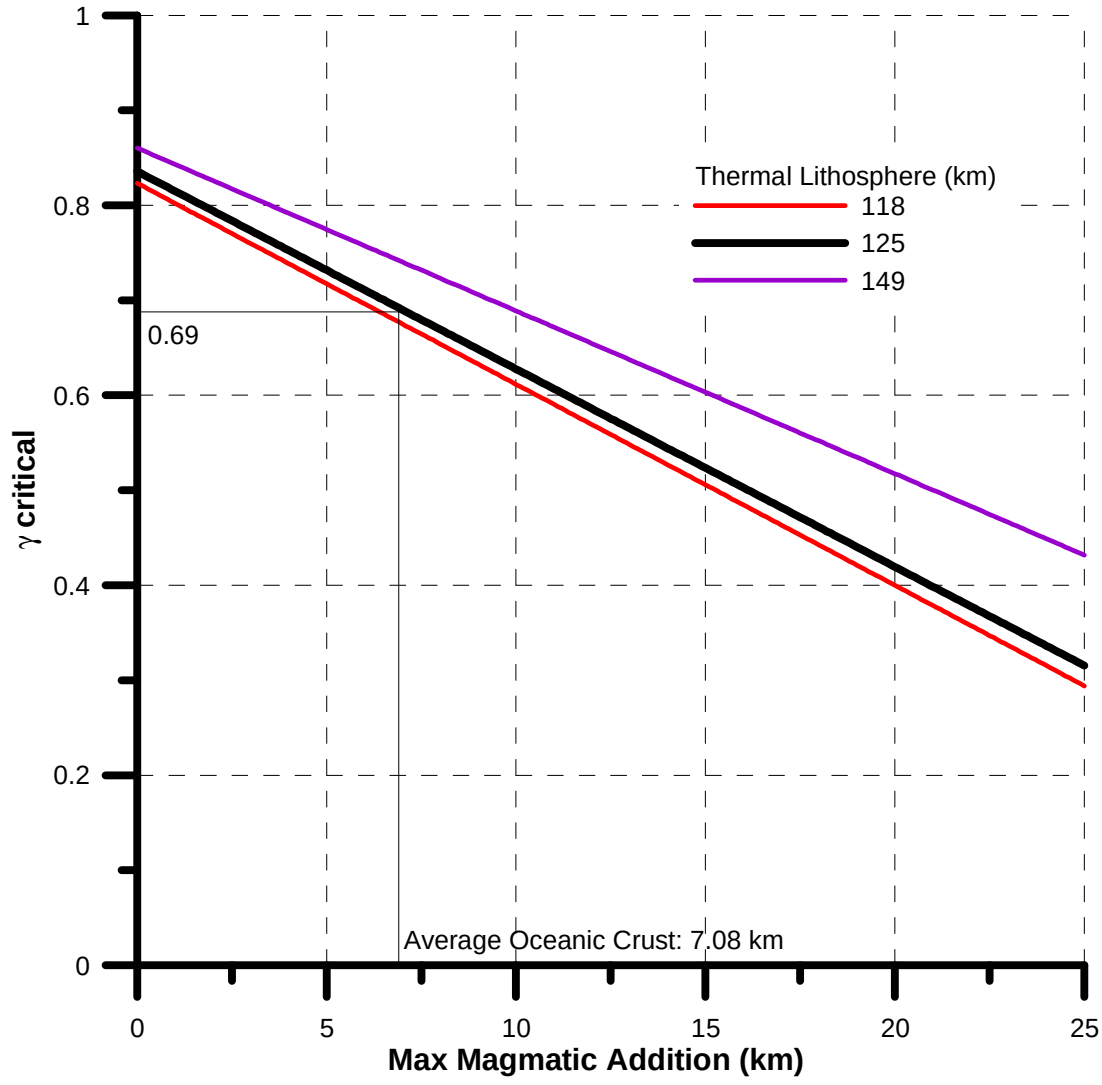

Figure 8.4: Linear variation of critical gamma with maximum magmatic addition for 118, 125 and 149 km-thick thermal lithospheres.

8.3 INITIAL SUBSIDENCE FROM THE ISOSTATIC RESPONSE TO SYN-RIFT LOADS

Initial subsidence S_i corresponds to the resultant isostatic compensation for the sum of the crustal and thermal loads, created by lithosphere thinning during the syn-rift phase:

$$S_i = \frac{L_{ct} + L_{th}}{\Delta\rho_2}, \qquad (8.12)$$

where L_{ct} is the crustal thinning load, L_{th} is the lithosphere thinning thermal load, $\Delta\rho_2$ = (ρ_a-ρ_w) and ρ_a = $\rho_{0.}$(*1*-αT_m).

The comparison of the initial subsidence S_i calculated with equation 2.5 from the depth-uniform lithosphere stretching model (McKenzie, 1978) and calculated numerically with equation 8.14 is presented in figure 8.5. The same lithosphere parameters of the DULSM model were applied, as well as initial crustal thickness of 31 km (table 2-1) and a depth sampling interval Δz of 1000 m for the numerical model. The maximum difference between the numerical and analytical determinations is around 50 m for γ= 0.99, less than 2 %.

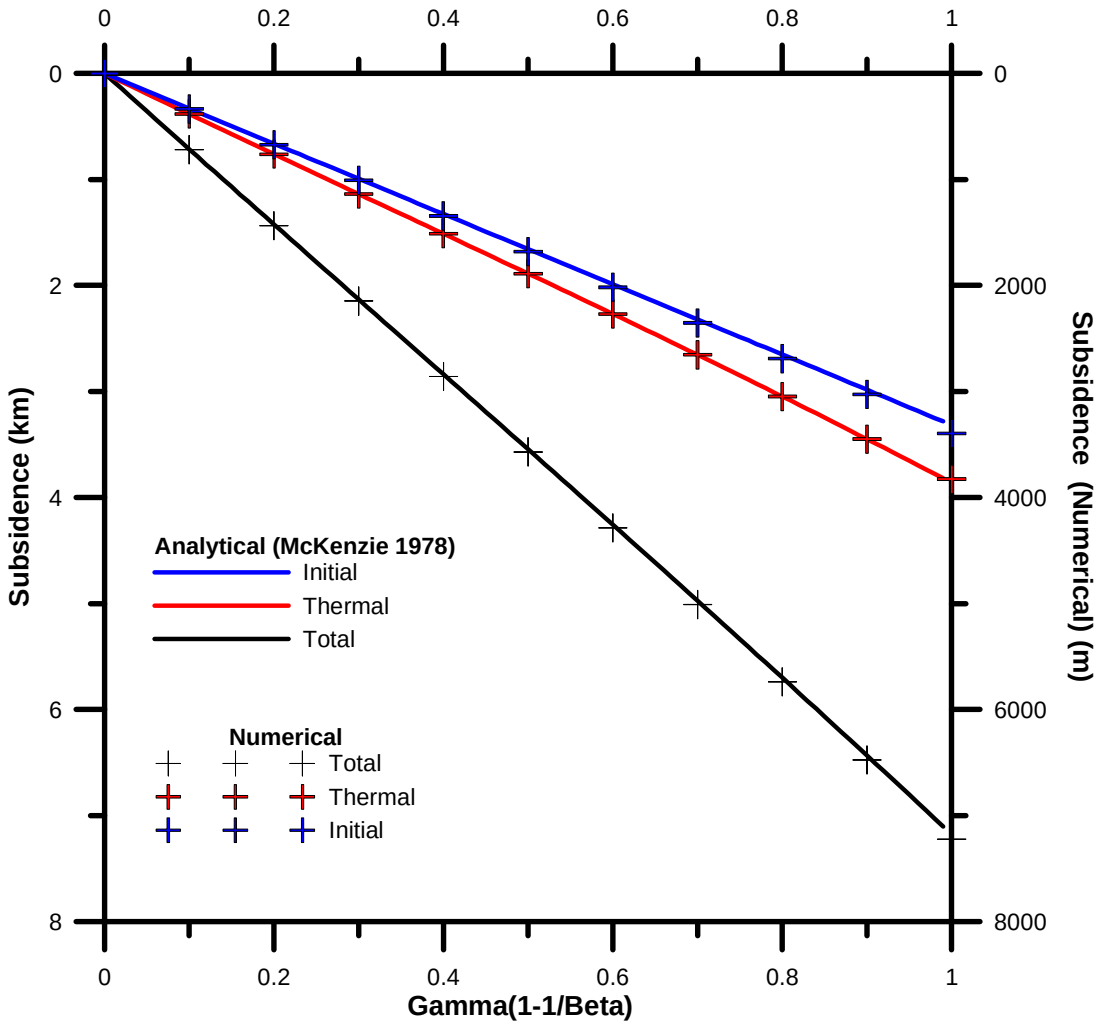

Figure 8.5: Comparison of initial, thermal and total subsidence calculated analytically with McKenzie (1978) equations and numerically with the method developed in this thesis. McKenzie (1978) parameters were used, including a 125 km-thick lithosphere, 31 km-thick crust and crustal density of 2800 kg m^{-3}. Thermal subsidence was computed for 150 Myr.

8.4 Post-Rift Lithosphere Cooling And Subsidence

The dissipation of the thermal anomaly with time in the plate cooling model (Parsons and Sclater, 1977) is defined by the partial derivatives equation (PDE) of the heat conservation (equation A.6, Appendix I). Initially, assuming no heat generation and only vertical heat conduction, the PDE becomes:

$$\rho \cdot C_p \cdot \frac{\partial T}{\partial t} = k \frac{\partial^2 T}{\partial z^2}, \qquad (2.6)$$

where T is temperature, t is time, z is depth ρ, C_p and k are, respectively, density, heat capacity and thermal conductivity of lithosphere rocks, while $\kappa = k / \rho C_p$ is the thermal diffusivity.

Equation 2.6 can be solved numerically by the explicit finite differences method (Farlow, 1993) through the definition of a grid with m+1 nodes in the depth dimension and n+1 nodes in the time dimension, where Δz is depth step and Δt is time step (figure 8.6). The dissipation of the thermal anomaly is calculated until a time $n.\Delta t$. The definition of the initial and boundary conditions at the top and at base of the initial plate thickness are necessary for the calculation of the dissipation of the thermal anomaly. The initial condition is given by the thermal anomaly caused by lithosphere thinning in the rift phase, for time t = 0, while the boundary conditions are the temperatures T_0 at the surface and T_m at the base of reference lithosphere a:

Initial Condition: $$T(z,0) = \begin{cases} \dfrac{T_m \cdot z \cdot \beta}{a} \text{, for } 0 < z < a/\beta \text{ and} \end{cases} \quad (8.13)$$

$$T(z,0) = T_m \text{, for } z \geq a/\beta. \quad (8.14)$$

Boundary Conditions: $$\begin{cases} T(0,t) = 0 \\ T(a,t) = T_m \end{cases} \text{, for } 0 < t < \infty. \quad (8.15)$$

For a time step i, the thermal gradients between a depth node j and the upper and lower neighbours j-1 and j+1 (figure 8.6) are given respectively by the equations:

$$\frac{\partial T}{\partial z} = \frac{T_j - T_{j-1}}{\Delta z} \text{ and} \quad (8.16)$$

$$\frac{\partial T}{\partial z} = \frac{T_{j+1} - T_j}{\Delta z}. \quad (8.17)$$

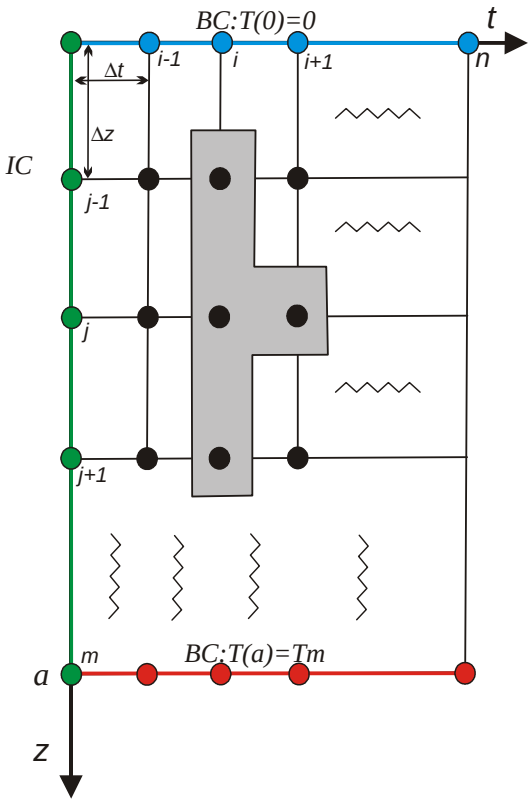

Figure 8.6: Schematic representation of the explicit finite differences method, modified from (Farlow, 1993).

Hence, the second derivative of temperature in depth between the lower and upper nodes, j-1 and j+1, corresponds to:

$$\frac{\partial^2 T}{\partial z^2} = \frac{\dfrac{T_{i,j+1} - T_{i,j}}{\Delta z} - \dfrac{T_{i,j} - T_{i,j-1}}{\Delta z}}{\Delta z}. \qquad (8.18a)$$

$$\frac{\partial^2 T}{\partial z^2} = \frac{T_{i,j+1} - 2T_{i,j} + T_{i,j-1}}{\Delta z^2}. \qquad (8.18b)$$

The derivative of the temperature with time for a time step i+1, after a time step i, corresponds to:

$$\frac{\partial T}{\partial t} = \frac{\left(T_{i+1,j} - T_{i,j}\right)}{\Delta t}. \qquad (8.19)$$

Therefore the temperature along a mantle rocks column that had the geothermal gradient increased due to lithosphere thinning can be determined by substitution of

the partial derivatives in equation 2.6 by the explicit finite differences of equations 8.18 and 8.19, initially ignoring the radiogenic contribution:

$$T_{i+1,j} = T_{i,j} + \frac{\Delta t}{\rho C_p} \cdot \left\{ \frac{k}{\Delta z^2} \cdot \left[T_{i.j+1} - 2T_{i,j} + T_{i,j-1} \right] \right\}. \qquad (8.20)$$

The approximation of the cooling plate model partial derivatives by finite differences requires adequate choices of the time and depth steps, Δt and Δz respectively. It has been proved that for the method to work the relationship $\Delta t/\Delta z^2 \leq 0.5$ must be followed (Farlow, 1993). Smaller steps sizes decrease truncation errors, inherent to numerical approximations, but steps too small increase roundoff computations errors. For a given depth step Δz, the critical time step Δt_{crit} is the limit for convergence of the solution (Caban, 1991):

$$\Delta t_{crit} = \frac{\Delta z^2}{4} \cdot \frac{\rho C_p}{k}. \qquad (8.21)$$

Table 8-1 presents the critical time steps in seconds and in years for different depth interval sampling of a 125 km-thick lithosphere and the selected time steps, which must be an integer number, less than the critical time step and multiple of the total time after break-up:

Table 8-1: Critical time steps in seconds and in years for different depth sampling intervals. The selected time steps must be multiple of the thermal subsidence time.

Δz (m)	Δt_{crit} (sec)	Δt_{crit} (yr)	Δt (yr) selected
12500	48562500000000	1538884.36	1150000
5000	7770000000000	246221.50	200000
2500	1942500000000	61555.37	50000
1250	485625000000	15388.84	15000
1000	310800000000	9848.86	5000
500	77700000000	2462.21	1000
250	19425000000	615.55	500
100	3108000000	98.49	50
10	31080000	0.98	0.5

8.4.1 RADIOGENIC HEAT PRODUCTION AND THE CONTINENTAL LITHOSPHERE GEOTHERM

Radiogenic elements tend to be concentrated in granitic plutonic bodies in the shallow levels of the crust. The concentration of radiogenic elements and the radiogenic heat production are practically impossible to be directly evaluated along a continental crust column. The radiogenic heat generated *A* in the continental crust can be modelled by an exponential depth decay equation (figure 8.7):

$$A = A_0 \exp(-z/z_r), \tag{8.22}$$

where $A_0=\rho_c.H_0$ is the surface heat production, H_0 is the heat production rate per unit mass at the surface, ρ_c is the density of the upper crust rocks, and z_r is the length scale of the exponential decrease of the radiogenic heat production, in the order of 8-15 km. The model of exponential decay of the radiogenic heat production with depth is one of the most accepted and utilized, but alternative models can be more appropriate in some circumstances (Turcotte and Schubert, 2002). One of the problems of the exponential decay model is that it can predict too low radiogenic heat production *A* for the lower crust, close to 0 μWm^{-3}, whereas many exposed lower crust regions present rocks with radiogenic heat production around 1 $\mu W\ m^{-3}$ (Jaupart and Mareschal, 1999).

In this thesis, the exponential radiogenic heat decay model with the same z_r of 15 km is assumed in all modelling for consistency. The contribution of the radiogenic heat generated in the continental crust to the heat flow corresponds to the integral of equation 8.22:

$$\int_0^\infty A_0 \exp(-z/z_r)dz = A_0 \cdot z_r \tag{8.23}$$

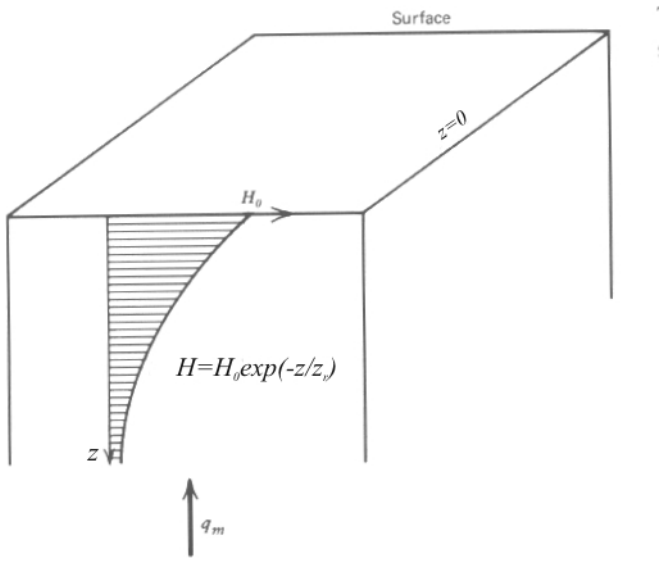

Figure 8.7: Model of exponential decay with depth of the heat production rate per unit mass at the surface (Turcotte and Schubert, 2002).

The heat production rate H_0 is a parameter related to composition, being larger for rocks rich in radioactive elements, *K*, *U* and *Th*. Granitic rocks are rich in radioactive elements, while mafic and ultramafic are poor. Generally, the product $\rho_c.H_0$ is designated as the constant A_0, obtained from direct rock samples measurements or from gamma-spectrometric surveys. The effect of radiogenic heat generated in the crust can be considered in the thermal load by including its contribution to the explicit finite differences equation 8.22:

$$T_{i+1,j} = T_{i,j} + \frac{\Delta t}{\rho C_p} \cdot \left\{ \frac{k}{\Delta z^2} \cdot \left[T_{i.j+1} - 2T_{i,j} + T_{i,j-1} \right] + A_0 \cdot \exp\left(-z/z_r\right) \right\}. \qquad (8.24)$$

STEADY STATE CONTINENTAL GEOTHERM

Instead of assuming the simplified linear lithosphere geotherm of the plate cooling model (Parsons and Sclater, 1977), realistic reference continental lithosphere with radiogenic heat production can be numerically determined with explicit finite differences (equation 8.26), calculating the thermal structure a very long time after a thermal perturbation, until the steady state is reached (figure 8.8).

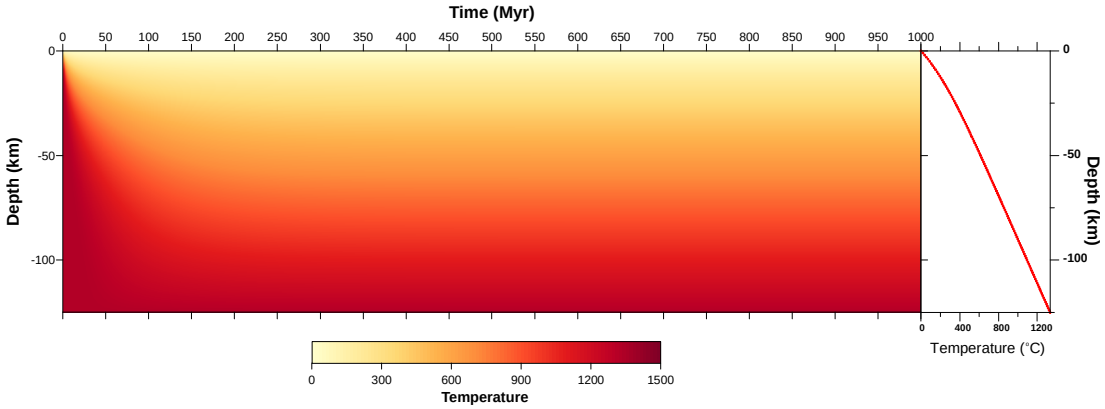

Figure 8.8: Steady state geotherm of a continental lithosphere with radiogenic heat production, diagram on the right side, determined by the dissipation of a thermal perturbation after 500 Myr.

8.4.2 Combined Isostatic Response to Crustal and Thermal Loads

Total subsidence S^t at a time t after break-up is calculated from the variation of the thermal load along time, after the initial thermal perturbation. During dissipation of the thermal anomaly, the column of raised geothermal gradient rocks becomes cooler and the difference in temperature between this column and the initial or reference lithosphere column T decreases. So, the thermal load L_{th} also decreases, while the crustal load keeps the same as in equation 8.14, which then results in post-rift subsidence:

$$S^t = \frac{L_{ct} + L_{th}{}^t}{\Delta\rho_2}. \qquad (8.25)$$

Equation 8.27 is analogous to equation 8.12 for initial subsidence, applied for times larger than 0 Myr. Hence, thermal subsidence corresponds to the difference between total and initial subsidence, which ultimately corresponds to the difference between the final and initial thermal loads:

$$S_{th}{}^t = \frac{\left(L_{ct} + L_{th}{}^t\right) - \left(L_{ct} + L_{th}{}^0\right)}{\Delta\rho_2} = \frac{\left(L_{th}{}^t - L_{th}{}^0\right)}{\Delta\rho_2}. \qquad (8.26)$$

Equation 8.28 is analogous to equation 2.12, the analytical solution for thermal subsidence and oceanic elevation from the depth-uniform stretching model (DULSM) and from the plate cooling model (PSM) (McKenzie, 1978; Parsons and Sclater, 1977). However, while the "fluid" density considered in the isostatic compensation density contrast $\Delta\rho_2$ was assumed as the surface mantle density ρ_0 in equation 2.12, equations 8.25 and 8.26 assume the asthenosphere density ρ_0, which is consistent with the equation 8.14 for initial subsidence.

The comparison of the thermal subsidence S_{th} after 150 Myr, calculated using equation 2.12 (McKenzie, 1978), with the thermal subsidence calculated numerically using equation 8.28 is also presented in figure 8.5. A time step of 5000 years was used in the explicit finite difference solution of the thermal model. The maximum difference between the numerical and analytical determinations is around 50 m for γ=0.99, which is less than 1 %.

8.5 Subsidence as Flexural Isostatic Response to Crustal and Thermal Loads

In order to invert numerically lithosphere thinning from total subsidence profile across a continental rifted margin, $\gamma(S(x))$, it is necessary to define a forward model function that relates subsidence to lithosphere thinning in distance $S(\gamma(x))$. Subsidence is computed as the sum of the flexural isostatic response for the crustal and thermal loads, $w_c(x)$ and $w_{th}(x)$ respectively, using an average elastic thickness *Te*:

$$S(x) = w_c(x) + w_{th}(x). \qquad (8.27)$$

The crustal and thermal loads are defined by the upper and lower plate thinning values across a continental rifted margin, $\gamma_1(x)$ and $\gamma_2(x)$, which start with 0.0 in the basin border and reach 1.0 at the continent-ocean boundary (COB). The thermal load is computed for the age of the continental break-up at the studied margin. For depth-uniform thinning, upper and lower plate thinning are the same.

The crustal and thermal loads are initially converted from the space domain to the wave domain through a Fourier transform, using the *Fast Fourier Transform* (Press et al., 2007). To avoid border effects of the Fourier transform, each load is placed in the middle of a larger profile and then re-sampled in 2^n intervals (figure 8.9). The distance between the limits of the original and the modified profiles must be at least ten times the elastic thickness *Te* (Turcotte and Schubert, 2002). As effective elastic thickness *Te* in the order of 3 to 5 km were used in the flexural backstripping of the cross-sections (Chapter 5) and the original profiles are around 300 km wide, so the extended profiles must be at least 400 km wide. The first and last values of each load are extrapolated to the terminations of the extended profile.

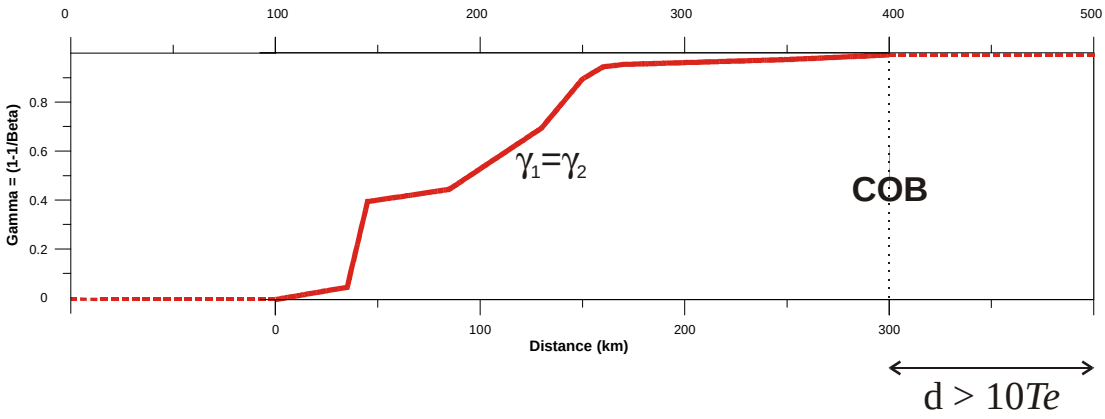

Figure 8.9: Synthetic lithosphere thinning profile of a continental rifted margin, extrapolated in the extremities to be used as a linear load in a Fourier transform.

The flexural isostatic compensations for the crustal and thermal loads are then calculated in the wave domain through equation 5.2:

$$w(k) = \frac{\Delta\rho_1}{\Delta\rho_2}\left[1 + \frac{DK^4}{\Delta\rho_2 g}\right]^{-1} \cdot l(k), \qquad (5.2)$$

The isostatic compensation for each load is then brought back to the space domain through the inverse of their Fourier Transform.

8.6 SUMMARY

A numerical model that calculates total subsidence from thinning profiles was developed to be used in next chapters as a forward model for the numerical inversion. Subsidence is calculated as the sum of the flexural isostatic compensations for the crustal and thermal loads at the age of the margin since continental break-up. The crustal load corresponds to the product between the crustal thickness variation due to thinning by the density contrast between the removed crust and the added mantle. Magmatic addition has an opposing effect to crustal thinning and is subtracted from the crustal thickness variation. Crustal thickness decrease can also be determined for depth-dependent thinning in relation to a detachment depth.

Thermal load arises from the difference in temperature between an initial continental lithosphere and that resulted from lithosphere thinning in the rift phase. Dissipation of the thermal anomaly is calculated using the explicit finite differences method of solution of the heat conservation equation. The reference continental geotherm with radiogenic heat production from the crust is also calculated by explicit finite differences for long thermal equilibrium.

CHAPTER 9

9. THE CONTROL ON INITIAL AND THERMAL SUBSIDENCE BY CONTINENTAL SHIELD GEOTHERM

9.1 INTRODUCTION

Three assumptions of the depth-uniform lithosphere stretching model (McKenzie, 1978), need to be reviewed when considering continental shield lithosphere: 1) that the surface elevation is at sea-level during break-up time; 2) that the continental lithosphere thickness is the same as that of an old oceanic lithosphere, determined by the PSM plate cooling model (Parsons and Sclater, 1977), and 3) that radiogenic heat production from the continental crust can be neglected. These assumptions are invalid for continental lithosphere, especially of shields. Continental shield has thickness of the order of 200 km or more (Jaupart and Mareschal, 1999), elevation of a few hundred meters above sea-level and a geothermal field modified by radiogenic heat production. The purpose of this chapter is to incorporate the control by continental shield geotherm on the total subsidence forward model.

The modifications of the continental lithosphere stretching and thinning model and resulting subsidence seek to guarantee continuity of initial subsidence with oceanic bathymetry across the ocean-continent transition (OCT), as continental lithosphere thinning γ varies from 0 to 1. Initial subsidence of extremely thinned lithosphere at the continent-ocean lithosphere boundary (COLB) must converge with that of the adjacent oceanic elevation. However, some combinations of initial continental lithosphere thickness, crustal thickness, radiogenic heat production from the crust and crustal density result in initial subsidence very different from the mid-

ocean ridge bathymetry. These differences are due to initial elevation at the continent interiors. The hypsometric curve of the Earth shows that elevation is bimodal (figure 9.1). The continents have elevations predominantly between 500 and 0 m, while the oceans bathymetries are predominantly between 4000 and 6000 meters below sea-level.

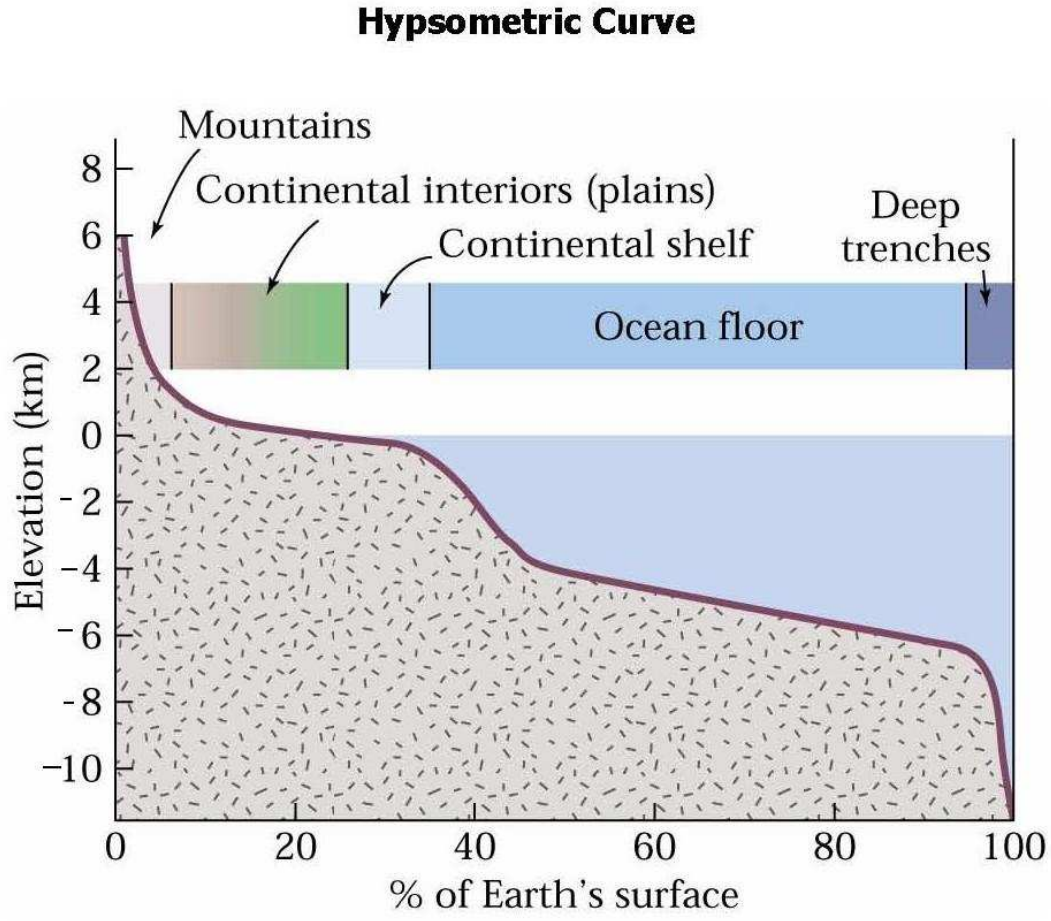

Figure 9.1: Hypsometric curve of the Earth, the cumulative frequency of elevation from (Marshak, 2008).

Continuity of thermal subsidence is also expected from the border of a continental rifted margin where γ=0 towards the continent-ocean lithosphere boundary (COLB), where γ=1. Close to the margin border, the thermal anomaly due to small lithosphere thinning cools down towards the initial continental lithosphere

thickness. However, for extreme lithosphere thinning close to the COLB, the thermal anomaly must cool down to an old oceanic lithosphere thickness instead of to the reference continental lithosphere. Therefore, in this case the lower thermal boundary condition to the lithosphere thermal plate model must be as that for an old oceanic lithosphere.

9.2 The Effect Of Initial Elevation Of Continental Lithosphere In Subsidence Calculations

Infinitely thinned continental lithosphere must be replaced by asthenosphere if magmatic addition is ignored. Therefore initial subsidence should correspond to the asthenosphere geoid h_a, a hypothetical surface below sea-level to which the asthenosphere would rise if it were not confined by the lithosphere (Lachenbruch and Morgan, 1990; Turcotte et al., 1977). The asthenosphere geoid elevation h_a can be estimated through the isostatic balance between a free asthenosphere column and a column composed by average mid-ocean ridge bathymetry h_{MOR}, average oceanic crust t_{oc} on top of an asthenosphere column (figure 9.2):

$$h_a = \frac{h_{MOR}\rho_w + t_{oc}\rho_{oc} - (h_{MOR} + t_{oc})\rho_a}{(\rho_{in} - \rho_a)}, \qquad (9.1)$$

where ρ_{oc} is oceanic crust density, ρ_a is the asthenosphere density and ρ_{in} is the infill material density. The average mid-ocean ridge bathymetry can be interpreted from the empirical relationships between sediment-corrected oceanic bathymetry with age, table 2-2, and varies between 2500 and 2650 m (Crosby and McKenzie, 2009; Parsons and Sclater, 1977; Stein and Stein, 1992). A surface mantle density of 3330 kg m^{-3} corresponds to an asthenosphere density of 3184 kg m^{-3}, allowing for thermal expansion.

Assuming a mid-ocean ridge depth of 2652 m (Crosby and McKenzie, 2009), average oceanic crust thickness of 7080 m (White et al., 1992), crustal density of 2850 kg m^{-3}, asthenosphere density of 3184 kg m^{-3} and water infill with density of 1000 kg m^{-3}, the asthenosphere geoid corresponds to a depth of 3734 m below sea-level. However, in continental areas the free asthenosphere must be assumed as resting under air instead of water, and the infill density is zero. The air-loaded asthenosphere geoid corresponds to a depth of 2563 m below sea-level according to the above parameters. Using different crustal and lithosphere parameters, Turcotte et al (1977) found the water-loaded asthenosphere geoid to be 3.25 km below sea-level, while Lachenbruch & Morgan (1990) calculated a value of 3.5 km below sea-level. Additionally, Lachenbruch and Morgan (1990) found a value of 2.4 km for the air-loaded asthenosphere geoid.

The forward model developed in Chapter 8 to determine subsidence as a function of lithosphere thinning was used to investigate the variation of initial subsidence S_i with lithosphere thickness, crustal thickness, crustal density and radiogenic heat production for $\beta = 1000$ ($\gamma = 0.999$). The models were calculated for combinations of parameters according to their expected ranges, which are listed in table 9-1. Lithosphere thickness were considered from the lowest estimates for old oceans, 90 km (Stein and Stein, 1992) to the largest estimates for continental shields, 325 km (Jaupart and Mareschal, 1999). The continental crustal thickness were varied from a lower limit of 30 km, close to the thickness of 31 km commonly used in geodynamic studies (Karner and Driscoll, 1999; McKenzie, 1978), and 45 km, an upper limit close to the standard deviation of the average continental thickness obtained by (Christensen and Mooney, 1995). The crustal density was varied from the value commonly used in the literature (Hellinger and Sclater, 1983; McKenzie,

1978), 2800 kg m^{-3}, to the density of a mafic crust, 2900 kg m^{-3}. The radiogenic heat contribution was calculated by the exponential decay equation 8.22:

$$A = A_0 \exp(-z/z_r). \quad (8.22)$$

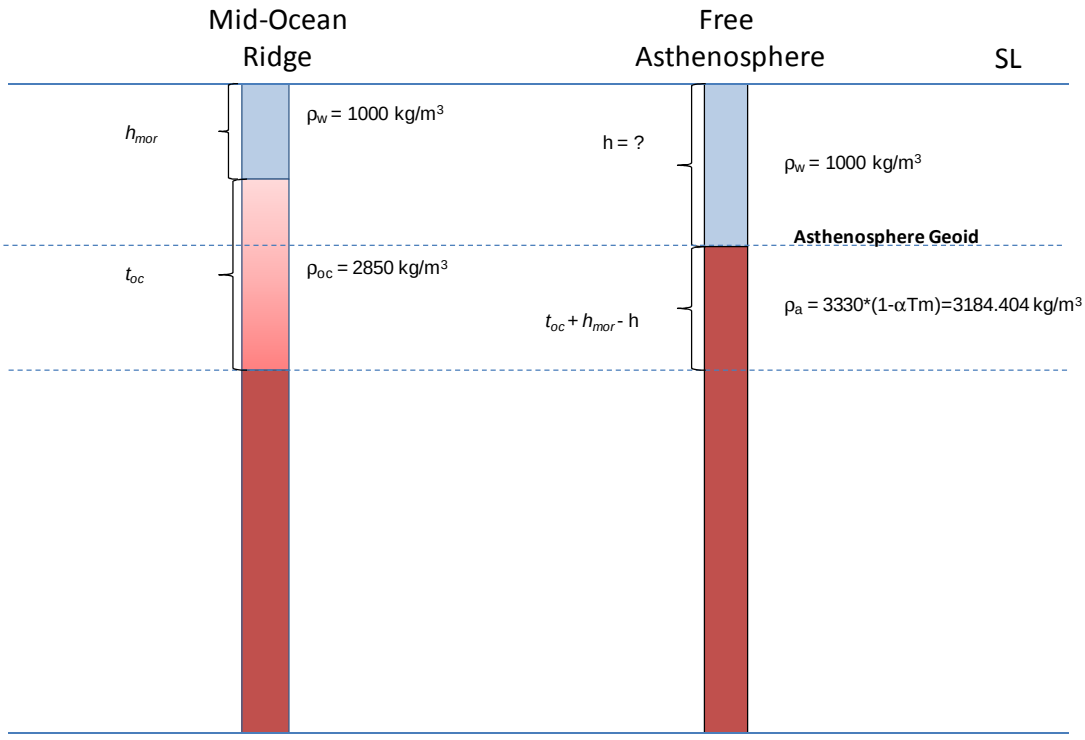

Figure 9.2: Local isostatic equilibrium for the determination of the asthenosphere geoid h.

The surface heat generation per volume, $A_0=\rho_c.H_0$, varied from 0 μW m^{-3}, assumed by the depth-uniform lithosphere stretching model (McKenzie, 1978), to 6.0 μW m^{-3}, which may be considered as an upper bound limit. Radiogenic depth decay constant z_r of 15 km was assumed.

Table 9-1: Critical time steps in seconds and in years for different depth sampling intervals. The selected time steps must be multiple of the thermal subsidence time.

Parameters	**Variation**					
Lithosphere Thickness (km)	90	125	175	225	275	325
Continental Crust Thickness (km)	30		37.5		45	
Continental Crust Density (kg m^{-3})	2800		2850		2900	
Surface Heat Generation per unit volume A_0 (μW m^{-3})	0	2	4		6	

The heat flow calculated at the base of the lithosphere is dependent on the lithosphere thickness and on the radiogenic heat production from the crust and is smaller in continental shields than in oceanic lithosphere. Basal heat flow in the range between 10-15 mW m^{-2} was estimated for the Canadian Shield by correcting the radiogenic heat production from the crust, while a slightly higher value was estimated for the Kaapvaal Craton in South Africa, 17 mW m^{-2} (Jaupart and Mareschal, 1999). The basal heat flow of an old oceanic lithosphere was determined by the plate cooling model as 33 mW m^{-2} (Parsons and Sclater, 1977). These differences of basal heat flow suggest variation in sub-lithospheric mantle convection from oceanic to continental cratonic regions.

In the diagrams of figure 9.3, initial subsidence is plotted downwards against the heat flow at the base of reference continental lithosphere. The basal heat flow is calculated with equation A.1, using the temperature gradient between the two lowermost nodes of the steady state continental geotherm:

$$q = -k \cdot \frac{dT}{dz}. \qquad \text{(A.1)}$$

Initial subsidence increases with smaller initial lithosphere thickness (figure 9.3). Models of cratonic settings with lithosphere thickness between 250 and 350 km are plotted in the range of continental shields heat flow, from 10 to 17 mW m^{-2}, whereas experiments with smaller lithosphere thickness are plotted closer to the old ocean heat flow, 33 mW m^{-2}.

The difference between the water-loaded asthenosphere geoid h_a and the initial subsidence of extremely thinned continental lithosphere $S_i^{\beta=1000}$ is the initial elevation of the continental lithosphere. If initial subsidence is smaller than the water-loaded asthenosphere geoid, it implies in initial elevation below sea-level in

continental areas, with positive sign if subsidence is positive downwards, whereas initial subsidence greater than the water-loaded asthenosphere geoid implies in initial elevation above sea level, with negative sign if subsidence is positive downwards (figure 9.4).

If radiogenic heat production is neglected and the continental crustal density of 2800 kg m^{-3}, usually assumed in the literature , is considered, the model with crustal thickness around 32 km and lithosphere thickness of 125 km results in initial subsidence close to the wet asthenosphere geoid and with basal heat flow similar to old oceans (figure 9.3a), around 33 mW m^{-2}. For this special situation of a platform initially at sea-level, the analytical solution of the depth-uniform stretching model (McKenzie, 1978) can be applied. However, for continental crustal density of 2800 kg m^{-3}, crustal thickness around 32 km and zero radiogenic heat production, the water-loaded initial elevation of shields with lithosphere thickness larger than 200 km should be many kilometres above sea-level (figure 9.4a). As a consequence, some combinations of parameters seem to be highly unrealistic, such as those with lithosphere thickness larger than 200 km and smaller than 100 km with crustal thickness smaller than 38 km (figure 9.4a).

Still ignoring radiogenic heat production but assuming the preferred average continental crust density used in this thesis, 2850 kg m^{-3}, the water-loaded asthenosphere geoid can be modelled with lithosphere thickness of 125 km and crustal thickness around 34 km (figure 9.3b). Increasing crustal density has the effect of decreasing initial subsidence, but models with large lithosphere thickness results in even more unrealistic water-loaded elevation (figure 9.4b). The effect of increasing surface radiogenic heat production A_0 for a fixed crustal thickness is to

produce larger initial subsidence (figure 9.3c), which brings shields models predictions closer to the asthenosphere geoid.

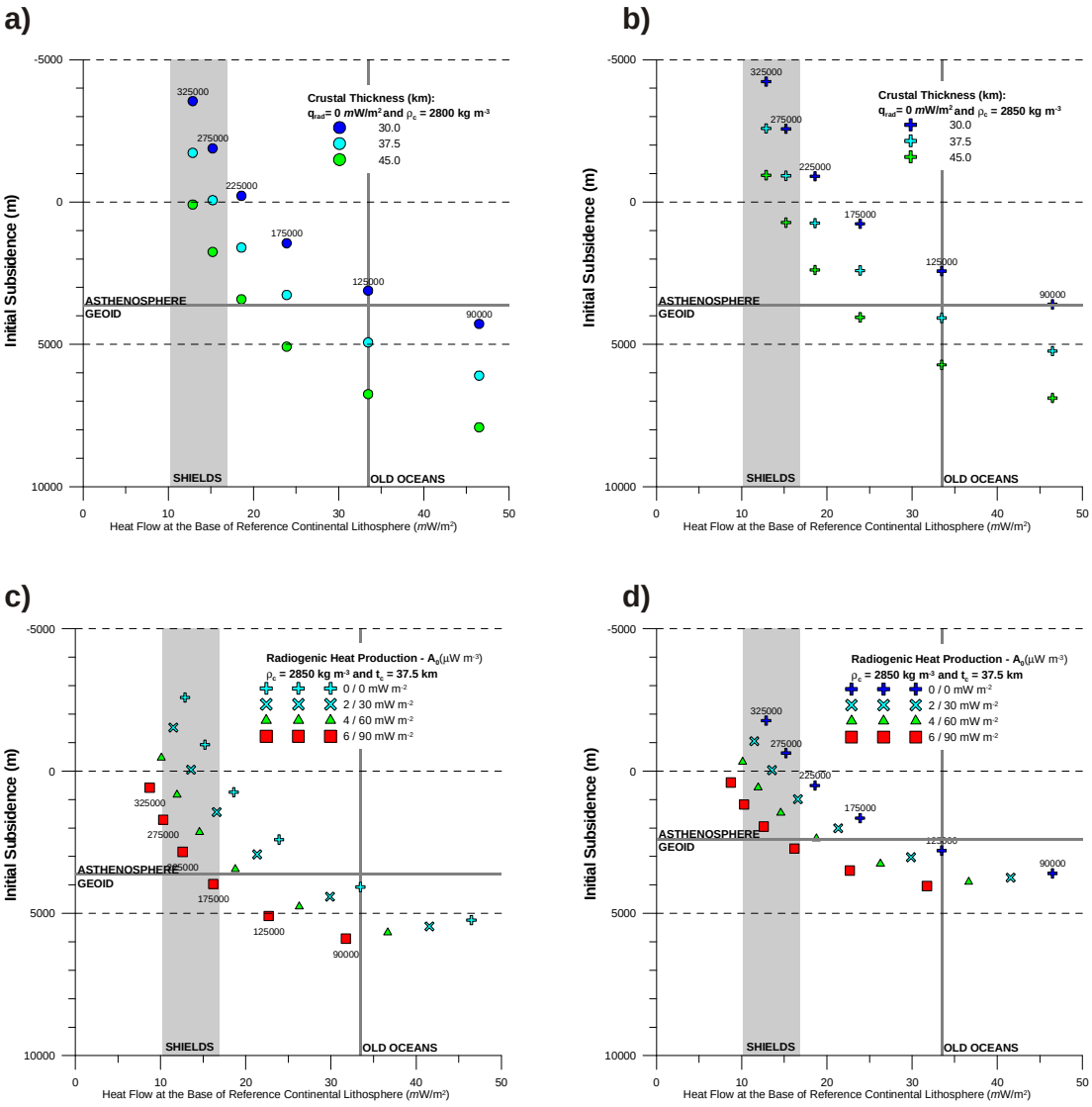

Figure 9.3: Sensitivity of initial subsidence for β=1000 to: a) crustal thickness, water-loaded; b) effect of increasing crustal density, water-loaded; c) surface radiogenic heat production, water-loaded, and d) surface radiogenic heat production, air-loaded.

In order to be compared with real elevation, initial subsidence and initial elevation need to be calculated air-loaded (figures 9.3d and 9.4d). For instance, the water-loaded initial subsidence for continental crustal thickness of 37.5 km, crustal density of 2850 kg m^{-3}, 225 km-thick continental lithosphere and surface radiogenic heat production of 6 μW m^{-3} is 2839 meters (figure 9.3c), whereas the air-loaded

subsidence with these parameters is 1946 m (figure 9.4c). For this same set of parameters, the corresponding water-loaded initial elevation is 897 m below sea-level and the air-loaded elevation is 615 m below sea-level (figures 9.3d and 9.4d).

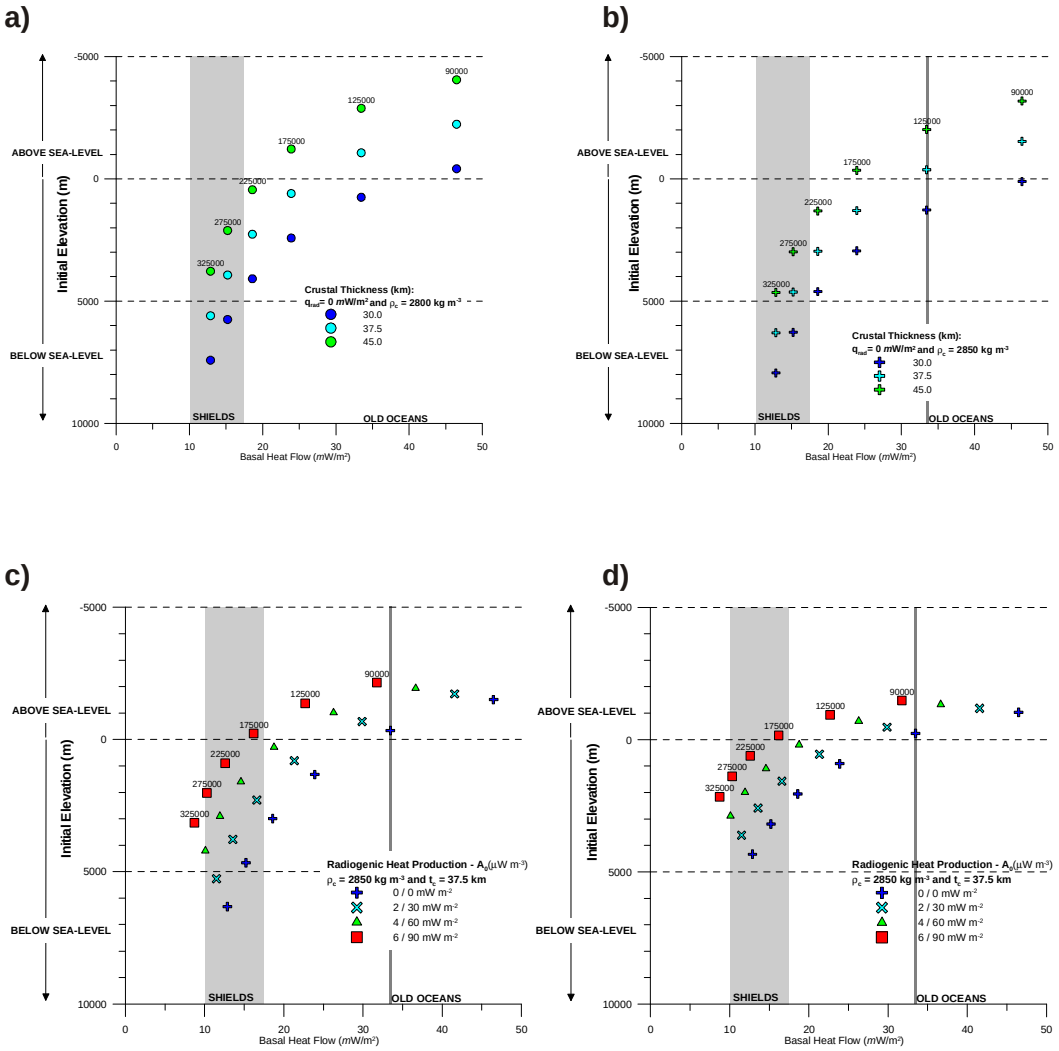

Figure 9.4: Sensitivity of initial elevation to: a) crustal thickness, water-loaded; b) effect of increasing crustal density, water-loaded; c) surface radiogenic heat production, water-loaded, and d) surface radiogenic heat production, air-loaded.

The correction of subsidence for the initial elevation comprises three steps:

1) Initial subsidence S_i^{∞} for extremely thinned reference continental lithosphere ($\beta=\infty$) is computed without magmatic addition. The thermal load L_{th}^{∞} is defined by the temperature difference between the steady state continental lithosphere and the asthenosphere:

$$S_i^{\infty} = \frac{L_{ct} + L_{th}^{\infty}}{\Delta\rho_2}. \quad (9.2)$$

2) The initial subsidence S_i^{∞} for extremely thinned reference continental lithosphere is subtracted from the water-loaded asthenosphere geoid resulting in the water-loaded elevation correction *elw*.

$$elw = h_a - S_i^{\infty} \quad (9.3)$$

3) The water-loaded elevation correction *elw* is then added to the sum of the flexural isostatic response for the crustal and thermal loads, $w_c(x)$ and $w_{th}(x)$ equation 8.27, respectively:

$$S(x) = w_c(x) + w_{th}(x) + elw. \quad (8.27)$$

9.3 The Variation of the Lower Boundary Condition Depth of the Lithosphere Thermal Model Across the Ocean-Continent Transition

The dissipation of a thermal anomaly caused by continental lithosphere thinning or by upwelling of the asthenosphere in the mid-ocean ridge is controlled by a lower boundary condition that limits the plate cooling, which corresponds to the depth of the base of a cold continental or oceanic lithosphere. The thermal anomaly of an oceanic lithosphere dissipates to the depth of an old ocean lithosphere, 125 km, according to the lithosphere plate cooling model (Parsons and Sclater, 1977). Likewise, the thermal anomaly of an extremely thinned continental lithosphere, close to the COLB, is expected to dissipate to the depth of an old ocean lithosphere. However, if the continental lithosphere is thicker than an old oceanic lithosphere, the

thermal anomaly due to small lithosphere thinning will be dissipated to a depth close to the initial continental lithosphere thickness.

In order to keep lithosphere thermal subsidence continuity across an ocean-continent transition (OCT), from unthinned continental lithosphere to oceanic lithosphere, a linear variation of the depth to the lower boundary condition of the lithosphere thermal model with lithosphere thinning (γ=1-1/β) is proposed, as shown in figure 9.5. It is assumed that the depth to the lower thermal boundary condition a_{ref} varies linearly with lithosphere thinning from the depth of the continental lithosphere at the margin border (γ=0), a_c, to the depth of an old oceanic lithosphere at the COLB (γ=1), a_o:

$$a_{ref} = a_c + (a_o - a_c) \cdot \gamma \,. \qquad (9.5),$$

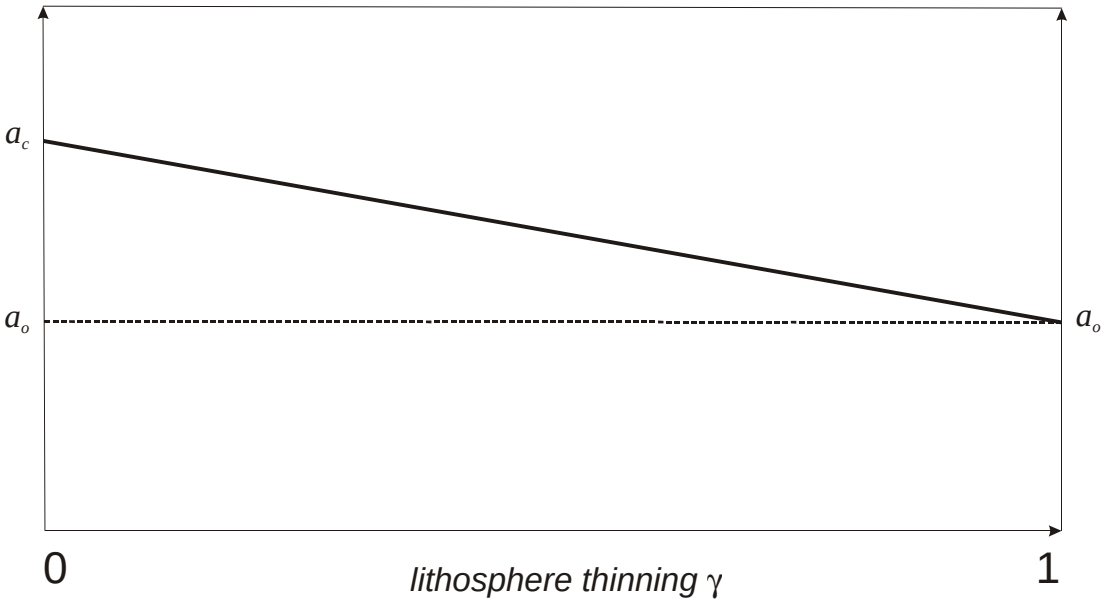

Figure 9.5: Linear variation of the depth to the lower thermal boundary condition with lithosphere thinning (γ=1-1/β).

Diagram 9.6d compares total subsidence as a function of lithosphere thinning applied to a 325 km-thick continental lithosphere, corrected and uncorrected by the variation of the depth to the lithosphere lower thermal boundary. Elevation

correction is not applied. Diagrams 9.6a and 9.6b show the dissipation of the thermal anomaly of an originally 325 km-thick plate due to 100 times thinning (β=100 and γ=0.99). In the uncorrected case (figure 9.6a), the thermal anomaly dissipates towards that of the continental geotherm, while in the corrected case the thermal anomaly dissipates towards that of an old ocean basin lithosphere (figure 9.6b). After 150 Myr, the corrected thermal anomaly is larger than the uncorrected (figure 9.6c), which implies that corrected subsidence is smaller than uncorrected (figure 9.6d and e).

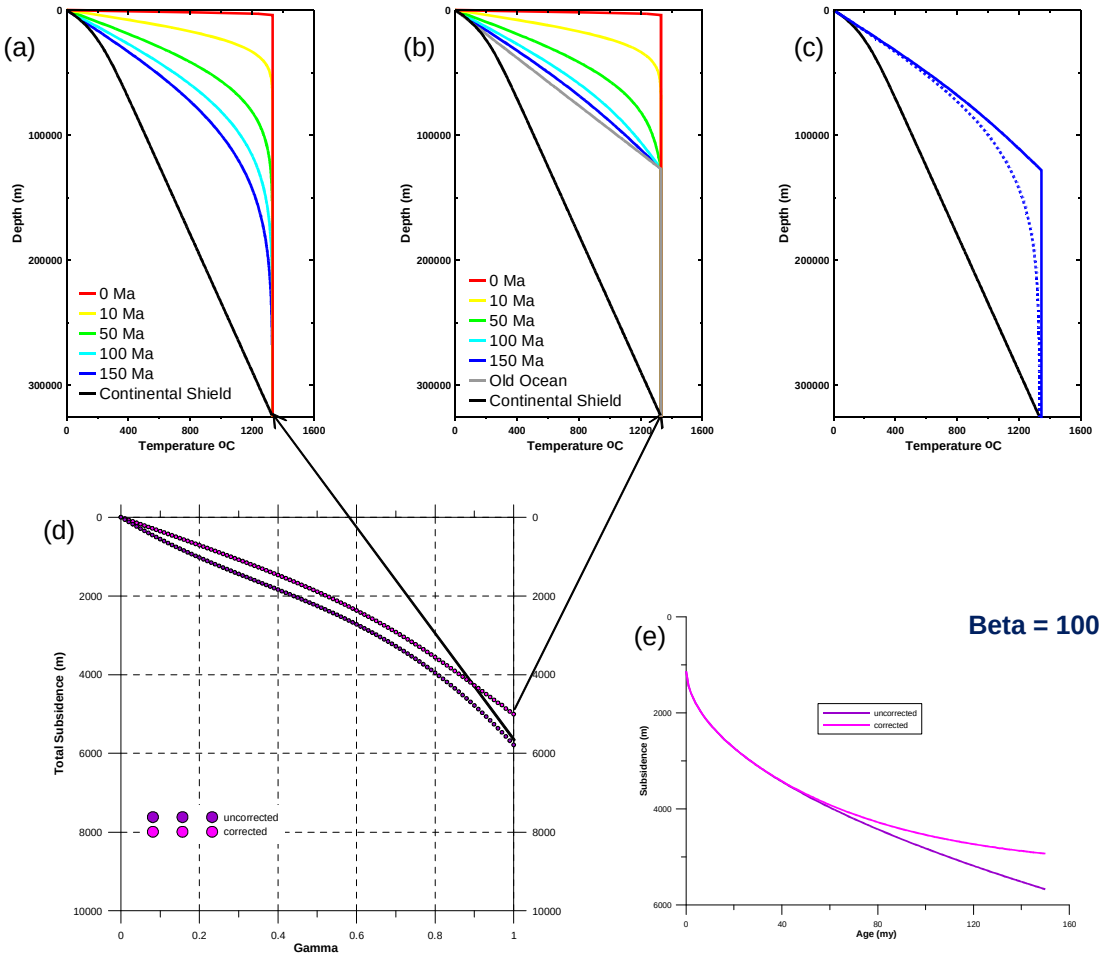

Figure 9.6: Effect of the correction of the lithosphere lower thermal boundary for an initial continental lithosphere 325 km-thick, β=100: a) uncorrected evolution of geotherm from 0 to 150 Myr; b) corrected evolution of geotherm from 0 to 150 Myr; c) comparison of corrected and uncorrected geotherm after 150 Myr, d) total subsidence variation with lithosphere thinning (γ=1-1/β), and e) comparison of corrected and uncorrected subsidence evolution with time.

9.4 CONCLUSIONS

The continental lithosphere is different from that of an old oceanic lithosphere assumed in the analytical solutions of the depth-uniform lithosphere stretching model (McKenzie, 1978). Continental lithosphere is thicker than oceanic lithosphere, with initial elevation above sea-level and radiogenic heat production that modifies the geotherm. In order to keep continuity of lithosphere thermal and subsidence from the border of an unstretched continental margin to the continent-ocean lithosphere boundary (COLB) and adjacent oceanic crust, two modifications were implemented in the forward model to calculate subsidence as function of lithosphere and crustal thinning: 1) a correction for the water-loaded initial elevation and 2) a linear relationship between the lower thermal boundary depth condition for the plate cooling model and the lithosphere thinning.

The correction for the water-loaded initial elevation is determined through the difference between the initial subsidence of an infinitely thinned lithosphere and the water-loaded mantle geoid. This correction is added to the subsidence determined as isostatic compensation for the crustal and thermal load. This correction is sensitive to the radiogenic heat production from the crust and for the lithosphere and crustal thickness. The evaluation of these parameters for the basement of the six Northeastern Brazilian cross-sections is presented in Chapter 11. The model sensitivities to elevation correction indicates that some combinations of crustal and lithosphere parameters imply unrealistic elevations, such as lithosphere thickness larger than 200 km with crustal thickness smaller than 38 km. The lower thermal boundary depth condition for the plate cooling model is assumed as a linear function of the lithosphere thinning factor ($\gamma=1-1/\beta$) from the continental lithosphere depth to the old ocean lithosphere depth.

CHAPTER 10

10. A NEW METHOD FOR THE INVERSION OF LITHOSPHERE THINNING FROM TOTAL SUBSIDENCE PROFILES

10.1 INTRODUCTION

The ocean-continent transition (OCT) can be complex in continental rifted margins and the COB location difficult in particular where the continental crust and continental lithosphere limits may be different (Pickup et al., 1996; Whitmarsh et al., 2001). This problem can be addressed through the comparison of crustal and lithosphere thinning profiles, measured along continental rifted margins. While crustal thinning is determined from gravity inversion, as presented in Chapter 7, lithosphere thinning can be inverted from total subsidence profiles, determined by flexural backstripping of geological cross-sections.

Subsidence profile calculation across a rifted margin resulting from crustal and thermal loads was developed in previous chapters using a numerical method. As the crustal and thermal loads are dependent on continental crustal and lithosphere thinning profiles, subsidence can also be determined as a function of lithosphere thinning. The purpose of this chapter is the development of a numerical method to invert lithosphere thinning from water-loaded subsidence profiles. It is assumed that: 1) sediment loading corrected basement depth corresponds to total subsidence since the rift onset and 2) total subsidence is a consequence of whole lithosphere thinning.

The challenge is to obtain a method that finds the lithosphere thinning profile that generates the observed total subsidence profile. The numerical inversion of lithosphere thinning from water-loaded subsidence uses the Powell's Method for

minimization of a multivariable misfit function. The misfit function to be minimized corresponds to the sum of the squared differences between observed and calculated subsidence plus a term to provide a minimum curvature solution.

10.2 Minimization of a Multivariable Function Using Powell's Method

The Powell's Method performs the minimization of a multidimensional function *f* with *N* variables through a sequence of linear minimizations (Press et al., 2007). Powell's method minimization tries to find selected directions along narrow minimization valleys instead of *N* conjugate directions and does not involve derivatives calculation (Press et al., 2007). The linear minimizations require a one-dimensional minimization sub-algorithm. From an initial point *P(N)*, a generalized coordinate in the N-dimensional variable space, the minimization proceeds along a vector direction using one-dimensional methods, golden section search and parabolic interpolation (Press et al., 2007). From a set of an initial variable directions u_1, u_2, ..., u_n, the minimum of the first direction is initially found, then from there along the second direction to its minimum, cycling through the whole set of directions as many iterations are necessary until the function stops decreasing (Press et al., 2007).

10.3 Thinning Profile Inversion Through Powell's Method

The misfit function $f_m(\gamma(i))$ to be minimized through Powell's Method corresponds to the sum of the squared differences between observed and calculated subsidence:

$$f_m(\gamma(i)) = \sum_{i=1}^{n} [s_{obs}(i) - s_{cal}(\gamma(i))]^2 , \qquad (10.1)$$

where $s_{obs}(i)$ are the i samples of observed total subsidence along a profile and $s_{cal}(\gamma(i))$ is the calculated subsidence at each point i, corresponding to lithosphere thinning $\gamma(i)$. The aim of the minimization is to achieve the smallest value as possible of this misfit function between observed and calculated subsidence profiles. The misfit function variables were considered as discrete values of $\gamma(i)$, equally spaced along the profile. Powell's Method minimization starts with an initial point $P(\gamma_i)$ defined by a set of initial variables, which is an initial guess about the lithosphere thinning $\gamma(i)$ profile. In this thesis, the $\gamma(i)$ parameters were initialized with lithosphere thinning factor of 1.0.

In order to provide controlled smoothing for the thinning profiles, a minimum curvature term was added to the misfit function. The additional term corresponds to the second partial derivative of the lithosphere thinning profile:

$$f_\gamma = \lambda \sum_{i=1}^{n-1} \left(\frac{\gamma_{i+1} + \gamma_{i-1} - 2\gamma_i}{\Delta x^2} \right)^2 . \qquad (10.2)$$

This term is multiplied by a smoothing factor λ to bring the lithosphere thinning second derivative term to the same order of magnitude as the sum of the squared differences between observed and calculated subsidence. Therefore, the target function becomes the sum of a measure of the observed and calculated subsidence misfit and a measure of the inverted lithosphere thinning profile curvature:

$$f = f_m + f_\gamma = \sum_{i=1}^{n} \left[s_{obs}(i) - s_{cal}(\gamma(i)) \right]^2 + \lambda \sum_{i=1}^{n-1} \left(\frac{\gamma_{i+1} + \gamma_{i-1} - 2\gamma_i}{\Delta x^2} \right)^2 \qquad (10.3)$$

Table 10-1: Parameters used in the synthetic forward model.

Layer	***Parameters***	***Symbols and units***	
Water	*density*	ρ_w *(kg* m^{-3}*)*	*1000*
Mantle	*density*	ρ_0 *(kg* m^{-3}*)*	*3330*
	heat capacity	*Cp (J* kg^{-1} C^{-1}*)*	*1171.52*
	thermal conductivity	*Km (W* m^{-1} K^{-1}*)*	*3.138*
	old oceanic lithosphere thickness	*a (km)*	*125*
	basal temperature	*Tm (*^oC*)*	*1333*
	thermal expansion coefficient	α *(*$^oC^{-1}$*)*	*3.28E-05*
Crust	*density*	ρ_c *(kg* m^{-3}*)*	*2850*
	thickness	t_c *(km)*	*35.959*
Lithosphere	*thermal subsidence time*	*Ma*	*150*
	effective elastic thickness	*Te (km)*	*5*

The effects of data sampling interval, smoothing factor and effective elastic thickness were investigated with a synthetic example (figure 10.1). The results and sensitivities using *Te*=0 and *Te*=5 km are shown in figure 10.2. In these sensitivity tests, the synthetic subsidence profiles were calculated from a synthetic continental thinning profile using the forward numerical method developed in chapters 8 and 9 with lithosphere parameters presented in Table 10-1. The crustal thickness of 35.959 km, corresponds to a crust with density of 2850 kg m^{-3} in a continental lithosphere 125-km thick, with top surface initially at sea-level (0 meter elevation). The synthetic continental lithosphere thinning profile starts onshore and then slowly increases representing a shallow platform up to 40 km (figure 10.1a). This segment is followed by a sharp increase in lithosphere thinning between 40 and 50 km that represents a hinge line. Then, the ocean-continent transition develops from 50 to 150 km with increasing lithosphere thinning, until the continent-ocean boundary is reached with thinning factor of 0.95 at approximately 150 km.

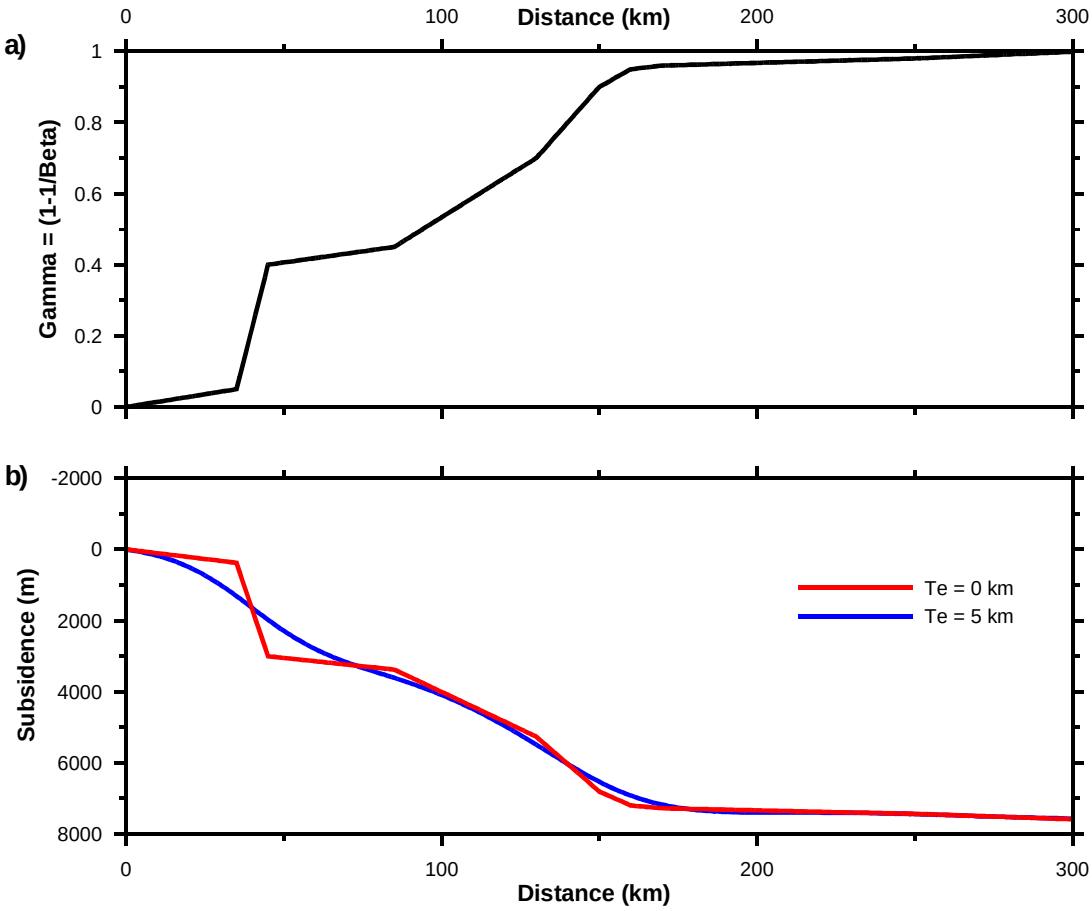

Figure 10.1: a) Synthetic profile of lithosphere thinning (*γ*) across a continental rifted margin, from the continental border (γ=0) to the COB (γ=1). b) Total subsidence profiles calculated with the gamma profile in a) with effective elastic thickness of Te = 0 km and Te = 5 km.

The inversions of the synthetic example with *Te* = 0 km resulted in perfect recovery of continental lithosphere thinning (γ) profile and subsidence for a sample interval (dx) of 1 km (original), 5 km and 10 km (figure 10.2a). The inversions took less than 1 minute with less than 11 iterations and the misfits were less than 27 meters (table 10-2).

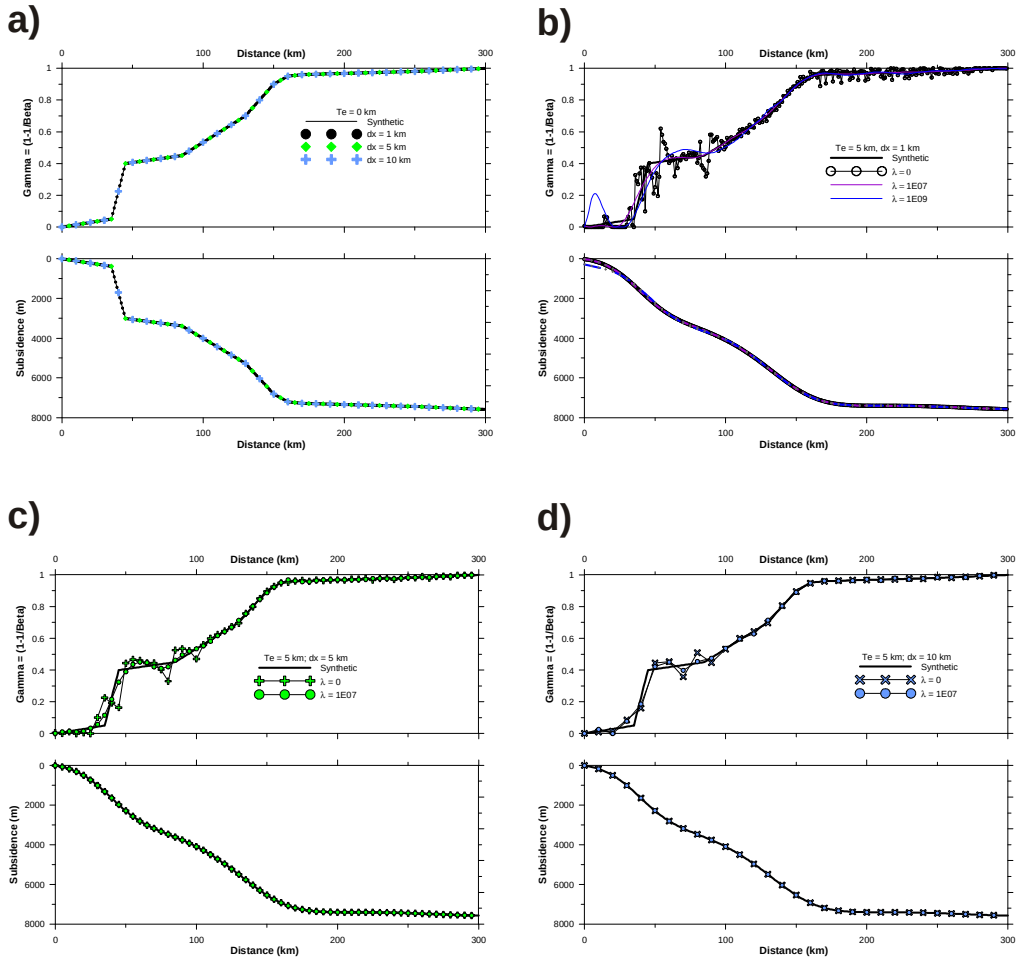

Figure 10.2: Sensitivities of the synthetic model to effective elastic thickness *Te* and interval sampling dx: a) *Te* = 0 km and dx = 1, 5 and 10 km; b) *Te* = 5 km, dx = 1 km, c) *Te* = 5 km, dx = 5 km, and d) *Te* = 5 km, dx = 10 km.

For lithosphere elastic thickness *Te* = 5 km and original sampling interval of 1 km, a noisy gamma profile is produced by inversion after 40 minutes of computation, which generates a perfect fit of observed and calculated subsidence (figure 10.2b). Sampling the function at intervals larger than the original spacing provides a smoother solution, which may better represent the predominantly ductile deformation of the lithosphere. For the same *Te* = 5 km, the inversions with 5 and 10 km sampling intervals resulted in smaller misfit, in less computation time (table 10-2), but still with noisy lithosphere thinning results (figure 10c-d). The inversion generates high frequency noise when finite lithosphere flexural strength is considered. This result is expected because high frequencies are filtered when a

subsidence profile is calculated using flexural isostatic response. Then, a numerical inversion of a subsidence profile calculated using flexural isostatic response has an opposing effect of the flexural backstripping, returning high frequencies.

Table 10-2: Parameters and results of the models calculated with the synthetic profiles, shown in figure 10.2.

Te (km)	Dx (km)	Nf*	λ	Misfit	iterations	Time (min)
0	1	512	0	26.92	11	2
0	5	128	0	0.02	8	1
0	10	64	0	0.00	8	1
5	1	512	0	603.78	288	43
5	5	128	0	128.13	169	2
5	10	64	0	29.78	90	1
5	1	512	10^7	1046.80	140	18
5	5	128	10^7	1123.86	117	2
5	10	64	10^7	155.67	83	1

* Number of samples for the Fourier transform.

A smoothing factor of 10^7 provides effective smoothing for the synthetic inversion examples, but it must vary depending on the value of the elastic thickness and the geometry of the subsidence profile. The inversions using a smoothing factor $\lambda = 10^7$ for lateral sampling interval of 1, 5 and 10 km resulted in gamma profiles very close to the synthetic original (figures 10.2c-d) with computational time decreasing with increasing sampling interval (table 10-2). However, excessive smoothing generates artefacts in the proximal parts of the profiles, especially with small sampling intervals. The application of a smoothing factor of 10^9 with a 1-km sampling interval resulted in an unrealistic high frequency "hump" in the proximal thinning profile (figure 10.2b).

10.4 SUMMARY

The inversion of lithosphere thinning from total subsidence profiles used the Powell's Method, a multidimensional minimization. The minimized misfit function

corresponds to the sum of the squared differences between observed and calculated subsidence in function of lithosphere thinning (γ). Total subsidence is calculated for the time after break-up using a forward numerical model developed and described in chapters 8 and 9. A minimum curvature term of the lithosphere thinning profile was added to the misfit function in order to smooth the inverted lithosphere thinning profile. The main inversion parameters are the discrete lateral sampling interval distance of the observed subsidence and the smoothing factor. The analysis of a synthetic example showed that the numerical inversion can be very fast if elastic thickness is not considered. The inversion of lithosphere thinning generates high frequency noise when flexural isostasy is considered. Observed subsidence sampling of 5 or 10 km decrease the computational time and provide some smoothing, reproducing the lateral distribution of ductile lithosphere thinning.

CHAPTER 11

11. OCT LITHOSPHERE THINNING FROM SUBSIDENCE INVERSION FOR THE NORTHEAST BRAZILIAN RIFTED MARGIN

11.1 INTRODUCTION

This chapter presents the results of the subsidence inversion to produce lithosphere thinning for the six cross-sections of the Northeast Brazilian rifted margin. The continent-ocean lithosphere boundaries (COLB) are located where lithosphere thinning (γ_l) reaches 1. The lithosphere thinning reaches 1 where the total subsidence depth reaches the sediment-corrected bathymetry of the adjacent oceanic crust. The crustal and lithosphere parameters selected for the subsidence calculations and the numerical inversion parameters are initially discussed. The variation of lithosphere thickness with elevation has been investigated through sensitivity analysis, as well as the effects of the numerical inversion parameters, the smoothing factor (λ) and the lateral sampling interval (dx).

11.2 CONTINENTAL LITHOSPHERE PARAMETERS USED IN THE SUBSIDENCE ANALYSIS

The lithospheric mantle parameters assumed and derived by the plate cooling model (Parsons and Sclater, 1977) were applied in the subsidence calculations (table 11-1). The average global crustal density of 2850 kgm^{-3} (Carlson and Herrick, 1990; Christensen and Mooney, 1995) was assumed for the lithosphere thinning inversion, as it was for the gravity inversion (table 11-1). A break-up age of 115 Ma was used, which corresponds to the age of onset of thermal subsidence in Northeast Brazilian

rifted margin. Changing the thermal subsidence duration to the rift climax age, around 124 Ma, or to the end of the brittle tectonics in the region, around 112 Ma, would only cause minor changes in total subsidence. An effective elastic thickness *Te* of 3 km, used to define the lithosphere flexural strength in the determination of the water-loaded subsidence profiles through flexural backstripping, chapter 5, was also applied in the forward total subsidence calculation used in the numerical inversion of the lithosphere thinning.

Table 11-1: Parameters used in the numerical modelling.

	Parameters	*Symbols and units*	
Water	*density*	ρ_w *(kg* m^{-3}*)*	*1000*
Mantle	*density*	ρ_0 *(kg* m^{-3}*)*	*3330*
	heat capacity	*Cp (J* kg^{-1} C^{-1}*)*	*1171.52*
	thermal conductivity	*Km (W* m^{-1} K^{-1}*)*	*3.138*
	old oceanic lithosphere thickness	*a (km)*	*125*
	basal temperature	*Tm (*^oC*)*	*1333*
	thermal expansion coefficient	α *(*$^oC^{-1}$*)*	*3.28E-05*
Crust	*density*	ρ_c *(kg* m^{-3}*)*	*2850*
	thickness[1]	t_c *(km)*	*38-39*
	thermal subsidence time	*Ma*	*115*
	effective elastic thickness[2]	*Te(km)*	*3*

1: from gravity inversion. 2: same as used in flexural backstripping.

Some parameters are different for each margin sector sampled by the cross-sections. Gravity inversion suggested that the initial crustal thickness varies along the margin between 38 and 39 km (table 11-2). Moreover, the maximum magmatic addition predicted by the residual depth anomaly analysis also varies and has implication for the subsidence prediction. The initial continental lithosphere thickness depends on combinations of initial elevation and radiogenic heat production (figure 9.4) through isostatic balance. As a consequence, lithosphere thickness can be constrained by combinations of air-loaded initial elevation and radiogenic heat production data for the area.

Table 11-2: Crustal and lithosphere parameters applied in the lithosphere thinning inversions of the selected cross-sections.

Profile	a (km)	T_c (km)[1]	A_0 (μW m^{-3})	M_{ma} (km)[2]	γ_c
ALM-JEQ	152	39.0	1.0	4.6	0.79
JAC	152	39.0	1.0	7.1	0.75
SES	148	38.0	1.5	8.3	0.72
SEN	144	38.0	1.0	8.3	0.70
ALN	152	39.0	2.0	7.1	0.75
PEP	159	39.0	2.0	8.3	0.75
USM[3]	125	35.959	0.	0.0	1.0

1- Determined by gravity inversion; 2 - Determined by RDA analysis; 3 - Parameters of the McKenzie (1978) model

11.2.1 Surface Radiogenic Heat Production In Northeast Brazilian Rifted Margin

Surface radiogenic heat production A_0 has been determined for the Northeast Brazilian Rifted margin basement from aeroradiometric Th, U and K concentrations data between Jacuípe and Alagoas (ENCAL S/A, 1978), and from rock sampling measurements between Jequitinhonha and Recôncavo (Sapucaia et al., 2005). The surface radiogenic heat production map calculated with aeroradiometric data of the *Baixo São Francisco* Project for the Brazilian Geological Survey (CPRM – *Companhia de Pesquisa de Recursos Minerais*) presents a clear correlation with the geological provinces (figure 11.1). Surface radiogenic heat production was calculated from the Th, U and K concentrations with the (Rybach, 1986) formula, using average rock density of 2700 kg.m^{-3} (Hamsi et al., 2004).

The Pernambuco-Alagoas massif shows a high surface heat production A_0 due to its granitic composition, while the lowest values occur in the metasediments of the Sergipano fold belt. The high grade metamorphic rocks of São Francisco craton to the south present intermediary values (figure 11.1). Surface heat production has a great effect on surface heat flow, explaining its high frequency variability in the

North American craton (Mareschal and Jaupart, 2004). However, the relationship between surface and basal lithosphere heat flow must be averaged in wavelengths greater than 500 km (Mareschal and Jaupart, 2004). Therefore, average surface heat production was interpreted for each tectonic province sampled by the cross-sections

In the Pernambuco-Alagoas massif, the basement of the two northernmost cross-sections, the surface radiogenic heat is larger than 1.5 μWm^{-3} and reaches locally 6.0 μWm^{-3}. An average surface radiogenic heat of 2.0 μWm^{-3} was interpreted for this area (figure 11.1 and table 11-2). The medium grade metasediments of the northern segment of the Sergipano fold belt, the basement of Sergipe-North cross-section, show an average surface heat contribution of 1.0 μWm^{-3}. The basement of the Sergipe-South cross-section, composed by low grade metasediments of the southern Sergipano fold belt, has surface radiogenic heat of around 1.5 μWm^{-3}. To the south, the basement of Jacuípe in the São Francisco Craton has an average surface heat production of 1.0 μWm^{-3}.

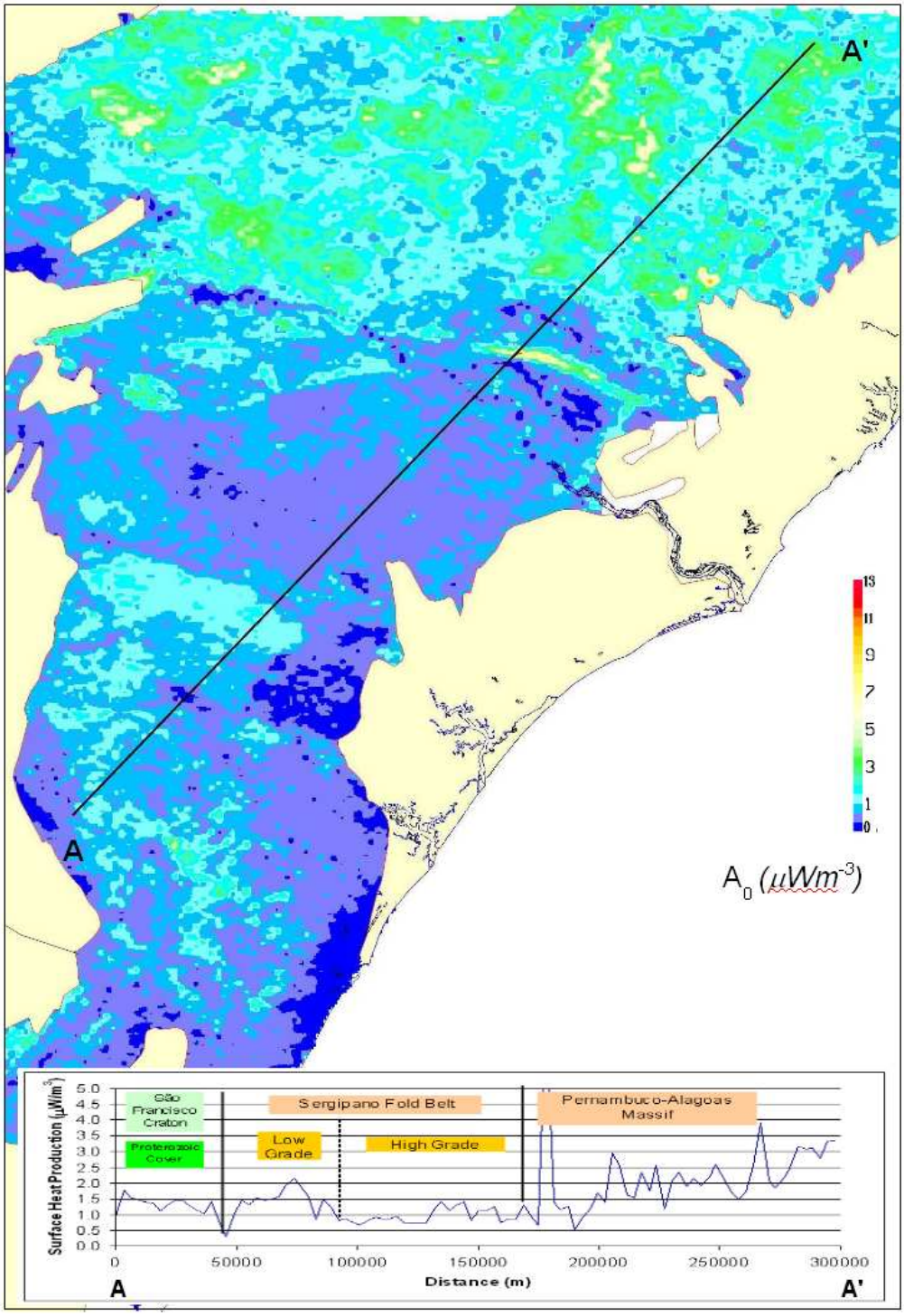

Figure 11.1: Radiogenic surface heat production map of Jacuípe, Sergipe and Alagoas basement, calculated from U, Th and K concentrations of the *Projeto Baixo São Francisco* aeroradiometric survey (ENCAL S/A, 1978).

Surface radiogenic heat measured in the São Francisco Craton basement rocks, sampled between Jequitinhonha and Recôncavo (Sapucaia et al., 2005), ranges

from 0.01 to 6.0 μWm^{-3}, with highest value of 11.0 μWm^{-3} (figure 11.2b). The measurements present a log-normal distribution with highest contribution from the classes of less than 2.0 μW m^{-3}. The largest values come from granitic rocks enriched in radioactive elements (figure 11.2a). An average surface heat contribution of 1.0 μWm^{-3} was also interpreted for this area (table 11-2), which is the basement of Almada-Jequitinhonha cross-section.

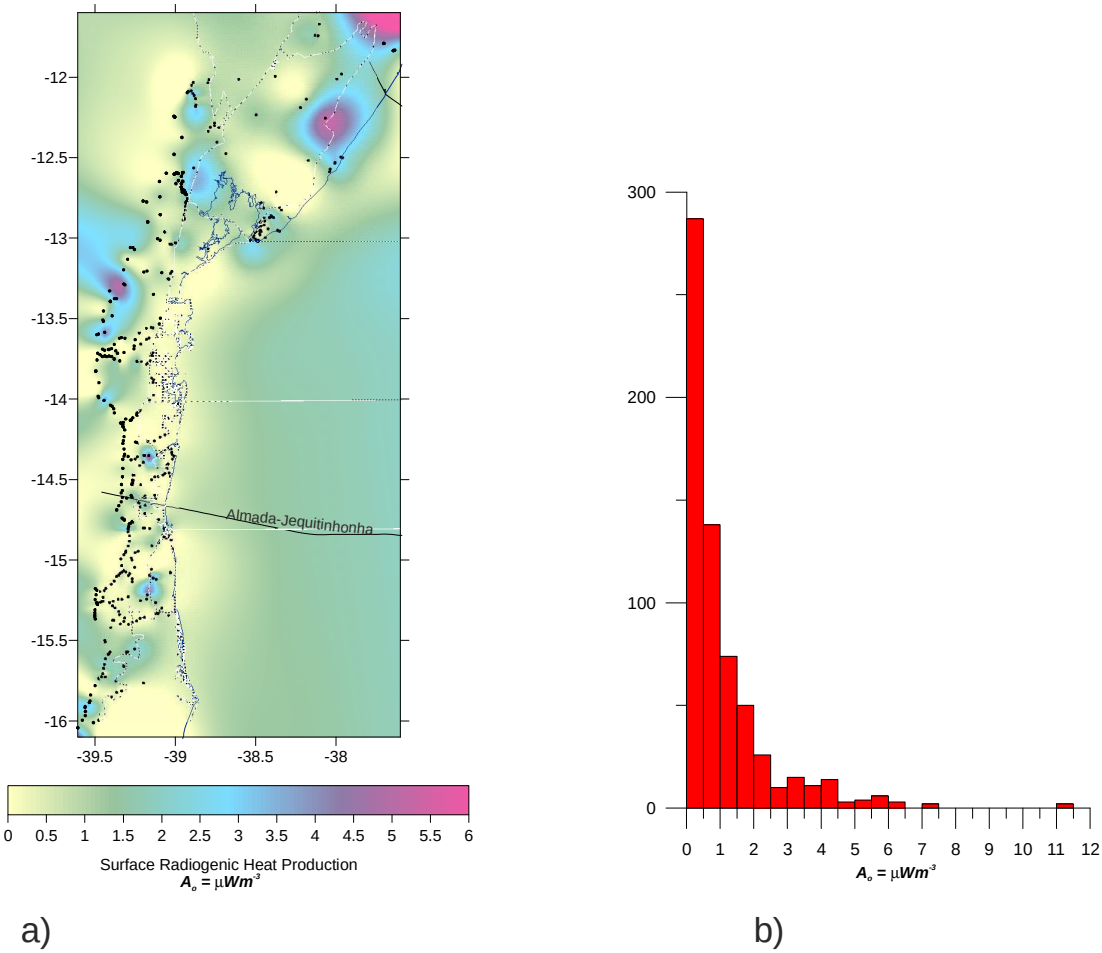

a) b)

Figure 11.2: Surface radiogenic heat A_0 based on measurements of U, Th and K concentrations in rock samples of the basement of Jequitinhonha, Almada, Camamu and Recôncavo basins carried out in the GEOTERM project (Sapucaia et al., 2005). a) Map and b) Frequency histogram.

11.2.2 Lithosphere Thickness Constrained by Air-Loaded Initial Elevation

The numerical code developed in chapters 8 and 9 to determine subsidence as a function of lithosphere thinning was used to investigate the variation of initial air-loaded elevation with lithosphere thickness, for the crustal thickness and radiogenic heat production determined for each cross-section (figure 11.3). The radiogenic heat contribution was calculated through the integral of the exponential decay equation 7.24:

$$\int_0^{\infty} A_0 \exp(-z/z_r)dz = A_0 \cdot z_r \qquad (8.24)$$

The same radiogenic depth decay z_r of 15 km, which corresponds to an average upper crust thickness, was assumed for all cross-sections.

Isostatic equilibrium with the asthenosphere geoid implies that, for each combination of radiogenic heat production and crustal thickness, the range of initial air-loaded elevation compatible with continental interiors, between 0 and 500 m, corresponds to a range of lithosphere thickness (figure 11.3). As an example, for the Almada-Jequitinhonha set of parameters, lithosphere thickness can vary from 128 km to 152 km, corresponding to 0 to 500 m elevation (figure 11.3). The Almada-Jequitinhonha and Jacuípe air-loaded initial elevations did not plot with basal heat flow of continental shields, either because the radiogenic heat was underestimated by the exponential decay model assumed or because this region is in a border of a continental shield.

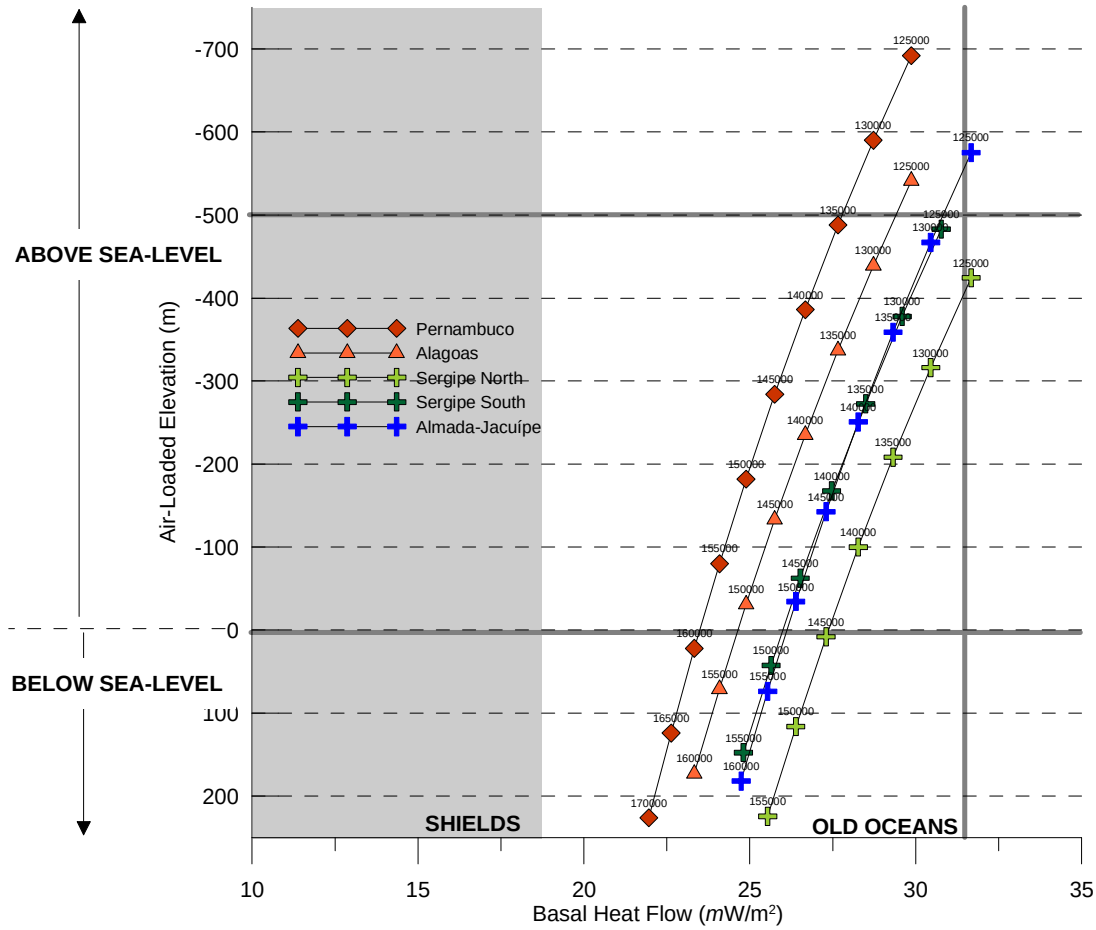

Figure 11.3: Relationship between air-loaded initial elevation and basal heat flow for combination of crustal thickness and radiogenic heat production of each cross-section, based on isostatic equilibrium with the air-loaded asthenosphere geoid. For each cross-section, air-loaded elevation varies with lithosphere thickness, labelled above the symbols.

11.3 Sensitivities Tests for Almada-Jequitinhonha Cross-Section

The Almada-Jequitinhonha cross-section was selected for sensitivity tests to the lithosphere thinning inversion parameters: smoothing factor (λ) and lateral sampling interval (dx). Sensitivity tests were also run for lithosphere thickness and magmatic addition. The Almada-Jequitinhonha cross-section was selected for the sensitivity tests because its interpretation is the most unequivocal and because it is the least affected by magmatic rock bodies. The sensitivity tests for smoothing factor, lateral sampling interval and magmatic addition were performed considering

lithosphere thickness of 152 km, which corresponds to zero initial elevation for the assumed crustal thickness and density. A maximum magmatic addition of 4.6 km, evaluated from the RDA analysis (Chapter 6), was used for the smoothing factor, lateral sampling interval and lithosphere thickness sensitivities tests. In the sensitivity tests (figures 11.4 and 11.6 to 11.8), lithosphere thinning profiles are shown at the top and subsidence profiles are shown at the bottom.

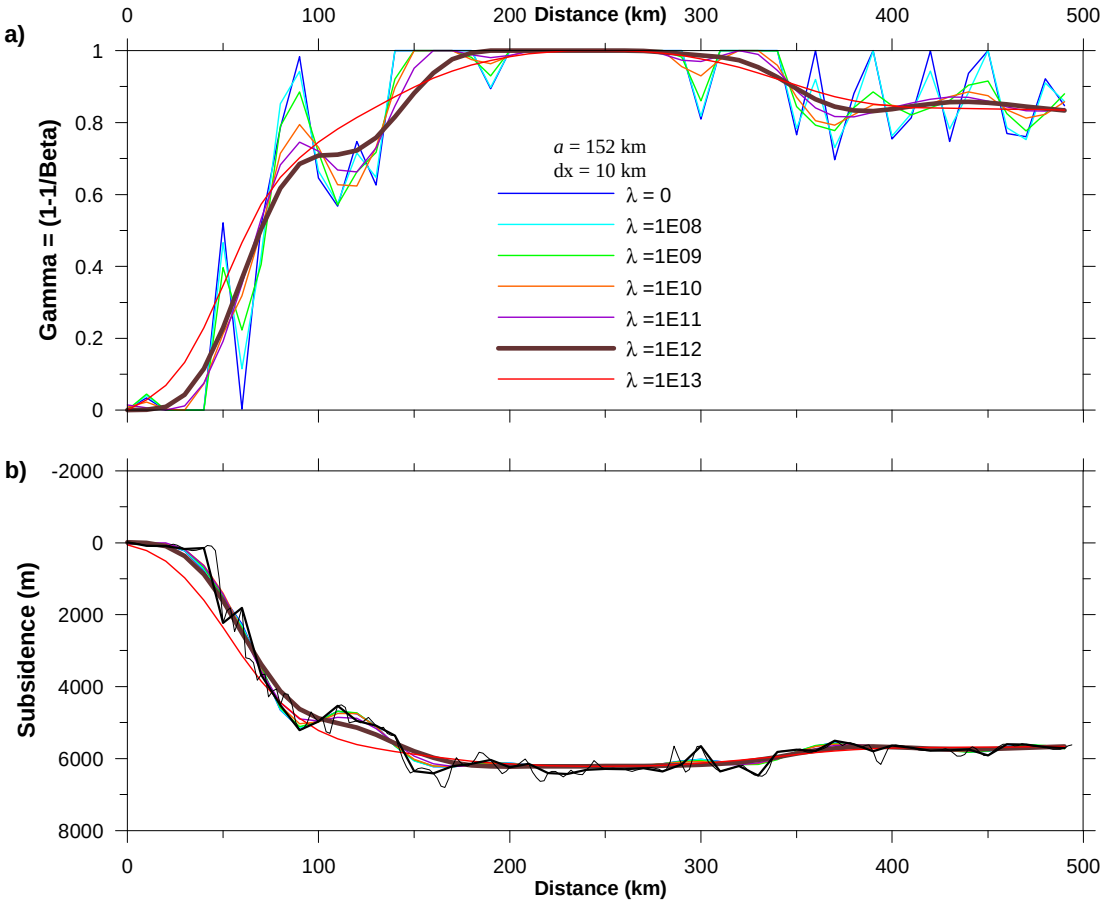

Figure 11.4: Sensitivity tests for smoothing factor (λ) applied to Almada-Jequitinhonha cross-section, using interval sampling distance of 10 km and lithosphere thickness of 152 km: a) lithosphere thinning profiles, b) subsidence profiles, in black the observed total subsidence.

SENSITIVITY TESTS TO THE SMOOTHING FACTOR (λ)

The sensitivity to smoothing factors (λ) 0, 1, 10^7, 10^8, 10^9, 10^{10}, 10^{11}, 10^{12} and 10^{13} was performed with horizontal sampling at each 10 km (figure 11.4). There is practically no difference among the inversions run with smoothing factor λ from 0

to 10^7, because the smoothing factor term of equation 10.3 is too low compared to the misfit term.

$$f = \sum_{i=1}^{n} [s_{obs}(i) - s_{cal}(\gamma(i))]^2 + \lambda \sum_{i=1}^{n-1} \left(\frac{\gamma_{i+1} + \gamma_{i-1} - 2\gamma_i}{\Delta x^2} \right)^2 \qquad (10.3)$$

The selection of the smoothing factor is subjective. The inversion with smoothing factor of 10^{12} was preferred for the Almada-Jequitinhonha cross-section, providing a reasonable smoothing, while still keeping geological information (figure 11.4a). Inversions with smaller smoothing factor result in spiky thinning profiles. A smoothing factor too large may overcome the lithosphere thinning term, hiding the lithosphere structure information. The inversion with smoothing factor of $\lambda=10^{13}$, although still reasonable, did not result in a good fit of the observed subsidence (figure 11.4b). The best smoothing factor generally is around the inflection of the misfit function, where the smoothing component in equation 10.3 reaches the same order of magnitude as the subsidence misfit term (figure 11.5). It was not possible to find numerical criteria to select the best λ. The smoothing factor of $\lambda=10^{12}$ was considered the most appropriate for all cross-sections, Appendix II.

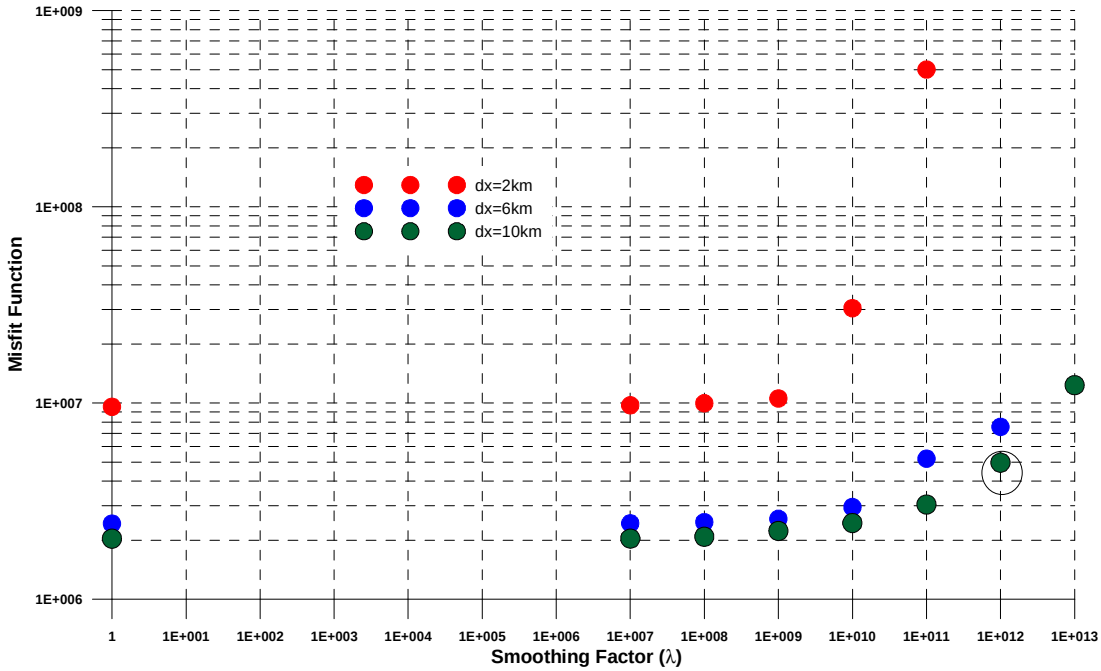

Figure 11.5: Plot of misfit function *f* against smoothing factor λ for the inversion of the lithosphere thinning of Almada-Jequitinhonha cross-section using lateral sampling distance dx of 2, 6 and 10 km. The inversions with dx = 6 km and λ greater than 10^{13} and with dx = 10 km and λ greter than 10^{11} took very long time and resulted in over-smoothed profiles.

SENSITIVITY TESTS TO LATERAL SAMPLING (DX)

Sensitivity tests to horizontal sampling results are shown in figures 11.5 and 11.6. The selected smoothing factor using 10-km of lateral sampling is $\lambda=10^{12}$. The inversion with lateral sampling at each 6-km using the same smoothing factor results in similar good fit of subsidence profiles beyond 50 km of distance. However, unrealistic thinning factor and poor subsidence fit are observed between 0 and 50 km. For sampling at each 2 km, even lesser smoothing factor, $\lambda=10^{10}$, results in this type of distortion (figure 11.6). This distortion at distances less than 50 km seems to be a characteristic of the minimum curvature approach if flexural isostasy is considered, especially when high frequencies subsidence is sampled. Therefore, the simulations for all cross-sections were run with water-loaded subsidence sampled at each 10 km.

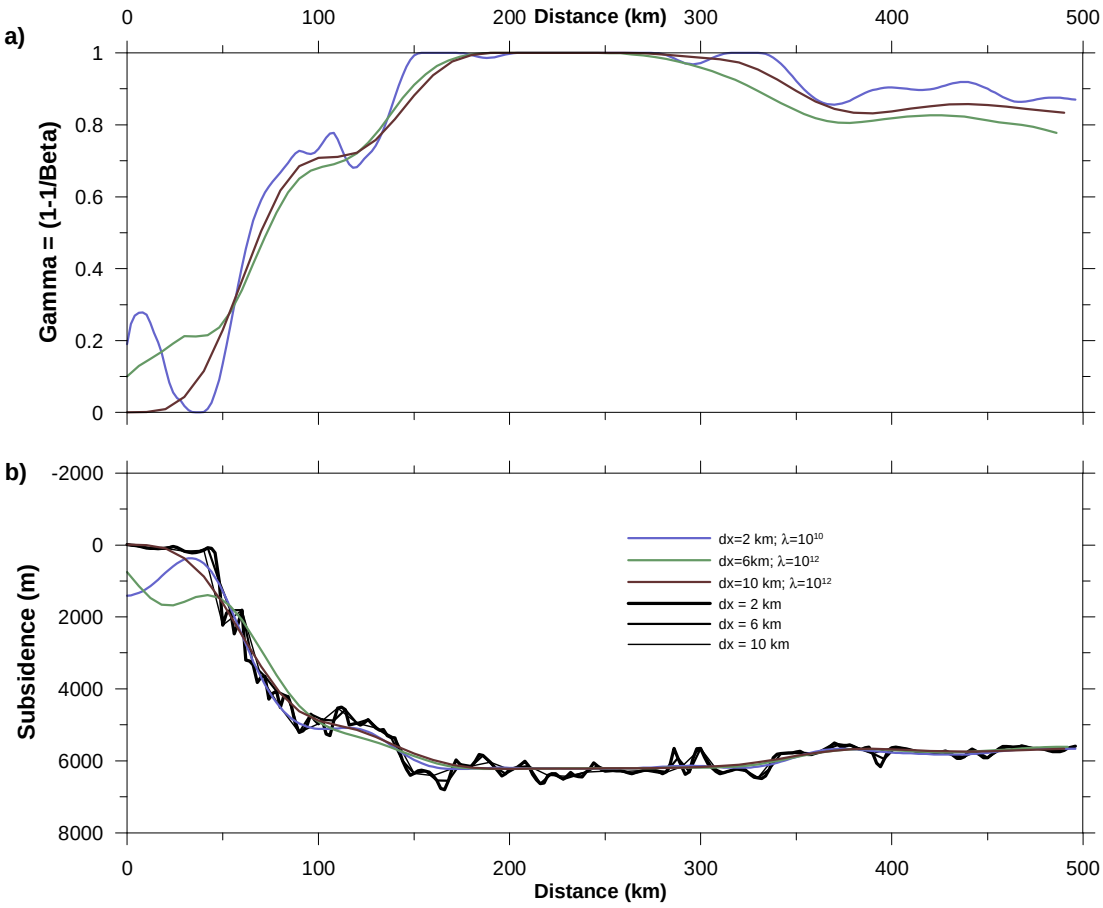

Figure 11.6: Sensitivity tests for lateral sampling distance (dx) applied to Almada-Jequitinhonha cross-section, using lithosphere thickness of 152 km: a) lithosphere thinning profiles, b) subsidence profiles, in black the observed total subsidence. The same colours were used for the thinning profiles in a) and for the calculated subsidence in b). Black lines on the lower diagram correspond to different sampling of the observed subsidence.

SENSITIVITY TESTS TO LITHOSPHERE THICKNESS (A)

Sensitivity of the lithosphere thinning inversion to the lithosphere thickness was performed considering the range of continental interior elevation: 0, 100, 200, 300, 400 and 500 m (figure 11.7). For the crustal thickness and surface radiogenic heat obtained for Almada-Jequitinhonha region (table 11-2), these elevations correspond respectively to lithosphere thickness of 152, 147, 142, 138, 133 and 128 km (figure 11.3). The parameters of equation 8.5 that relates critical gamma to maximum magmatic addition were obtained for each lithosphere thickness (table 11-3).

$$\gamma_{crit} = a_1 * t_{oc} + a_2, \quad (8.5)$$

Table 11-3: Parameters to determine the critical gamma for magmatic addition (equation 8.5) for the lithosphere thickness of Almada Jequitinhonha region corresponding to the range of continental elevation.

Air-Loaded Elevation (m)	Lithosphere Thickness (km)	a_1	a_2
0	152	-0.01641	0.864296
100	147	-0.01761	0.858504
200	142	-0.01855	0.853183
300	138	-0.01935	0.847863
400	133	-0.02001	0.842543
500	128	-0.02053	0.837222

Lithosphere thinning inversion run with initial elevation larger than 0 m tend to overestimate the thinning factor in the proximal region, extrapolated onto the basement, as the elevation in this region is accounted as subsidence. In figure 11.7a, the overestimation of the thinning profile is observed with initial elevation larger than 200 m. A linear variation of the proximal thinning profile, between 0 and 25 km of distance, should be expected for the inversions with initial elevation from 0 to 500 m. However, this linear variation is not clearly characterized in figure 11.7a, probably due to the effect of the minimum curvature smoothing. The preferred fit for the Almada-Jequitinhonha cross-section was with 0 m elevation and lithosphere thickness of 152 km due to the small elevation of the basement region (figure 11.7). Therefore, as the elevation in the regions extrapolated into the basement of all cross-sections is low, for consistency lithosphere thicknesses corresponding to 0 m elevation were applied in the lithosphere thinning inversions of all cross-sections.

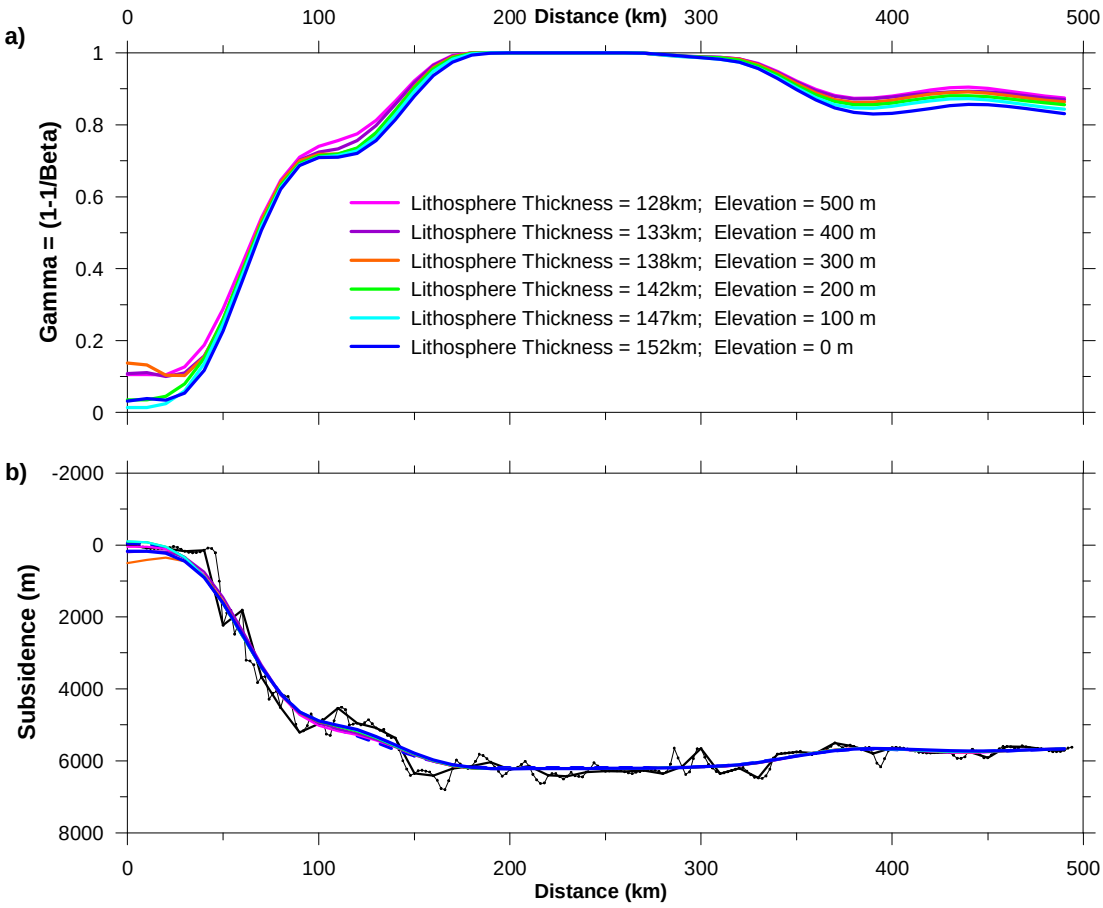

Figure 11.7: Sensitivity tests for lithosphere thickness (a) corresponding to the range of initial elevation of continental interiors (0 to 500 m) applied to the Almada-Jequitinhonha cross-section: a) lithosphere thinning profiles, b) subsidence profiles, in black the observed total subsidence. Smoothing factor of $\lambda = 10^{12}$ was applied for all inversions.

SENSITIVITY TESTS TO MAXIMUM MAGMATIC ADDITION (M_{MA})

Sensitivity of lithosphere thinning inversion of the Almada-Jequitinhonha cross-section to maximum magmatic addition M_{ma} was performed considering the range of igneous oceanic crust thickness from magma-poor to normal settings: 0, 1, 2, 3, 4. 5 , 6, 7 and 8 km (figure 11.8). The sensitivities tests were run using lithosphere thickness of 152 km, corresponding to 0 m initial elevation, and using the smoothing factor $\lambda=10^{12}$. Inversions with maximum magmatic addition from 0 to 4 km result in good fit of total subsidence (figure 11.8b), but the continental lithosphere thinning does not reach 1.0, implying that the continental lithosphere would not have been completely thinned. Inversions with maximum magmatic

addition larger than 5 km underestimate the subsidence between 150 and 330 km. The best solution seems to be with the maximum magmatic addition evaluated from the RDA analysis, around 4.6 km (chapter 6). The observed subsidence of the oceanic crust segment beyond 330 km fits well with magmatic addition of 7 km (figure 11.8b) suggesting variation of magmatic addition along the profile.

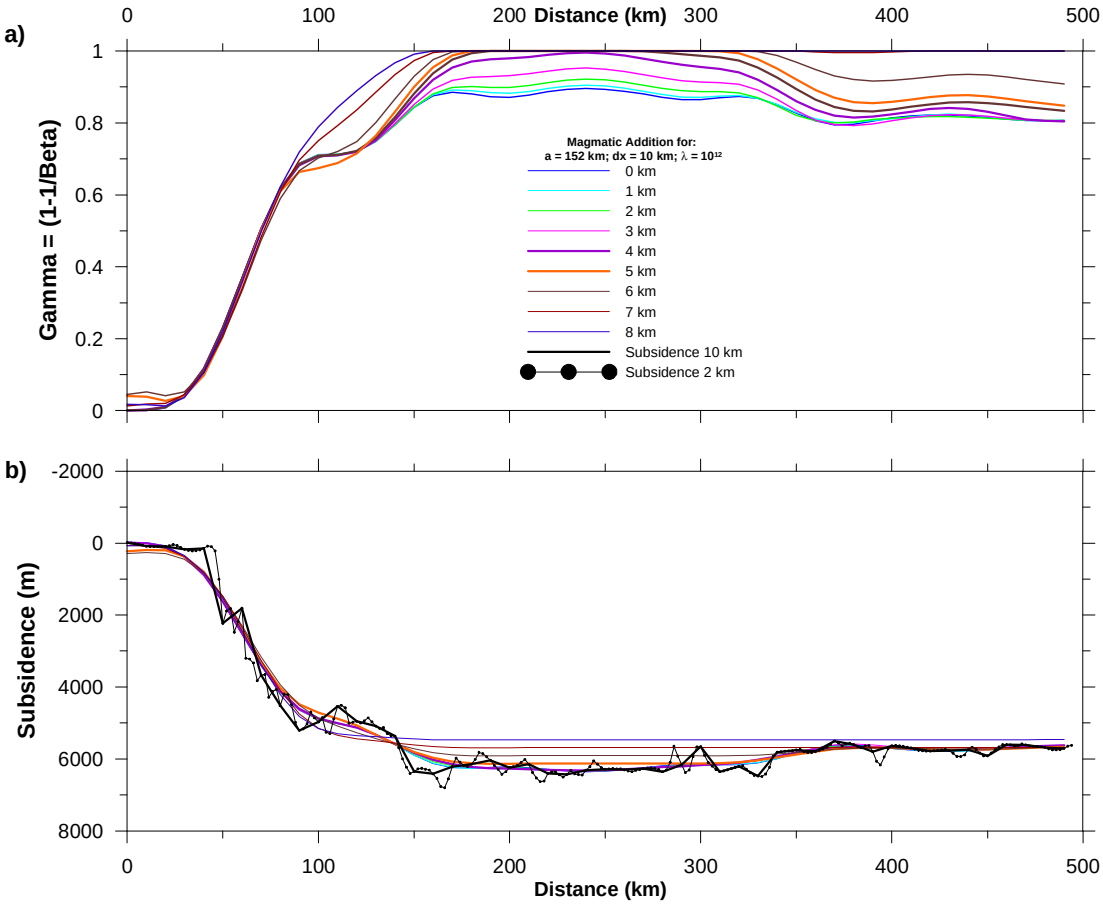

Figure 11.8: Sensitivity tests for 0 to 8 km of maximum magmatic addition (M_{ma}) applied to the Almada-Jequitinhonha cross-section: a) lithosphere thinning profiles, b) subsidence profiles, in black the observed total subsidence.

11.4 Lithosphere Thinning Inversion Results for The Selected Cross-Sections

The lithosphere thinning inversions were run with a lateral data sampling interval of 10-km. Visual selection of the best lambda was carried out for each cross-

section, as performed for Almada-Jequitinhonha cross-section in figure 11.4. The preferred smoothing factor for all the cross-sections was 10^{12}. The crustal and lithosphere parameters applied for each cross-section are presented in tables 11-1 and 11-3. The lithosphere thinning results are presented in figures 11.9 to 11.14 together with the crustal thinning results from the gravity inversion, for reference. Both results are discussed in Chapter 12. For each figure, the crustal architecture is presented at the top with the thinning profiles presented in the middle diagram and the observed and calculated subsidence profiles presented on the bottom diagram. In this chapter, the results of the lithosphere thinning inversion are interpreted, while in the next chapter, these results are compared with those from the gravity inversion and residual depth anomaly analysis.

11.4.1 ALMADA-JEQUITINHONHA LITHOSPHERE THINNING PROFILE

The lithosphere thinning inversions of the Almada-Jequitinhonha cross-section were run with initial lithosphere thickness of 152 km, surface radiogenic heat of 1.0 μWm^{-3} and initial crustal thickness of 39 km (table 11-2). The lithosphere thinning profile of Almada-Jequitinhonha was inverted with $\lambda=10^{12}$ and maximum magmatic addition of 4.6 km, and suggests the location of the continent-ocean lithosphere boundary (COLB) at around 175 km (figure 11.9b). The observed and calculated subsidence fit is good (figure 11.9c).

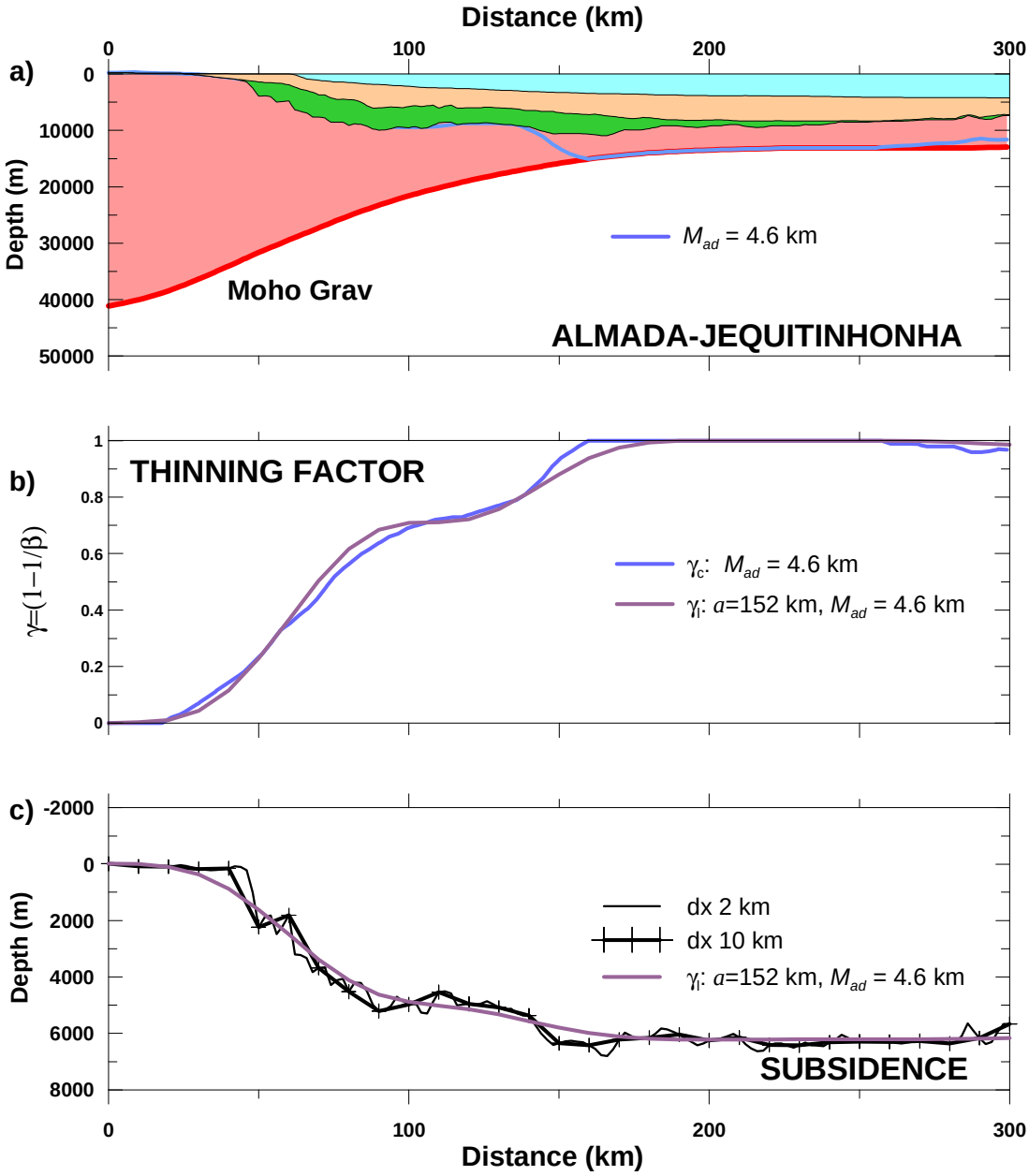

Figure 11.9: Lithosphere thinning inversion results for the Almada-Jequitinhonha cross-section: a) geological cross section, post-rift in beige, rift in green, Moho is the thick red line and the continental-ocean crustal boundary from gravity inversion is plotted in electric blue line. b) Lithosphere thinning profiles (in purple) compared with the crustal thinning profiles from the gravity inversion (in electric blue). c) Fit of calculated subsidence (purple line) with observed subsidence (in black).

11.4.2 JACUÍPE LITHOSPHERE THINNING PROFILE

The lithosphere thinning inversions of Jacuípe cross-section were run with the same surface heat production and crustal and lithosphere thickness as the Almada-Jequitinhonha cross-section (table 11-2). The lithosphere thinning profile

inverted with $\lambda=10^{12}$ and maximum magmatic addition of 7.08 km shows a smooth solution (figure 11.10b) that indicates a COLB location at 180 km.

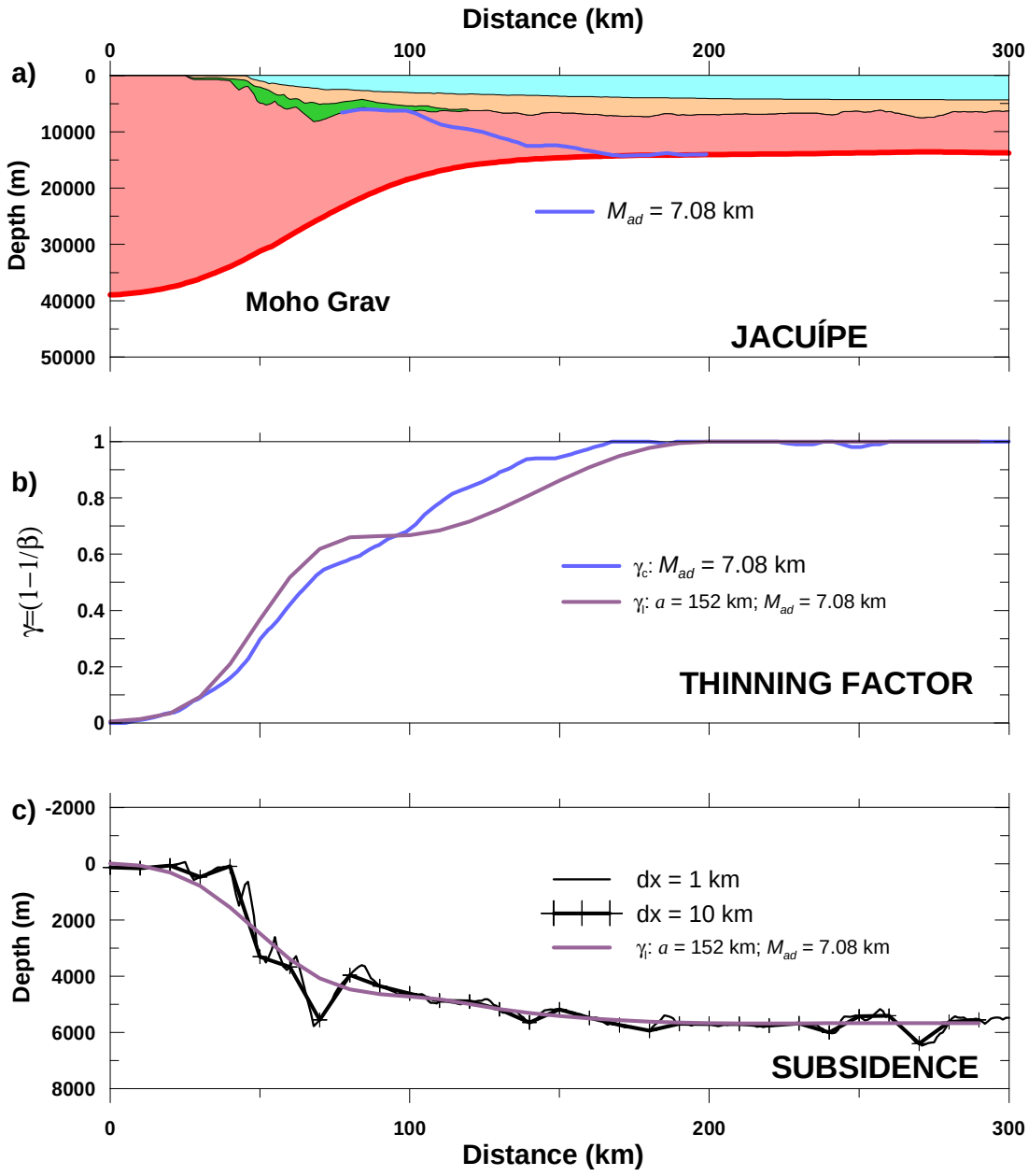

Figure 11.10: Lithosphere thinning inversion results for Jacuípe cross-section: a) geological cross section, post-rift in beige, rift in green, Moho is the thick red line and the continental-ocean crustal boundary from gravity inversion is plotted in electric blue line. b) Lithosphere thinning profiles (in purple) compared with the crustal thinning profiles from the gravity inversion (in electric blue). c) Fit of calculated subsidence (purple line) with observed subsidence (in black).

11.4.3 SERGIPE-SOUTH LITHOSPHERE THINNING PROFILE

The lithosphere thinning inversions of the Sergipe-South cross-section were run with the initial lithosphere thickness of 148 km, surface radiogenic heat of 1.5 μWm^{-3} and initial crustal thickness of 38 km (table 11-2). The lithosphere thinning profile inverted with $\lambda=10^{12}$ and maximum magmatic addition of 8.3 km interpreted from the RDA analysis, presents a smooth solution that indicates the COLB location at around 240 km (figure 11.11b).

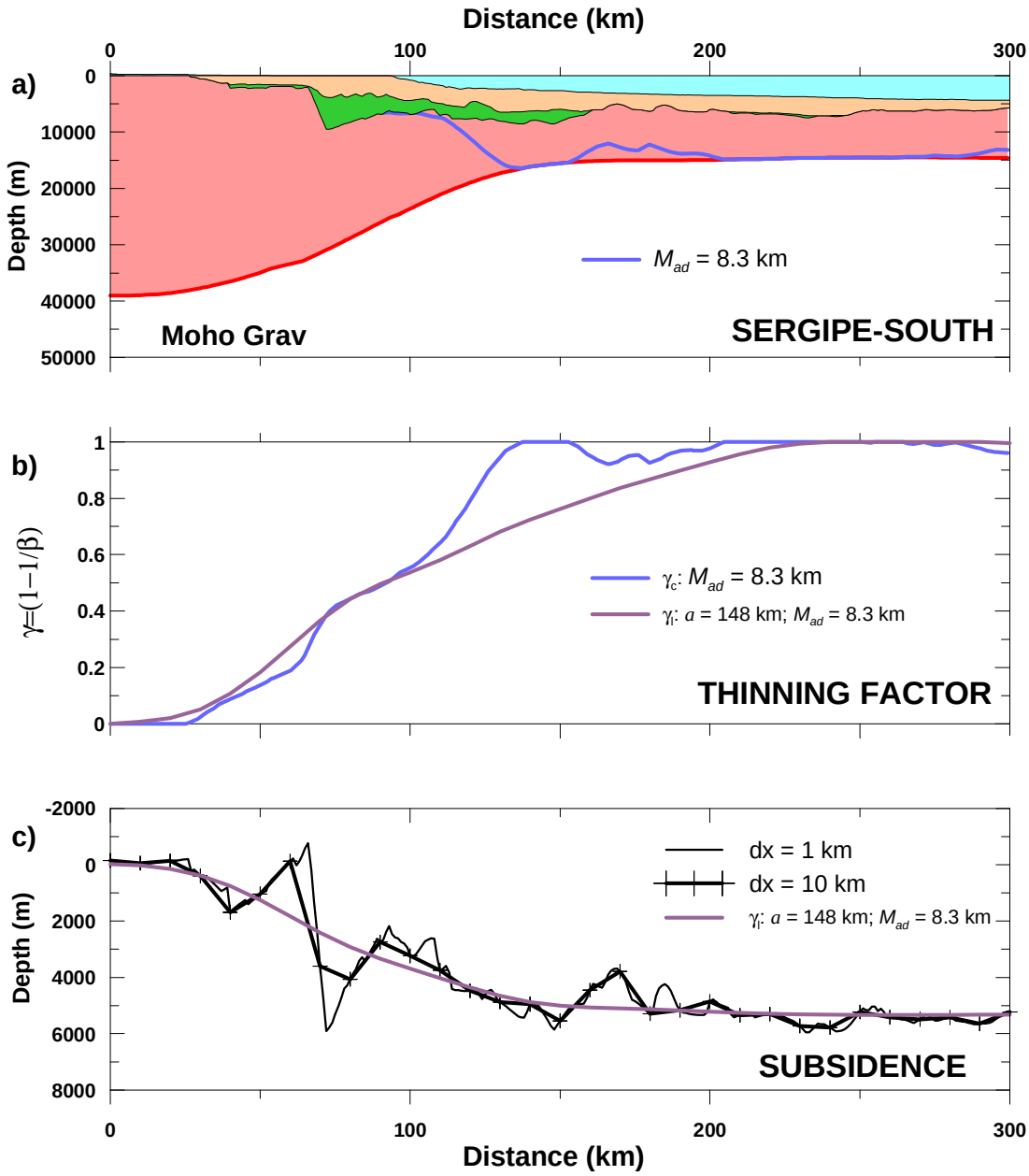

Figure 11.11: Lithosphere thinning inversion results for Sergipe South cross-section: a) geological cross section, post-rift in beige, rift in green, Moho is the thick red line and the continental-ocean crustal boundary from gravity inversion is plotted in electric blue line. b) Lithosphere thinning profiles (in purple) compared with the crustal thinning profiles from the gravity inversion (in electric blue). c) Fit of calculated subsidence (purple line) with observed subsidence (in black).

SERGIPE-NORTH LITHOSPHERE THINNING PROFILE

The lithosphere thinning inversions of the Sergipe-North cross-section were run with the initial lithosphere thickness of 144 km, surface radiogenic heat of 1.0 μWm^{-3} and initial crustal thickness of 38 km (table 11-2). The lithosphere thinning

profile inverted with $\lambda=10^{12}$ and maximum magmatic addition of 8.3 km interpreted from the RDA analysis, presents a smooth solution that indicates the COLB location at around 300 km.

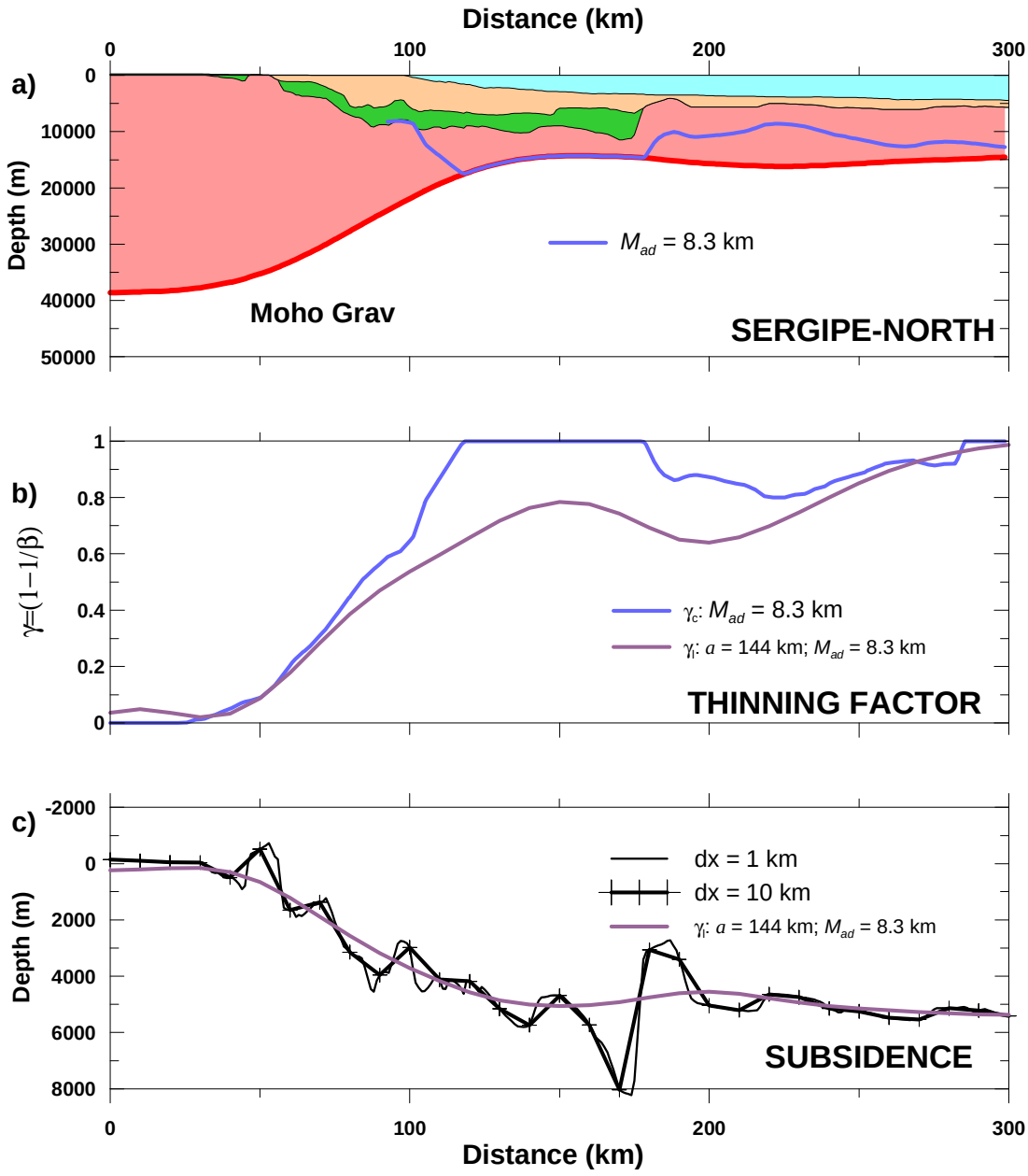

Figure 11.12: Lithosphere thinning inversion results for Sergipe North cross-section: a) geological cross section, post-rift in beige, rift in green, Moho is the thick red line and the continental-ocean crustal boundary from gravity inversion is plotted in electric blue line. b) Lithosphere thinning profiles (in purple) compared with the crustal thinning profiles from the gravity inversion (in electric blue). c) Fit of calculated subsidence (purple line) with observed subsidence (in black).

11.4.4 ALAGOAS LITHOSPHERE THINNING PROFILE

The lithosphere thinning inversions of the Alagoas cross-section were run with the initial lithosphere thickness of 152 km, surface radiogenic heat of 2.0 μWm^{-3} and initial crustal thickness of 38 km (table 11-2). The lithosphere thinning profile inverted with $\lambda=10^{12}$ and maximum magmatic addition of 7.08 km interpreted from the RDA analysis, presents a smooth solution that indicates the COLB location at around 170 km, similar to the crustal thinning from the gravity inversion, (figure 11.13c).

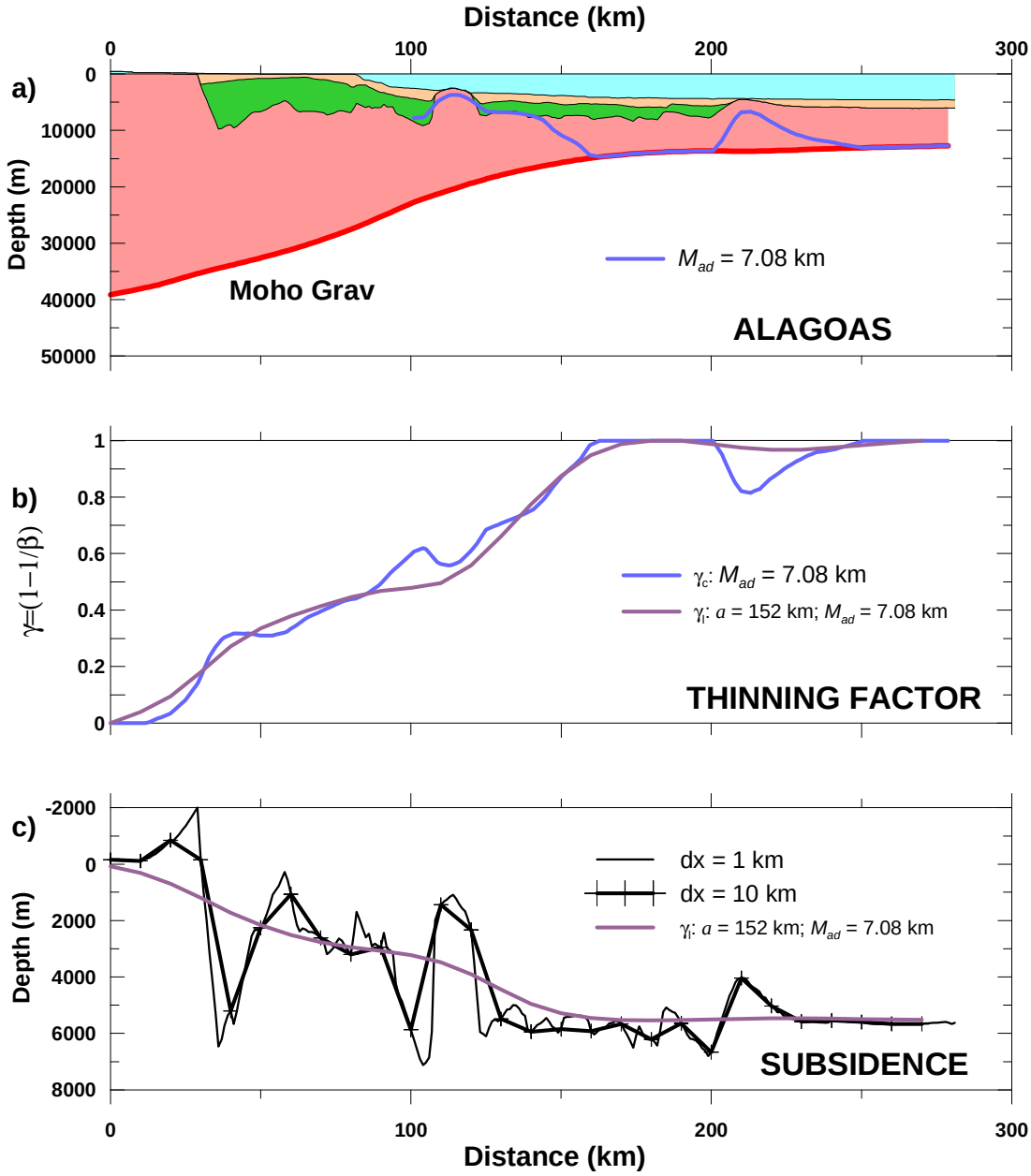

Figure 11.13: Lithosphere thinning inversion results for Alagoas cross-section: a) geological cross section, post-rift in beige, rift in green, Moho is the thick red line and the continental-ocean crustal boundary from gravity inversion is plotted in electric blue line. b) Lithosphere thinning profiles (in purple) compared with the crustal thinning profiles from the gravity inversion (in electric blue). c) Fit of calculated subsidence (purple line) with observed subsidence (in black).

11.4.5 Pernambuco Lithosphere Thinning Profile

The lithosphere thinning inversions of the Pernambuco cross-section were run with initial lithosphere thickness of 159 km, surface radiogenic heat of 2.0 μWm^{-3} and initial crustal thickness of 39 km (table 11-2). The lithosphere thinning profile

inverted with $\lambda=10^{12}$ and maximum magmatic addition of 8.3 km interpreted from the RDA analysis, presents a smooth solution that indicates the COLB location at around 240 km, similar to the crustal thinning from the gravity inversion, (figure 11.14c). But beyond this point, oceanic crust basement is deeper and it is better fit with maximum magmatic addition of 6.5 km, which also suggests variation in magmatic addition across this margin.

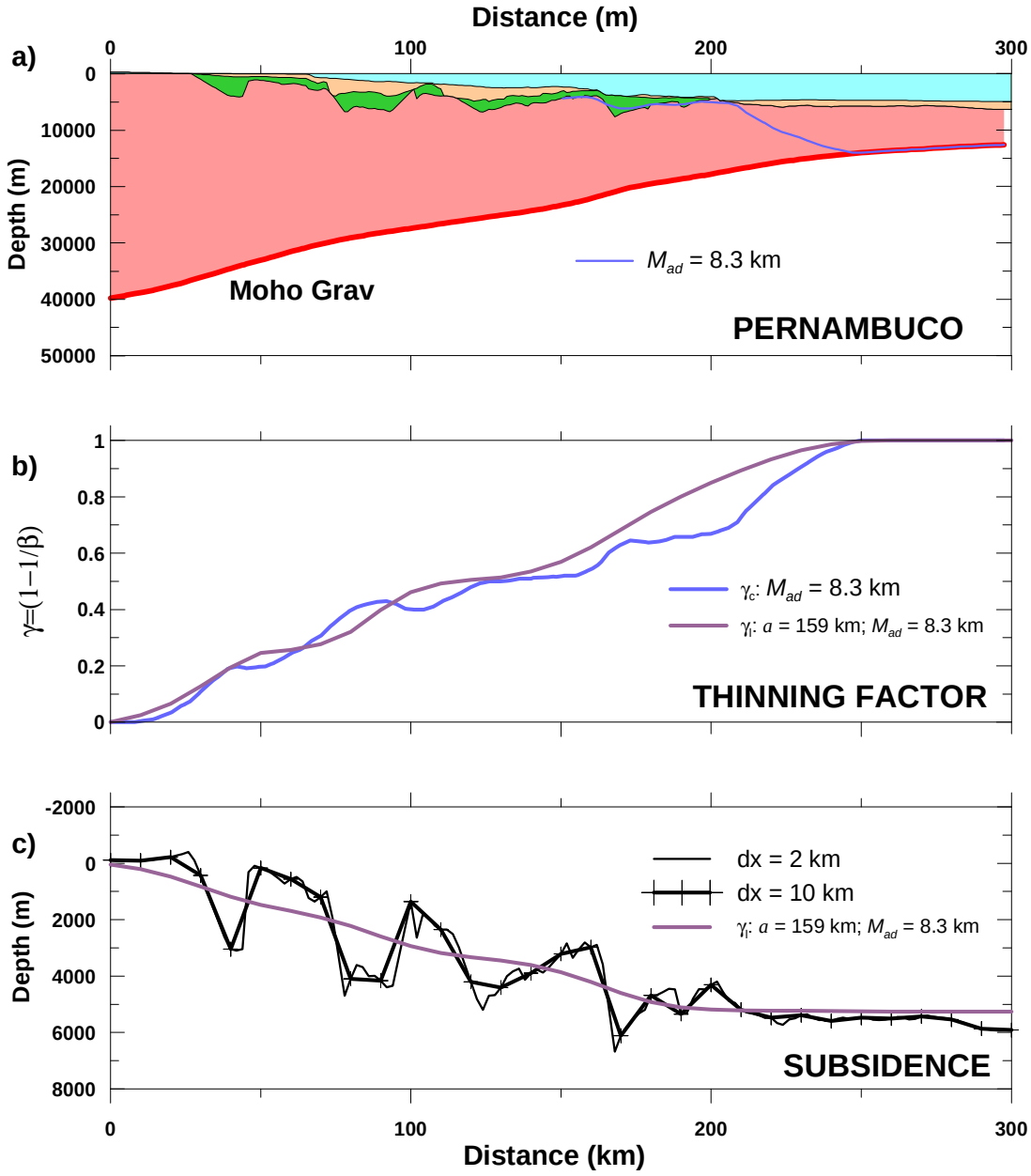

Figure 11.14: Lithosphere thinning inversion results for Pernambuco cross-section: a) geological cross section, post-rift in beige, rift in green, Moho is the thick red line and the continental-ocean crustal boundary from gravity inversion is plotted in electric blue line. b) Lithosphere thinning profiles (in purple) compared with the crustal thinning profiles from the gravity inversion (in electric blue). c) Fit of calculated subsidence (purple line) with observed subsidence (in black).

11.5 CONCLUSIONS

The lithosphere thinning profiles of the six cross-sections of the Northeast Brazilian rifted margin were inverted from forward modelled subsidence profiles

using the Powell's method with minimum curvature. The same depth constant of 15 km for the exponential decay of the radiogenic heat production with depth was assumed for all segments of the margins. The surface heat production was interpreted from aeroradiometric and rock sample data, ranging from 1.0 μWm^{-3}, in Almada, Jacuípe and North Sergipe, to 2.0 μWm^{-3} in Alagoas and Pernambuco.

Continental lithosphere thicknesses corresponding to zero elevation were applied in the lithosphere thinning inversions for all cross-sections due to the low present-day elevation of the onshore basement region sampled by the cross-sections. The numerical inversions were performed with data sampled every 10 km. Smaller sampling intervals result in high frequency distortion of the thinning profile close to the continental border. Sensitivity analyses for the smoothing factor (λ) were performed for all cross sections, suggesting best values of 10^{12}.

The preferred lithosphere thinning inversion for the Almada-Jequitinhonha cross-section was run with maximum magmatic addition of 4.6 km, and shows a ramp-flat-ramp geometry. The lithosphere thinning profile suggests a COLB at 175 km. The lithosphere thinning inversion of the Jacuípe cross-section was run with maximum magmatic addition of 8.3 km and resulted in the location of the COLB at 180 km.

The preferred lithosphere thinning profile of Sergipe-South cross-section was inverted from subsidence with maximum magmatic addition of 8.3 km and suggests the COLB location at 240 km. The preferred lithosphere thinning profile for the Sergipe-North cross-section was inverted with magmatic addition of 8.3 km and suggests the COLB location at around 300 km. Similarly, the lithosphere thinning profile of Alagoas was inverted with magmatic addition of 7.08 km and suggests the COLB location at 170 km. Finally, the lithosphere thinning inversion for the

Pernambuco cross-section was run with a maximum magmatic addition of 8.3 km, and resulted in the location of the COLB at 240 km.

CHAPTER 12

12. DISCUSSION AND CONCLUSIONS

12.1 INTRODUCTION

The first aim of this thesis was the development of a methodology and a workflow to identify the ocean-continent transition and to locate the continent-ocean crustal and lithosphere boundaries, COCB and COLB respectively, in continental rifted margins. The workflow comprises: 1) the determination of sediment-corrected basement depth profiles, 2) the analysis of the residual depth anomalies of the oceanic crust and its extrapolation into the rifted margin, 3) the gravity inversion of the Moho with crustal thinning determination and 4) the inversion of lithosphere thinning using subsidence analysis. This workflow is appropriate for regions without crustal thickness information. The calibration of the gravity inversion through the fit of the residual depth anomaly in unequivocal oceanic crust is a new approach to determine the reference Moho depth in areas without seismic refraction data.

The second aim was the application of the methodology and workflow for segments of the Northeast Brazilian rifted margins. The complexity of this rifted margin OCT is due to variable extrusive and intrusive magmatism, change from synthetic to antithetic faulting and poor seismic quality. Interpretations of the existing COCB location based on seismic reflection data were tested by the numerical techniques. The purpose of this discussion is to evaluate whether the application of the numerical techniques and workflow to the Northeast Brazil was successful in locating the COCB and COLB.

12.2 COCB AND COLB LOCATIONS

The locations of the COCB from RDA analysis and gravity inversion of the Moho and the locations of the COLB from subsidence analysis are compared with the initial seismic interpretation of the COCB. The smoothed RDA profile from the gravity inversion permits a better COCB identification than the noisy RDA profile from the total subsidence. The COCB identification with the RDA analysis and the COLB identification with the subsidence analysis both assume that the sediment-corrected basement depth increases continuously from shallow depths in the OCT towards the sediment-corrected adjacent oceanic crust depth (figure 12.1). Conversely, the COCB identification with the gravity inversion assumes that the continental crust thins continuously towards the adjacent oceanic crust thickness (figure 12.1). Moreover, both the subsidence analysis and the gravity inversion assume that magmatic addition increases linearly after a threshold of lithosphere thinning.

The cross-sections of Almada-Jequitinhonha and Jacuípe to the south and Pernambuco to the north present results more consistent with the above assumptions. Due to the presence of intrusive bodies close to the COCB and because sediment-corrected depth and crustal thickness does not seem to evolve continuously towards the oceanic crust values, the Sergipe-South, Sergipe-North and Alagoas cross-sections present results that require careful interpretation. Figures 12.2 to 12.7 show the results of RDA analysis and crustal thinning from gravity inversion (figures 7.9 to 7.14) compared with the results of lithosphere thinning (figures 11.9 to 11.14).

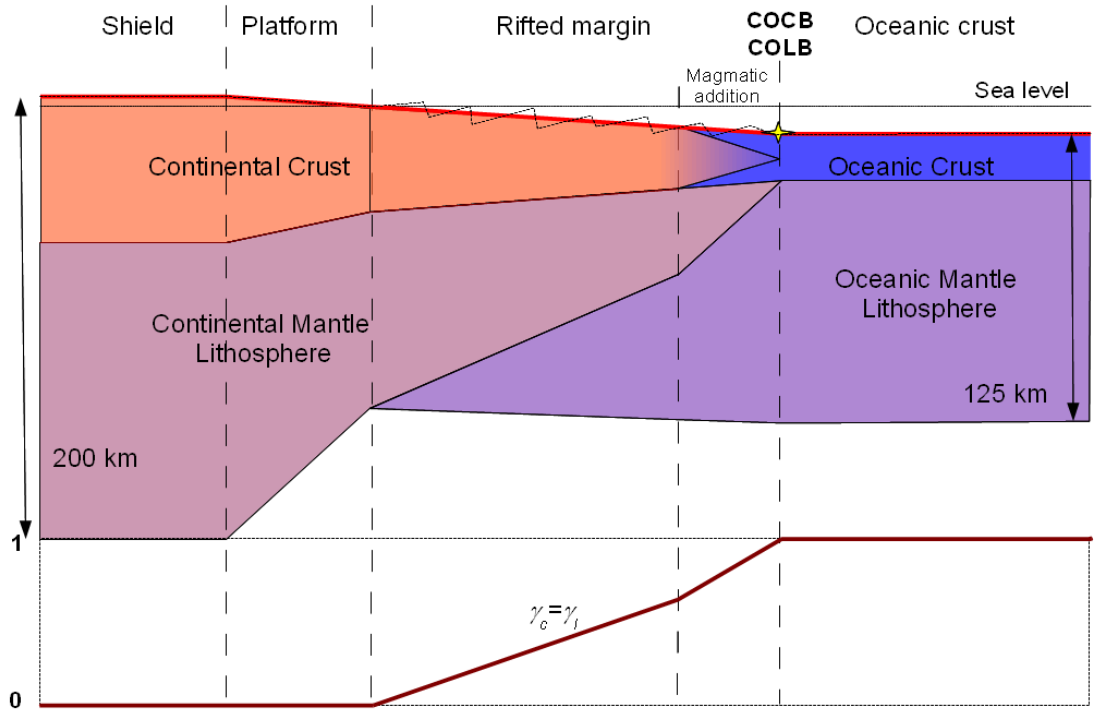

Figure 12.1. Schematic cross-section of a rifted continental margin with normal magmatic addition and coincident COCB and COLB. RDA analysis and subsidence analysis assume that the sediment-corrected depth profile (red line) evolves continuously towards the depth of the adjacent oceanic crust (yellow cross). Gravity inversion assumes that the continental crust thins continuously towards the thickness of the adjacent oceanic crust, controlled by magmatic addition.

ALMADA-JEQUITINHONHA CROSS-SECTION

The interpretation of syn-rift packages in seismic section suggests the location of the COCB at around 245 km of distance (figure 12.2a). The Almada-Jequitinhonha rifted margin can be interpreted as magma-poor based on the RDA profile. The COCB location is suggested at 160 km by the inflection of the gravity RDA profile (figure 12.2b). The gravity inversion indicates that crustal thinning γ_c evolves through magmatic addition from around 0.7 to 1 between 140 and 160 km of distance (figure 12.2a, d), which COCB corroborates the inflection in the gravity RDA profile.

If the COCB location indicated by the RDA and by the crustal thinning profiles is correct, the whole sedimentary package interpreted between the basement and the base of the salt in the graben beyond 160 km should be reviewed. A re-

evaluation of the RDA points to a preferred COCB position at around 180 km. The COLB location suggested by the lithosphere thinning profile at around 175 km is close to the preferred position, where syn-rift sediments pinch out (figure 12.2a).

The lithosphere thinning profile is strikingly similar to the crustal thinning (figure 12.2d). Both lithosphere and crustal thinning profiles present a ramp-flat-ramp geometry, with a steady increase from 0 to 0.7 between 50 and 80 km of distance. Then lithosphere and crustal thinning increase with a very low gradient between 80 and 130 km. Finally, another steady increase of the lithosphere thinning from 0.7 to 1.0 occurs until distance 180 km. The flat-ramp developed between 80 and 180 km of distance corresponds to a magma-poor ocean-continent transition (OCT), characterised by change from synthetic to antithetic faulting.

The lithosphere thinning profiles calculated with parameters of the depth-uniform lithosphere stretching model, DULSM (McKenzie, 1978), (table 11-2) with and without magmatic addition are also shown in figure 12.2d. Crustal density of 2850 kg m^{-3}, no radiogenic heat production and crustal thickness compatible with zero elevation were applied for the uniform stretching model. The results are similar to the lithosphere inversion with lithosphere thickness of 152 km (figure 12.2a).

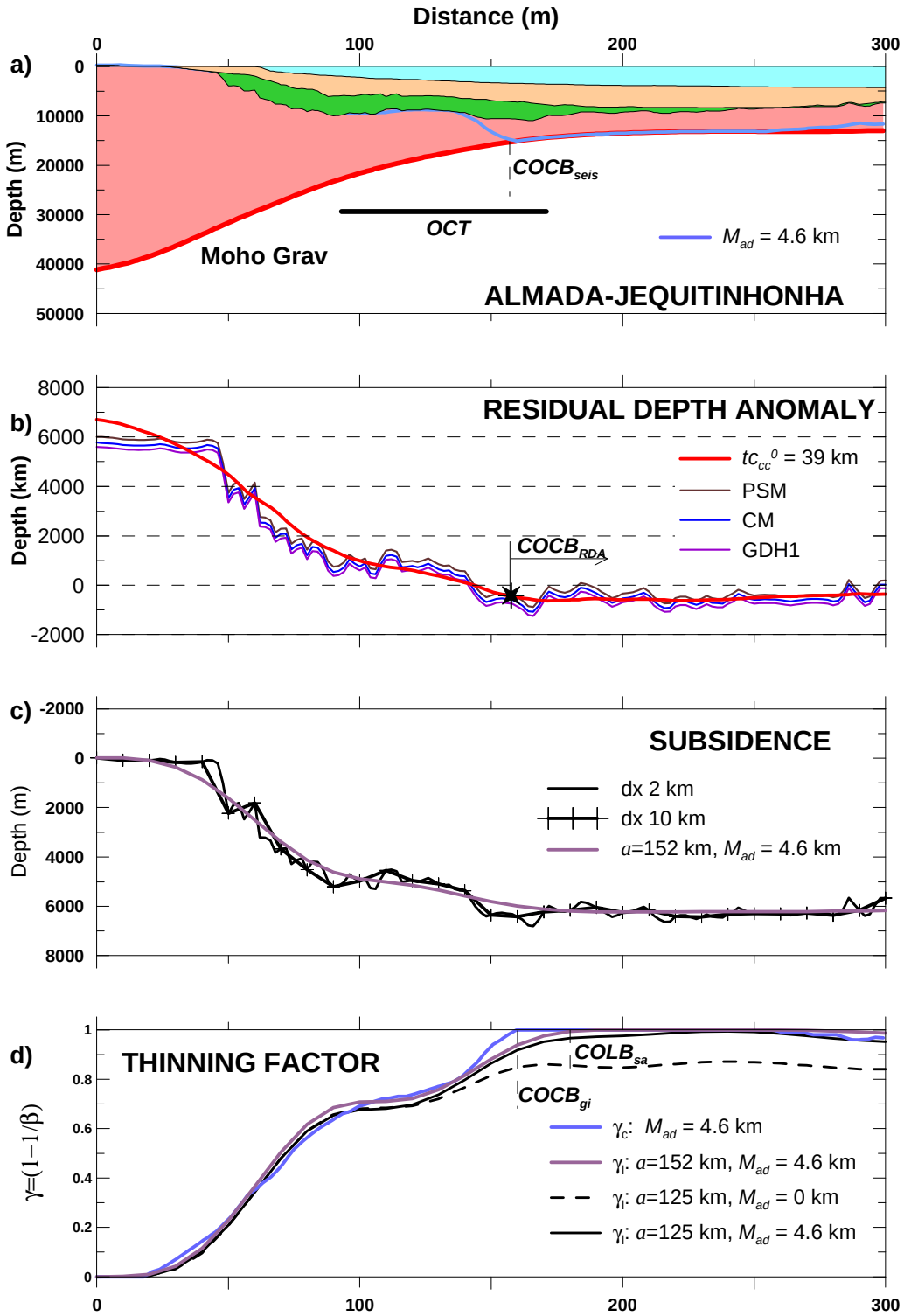

Figure 12.2: Almada-Jequitinhonha results: a) geological cross section; b) fit of RDA from gravity inversion (red line) to RDA from flexural backstripping, c) fit of calculated subsidence (purple line) with observed subsidence (black) and d) lithosphere thinning profiles compared with crustal thinning profiles from the gravity inversion.

JACUÍPE CROSS-SECTION

The seismic interpretation suggests a COCB location around distance 120 km, where the pre-Neoaptian sediments pinch out (figure 12.3a). Based on the RDA data, the Jacuípe margin can be interpreted as normal in terms of magmatic addition, in spite of the presence of seaward dipping reflectors. The gravity RDA profile suggests a COCB location farther offshore at 170 km (figure 12.3b). The gravity inversion indicates that crustal thinning γ_c evolves through magmatic addition from around 0.7 to 1 between 100 and 170 km of distance (figure 12.3a, d), which COCB corroborates the inflection in the gravity RDA profile. The COLB location indicated by the lithosphere thinning profile at 190 km is close to the COCB suggested by the crustal thinning profile (figure 12.3d).

Lithosphere thinning is greater than crustal thinning until 90 km of distance, where they cross each other. The OCT is interpreted as being located between 90 km and 170 km of distance, from the position where magmatic addition starts to the COLB location, corresponding to the region of development of seaward dipping reflectors. The approximately coincident COCB and COLB are located further offshore than the COCB location suggested by the seismic interpretation.

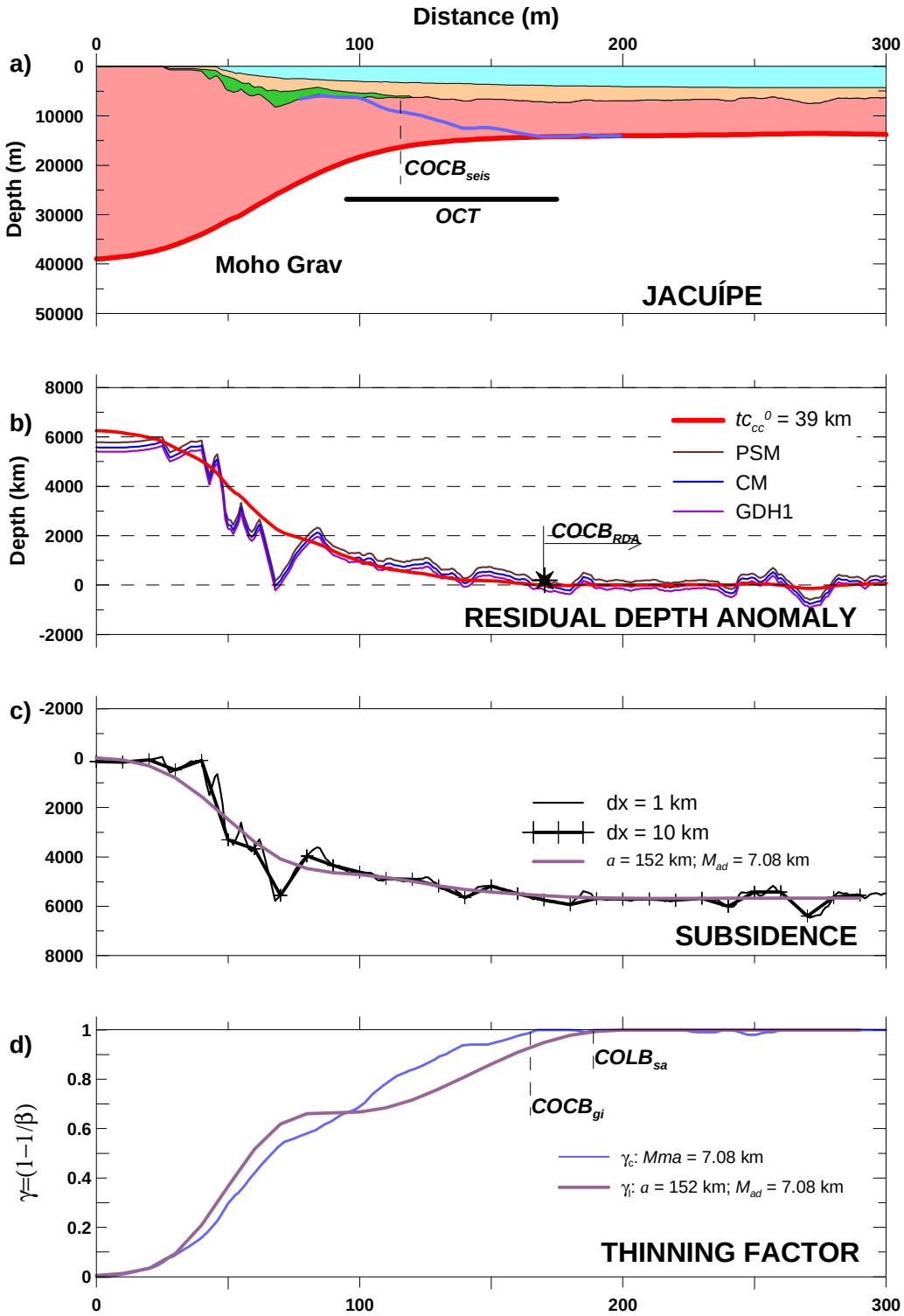

Figure 12.3: Jacuípe cross-section results: a) geological cross section; b) fit of RDA from gravity inversion (red line) to RDA from flexural backstripping, c) fit of calculated subsidence (purple line) with observed subsidence (black) and d) lithosphere thinning profiles compared with crustal thinning profiles from the gravity inversion.

SERGIPE-SOUTH CROSS-SECTION

The seismic interpretation of the Sergipe-South cross-section suggests the location of the COCB at 160 km, where the pre-Neoaptian sediments are limited by an antithetic fault (figure 12.4a). The inflection of gravity RDA profile to the oceanic crust background suggests a COCB location a little onshore, at 140 km (figure 12.4b). The sediment-corrected basement depth profile reaches depths larger than expected for the adjacent oceanic crust between 135 and 150 km. The gravity inversion, calculated with magmatic addition of 8.3 km, which corresponds to the interpreted RDA, suggests that crustal thinning γ_c evolves through magmatic addition from around 0.7 to 1 between 110 and 135 km (figure 12.4a, d). The crust in the 135 to 150 km region is thinner than predicted for the adjacent oceanic crust by the RDA profile. The COCB location determined by the gravity inversion is compatible with the hypothesis that the whole strata package, interpreted between 135 and 150 km, should correspond to volcanic rocks deposited over thin oceanic crust.

An alternative interpretation is preferred in which the crustal thinning between 135 and 150 km would have been developed under magma-poor conditions (figure 12.4d). The crustal thinning beyond 150 km would have been developed under slightly magma rich conditions, with maximum magmatic addition of 8.3 km, and the COCB at 160 km, where syn-rift sediments are limited by an antithetic fault.

The lithosphere thinning profile calculated with magmatic addition of 8.3 km (figure 12.4d), indicates the COLB is located at around 225 km of distance. However, the preferred COCB and COLB locations are at the same position, 160 km. The region between 160 and 220 km is interpreted as thickened igneous crust related to the early post-break-up Bahia seamounts. The OCT is re-interpreted between the position where antithetic faulting starts and the position where the anomalous

igneous crust block starts, from 115 km to 160 km of distance respectively (figure 12.4d). The lithosphere and crustal thinning profiles calculated with 0.0 km of magmatic addition are close to each other from distance 0 to 160 km.

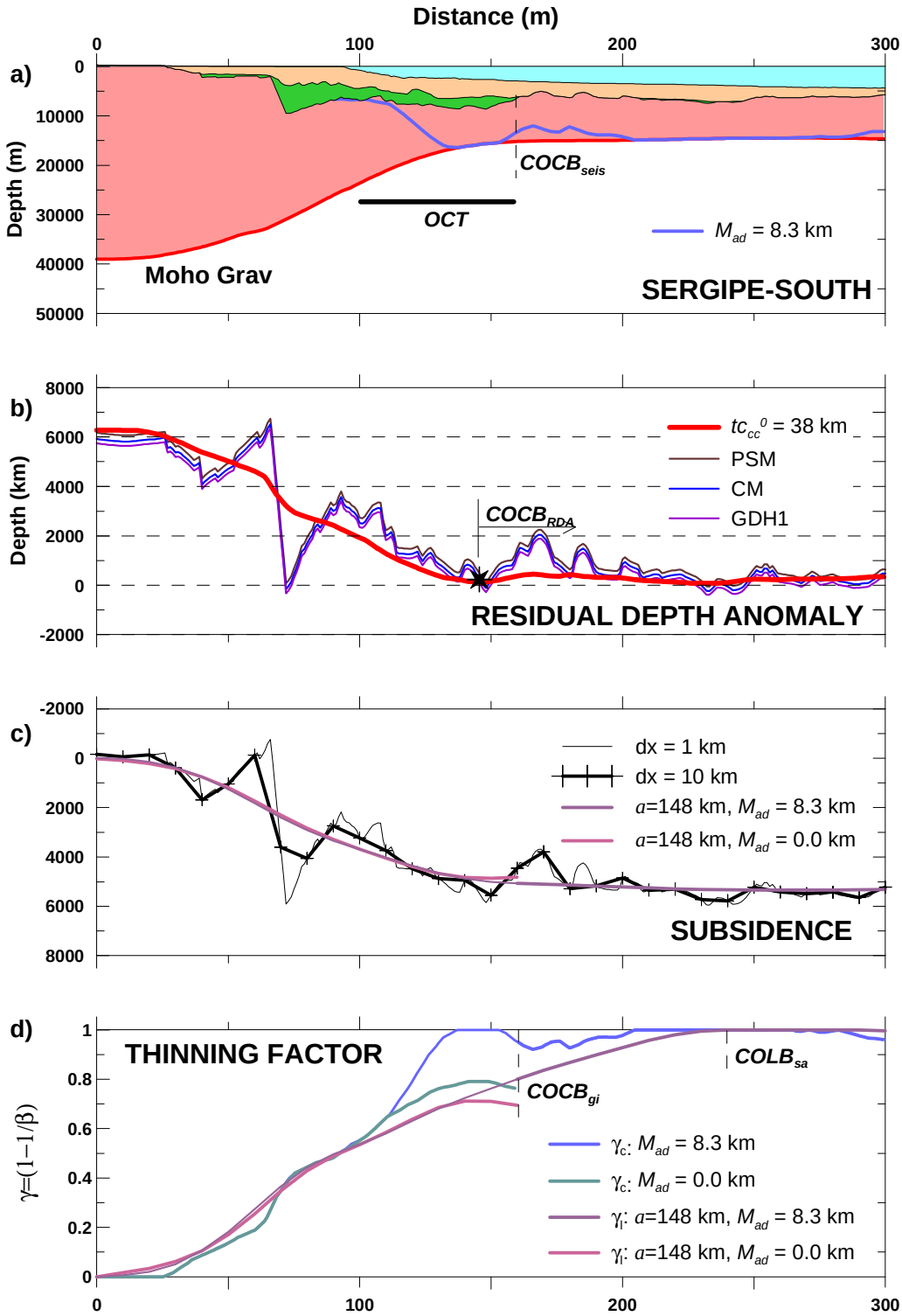

Figure 12.4: Sergipe South results: a) geological cross section; b) fit of RDA from gravity inversion (red line) to RDA from flexural backstripping, c) fit of calculated subsidence (purple line) with observed subsidence (black) and d) lithosphere thinning profiles compared with crustal thinning profiles from the gravity inversion. In green, crustal thinning without magmatic addition, and in rose, lithosphere thinning without magmatic addition, both until 160 km. In blue, crustal thinning maximum magmatic addition of 8.3 km, and in plum, lithosphere thinning with maximum magmatic addition of 8.3 km, both beyond 160 km.

SERGIPE-NORTH CROSS-SECTION

The seismic interpretation suggests that the location of the COCB is at 180 km, where the pre-Neoaptian sediments are limited by an antithetic fault (figure 12.5a). This fault is registered on the RDA profile as a sharp discontinuity (figure 12.5b). The inflection of gravity RDA profile to the oceanic crust background suggests a COCB location at 140 km (figure 12.5b). The sediment-corrected basement depth profile reaches depths larger than expected for the adjacent oceanic crust between 135 and 175 km (figure 12.5c). The gravity inversion, calculated with magmatic addition of 8.3 km, which corresponds to the interpreted RDA, suggests that crustal thinning γ_c, evolves through magmatic addition from around 0.7 to 1 between 100 and 130 km of distance (figure 12.5a, d). Similarly to Sergipe-South cross-section, the crust in the 135 to 175 km region is thinner than predicted for the adjacent oceanic crust by the RDA profile. The COCB location determined by the gravity inversion implies that the whole strata package interpreted between 110 and 175 km of distance should correspond to volcanic rocks deposited over too thin oceanic crust. This region is followed by a thick oceanic crust block, between 175 and 240 km.

According to the preferred alternative interpretation, the crustal thinning between 110 and the COCB at 175 km would have been developed under magma-poor conditions (figure 12.5d). The crustal thinning beyond 175 km would have been developed under slightly magma rich conditions, with maximum magmatic addition of 8.3 km,.

The lithosphere thinning profile calculated with maximum magmatic addition of 8.3 km (figure 12.5d) reaches a peak of γ_c=1 at around 300 km. However, the preferred COCB and COLB are at the same position, around 175 km. The region

between 175 and 270 km is interpreted as thickened igneous crust related to the early post-break-up Bahia seamounts. The OCT is interpreted between the position where antithetic faulting starts and the limit of the thick igneous crust block, from 115 km to 175 km of distance respectively. The crustal thinning is larger than lithosphere thinning from 60 to 175 km of distance. However it is not clear whether this difference is real or is in the error margins of the determinations..

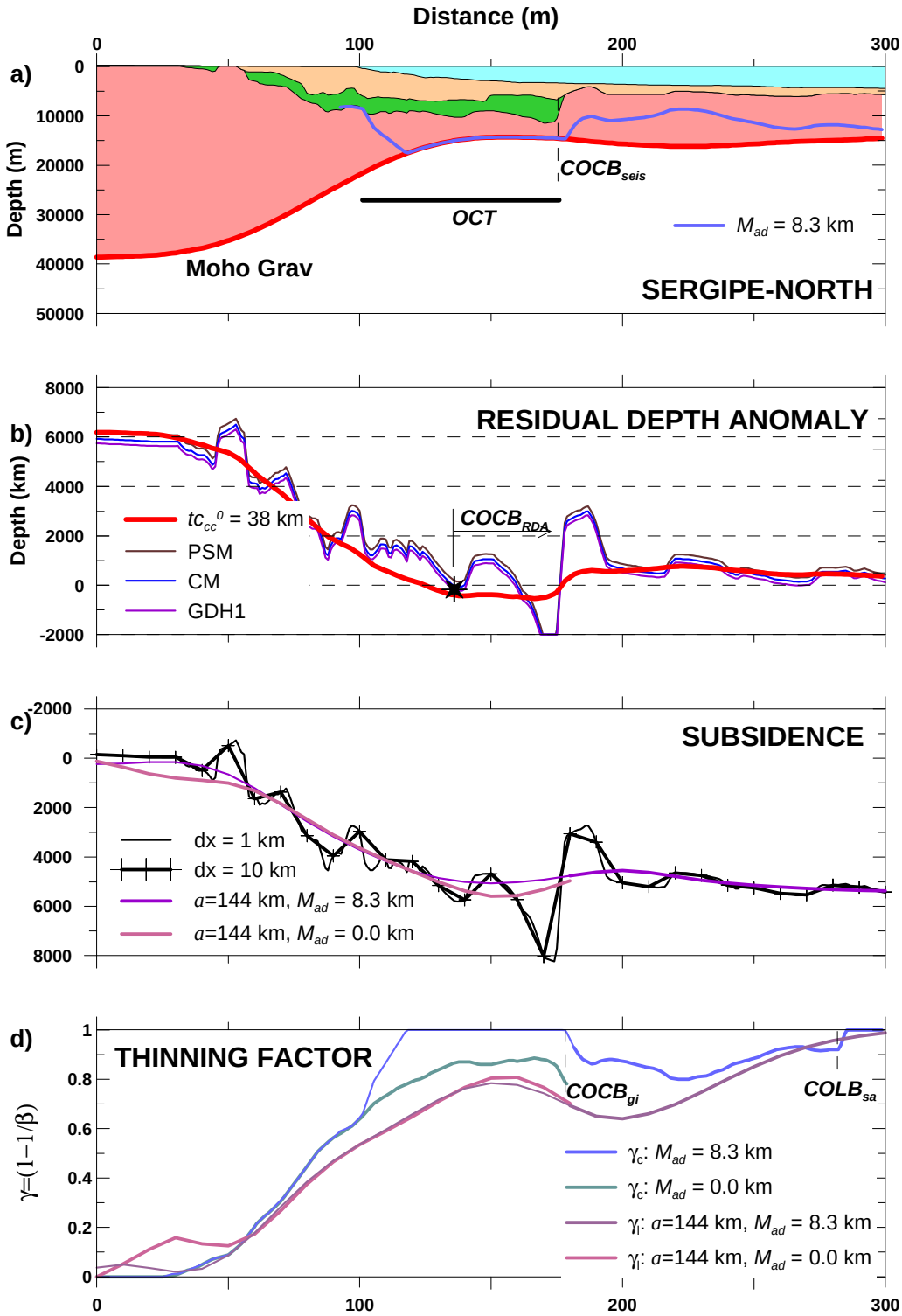

Figure 12.5: Sergipe North results: a) geological cross section; b) fit of RDA from gravity inversion (red line) to RDA from flexural backstripping, c) fit of calculated subsidence (purple line) with observed subsidence (black) and d) lithosphere thinning profiles compared with crustal thinning profiles from the gravity inversion. In green, crustal thinning without magmatic addition, and in rose, lithosphere thinning without magmatic addition, both until 170 km. In blue, crustal thinning maximum magmatic addition of 8.3 km, and in plum, lithosphere thinning with maximum magmatic addition of 8.3 km, both beyond 170 km.

ALAGOAS CROSS-SECTION

The seismic interpretation suggests that the location of the COCB is at 200 km of distance, where pre-Neoaptian sediments are bounded by an antithetic fault (figure 12.6a). Similarly to Sergipe North cross-section, this fault is registered in the RDA profile as a sharp discontinuity (figure 12.6b). The inflection of the gravity RDA profile to the oceanic crust background suggests a COCB location at 170 km (figure 12.6b). The sediment-corrected basement depth profile reaches depths larger than expected for the adjacent oceanic crust between 120 and 210 km (figure 12.6c). The gravity inversion suggests that crustal thinning γ_c, evolves through magmatic addition from around 0.7 to 1 between 140 and 160 km of distance (figure 12.6a, d). Similarly to Sergipe-South and Sergipe-North cross-sections, the crust in the 135 to 175 km region is thinner than predicted for the adjacent oceanic crust by the RDA profile and the whole strata package interpreted between 160 and 210 km should correspond to volcanic rocks deposited over thin oceanic crust. This region is followed by a structural high, between 210 and 225 km.

According to the preferred alternative interpretation, the crustal thinning between 100 and 210 km would have been developed under magma-poor conditions (figure 12.6d). The crustal thinning beyond 210 km would have been developed under normal magmatic addition, around 7.1 km, and the COCB would be located at 270 km.

The lithosphere thinning profile calculated with the maximum magmatic addition that corresponds to the interpreted RDA (figure 12.6d), suggests a COLB location at 250 km. However, the preferred COCB and COLB are at the same position, around 210 km. The region between 210 and 225 km is interpreted as thickened igneous crust related to the early post-break-up Bahia seamounts. The

OCT is interpreted between the volcanic Maceió High and the limit of the thick igneous crust block, from 125 km to 210 km of distance respectively. The lithosphere thinning profile is practically coincident with the crustal thinning profile from 0 to 210 km (figure 12.6d).

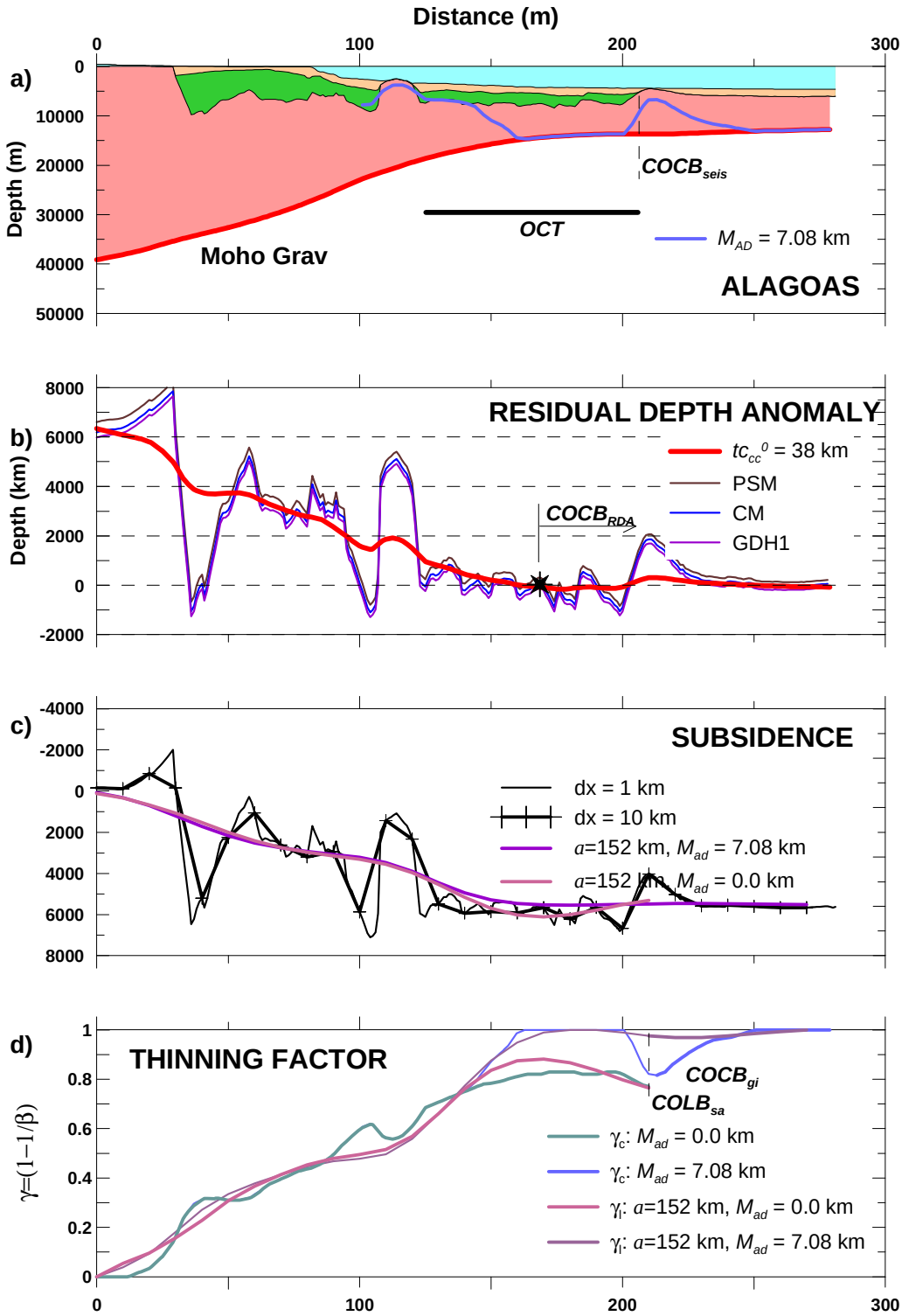

Figure 12.6: Alagoas results: a) geological cross section; b) fit of RDA from gravity inversion (red line) to RDA from flexural backstripping, c) fit of calculated subsidence (purple line) with observed subsidence (black) and d) lithosphere thinning profiles compared with crustal thinning profiles from the gravity inversion. In green, crustal thinning without magmatic addition, and in rose, lithosphere thinning without magmatic addition, both until 210 km. In blue, crustal thinning maximum magmatic addition of 7.08 km, and in plum, lithosphere thinning with maximum magmatic addition of 7.08 km, both beyond 210 km

PERNAMBUCO CROSS-SECTION

The Pernambuco cross-section has a COCB location well defined by seismic interpretation at 210 km (figure 12.7a), close to an inflection of the RDA profile at 225 km (figure 12.7b). The Pernambuco margin can be interpreted as slightly magma-rich based on the RDA data. The gravity inversion, calculated with magmatic addition of 8.3 km, which corresponds to the interpreted RDA, indicates that crustal thinning γ_c, evolves through magmatic addition from around 0.7 to 1 between distances 200 and 250 km (figure 12.7a, d). The lithosphere thinning profile, calculated with maximum magmatic addition of 8.3 km (figure 12.7d), suggests the COLB location further offshore at 250 km, near the COCB gravity inversion. The crustal and lithosphere thinning profiles are nearly coincident until around 130 km. Beyond this position, lithosphere thinning increases faster than crustal thinning. However it is not clear whether this difference is real or due to the smoothing of the lithosphere thinning profile, in the margin of error of the techniques. The OCT corresponds to the region of the Pernambuco Plateau, starting where the lithosphere thinning reaches 0.4, until the COCB.

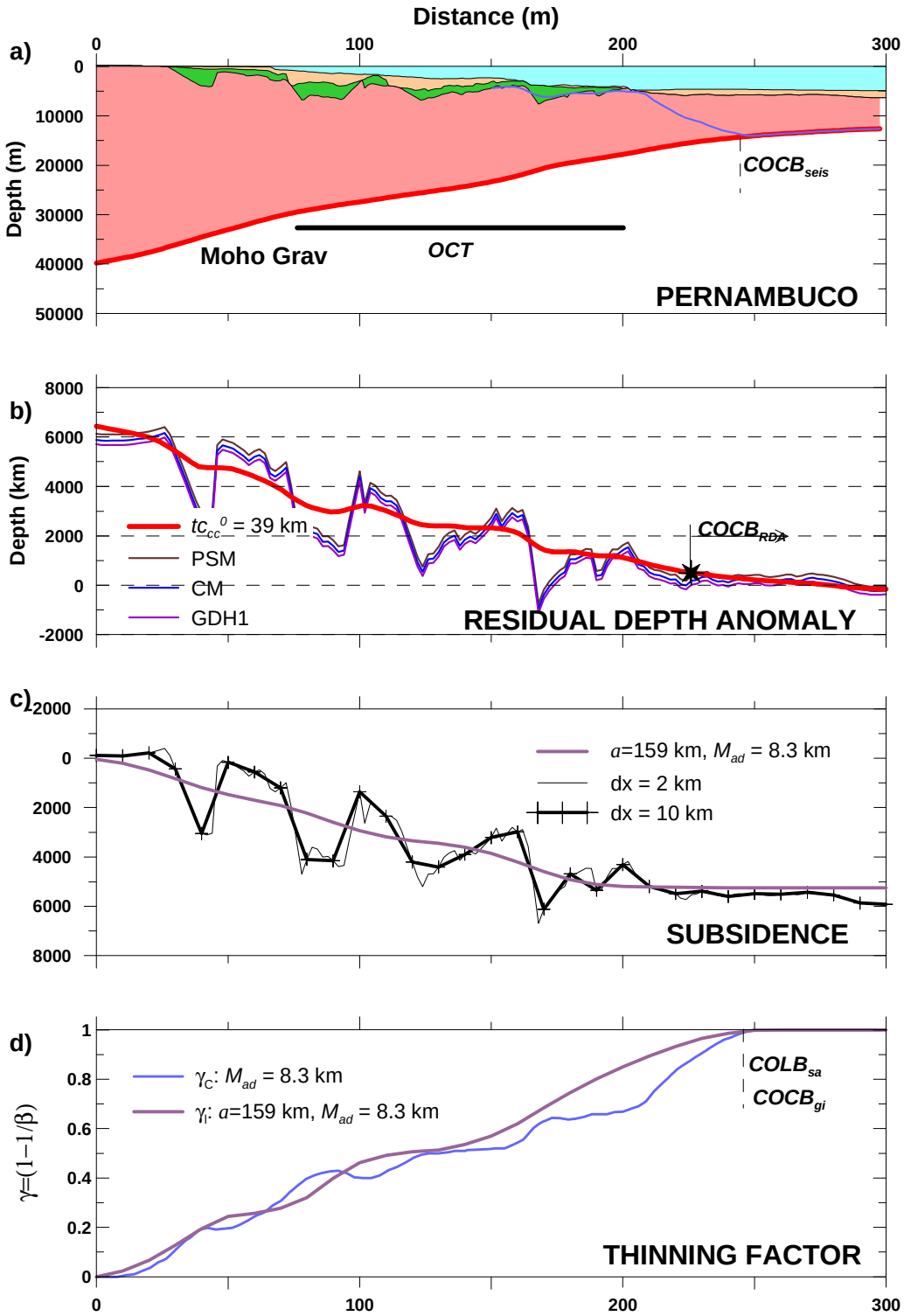

Figure 12.7: Pernambuco results: a) geological cross section; b) fit of RDA from gravity inversion (red line) to RDA from flexural backstripping, c) fit of calculated subsidence (purple line) with observed subsidence (black) and d) lithosphere thinning profiles compared with crustal thinning profiles from the gravity inversion

12.3 The Ocean-Continent Transition Segments of the Northeast Brazilian Rifted Margin

The ocean-continent transition (OCT) of each segment of the Northeast Brazilian Rifted Margin was recognized based on the combined interpretation of the RDA analysis and of the crustal and lithosphere thinning profiles determined here. It is not appropriate to use the free air gravity anomaly to interpret the OCT because it is a combination of several sources of density contrasts. The influence of the sedimentary succession is especially strong in the studied margin. However, the OCT limits interpreted with the workflow developed in this study could be tentatively extrapolated into each margin segment using the corresponding free-air anomaly pattern (figure 12.8). Besides their distinct magmatic addition and tectonic style, each margin segment is characterized by a different free-air gravity anomaly pattern.

The Magma Poor OCT of Almada-Jequitinhonha

The interpretation of the Almada-Jequitinhonha OCT by the combined numerical techniques is between 80 and 180 km of distance in the studied cross-section (figures 12.2a and 12.8a, b). The cross-section does not show evidence of magmatism and is characterised by antithetic faulting in the OCT, coincident with the decreasing gradient of the free air gravity anomaly that follows the edge effect. The low free-air gravity anomaly developed on the Almada-Jequitinhonha rifted margin is due to the thick post-rift sedimentary succession. According to the RDA analysis and gravity inversion, the magmatic addition of 4.6 km develops in a 30-km wide region (figure 12.2a). This magma-poor rifted margin seems to be separated from the Camamu-Jacuípe rifted margin to the north by the Mutá Accommodation Zone, MAZ (figure 12.8a).

THE MAGMA NORMAL OCT OF CAMAMU-JACUÍPE

The interpretation of the Camamu-Jacuípe OCT by the combined numerical techniques is between 90 and 170 km of distance in the studied cross-section (figures 12.3a and 12.8a, c) and corresponds to the region of magmatic addition by decompression melting of mantle rocks due to lithosphere thinning. According to the RDA analysis and gravity inversion, the magmatic addition of 7.1 km develops in a 70-km wide region (figure 12.2a). Magmatic addition resulted in extrusive magmatic rocks, imaged as seaward dipping reflectors in the studied cross-section and in other cross-sections of Jacuípe. The zone of magmatic addition corresponds to a gravimetric high developed offshore from the free-air gravity anomaly edge effect (figure 12.8a, c). This gravimetric high reaches great magnitude in the Camamu margin, suggesting maximum SDR thickening. In spite of the presence of magmatic rocks identified as SDR, Jacuípe margin seems to be related to normal adjacent oceanic crust, according to the residual depth anomaly (RDA). It is not clear whether the Camamu-Jacuípe SDR developed under the influence of the Santa Helena hot spot or by enhanced magmatism due to secondary mantle convection (Mutter et al., 1988). The Jacuípe OCT is separated from the Sergipe margin to the north by the Vaza Barris fault system, VB (figure 12.8a).

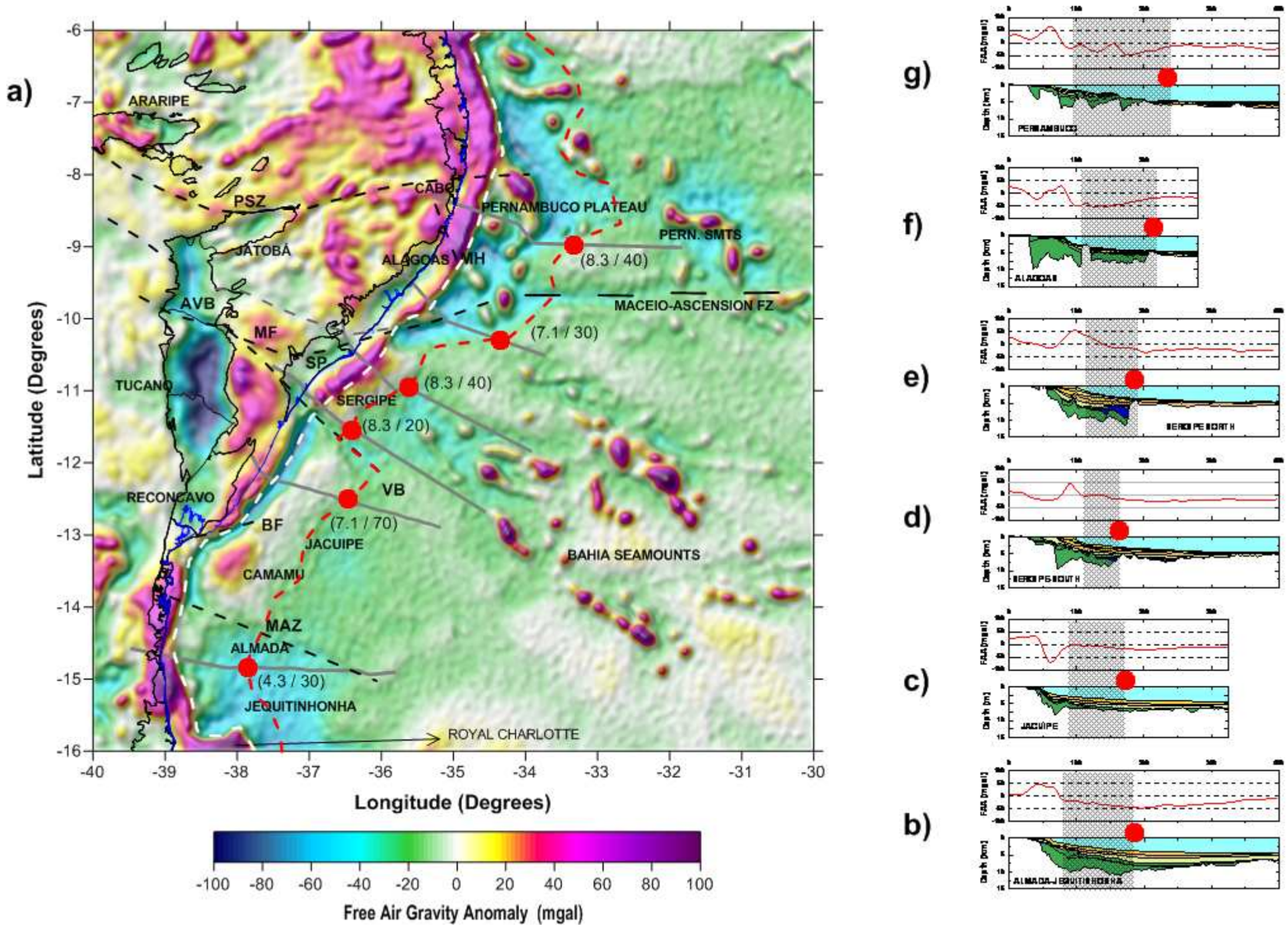

Figure 12.8. a) Free Air gravity anomaly map with the interpreted proximal limit of the OCT (white dashed line), the interpreted COCB (red dashed line), and the identified COCB locations (red circles, in parenthesis, the measured maximum amount and width of the magmatic addition). From b) to g) , cross-sections and free air gravity anomaly profiles with the identified COCB locations (red circles) and the OCT regions (hatched).

THE THIN CRUST REGION OF THE SERGIPE RIFTED MARGIN

The interpretation of the Sergipe-South and Sergipe-North cross-sections OCT by the combined numerical techniques is between the positions where antithetic faulting starts and the positions where the anomalous igneous crust blocks start (figures 12.4a, 12.5a and 12.8a, c, d). The Sergipe-South and Sergipe-North profiles show ocean-continent transitions (OCTs) with crust thinner than the adjacent oceanic crust, where the sediment-corrected basement profiles reach depths larger than the adjacent oceanic crust. The cross-sections are characterised by antithetic faulting in the OCT, coincident with a stable free-air gravimetric anomaly developed offshore from the edge effect (figure 12.8a, d, e).

Based on the RDA results for unequivocal oceanic crust segments, both crustal and lithosphere thinning inversions suggest an oceanic nature for these thinned crust regions. According to the RDA analysis and gravity inversion, the magmatic addition of 8.3 km develops in a 40-km wide region in Sergipe-South and in a 75-km wide region in Sergipe North (figures 12.4a and 12.5a), which corroborates the seismic interpretation of the seaward dipping reflectors as magmatic rocks of the oceanic crust (Mohriak et al., 1995). Seaward dipping reflectors correspond to sub-aerial extrusive igneous rocks that occur at volcanic margins (Hinz, 1981; White and McKenzie, 1989), which generally implies thick adjacent oceanic crust (10 km-thick or more). The thin crust segments of Sergipe margin are followed by blocks of thick oceanic crust probably associated with the Bahia seamounts (figure 12.8a). The preservation of the pre-rift succession and the lack of volcanism onshore and in shallow waters suggest that the St. Helena plume was not active on the margin during the rift phase. Moreover, the observed volcanism, although remarkable, cannot be associated to a large igneous province. The volcanic

mounds related to the Bahia seamounts appear to be intrusive in the syn-rift pile and of probable early post-rift age.

The RDA variation along the profiles suggests that magmatic addition can also vary during the development of a rifted margin. As a consequence, an alternative interpretation for the OCT in this margin is proposed: the thin crust segments have developed during the syn-rift with low magmatic addition, while the adjacent thick oceanic crust segments were created by increased magmatic addition after break-up time, when the St. Helena hot spot became active. However, the modelling results presented in this thesis could not refute the hypothesis that associates SDR to oceanic crust.

THE NORMAL TO SLIGHTLY MAGMA-RICH OCT OF ALAGOAS AND PERNAMBUCO

The interpretation of the Alagoas OCT by the combined numerical techniques is between 125 and 200 km of distance in the studied cross-section (figures 12.6a and 12.8a, f). Similarly to the Sergipe cross-sections, the Alagoas profile show ocean-continent transition with very thin crust, where the sediment-corrected basement profile reaches depths larger than the adjacent oceanic crust. The cross-section is characterised by antithetic and synthetic faulting in the OCT, coincident with low free air gravity anomaly that follows the edge effect. According to the RDA analysis and gravity inversion, the magmatic addition of 7.1 km develops in a 60-km wide region in Alagoas (figures 12.6a and 12.8a). The RDA in the oceanic crust suggests a normal margin, in spite of the intrusive volcanics, probably associated to the Bahia Seamounts.

The interpretation of the Pernambuco Plateau OCT by the combined numerical techniques is between 125 and 250 km of distance in the studied cross-section (figures 12.7a and 12.8a, g). Similarly to Alagoas, the cross-section is

characterised by antithetic and synthetic faulting in the OCT, coincident with low free air gravity anomaly that follows the edge effect. The RDA in the oceanic crust suggests a slightly rich margin, probably associated to the Pernambuco Seamounts that also seem to be early post-rift. According to the RDA analysis and gravity inversion, the magmatic addition of 8.3 km develops in a 40-km wide region in Pernambuco (figures 12.7a and 12.8a).

12.4 The Moho Depth Profiles

The Moho depth profiles determined by the gravity inversion are controlled by the distribution of the interpreted syn-rift pile. Moho hinges approximately coincident with the sedimentary basins hinges are configured for Jacuípe, Sergipe South and Sergipe North cross sections, which present narrow syn-rift distribution (figure 12.9c-e). The Moho depth profiles of Almada-Jequitinhonha, Alagoas and Pernambuco are smoother due to the wider distribution of syn-rift sediments (figure 12.9a, b, f and g).

12.5 The Width Variation of the Northeast Brazilian Rifted Margin

The rifted margin width, measured along the cross-sections, does not seem to vary significantly between Almada-Jequitinhonha and Sergipe North, ranging from 110 to 130 km. The COCB and COLB locations suggest that continental crust and lithosphere can extend farther offshore than the interpreted syn-rift packages in Jacuípe cross-section (figure 12.3a). So, although Jacuípe margin presents a narrow rift, the numerical analysis carried out in this study suggests that this margin can be wider. The offshore syn-rift sediments are either not imaged or have been eroded due to exhumation. In figure 12.8a, the Sergipe margin seems to be narrower, however as it extends onshore, the width is not different from the margin to the south. The Alagoas and Pernambuco margins are wider, around 170 km, in accordance with the position of the Pernambuco Plateau.

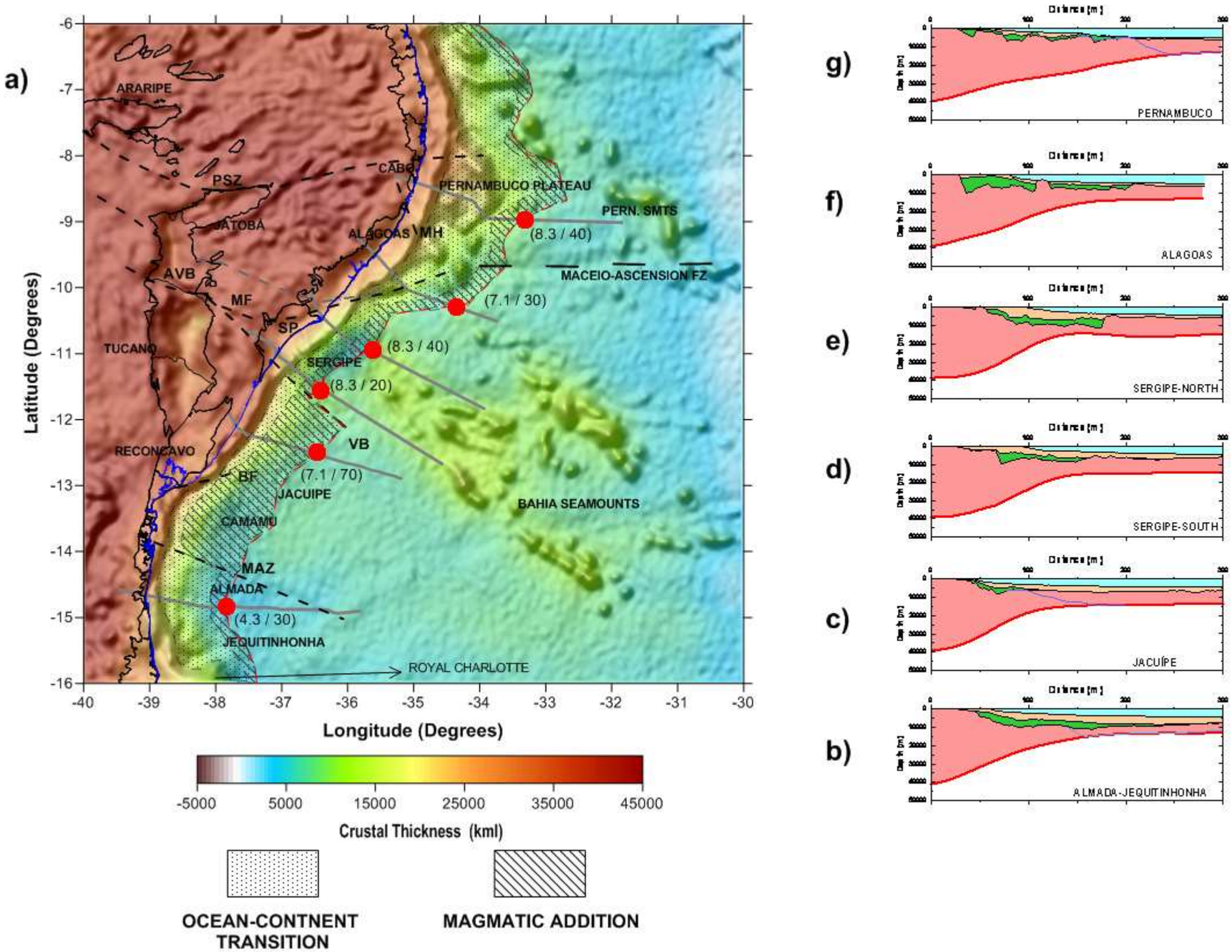

Figure 12.9. a) Crustal thickness map from gravity inversion, assuming reference crustal thickness of 38.5 km. with the interpreted OCT, the regions of magmatic addition, the interpreted, COCB (dashed red line), and the identified COCB locations (red circles, in parenthesis, the measured maximum amount and width of the magmatic addition). From b) to g) the crustal cross-sections determined by gravity inversion are shown.

12.6 CONCLUSIONS

12.6.1 METHODOLOGY AND WORKFLOW FOR THE DETERMINATION OF COCB AND COLB IN CONTINENTAL RIFTED MARGIN CROSS-SECTIONS

A workflow of numerical methods was developed to identify the ocean-continent transition (OCT) and to locate the continent-ocean crustal and lithosphere boundaries, COCB and COLB respectively, in continental rifted margins cross-sections. The workflow initially corrects the geological cross-sections for sediment loading using flexural backstripping, which results in sediment-corrected basement depth profiles.

The residual depth anomalies of the oceanic crust were determined from the sediment-corrected basement depth profiles. The inflection of RDA from higher values in the continental region of the margin to the background of the oceanic crust suggests the position of the COCB. However, this determination is not so accurate because the RDA profiles are noisy due to faults and igneous bodies. Average RDA interpreted in unequivocal segments of the oceanic crust was used to evaluate the maximum magmatic addition, which corresponds to the expected oceanic crust thickness.

Gravity inversion of the Moho was used to produce crustal thinning profiles. The gravity inversion was calibrated using RDA in order to constrain the reference Moho depth, assumed as equivalent to the initial crustal thickness. Crustal thickness is calculated from the inverted Moho depth and from the top basement. Crustal thinning is determined using the calibrated reference crustal thickness. The COCB location is interpreted to occur where γ_c=1 is reached, the position where the continental crust is completely thinned. It is assumed that crustal thickness decreases

continuously from the original continental crust thickness to the adjacent oceanic crust thickness. Crustal thinning is also controlled by a linear relationship between magmatic addition and lithosphere thinning after a lithosphere thinning threshold.

A numerical forward model to calculate total subsidence from lithosphere and crustal thinning was developed. Subsidence is calculated as the sum of the flexural isostatic response to crustal thinning and lithosphere thermal loads since continental break-up. The dissipation of the lithosphere and asthenosphere thermal anomaly was calculated by explicit finite differences. The steady state thermal equilibrium of the reference continental lithosphere was also calculated by explicit finite differences considering radiogenic heat production from the crust. The calculation of total subsidence from lithosphere thinning also incorporates the linear relationship between magmatic addition and lithosphere thinning.

In order to keep thermal and subsidence continuity from the border of a continental margin to the continent-ocean boundary (COB), two modifications were implemented in the numerical model to calculate subsidence from lithosphere and crustal thinning. Firstly, the correction for the water-loaded initial elevation is determined through the difference between the water-loaded mantle geoid and the initial subsidence of an infinitely thinned continental lithosphere. Secondly, the depth to the base of the thermal lithosphere is calculated as the average between the base of the continental lithosphere and the base of an old ocean lithosphere at the COB, weighted by the lithosphere thinning factor.

The lithosphere thinning inversions from total water-loaded subsidence profiles were calculated using the multidimensional minimization routine, Powell's Method. The minimized function corresponds to the sum of the squared differences between observed subsidence and calculated subsidence. Total subsidence is

calculated using the forward numerical model developed previously for the time after break-up. A minimum curvature of the lithosphere thinning term was added to the misfit function in order to eliminate high frequency noise.

The subsidence calculation used reference crustal thickness calibrated in the gravity inversion and maximum magmatic addition determined from the RDA. The same effective elastic thickness of 3 km, used to obtain sediment-corrected basement depth profiles, was also used in the subsidence calculation. Lithosphere thinning profiles indicate the COLB location where $\gamma_l=1$ is reached, assuming continuous increase of the sediment-corrected basement depth from the continent towards the depth of the adjacent oceanic crust.

12.6.2 Application Of The Methodology And Workflow For The Determination Of COCB And COLB For Segments Of The Northeast Brazilian Rifted Margin

The numerical methods workflow to identify the OCT and to locate the COCB and the COLB was applied to six cross-sections of the Northeast Brazilian margin, formed during the second phase of rupture of the Gondwana Supercontinent, with lithosphere stretching and thinning from 144 to 112 Ma and thermal subsidence since around 115 Ma. The cross-sections have been constructed by integration of reflection seismic sections from the sedimentary basins borders to the oceanic crust. The selected transects sample the following margin segments: Almada-Jequitinhonha, Jacuípe, Sergipe, Alagoas and Pernambuco.

The differences between the crustal and lithosphere thinning profiles of each cross-section are probably due to the smoothing applied to each profile and must be in the margin of error of the methodologies applied. The predicted COCB and COLB locations tend to be close to each other. The Northeastern Brazil margin varies from

magma-poor in the Almada-Jequitinhonha region to slightly magma-rich in Sergipe and Pernambuco, both affected by the Santa Helena Hot Spot. The RDA variation across the profiles suggests that the magmatic addition also varies across the margin. The Almada-Jequitinhonha margin can be interpreted as magma-poor based on the RDA data. The OCT corresponds to a region of antithetic faulting and low free air gravity anomaly. The COCB location suggested by the RDA and crustal thinning profiles is close to the COLB suggested by the lithosphere thinning profile.

The Jacuípe margin can be interpreted as presenting normal magmatic addition on the basis of the RDA results. The OCT corresponds to a region of development of magmatic addition, expressed in the seismic sections as seaward-dipping reflectors, and a relative high free-air gravity anomaly. Although Jacuípe margin presents a narrow rift, the numerical analysis here carried out suggests that this margin can be wider. Offshore syn-rift sediments are either not imaged or have been eroded due to exhumation.

The Sergipe margin is interpreted as magma-poor during rifting that evolved to slightly magma rich in the early post-rift, on the basis of the RDA results. The OCT corresponds to a region of continental crust thinner than the adjacent oceanic crust, of magmatic addition as seaward dipping reflectors, of antithetic faulting and of stable free-air gravity anomaly. The COCB location suggested by the RDA and crustal thinning profiles is onshore from the COCB indicated by seismic, while the COLB suggested by the lithosphere thinning profile is offshore of this position.

The Alagoas margin is interpreted as normal on the basis of the RDA results, while the Pernambuco margin is interpreted as slightly magma-rich. The OCT of both margins corresponds to a region of synthetic and antithetic faulting and low free-air gravity anomaly. Similarly to the Sergipe margin cross-sections, the COCB

location suggested by the RDA and crustal thinning profiles of Alagoas cross-section is located farther onshore from the COCB indicated by the preferred seismic, while the COLB suggested by the lithosphere thinning profile is offshore from this position. The COCB location of the Pernambuco cross-section, suggested by the RDA and crustal thinning profiles, is close to the COLB suggested by the lithosphere thinning profile.

Moho hinges coincident with the sedimentary basins hinges are configured for the cross-sections with limited distribution of syn-rift sediments, Jacuípe, Sergipe-South and Sergipe-North. The cross-sections with a wider distribution of syn-rift sediments (Almada-Jequitinhonha, Alagoas and Pernambuco) have smoother Moho profiles.

The rifted margin width, measured along the cross-sections, does not seem to vary significantly between Almada-Jequitinhonha and Sergipe North, ranging from 110 to 130 km, but it is wider in Alagoas ands Pernambuco, around 170 km.

The workflow can be considered as successful in locating the COCB and COLB positions and in identifying the OCT in the cross-sections of the Northeastern Brazil margin, although the assumptions of continuous increase of the sediment-corrected basement depth towards the oceanic crust background and of continuous decrease of continental crust thickness towards the adjacent oceanic crust thickness may not be valid in regions affected by post-rift volcanism as the Sergipe and Alagoas margins.

12.7 Further Work Suggestions

- The subsidence calculation used in the lithosphere thinning inversion assumed depth-uniform thinning. Depth-dependent thinning could be investigated

assuming the crustal thinning from gravity inversion (γ_1) and inverting for the sub-crustal thinning (γ_2).

- The model of exponential radiogenic heat decay could be revised for the studied basement segments, considering more refined crustal models that take into consideration the geology of the area.
- The lithosphere thinning inversion could be modified for 3D, similarly to the gravity inversion, using stratigraphic horizons depth maps instead of cross-sections.

APPENDIX I

THE HEAT CONSERVATION EQUATION

The Fourier Law states that the heat flow q along a limited region with thickness dz corresponds to the product of the thermal conductivity k of the material by the thermal gradient dT/dz, along the interfaces that limit the region:

$$q = -k \cdot \frac{dT}{dz}, \tag{A.1}$$

where the negative sign states that heat flows from high to low temperature interfaces. Additionally, the heat that flows into the region q_{in} and the heat that is stored in it q_{sto} must be in equilibrium with the heat that flows out q_{out} and the heat that is generated inside the region q_{gen} (Caban, 1991), figure 7.6:

$$q_{in} + q_{sto} = q_{out} + q_{gen}. \tag{A.2}$$

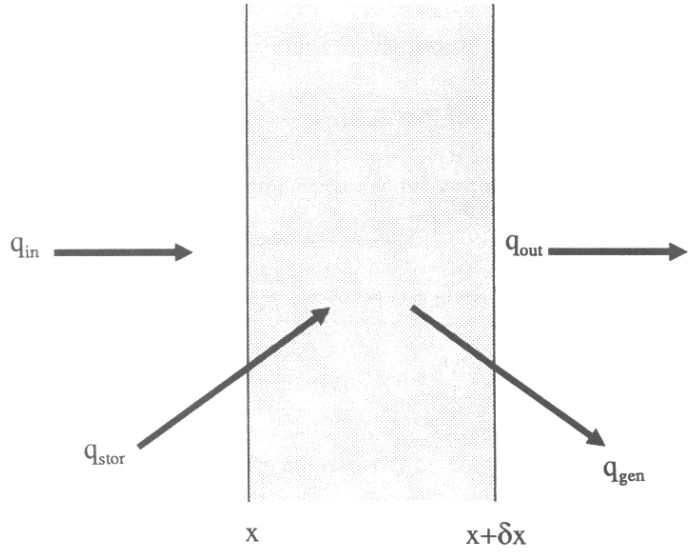

Figure A.0.1: Heat Conservation in an infinitesimal region

Solving q_{out}–q_{in} as a Taylor series (Turcotte and Schubert, 2002):

$$q_{out} - q_{in} = -k \frac{\partial^2 T}{\partial z^2} . \quad \text{(A.3)}$$

By its turn, the heat generated inside the considered region q_{gen} corresponds to the product of the heat production rate per unit of mass H by the density ρ of the medium:

$$q_{gen} = \rho H. \quad \text{(A.4)}$$

Finally, the rate of heat storage inside the region q_{sto} is given by:

$$q_{sto} = \rho \cdot C_p \cdot \frac{\partial T}{\partial t} . \quad \text{(A.5)}$$

Rearranging equation A.2 to isolate q_{sto}, the heat conservation equation is obtained as partial derivatives:

$$\rho \cdot C_p \cdot \frac{\partial T}{\partial t} = k \cdot \frac{\partial^2 T}{\partial z^2} + \rho H . \quad \text{(A.6)}$$

BIBLIOGRAPHY

Allen, P. A., and Allen, J. R., 2005, Basin Analysis: Principles and Applications, Oxford, Blackwell Science, 549 p.:

Almeida, C. B., Cruz, L. R., Jardim de Sá, E. F., Vasconcelos, P. M. P., and Medeiros, W. E., 2005, Tectônica e relações estratigráficas na Sub-bacia de Pernambuco, NE do Brasil: contribuição ao conhecimento do Rifte Sul-Atlântico: Boletim de Geociências da Petrobrás, v. 13, no. 2, p. 167-180.

Alves, E. C., and Costa, M. P. A., Interpretação Sismo-Estratigráfica da Porção Norte do Platô de Pernambuco e Suas Possíveis Correlações com a Bacia Pernambuco-Paraíba, *in* Proceedings XXXIV Congresso Brasileiro de Geologia, Goiânia, 1986, Volume 1, Sociedade Brasileira de Geologia, p. 286-297.

Asmus, H. E., and Carvalho, J. C., 1978, Condicionamento tectônico da sedimentação nas bacias marginais do nordeste brasileiro (Sergipe-Alagoas e Pernambuco-Paraíba), Projeto REMAC: Aspectos Estruturais da Margem Continental Leste e Sudeste do Brasil.: Rio de Janeiro, Petrobrás, p. 7-24.

Athy, L. F., 1930, Density, porosity and compaction of sedimentary rocks.: AAPG Bulletin, v. 14, p. 1-24.

Beaumont, C., Keen, C. E., and Boutilier, R., 1982, On the evolution of rifted continental margins - comparison of models and observations for the Nova-Scotian Margin: Geophysical Journal of the Royal Astronomical Society, v. 70, no. 3, p. 667-715.

Bott, M. H. P., 1960, The use of Rapid Digital Computing Methods for Direct Gravity Interpretation of Sedimentary Basins: Geophysical Journal of the Royal Astronomical Society, v. 3, no. 1, p. 63-67.

Bueno, G. V., 2004, Diacronismo de eventos no rifte Sul-Atlântico: Boletim de Geociências da Petrobrás, v. 12, no. 2, p. 203-229.

Caban, P. E., 1991, The Distribution of Deformation In The Lithosphere In Response To Vertical Loading And Extension [PhD Thesis 	]: University of Liverpool, 172 p.

Cainelli, C., and Mohriak, W. U., 1999, Some remarks on the evolution of sedimentary basins along the eastern Brazilian continental margin: Episodes, v. 22, no. 3, p. 206-216.

Caixeta, J. M., Milhomem, P. S., Witzke, R. E., Dupuy, I. S. S., and Gontijo, G. A., 2007, Bacia de Camamu: Boletim de Geociências da Petrobrás, v. 15, no. 2, p. 455-461.

Campos Neto, O. P. C., Lima, W. S., and Cruz, F. E. G., 2007, Bacia de Sergipe-Alagoas: Boletim de Geociências da Petrobrás, v. 15, no. 2, p. 405-415.

Carlson, R. L., and Herrick, C. N., 1990, Densities and Porosities in the Oceanic Crust and Their Variations with Depth and Age: Journal of Geophysical Research, v. 95, no. B6, p. 9153-9170.

Castro, A. C. M., 1987, The Northeastern Brazil And Gabon Basins: A Double Rifting System Associated With Multiple Crustal Detachment Surfaces.: Tectonics, v. 6, no. 6, p. 727-738.

-, 1988, Structural evolution of the Sergipe-Alagoas Basin, Brazil. [PhD Thesis: University of Rice, 183 p. p.

Chang, H. K., Kowsmann, R. O., and Figueiredo, A. M. F., 1991, Novos Conceitos Sobre o Desenvolvimento das Bacias Marginais do Leste Brasileiro., *in*

Gabaglia, G. P. R., and Milani, E. J., eds., Origem e Evolução de Bacias Sedimentares.: Rio de Janeiro,, Petrobrás, p. 269-289.

Chang, H. K., Kowsmann, R. O., Figueiredo, A. M. F., and Bender, A. A., 1992, Tectonics and stratigraphy of the East Brazil Rift System - an overview: Tectonophysics, v. 213, no. 1-2, p. 97-138.

Chappell, A. R., and Kusznir, N. J., 2008, Three-dimensional gravity inversion for Moho depth at rifted continental margins incorporating a lithosphere thermal gravity anomaly correction: Geophysical Journal International, v. 174, no. 1, p. 1-13.

Christensen, N. I., and Mooney, W. D., 1995, Seismic velocity structure and composition of the continental crust: A global view: J. Geophys. Res., v. 100, no. B6, p. 9761-9788.

Cordani, U. G., Brito Neves, B. B., Fuck, R. A., Porto, R., Thomaz Fo, A., and Cunha, F. M. B., 1984, Estudo preliminar de integração do Pré-Cambriano com os eventos tectônicos das bacias sedimentares brasileiras.: Rio de Janeiro, PETROBRAS/CENPES, p. 70 p.

Crosby, A. G., and McKenzie, D., 2009, An analysis of young ocean depth, gravity and global residual topography: Geophysical Journal International, v. 178, no. 3, p. 1198-1219.

Crosby, A. G., McKenzie, D., and Sclater, J. G., 2006, The relationship between depth, age and gravity in the oceans: Geophysical Journal International, v. 166, no. 2, p. 553-573.

Cruz, L. R., 2008, Caracterização Tectono-Estratigráfica da Seqüência Transicional na Sub-Bacia de Sergipe [PhD: UFRN, 169 p.

Davis, M., and Kusznir, N. J., Depth-dependent lithospheric stretching at rifted continental margins., *in* Proceedings NSF Rifted Margins Theoretical Institute, New York, 2004, Columbia University Press, p. 92–136.

de Wit, M. J., de Brito Neves, B. B., Trouw, R. A. J., and Pankhurst, R. J., 2008, Pre-Cenozoic correlations across the South Atlantic region: (the ties that bind): Geological Society, London, Special Publications, v. 294, no. 1, p. 1-8.

Divins, D. L., 2004, NGDC Total Sediment Thickness of the World's Oceans & Marginal Seas, Natl. Geophys. Data Cent.

D'el-Rey Silva, L. J. H., 1995, Tectonic evolution of the Sergipano Belt, NE Brazil: Tectonic implications: Revista Brasileira de Geociências, v. 25, no. 3, p. 185-202.

ENCAL S/A, E. C. E. A., 1978, Projeto Baixo São Francisco: Levantamento Aeromagnetométrico e Aerogamaespectrométrico. Relatório Final, Texto e Anexos Ministério das Minas e Energia, Departamento Nacional da Produção Mineral-DNPM, Companhia de Pesquisa de Recursos Minerais - CPRM, Convênio DNPM/CPRM.

Estrella, G. O., O Estágio Rift Nas Bacias Marginais Do Leste Brasileiro, *in* Proceedings XXVI Congresso Brasileiro de Geologia, Belém, Brazil, 1972, Volume 3, Sociedade Brasileira de Geologia, p. 29-34.

Falvey, D. A., 1974, The development of continental margins in plate tectonic theory.: The APEA Journal, v. 14, p. 95-107.

Farlow, S. F., 1993, Partial Differential Equations for Scientists and Engineers, Oxford, Dover Publications, Inc., 414 p.:

Fletcher, R., Kusznir, N., and Cheadle, M., 2009, Melt initiation and mantle exhumation at the Iberian rifted margin: Comparison of pure-shear and

upwelling-divergent flow models of continental breakup: Comptes Rendus Geosciences, v. 341, no. 5, p. 394-405.
Garcia, A. J. V., 1991, Paleogeografia do Nordeste Brasileiro no Jurássico Superior-Cretáceo Inferior: Geociências, v. 10, p. 37-56.
Gladczenko, T. P., Hinz, K., Eldholm, O., Meyer, H., Neben, S., and Skogseid, J., 1997, South Atlantic volcanic margins: Journal of the Geological Society, v. 154, p. 465-470.
Gomes, P. O., 2005, Tectonismo, Vulcanismo, Sedimentação e Processos Erosivos no Segmento Nordeste da Margem Continental Brasileira [PhD: UERJ, 184 p.
Gomes, P. O., Gomes, B. S., Palma, J. J. C., Jinno, K., and Souza, J. M., 2000, Ocean-Continent Transition and Tectonic Framework of the Oceanic Crust at the Continental Margin off NE Brazil: Results of LEPLAC Project, *in* Mohriak, W., and Talwani, M., eds., Atlantic Rifts and Continental Margins, Geological Society and American Geophysical Union, p. 331-354.
Greenhalgh, E. E., and Kusznir, N. J., 2007, Some Evidence for thin oceanic crust on the extinct Aegir Ridge, Norwegiab Basin, NE Atlantic derived from satellite gravity inversion: Geophysical Research Letters, v. 34, p. 1-5.
Hamsi, G. P. J., 1998, Investigação sobre a Extensão Litosférica da Bacia Sergipe-Alagoas [Masters Dissertation: UFOP, 185 p.
-, Modelo de Rifteamento Oblíquo na Bacia Sergipe-Alagoas, *in* Proceedings XLIII Congresso Brasileiro de Geologia, Aracaju, Brazil, 2006, Sociedade Brasileira de Geologia, p. 14.
Hamsi, G. P. J., Barros, F. A. R., Buonora, M. P. P., and Cortes, M. H., 2004, Modelo Crustal e Geotermal da Sub-Bacia Sergipe: Petrobras.
Hamsi, G. P. J., and Karner, G. D., Implicações do modelo de distensão litosférica dependente da profundidade na Bacia Sergipe-Alagoas, *in* Proceedings XLIII Congresso Brasileiro de Geologia, Aracaju, 2006, SBG, p. 9.
Hamsi, G. P. J., Karner, G. D., and Barros, F. A. R., A Crosta Transicional da Bacia Sergipe-Alagoas, *in* Proceedings XLIII Congresso Brasileiro de Geologia, Aracaju, 2006, Sociedade Brasileira de Geologia, p. 17.
Hellinger, S. J., and Sclater, J. G., 1983, Some comments on 2-layer extensional models for the evolution of sedimentary basins: Journal of Geophysical Research, v. 88, no. NB10, p. 8251-8269.
Hinz, K., 1981, A Hypothesis On Terrestrial Catastrophes: Wedges Of Very Thick Oceanward Dipping Layers Beneath Passive Continental Margins.: Geol. Jarb., v. E22, p. 3-28.
Jackson, M. P. A., Cramez, C., and Fonck, J.-M., 2000, Role of subaerial volcanic rocks and mantle plumes in creation of South Atlantic margins: implications for salt tectonics and source rocks: Marine and Petroleum Geology, v. 17, no. 4, p. 477-498.
Jarvis, G. T., and McKenzie, D., 1980, The development of sedimentary basins with finite extension rates: Earth and Planetary Science Letters, v. 48, p. 42-52.
Jaupart, C., and Mareschal, J. C., 1999, The thermal structure and thickness of continental roots: Lithos, v. 48, no. 1-4, p. 93-114.
Karner, G. D., and Driscoll, N. W., 1999, Style, timing and distribution of tectonic deformation across Exmouth Plateau, northwest Australia, determined from stratal architecture and quantitative basin modelling, Continental Tectonics: London, p. 271-311.

Karner, G. D., Driscoll, N. W., and Barker, D. H. N., 2003, Syn-rift regional subsidence across the West African continental margin: The role of lower plate ductile extension, *in* Arthur, T., Macgregor, D., and Cameron, N. R., eds., Petroleum Systems and Evolving Technologies in African Exploration and Production: London, The Geological Society, p. 105–129.

Karner, G. D., Driscoll, N. W., McGinnis, J. P., Brumbaugh, W. D., and Cameron, N. R., 1997, Tectonic significance of syn-rift sediment packages across the Gabon-Cabinda continental margin: Marine and Petroleum Geology, v. 14, no. 7/8, p. 973-1000.

Karner, G. D., Egan, S. S., and Weissel, J. K., 1992, Modeling the tectonic development of the Tucano and Sergipe-Alagoas rift basins, Brazil: Tectonophysics, v. 215, no. 1-2, p. 133-160.

Kearey, P., and Vine, J. V., 1996, Basin Analysis: Principles and Applications, Blackwell Science, 333 p.:

Korenaga, T., and Korenaga, J., 2008, Subsidence of normal oceanic lithosphere, apparent thermal expansivity, and seafloor flattening: Earth and Planetary Science Letters, v. 268, no. 1-2, p. 41-51.

Kusznir, N. J., and Karner, G. D., 1985, Dependence of the flexural rigidity of the continental lithosphere on rheology and temperature: Nature, v. 316, p. 138-142.

-, 2007, Continental lithospheric thinning and breakup in response to upwelling divergent mantle flow: application to the Woodlark, Newfoundland and Iberia margins, *in* Karner, G. D., Manatschal, G., and Pinheiro, L. M., eds., Imaging, Mapping and Modelling Continental Lithosphere Extension and Breakup, Volume 282: London, The Geological Society of London, p. 389–419.

Kusznir, N. J., Marsden, G., and Egan, S. S., 1991, A flexural-cantilever simple-shear/pure-shear model of continental lithosphere extension: applications to the Jeanne D'Arc basin, Grand banks and Viking Graben North Sea, *in* Roberts, A. M., Yielding, G., and Freeman, B., eds., Geometry of Normal Faults: London, The Geological Society, p. 41-60.

Kusznir, N. J., Roberts, A. M., and Morley, C., 1995, Forward and reverse modelling of rift basin formation, *in* Lambiase, J., ed., Hydrocarbon Habitat in Rift Basins: London, The Geological Society, p. 33–56.

Kuznir, N. J., and Park, R. G., 1987, The Extensional Strength Of The Continental Lithosphere: Its Dependence On Geothermal Gradient, And Crustal Composition And Thickness, *in* Coward, M. P., Dewey, J. F., and Hancock, P. L., eds., Continental Extensional Tectonics.: London, The Geological Society of London, p. 32-52.

Lachenbruch, A. H., and Morgan, P., 1990, Continental extension, magmatism and elevation; formal relations and rules of thumb: Tectonophysics, v. 174, no. 1-2, p. 39-62.

Lana, M. C., 1985, Rifteamento na Bacia Sergipe-Alagoas, Brasil. [Masters Dissertation: UFOP, 124 p.

-, 1991, Bacia Sergipe-Alagoas: uma Hipótese de Evolução Tectono-Sedimentar, *in* Gabaglia, G. R., and Milani, E. J., eds., Origem e Evolução das Bacias Sedimentares: Rio de Janeiro, Petrobras, p. 311-332.

Le Pichon, X., and Sibuet, J. C., 1981, Passive Margins - A Model Of Formation: Journal of Geophysical Research, v. 86, no. NB5, p. 3708-3720.

Long, L. E., Sial, A. N., Nekvasil, H., and Borba, G. S., 1986, Origin of granite at Cabo de Santo Agostinho, Northeast Brazil.: Contributions to Mineralogy and Petrology, v. 92, no. 3, p. 341-350.

Magnavita, L. P., and da Silva, H. T. F., 1995, Rift Border System: The Interplay Between Tectonics and Sedimentation in the Reconcavo Basin, Northeastern Brazil: AAPG Bulletin, v. 79, no. 11, p. 1590-1607.

Magnavita, L. P., Davison, I., and Kusznir, N. J., 1994, Rifting, erosion, and uplift history of the Recôncavo-Tucano-Jatobá Rift, northeast Brazil: Tectonics, v. 13, no. 2, p. 367-388.

Manatschal, G., 2004, New models for evolution of magma-poor rifted margins based on a review of data and concepts from West Iberia and the Alps: International Journal of Earth Sciences, v. 93, no. 3, p. 432-466.

Mareschal, J. C., and Jaupart, C., 2004, Variations of surface heat flow and lithospheric thermal structure beneath the North American craton: Earth and Planetary Science Letters, v. 223, no. 1-2, p. 65-77.

Marshak, S., 2008, Earth: Portrait of a Planet, W.W. Norton and Company.

Matos, R. M. D., 1999, History of the northeast Brazilian rift system: kinematic implications for the break-up between Brazil and West Africa, *in* London, T. G. S. o., ed., The Oil and Gas Habitats of the South Atlantic: London, p. 55-73.

McKenzie, D., 1978, Some remarks on the development of sedimentary basins.: Earth and Planetary Science Letters, v. 40, p. 25-32.

McKenzie, D., and Bickle, M. J., 1988, The volume and composition of melt generated by extension of the lithosphere: Journal of Petrology, v. 29, no. 3, p. 625-679.

McKenzie, D., Jackson, J., and Priestley, K., 2005, Thermal structure of oceanic and continental lithosphere: Earth and Planetary Science Letters, v. 233, no. 3-4, p. 337-349.

Menezes, P. E., and Milhomem, P. S., 2008, Tectônica de Sal nas Bacias de Cumuruxatiba, de Almada e de Camamu, *in* Mohriak, W., Szatmari, P., and Anjos, S. M. C., eds., Sal: Geologia e Tectônica. Exemplos nas Bacias Brasileiras: Rio de Janeiro, p. 250-271.

Milani, E. J., and Davison, I., 1988, Basement control and transfer tectonics in the Recôncavo-Tucano-Jatobá rift, Northeast Brazil: Tectonophysics, v. 154, no. 1-2, p. 41-50.

Milani, E. J., Rangel, H. D., Bueno, G. V., Stica, J. M., Winter, W. R., Caixeta, J. M., Pessoa Neto, O. C., and Campos Neto, O. P. C., 2007, Bacias Sedimentares Brasileiras - Cartas Estratigráficas. Introdução: Boletim de Geociências da Petrobrás, v. 15, no. 2, p. 183-205.

Mohriak, W., Bassetto, M., and Vieira, I. S., 2000, Tectonic Evolution of the Rift Basins in the Northeastern Brazilian Region, *in* Mohriak, W., and Talwani, M., eds., Atlantic Rifts and Continental Margins, Geological Society and American Geophysical Union, p. 293-315.

Mohriak, W. U., Bassetto, M., and Vieira, I. S., 1998, Crustal architecture and tectonic evolution of the Sergipe-Alagoas and Jacuípe basins, offshore northeastern Brazil: Tectonophysics, v. 288, p. 199-220.

Mohriak, W. U., Lira Rabelo, J. H., De Matos, R. D., and De Barros, M. C., 1995, Deep seismic reflection profiling of sedimentary basins offshore Brazil: Geological objectives and preliminary results in the Sergipe Basin: Journal of Geodynamics, v. 20, no. 4, p. 515-539.

Moulin, M., Aslanian, D., and Unternehr, P., 2010, A new starting point for the South and Equatorial Atlantic Ocean: Earth-Science Reviews, v. 98, no. 1-2, p. 1-37.

Mutter, J. C., Buck, W. R., and Zehnder, Z. M., 1988, Convective partial melting 1: A model for the formation of thick basaltic sequences during the initiation of spreading.: Journal of Geophysical Research, v. B2, no. 93, p. 1031-1048.

Müller, R. D., Sdrolias, M., Gaina, C., and Roest, W. R., 2008, Age, Spreading Rates, and Spreading Asymmetry of the World's Ocean Crust: Geochemistry Geophysics Geosystems, v. 9, no. 4, p. 1-19.

Nadin, P. A., and Kusznir, N. J., 1995, Paleocene uplift and Eocene subsidence in the northern North Atlantic from 2D forward and reverse stratigraphic modelling: Journal of the Geological Society, v. 152, p. 833–848.

Nascimento, M. A. L., and Souza, Z. S., 2005, Cabo de Santo Agostinho Granite, State of Pernambuco - The Only Known Cretaceous Granite in Brazil., *in* Winge, M., Schobbenhaus, C., Berbert-Born, M., Queiroz, E. T., Campos, D. A., Souza, C. R. G., and Fernandes, A. C. S., eds., Geological and Palaeontological Sites of Brazil.

Nürnberg, D., and Müller, R. D., 1991, The tectonic evolution of the South Atlantic from Late Jurassic to present: Tectonophysics, v. 191, no. 1-2, p. 27-53.

O'Connor, J. M., and Le Roex, A. P., 1992, South-Atlantic hot spor-plume systems: 1. Distribution of volcanism in time and space: Earth and Planetary Science Letters, v. 113, p. 343-364.

Oliveira, R. G., Medeiros, W. G., and Lins, F. A. P. L., Mapas Gravimétricos da Província Borborema, Nordeste do Brasil, *in* Proceedings II Simpósio Brasileiro de Geofísica, Natal, 2006, Sociedade Brasileira de Geofísica, p. 6.

Palma, J. J. C., 1984, Fisiografia da área oceânica, *in* Schobbenhaus, S., Campos, D. A., Derze, G. R., And Asmus, H. E., eds., Geologia do Brasil: Texto Explicativo do Mapa Geológico do Brasil e da Área Oceânica Adjacente Incluindo Depósitos Minerais, Escala 1:2500000.: Brasília, DGM/DNPM, p. 429-441.

Parker, R. L., 1973, The Rapid Calculation of Potential Anomalies: Geophysical Journal of the Royal Astronomical Society, v. 31, no. 4, p. 447-455.

Parsons, B., and Sclater, J. G., 1977, Analysis of variation of ocean-floor bathymetry and heat-flow with age: Journal of Geophysical Research, v. 82, no. 5, p. 803-827.

Pickup, S. L. B., Whitmarsh, R. B., Fowler, C. M. R., and Reston, T. J., 1996, Insight into the nature of the ocean–continent transition off West Iberia from a deep multichannel seismic reflection profile: Geology, v. 24, p. 1079–1082.

Pontes, C. E. S., Castro, F. C. C., Rodrigues, J. J. G., Alves, R. R. P., Castellani, R. T., Santos, S. F., and Monis, M. B., Reconhecimento tectônico e estratigráfico da Bacia Sergipe-Alagoas em águas profundas., *in* Proceedings II Congresso Brasileiro de Geofísica, Salvador, 1991, Volume 11, SBGf, p. 638-643.

Press, F., Siever, R., Grotzinger, J., and Jordan, T. H., 2004, Understanding Earth, New York, W. H. Freeman and Co., 567 p.:

Press, W. H., Teukolsky, S. A., Vetterling, W. T., and Flannery, B. P., 2007, Numerical recipes in Fortran 90: the art of parallel scientific computing, Cambridge, Cambridge University Press, 1234 p.:

Rangel, H. D., Oliveira, J. L. F., and Caixeta, J. M., 2007, Bacia de Jequitinhonha: Boletim de Geociências da Petrobrás, v. 15, no. 2, p. 475-483.

Reston, T. J., 2009, The extnsion discrepancy and syn-rift subsidence deficit at rifted margins: Petroleum Geoscience, v. 15, p. 217-237.

Roberts, A. M., Kusznir, N. J., Yielding, G., and Styles, P., 1998, 2D Flexural Backstripping Of Extensional Basins: The Need For A Sideways Glance: Petroleum Geoscience, v. 4, p. 327-338.

Rosendahl, B. R., Mohriak, W. U., Odegard, M. E., Turner, J. P., and Dickson, W. G., 2005, West Africa and Brazilian conjugate margins: crustal types, architecture, and plate configurations., 25th Bob F. Perkins Research Conference, Petroleum Systems of Divergent Continental Margin Basins: Houston, Texas, United States.

Royden, L., and Keen, C. E., 1980, Rifting process and thermal evolution of the continental margin of eastern Canada determined from subsidence curves.: Earth and Planetary Science Letters, v. 51, p. 343–356.

Rybach, L., 1986, Amount and significance of radioactive heat sources in sediments, *in* Burrus, J., ed., Thermal Modelling in Sedimentary Basins, Collection Colloques et Seminaires, Volume 44: Paris, Editions Technip.

Sandwell, D. T., and Smith, W. H. F., 1997, Marine gravity anomaly from Geosat and ERS-1 satellite altimetry: Journal of Geophysical Research, v. 102, no. B5, p. 10039-10054.

-, 2009, Global marine gravity from retracked Geosat and ERS-1 altimetry: Ridge segmentation versus spreading rate: J. Geophys. Res., v. 114, no. B1, p. B01411.

Sapucaia, N. J., Argollo, R. M., and Barbosa, J. S. F., 2005, Teores de Potássio, Urânio, Tório e Taxa de Produção de Calor Radiogênico no Embasamento Adjacente às Bacias Sedimentares de Camamu e Almada, Bahia, Brasil: Revista Brasileira de Geofísica, v. 23, no. 4, p. 453-475.

Sclater, J. G., and Christie, P. A. F., 1980, Continental stretching - an explanation of the Post-Mid-Cretaceous subsidence of the Central North-Sea Basin: Journal of Geophysical Research, v. 85, no. NB7, p. 3711-3739.

Sclater, J. G., Parsons, B., and Jaupart, C., 1981, Oceans and continents: similarities and differences in the mechanism of heat loss: Journal of Geophysical Research, v. 86, no. B12, p. 11535-11552.

Skogseid, J., 2001, Volcanic margins: geodynamic and exploration aspects: Marine and Petroleum Geology, v. 18, p. 457-461.

Stein, C. A., and Stein, S., 1992, A model for the global variation in oceanic depth and heat flow with lithospheric age: Nature, v. 359, no. 6391, p. 123-129.

Storey, B. C., 1995, The role of mantle plumes in continental breakup: case histories from Gondwanaland: Nature, v. 377, no. 28, p. 301-308.

Turcotte, D. L., Haxby, W. F., and Ockendon, J. R., 1977, Lithospheric instabilities, *in* Talwani, M., and Pitman III, W. C., eds., Island arcs, deep sea trenches and back-arc basins, Volume 1: Washington, D. C., American Geophysical Union, p. 63-69.

Turcotte, D. L., and Schubert, G., 2002, Geodynamics, Cambridge, Cambridge University Press, 456 p.:

Turner, J. P., Rosendahl, B. R., and Wilson, P. G., 2003, Structure and evolution of an obliquely sheared continental margin: Rio Muni, West Africa: Tectonophysics, v. 374, no. 1-2, p. 41-55.

Ussami, N., Karner, G. D., and Bott, M. H. P., 1986, Crustal detachment during South Atlantic rifting and formation of Tucano[mdash]Gabon basin system: Nature, v. 322, no. 6080, p. 629-632.

van Schmus, W. R., Oliveira, E. P., da Silva Filho, A. F., Toteu, S. F., Penaye, J., and Guimaraes, I. P., 2008, Proterozoic links between the Borborema Province, NE Brazil, and the Central African Fold Belt: Geological Society, London, Special Publications, v. 294, no. 1, p. 69-99.

Watts, A. B., 2001, Isostasy ans Flexure of the Lithosphere, Cambridge, Cambridge University Press, 458 p.:

Weissel, J. K., and Karner, G. D., 1989, Flexural uplift of rift flanks due to mechanical unloading of the lithosphere during distension: Journal of Geophysical Research, v. 94, no. B10, p. 13919-13950.

Wernicke, B., 1985, Uniform-sense normal simple shear of the continental lithosphere: Canadian Journal of Earth Sciences, v. 22, p. 108-125.

White, R., and McKenzie, D., 1989, Magmatism at rift zones - the generation of volcanic continental margins and flood basalts: Journal of Geophysical Research-Solid Earth and Planets, v. 94, no. B6, p. 7685-7729.

White, R. S., McKenzie, D., and Onions, R. K., 1992, Oceanic crustal thickness from seismic measurements and rare-earth element inversions: Journal of Geophysical Research-Solid Earth, v. 97, no. B13, p. 19683-19715.

White, R. S., Smith, L. K., Roberts, A. W., Christie, P. A. F., and Kusznir, N. J., 2008, Lower-crustal intrusion on the North Atlantic continental margin: Nature, v. 452, no. 7186, p. 460-464.

White, R. S., Spence, G. D., Fowler, S. R., McKenzie, D. P., Westbrook, G. K., and Bowen, A. N., 1987, Magmatism at rifted continental margins: Nature, v. 330, no. 6147, p. 439-444.

Whitmarsh, R. B., Manatschal, G., and Minshull, T. A., 2001, Evolution of magma-poor continental margins from rifting to sea-floor spreading: Nature, v. 413, p. 150–153.

Wilson, M., 1992, Magmatism and continental rifting during the opening of the South Atlantic Ocean: a consequence of Lower Cretaceous super plume activity?, Magmatism and the Causes of continental Break-up.: London, p. 241-255.